# POLITECNICO DI TORINO

MASTER's Degree in Energy and Nuclear Engineering


MASTER's Degree Thesis

# Numerical validation of the ECCO self-shielding model for LFR cells

Supervisors

Prof. Sandra DULLA

Nicolò ABRATE Ph.D.

Matteo FALABINO Ph.D.

Candidate

Leonardo DEL PICCOLO

OCTOBER 2025

# Acknowledgments

This study is the result of a collaboration with *new*cleo S.p.A. during an internship programme. I would like to express my sincere gratitude to all my colleagues at *new*cleo who supported me during my time there and that made an essential contribution to this work. In particular, I would like to thank Matteo Falabino, for his constant support, motivation, and guidance. His contribution — not only on the technical side, but also, and most importantly, on the human side — made this work possible. I am also deeply grateful to Gérald Rimpault for his valuable suggestions and for sharing his exceptional knowledge and experience in the field of nuclear engineering. My thanks also go to Daniele Tomatis and Sigtryggur Hauksson for their valuable feedback and assistance with this study. Finally, my heartfelt thanks to Nicolò Abrate and Sandra Dulla for their support and dedication during my two years at Politecnico di Torino.

As this study marks the end of a memorable and joyful university journey, I wish to express my gratitude to my colleagues, professors, and friends that shared their path with mine, even if only for a brief moment. Although a few words will never be enough to fully express it, my deepest gratitude goes to my family and to Benedetta, for being by my side every step of the way.

# Abstract

Following the Generation IV International Forum, interest in advanced reactor systems based on liquid metal cooling increased significantly in the last years. This has led to a greater demand for deterministic tools that can guarantee reliable results at a low computational cost. The ECCO cell code, adopted by the *new*cleo company for the design of its LFR units, produces condensed and homogenised cross sections for subsequent core calculations in ERANOS. Although ECCO was extensively validated for sodium fast reactor applications in the past, more limited studies have been carried out so far for lead fast reactors. The same applies to the generation of the input nuclear data libraries for the ECCO code.

This thesis aims at numerically validating the ECCO self-shielding module. The module is implemented in the code to perform energy averaging of cross sections within resonance intervals, to simplify their numerical integration. The first part of this work focuses on the analytical description of the methods employed in ECCO and the creation of nuclear data libraries. The second part delves into the numerical validation of the code by comparing LFR cell simulations with a Monte Carlo reference. This work shows that, when excessive discrepancies are found, they are mostly related to the processing of the nuclear data libraries rather than the numerical schemes in the code. Sensitivity and decomposition analyses are employed to evaluate the impact of such discrepancies. Ultimately, the processing scheme for preparing nuclear data libraries for ECCO is implemented and revised, suggesting solutions that could ease the validation process.

Hopefully, the findings of this study will contribute to upgrading and modernising the systems of codes for preparing nuclear data libraries for the ECCO code. This would lay the foundation for any subsequent validation activity on the ECCO code for lead coolant systems.

# Index

# List of Figures

# List of Tables

# Introduction

Over the last two decades, renewed interest in Generation IV nuclear fission reactors has grown rapidly following the Generation IV International Forum (GIF). Classified by the GIF into six main categories, these reactors aim at providing sustainable and safe energy at a low cost [1]. Among these categories are fast-spectrum reactors. This technology exploits the high energy content of uranium fuel through the breeding process, in which uranium isotopes undergo neutron capture and transmute into fissile isotopes such as Pu-239. In conventional thermal reactors, the once-through cycle exploits only a small percentage of uranium resources corresponding to the fissile U-235 isotope, which makes up just 0.7 % of natural uranium. At the end of the irradiation cycle, the non-fissile materials account for the radioactive waste that must be stored safely. Due to parasitic absorptions in U-238, plutonium isotopes tend to accumulate in the fuel. The resulting mixture of uranium and plutonium isotopes can be processed into Mixed Oxide Fuels (MOX) for the subsequent refuelling of both thermal and fast reactors. Fast reactors in particular enhance the energy release of MOX fuel through the fission of plutonium isotopes induced by fast neutrons, whose contribution is limited in thermal reactors. Therefore, fast reactors have the advantage of closing the fuel cycle, meaning that they can be refuelled with the residual material from thermal reactors, thereby making better use of the world's natural uranium reserves. Furthermore, the fast neutron spectrum can induce fission reactions in transuranic elements, such as americium and curium, thereby reducing the volume of nuclear waste. However, to achieve this, neutrons must not be moderated within the core. The most promising solution is to use liquid metals as coolants, whose heavy atoms prevent significant energy loss in collision with them. Depending on whether liquid lead or sodium is used as coolant, these reactors are classified as Lead Fast Reactors (LFR) or Sodium Fast Reactors (SFR), respectively.

In this context, the *new*cleo company aims at developing Small Modular Rectors (SMR) based on lead coolant technology. SMRs are small-scale units with limited output power (typically between 10 and 300 MWe), which can be manufactured in modules and assembled at the installation site. This could potentially solve the issues of construction delays and cost overruns that have affected the nuclear industry in recent years [2, 3]. For the design of its LFR units, *new*cleo adopted the ERANOS code and data system for neutronic calculations [4]. Developed by the Commissariat à l'Energie Atomique (CEA), the ERANOS system was employed for analysis and design of liquid-metal fast reactors. It includes transport codes, nuclear data libraries, and the ECCO cell and lattice code. The latter is the code used to generate energy-averaged and homogenised cross sections, calculated at the lattice level, for subsequent use in full core calculations [5]. To achieve this, the code relies on the Collision Probability (CP) method to determine the spatial distribution of flux in two-dimensional subassemblies. Furthermore, accurate treatment of resonant cross sections is performed using a fine energy group structure (1968 groups) alongside the Subgroup method. This method employs intra-group data within energy groups where resonances occur. Multigroup cross sections and subgroup data are included in the Nuclear Data Libraries (NDL), which are processed for ECCO by means of external codes, such as NJOY and CALENDF.

The Autorité de Sûreté Nucléaire (ASN) requires Scientific Computing Tools (SCT) that are used for safety studies to be validated within an assessed validity Range. This range includes

variations in geometrical and physical parameters that describe the evolution of relevant physical phenomena, for which the results of the SCT are assessed with a satisfactory accuracy [6]. Since the ERANOS release, the ECCO code has been extensively validated for SFR applications [5, 7, 8, 9]. In fact, ERANOS was originally developed as a primary tool to support the design and deployment of SFRs in France at the end of the last century. However, since the end of the Superphénix campaign, the ERANOS system has not undergone significant development. The same applies to the external tools for generating NDLs in the ECCO format. Furthermore, limited studies have been conducted so far to validate ECCO for LFR applications [10].

During previous ECCO validation studies, significant discrepancies were found between the ECCO and Monte Carlo results for LFR cells [11]. These differences are larger than those typically observed for SFR cells [9] and require further investigation to determine their origin. The aim of this thesis is to extend the previous numerical validation works performed on ECCO for LFR cells and to determine the cause of these discrepancies. A complete numerical validation of a neutronic code involves assessing the errors related to the uncertainties in the experimental nuclear data and to the resolution schemes[1]. Furthermore, the numerical validation is carried out by comparison with a reference SCT, such as a Monte Carlo code, provided the predictive performance of the latter is superior to that of the SCT being validated [6]. In the context of this thesis, the numerical validation will be performed on the ECCO self-shielding model, using the OpenMC Monte Carlo code as a reference. This will be carried out using the ENDF/B-VIII.0 ECCO library, which is the result of an independent evaluation. The reason for conducting the validation on a single module rather than the entire code is to identify the errors related to the individual components of the code, thereby decomposing the discrepancy observed between the ECCO and Monte Carlo results into its constituent parts. Indeed, validating the code for highly simplified cells rules out other numerical modules' contributions, leaving the self-shielding module as the sole potential source of error. As will be revealed from the analysis, the self-shielding module alone is sufficient to explain most of the discrepancy between ECCO and the Monte Carlo code.

The main contents of this thesis are organised as follows. The first three chapters delve into the analytical descriptions of the numerical models underlying the ECCO code. The first chapter provides an overview of some of the most popular mathematical models of the physical laws governing the transport of neutrons in a nuclear reactor. The second chapter then provides a description of the ECCO code and how the previous analytical models are applied within it. Finally, the third chapter illustrates the procedures for generating ECCO and OpenMC NDLs.

The second part of this work is dedicated to the validation of the ECCO self-shielding model. Chapter four presents the results of the sensitivity analysis conducted on a case study representative of LFR applications, namely the Nuclear Energy Agency (NEA) Lead-cooled Fast Reactor Benchmark [12]. Based on these findings, chapter five presents the results of the numerical validation of the ECCO self-shielding module. Where significant errors are found, chapter six assesses their effect on variables of interest for design purposes, such as the multiplication factor and Doppler reactivity change. This is performed through a decomposition analysis, which uses the results of the two previous chapters in conjunction. Finally, chapter seven outlines a potential procedure to mitigate the observed errors by modifying the reference procedures for generating ECCO libraries.

[1] G. Rimpault, private communication

# Part I

# Theoretical background

## Chapter 1

# Theoretical Background

The physical phenomena occurring in a nuclear fission reactor are described by the Neutron Transport Equation, which governs the behaviour of neutrons within the fuel, the coolant, and other media. Several approximations are typically introduced in a deterministic code to enable the transport equation to be solved numerically. The following provides an insight into the main steps that deterministic codes usually take to solve a criticality problem. This information will guide in understanding the way the ECCO cell code solves the physical problem, and the impact that each approximation has on the accuracy of the final solution.

## 1.1 The transport equation

The main purpose of a neutronic code is the solution of the Boltzmann equation, also known as the Neutron Transport Equation. This equation represents the linearisation of the Boltzmann kinetic theory under the hypothesis that neutrons never collide among them, which is indeed an extremely rare event in a nuclear reactor. Nevertheless, the preferred approach to derive the transport equation is a balance on the average number of neutrons contained within an infinitesimal volume of a six-dimensional phase space at a given instant in time [13, 14, 15], i.e.

$$n(\overline{r}, E, \overline{\Omega}, t)\ dV\ dE\ d\Omega, \tag{1.1}$$

where $n(\overline{r}, E, \overline{\Omega}, t)$ is the neutron angular density, which defines the expected number of neutrons per unit of volume $V$, energy $E$, and solid angle $\overline{\Omega}$ at time $t$ [14]. The interactions of neutrons with the medium are described by a quantity denoted as the microscopic cross section, $\sigma_x(E, \overline{\Omega}, t)$, which is related to the probability of a neutron undergoing a reaction $x$ with a nucleus. This quantity is actually the effective cross sectional area seen by the neutron colliding with the nucleus (which depends on the specific reaction and isotope and does not necessarily coincide with the geometric surface opposed by the atom) and is typically measured in $cm^2$ (or barns, where 1 barn = $10^{-24}$ $cm^2$) [13, 14]. Furthermore, the assumption of an isotropic medium enables the angular dependence in the cross section to be neglected, as the interactions of neutrons with the medium are assumed to be independent of the angular direction of the incident neutron. Instead, this quantity typically shows significant dependence on the incoming neutron energy [13, 14].

The product of the microscopic cross section by the isotope density yields the macroscopic cross section $\Sigma_x(\overline{r}, E, t) = N(\overline{r}, t)\sigma_x(E, t)$, which is the probability per unit of path length of a neutron undergoing a reaction $x$ when colliding with the medium. Therefore, considering $v\ dt$ as the distance travelled by a neutron moving with velocity $v$ in an interval of time $dt$, the quantity

$$RR_x(\overline{r}, E, \overline{\Omega}, t) = n(\overline{r}, E, \overline{\Omega}, t)\ v\ \Sigma_x(\overline{r}, E, t)\ dt\ dV\ dE\ d\Omega, \tag{1.2}$$

denoted as reaction rate, represents the expected number of reactions $x$ occurring along this distance for neutrons in position $\overline{r}$, with energy $E$ and angular direction $\overline{\Omega}$, at time $t$ [15, 13]. The

quantity $\phi(\overline{r}, E, \overline{\Omega}, t) = n(\overline{r}, E, \overline{\Omega}, t)\ v$, which is defined as the angular neutron flux, physically represent the track length travelled by neutrons per unit of phase space volume and time [15]. This is a fundamental quantity in fission reactor physics: once the medium composition and cross sections are known, knowledge of the angular flux allows to compute the distribution of reaction rates in the medium [13, 14, 15].

The Boltzmann equation is expressed as a balance of reactions contributing to the appearance and disappearance of neutrons within an infinitesimal phase space volume $dV\ dE\ d\Omega$ per unit of time [13, 16, 17], which leads to

$$\begin{aligned}\frac{1}{v}\frac{\partial\phi(\overline{r}, E, \overline{\Omega}, t)}{\partial t} + \overline{\Omega}\cdot\nabla\phi(\overline{r}, E, \overline{\Omega}, t) + \Sigma_t(\overline{r}, E, t)\phi(\overline{r}, E, \overline{\Omega}, t) = \\ \oint_{4\pi} d\Omega' \int_0^\infty dE'\ \Sigma_s(\overline{r}, E' \to E, \overline{\Omega}' \to \overline{\Omega}, t)\phi(\overline{r}, E', \overline{\Omega}', t) + \\ \frac{\chi(E)}{4\pi}\int_0^\infty dE'\ \nu\Sigma_f(\overline{r}, E', t)\Phi(\overline{r}, E', t) + S(\overline{r}, E, \overline{\Omega}, t).\end{aligned} \tag{1.3}$$

The second and third terms on the left-hand side (LHS) represent the removal of neutrons from the phase space volume. The former is the net leakage of neutrons through the boundaries of the domain, while the latter represents the neutrons removed from the phase space by any type of collision with the medium, where $\Sigma_t(\overline{r}, E, t)$ denotes the total cross section [13, 16, 14].

The terms on the right-hand side (RHS) accounts for neutrons that appear within the phase space volume. The first term on the RHS gives the number of neutrons entering in the phase space volume as a result of scattering reactions involving neutrons of any energy and direction. This is expressed through the scattering cross section $\Sigma_s(\overline{r}, E' \to E, \overline{\Omega}' \to \overline{\Omega}, t)$, which gives the probability per unit of path length of a neutron undergoing a scattering reaction with energy $E'$ and angular direction $\overline{\Omega}'$ being emitted with energy $E$ and direction $\overline{\Omega}$ [13, 16, 14]. The second term on the RHS represents the number of neutrons emitted by fission reactions. Assuming isotropic fission, a neutron has the same probability of being emitted in any direction. Therefore, the fission spectrum $\chi(E, \overline{\Omega})$, which gives the probability of a neutron being emitted with energy $E$ and direction $\overline{\Omega}$, simplifies to $\chi(E)/4\pi$. This allows the fission source to be expressed in terms of the neutron scalar flux $\Phi(\overline{r}, E', t)$, which is defined as

$$\Phi(\overline{r}, E, t) = \oint d\overline{\Omega}\ \phi(\overline{r}, E, \overline{\Omega}, t) \tag{1.4}$$

i.e. the integration of the angular flux over all directions. Furthermore, $\nu$ denotes the average number of neutrons emitted by a fission reaction [13, 16, 14]. Finally, the term $S(\overline{r}, E, \overline{\Omega}, t)$ represents a generic neutron source.

The Boltzmann equation is therefore an integro-differential equation that is solved for the angular flux by imposing boundary and initial conditions (BC & IC), which reads

$$\phi(\overline{r}, E, \overline{\Omega}, t = 0) = \phi_0(\overline{r}, E, \overline{\Omega}), \tag{1.5}$$

$$\phi^-(\overline{r}_B, E, \overline{\Omega}_{in}, t) = \beta(\overline{r}'_B \to \overline{r}_B, \overline{\Omega}_{out} \to \overline{\Omega}_{in})\phi^+(\overline{r}'_B, E, \overline{\Omega}_{out}, t) + \phi_{in}(\overline{r}_B, E, \overline{\Omega}_{in}, t), \tag{1.6}$$

with $\overline{r}_B$ being a position on the domain boundary, $\overline{\Omega}_{in}$ denoting the incoming direction, such that $\overline{\Omega}\cdot\hat{n}(\overline{r}_B) < 0$, and $\overline{\Omega}_{out}$ denoting the outgoing direction, such that $\overline{\Omega}\cdot\hat{n}(\overline{r}_B) > 0$, with $\hat{n}(\overline{r}_B)$ being the normal vector to the boundary surface in position $\overline{r}_B$ [13, 17, 18]. The term $\beta$ denotes the albedo parameter, which determines the fraction of outgoing flux that is reintroduced into the system. In the case of a vacuum BC, which is one of the most frequent in reactor physics, the parameter is equal to zero, and the flux at the boundaries coincides with the imposed incoming flux, $\phi_{in}(\overline{r}_B, E, \overline{\Omega}_{in}, t)$ [13, 17, 18].

### 1.1.1 The criticality problem and the Power Iteration method

The steady-state homogeneous transport equation describes the equilibrium between neutron losses and neutrons generated by fissions in the nuclear reactor. This equation is obtained by introducing the multiplication factor $k$ in Eq. (1.3), which leads to

$$\begin{aligned}\overline{\Omega}\cdot\nabla\phi(\overline{r},E,\overline{\Omega})+\Sigma_t(\overline{r},E)\phi(\overline{r},E,\overline{\Omega})=\oint_{4\pi}d\Omega'\int_0^\infty dE'\ \Sigma_s(\overline{r},E'\to E,\overline{\Omega}'\to\overline{\Omega})\phi(\overline{r},E',\overline{\Omega}')\\ +\frac{1}{k}\frac{\chi(E)}{4\pi}\int_0^\infty dE'\ \nu\Sigma_f(\overline{r},E')\Phi(\overline{r},E'),\end{aligned} \tag{1.7}$$

where $k$ can be seen as the parameter that properly tunes the fission source ensuring the particle balance between productions and losses. In fact, the introduction of the multiplication factor transforms Eq. (1.3) into an eigenvalue problem [13, 14] where $k$ is the largest eigenvalue, and the flux $\phi$ is the associated eigenfunction. A self-sustaining system characterised by a $k$ equal to 1 is said to be critical.

In order to detail one of the most common approaches to the solution of Eq. (1.7), this equation is expressed in a more pragmatic manner through the use of operators notation, i.e.

$$\hat{T}\phi=\hat{\theta}_s\phi+\frac{1}{k}\hat{F}\phi, \tag{1.8}$$

where $\hat{T}$ is the displacement-plus-removal operator and $\hat{\theta}_s$ and $\hat{F}$ are the scattering and fission operators, respectively. The solution to this equation is performed with the power iteration method [13], iteratively building a source term computed from the flux and the eigenvalue. For the n-th iteration, the source is built as

$$S_f^{(n)}=\frac{1}{k^{(n)}}\hat{F}\phi^{(n)}, \tag{1.9}$$

and this term is inserted in Eq. (1.8) to obtain

$$\hat{T}\phi^{(n+1)}=\hat{\theta}_s\phi^{(n+1)}+S_f^{(n)}. \tag{1.10}$$

The solution of Eq. (1.10) will provide the flux at iteration $i+1$. At each iteration, the eigenvalue is updated according to

$$k^{(n+1)}=k^{(n)}\frac{\langle\hat{F}\phi^{(n+1)}\rangle}{\langle\hat{F}\phi^{(n)}\rangle}, \tag{1.11}$$

where the terms enclosed within the brackets $\langle\rangle$ denote an integration in the phase space domain. Starting from an initial guess $S_f^0$, the problem is solved iteratively until a convergence on the eigenvalue is reached. These series of iterations takes the name of outer iterations. The resolution of Eq. (1.10) by inverting the operators is in turn extremely challenging, and alternative methods, some of them outlined in the following sections, are employed to address the spatial, energy, and angular direction dependences of the transport equation.

Before entering into the details of these methods, it is common practice to handle the scattering term in a more convenient way. Typically, the medium is assumed to be isotropic, meaning that the scattering cross section has an angular dependence only on the cosine of the scattering angle $\mu_0$. Furthermore, the scattering cross section is expressed through an expansion with its projection on the Legendre polynomials evaluated in the cosine of the scattering angle, i.e.

$$\Sigma_s(\overline{r},E'\to E,\overline{\Omega}'\to\overline{\Omega})\approx\sum_{l=0}^{L}\frac{2l+1}{4\pi}\Sigma_{s,l}(\overline{r},E'\to E)P_l(\mu_0). \tag{1.12}$$

The approximation in the expansion above is given by the truncation of the summation up to the anisotropy order $L$ [14]. The Legendre polynomial is then expanded in terms of Legendre

associated functions first and with the spherical harmonics afterwards. The reader may refer to Appendix A for the definitions of the Legendre polynomials, the Legendre associated functions and spherical harmonics, in addition to the complete derivation of the scattering term. The final shape of the transport equation reads as

$$\begin{aligned}\overline{\Omega}\cdot\nabla\phi(\overline{r},E,\overline{\Omega})+\Sigma_t(\overline{r},E)\phi(\overline{r},E,\overline{\Omega})=&\int_0^\infty dE'\ \sum_{l=0}^{L}\Sigma_{s,l}(\overline{r},E'\to E)\sum_{\beta=-l}^{l}Y_l^\beta(\overline{\Omega})\phi_l^\beta(\overline{r},E')\\&+\frac{1}{k}\frac{\chi(E)}{4\pi}\int_0^\infty dE'\ \nu\Sigma_f(\overline{r},E')\Phi(\overline{r},E'),\end{aligned}\tag{1.13}$$

where $\phi_l^\beta(\overline{r},E')$ are the moments of the angular flux, which are defined as the projection of the angular flux over the adjoint spherical harmonics base, i.e.

$$\phi_l^\beta(\overline{r},E)=\oint_{4\pi}d\Omega'\phi(\overline{r},E,\overline{\Omega}')Y_l^{\beta*}(\overline{\Omega}').\tag{1.14}$$

Several numerical models have been developed for the resolution of Eq. (1.13). Deterministic models solve the transport equation by introducing a series of discretisation of the spatial, energy, and angular variables. The following sections will detail a few of the main approximations that are introduced in deterministic codes, focusing specifically on those implemented in ECCO. Monte Carlo methods, on the other hand, aim to estimate a variable of interest by averaging the behaviour of a sufficiently large number of neutron histories, sampled in accordance with the physical laws that describe their transport and interactions with matter. In this sense, MC methods are considered reference methods as they do not rely on discretisations. However, the benefit of retrieving very accurate solutions is coupled with large computational costs. This class of methods will be addressed later on in this chapter.

## 1.2 The multigroup approach

Inside a nuclear reactor, neutrons exhibit energies spanning several orders of magnitude, from 20 MeV to a few meV. To address the dependencies over such a wide energy range, the multigroup formalism is customarily used in deterministic codes, including ECCO [14, 13, 19].

This method discretises the energy range into a series of G energy intervals, as illustrated in figure 1.1. The conventional nomenclature prescribes that the index of the interval increases with decreasing energy values. In general, a standard nomenclature is attributed to significant energy intervals, whose boundaries depend on the context. The thermal range is defined as the interval containing neutrons with an energy of the same magnitude of the energy scale associated with thermal agitation of the medium's atoms. This ranges from few eV to fractions of meV. The fast range contains neutrons with energy of the order of MeV to KeV. The term epithermal range is then used to describe the interval between.

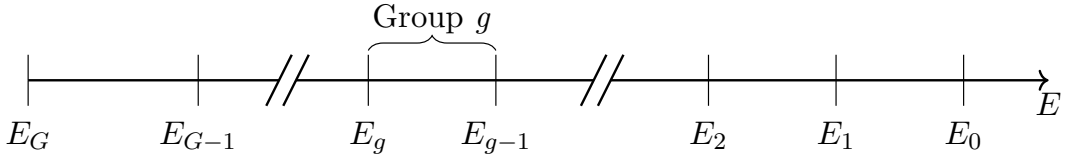


*Figure 1.1: The multigroup model subdivision of the continuous energy range into a series of G discrete groups. It can be noted that as the index of the energy interval increases, the energy decreases.*

The number and boundaries of each energy interval, also known as energy group, are entirely arbitrary. For instance, within ECCO they are chosen to be constant and equivalent to a specific

lethargy window. Given the strong dependence of the cross sections on the energy variable, it should be clear from now on that the refinement of the energy discretisation will strongly affect the final accuracy of the solution.

The next step is to integrate Eq. (1.13) on the energy group $g$, defined by the energy interval $[E_g, E_{g-1}]$, i.e.

$$\begin{aligned}\int_{E_g}^{E_{g-1}} dE\ \overline{\Omega}\cdot\nabla\phi(\overline{r},E,\overline{\Omega}) + \int_{E_g}^{E_{g-1}} dE\ \Sigma_t(\overline{r},E)\phi(\overline{r},E,\overline{\Omega}) = \\ \int_{E_g}^{E_{g-1}} dE\ \sum_{g'=1}^{G}\int_{E_{g'}}^{E_{g'-1}} dE'\ \ \sum_{l=0}^{L}\Sigma_{s,l}(\overline{r},E'\to E)\sum_{\beta=-l}^{l} Y_l^{\beta}(\overline{\Omega})\phi_l^{\beta}(\overline{r},E') \\ + \int_{E_g}^{E_{g-1}} dE\ \frac{1}{k}\frac{\chi(E)}{4\pi}\sum_{g'=1}^{G}\int_{E_{g'}}^{E_{g'-1}} dE'\ \nu\Sigma_f(\overline{r},E')\Phi(\overline{r},E') \quad \text{for } g=1\dots G\end{aligned} \tag{1.15}$$

Next, the multigroup angular flux for a generic energy group $g$ is defined as

$$\phi_g(\overline{r},\overline{\Omega}) = \int_{E_g}^{E_{g-1}} dE\ \phi(\overline{r},E,\overline{\Omega}), \tag{1.16}$$

and used to define the multigroup total cross section

$$\Sigma_{t,g}(\overline{r},\overline{\Omega}) = \frac{\int_{E_g}^{E_{g-1}} dE\ \Sigma_t(\overline{r},E,\overline{\Omega})\phi(\overline{r},E,\overline{\Omega})}{\phi_g(\overline{r},\overline{\Omega})}. \tag{1.17}$$

This procedure, also known as energy condensation, requires further discussion. First, this definition ensures the preservation of the reaction rates within each group, as it can be observed by taking the multigroup flux from the denominator of the above expression to the LHS. Secondly, the cross section now depends on the angular direction, thereby increasing the level of complexity of the solution and requiring a large amount of data to be stored. Therefore, the common practice is to use the scalar flux as a weighting function for the computation of the multigroup cross sections [20, 17, 21].

Still, the shape of the scalar flux is not known *a priori*, since it is the solution of the transport equation itself, leading to what would seem a contradiction. Hence, preparation of the multigroup cross section is usually performed using well-known shapes of the scalar flux in specific energy ranges. For example, it could be possible to use the thermal Maxwellian distribution in the low-energy region, the fission spectrum in the high-energy region, or the $1/E$ shape in the slowing-down region [22, 23]. In a similar fashion, the other multigroup parameters are defined, i.e.

$$\phi_{l,g}^{\beta}(\overline{r}) = \int_{E_g}^{E_{g-1}} dE\ \phi_l^{\beta}(\overline{r},E), \tag{1.18}$$

$$\chi_g = \int_{E_g}^{E_{g-1}} dE\ \chi(E), \tag{1.19}$$

$$\nu\Sigma_{f,g'}(\overline{r}) = \frac{\int_{E_{g'}}^{E_{g'-1}} dE'\ \nu\Sigma_f(\overline{r},E')\Phi(\overline{r},E')}{\Phi_g(\overline{r})}, \tag{1.20}$$

$$\Sigma_{s,l,gg'}(\overline{r}) = \frac{\int_{E_g}^{E_{g-1}} dE\ \int_{E_{g'}}^{E_{g'-1}} dE'\ \Sigma_{s,l}(\overline{r},E'\to E)\phi_l^{\beta}(\overline{r},E')}{\phi_{l,g'}^{\beta}(\overline{r})}. \tag{1.21}$$

The term in (1.21) is also referred to as the group-transfer cross section and represents the probability for a neutron to be scattered from the group $g'$ to the group $g$. As in the previous case, it can be computed by means of the scalar flux rather than the moments of the angular

flux. By making this hypothesis, the Boltzmann equation is expressed as

$$\overline{\Omega}\cdot\nabla\phi_g(\overline{r},\overline{\Omega})+\Sigma_{t,g}(\overline{r})\phi_g(\overline{r},\overline{\Omega})= \sum_{g'=1}^{G}\sum_{l=0}^{L}\Sigma_{s,l,gg'}(\overline{r})\sum_{\beta=-l}^{l}Y_l^{\beta}(\overline{\Omega})\phi_{l,g'}^{\beta}(\overline{r})+\frac{1}{k}\frac{\chi_g}{4\pi}\sum_{g'=1}^{G}\nu\Sigma_{f,g'}(\overline{r})\Phi_{g'}(\overline{r}) \quad \text{for } g=1\dots G. \tag{1.22}$$

The scattering source for the group $g$ is defined as the sum of all neutrons that, scattered from every group $g' \neq g$, reach the specific group $g$. This can be added to the fission source, fixed from the outer iterations, to obtain the source term for group $g$, which reads

$$Q_g(\overline{r},\overline{\Omega})=\sum_{g'\neq g}^{G}\sum_{l=0}^{L}\Sigma_{s,l,gg'}(\overline{r})\sum_{\beta=-l}^{l}Y_l^{\beta}(\overline{\Omega})\phi_{l,g'}^{\beta}(\overline{r})+\frac{1}{k}\frac{\chi_g}{4\pi}\sum_{g'=1}^{G}\nu\Sigma_{f,g'}(\overline{r})\Phi_{g'}(\overline{r}), \tag{1.23}$$

allowing the transport equation to be expressed in a more convenient form, i.e.

$$\overline{\Omega}\cdot\nabla\phi_g(\overline{r},\overline{\Omega})+\Sigma_{t,g}(\overline{r})\phi_g(\overline{r},\overline{\Omega})-\sum_{l=0}^{L}\Sigma_{s,l,gg}(\overline{r})\sum_{\beta=-l}^{l}Y_l^{\beta}(\overline{\Omega})\phi_{l,g}^{\beta}(\overline{r})=Q_g(\overline{r},\overline{\Omega}) \quad \text{for } g=1\dots G, \tag{1.24}$$

where the self-scattering term, which expresses the neutrons that undergoing scattering in $g$ are re-emitted in the same group, is made explicit in the LHS. The system of equations described by Eq. (1.24) provides the angular flux $\phi_g(\overline{r},\overline{\Omega})$ for each energy group. Fixed the fission source, the system of equations described in Eq. (1.24) consists of a set of equations coupled together by the scattering source in $Q_g$. Since up-scattering (collisions in which the neutrons increase their energy, moving from lower energy groups to high energy groups) is absent outside the thermal range, the coupling between the energy groups is for the most part lower triangular [19, 17]. This considerably facilitate the solution of Eq. (1.24), since the flux of the highest energy group $\phi_1$ can be retrieved and used to compute the down-scattering source of the second group. Then, $\phi_1$ and $\phi_2$ are used to compute the source of the third group, and so forth for all groups outside the thermal range, within the framework of the Gauss-Siedel method [24]. Within the thermal region, the up-scattering generates an almost full coupling between the energy groups, and the solution of Eq. (1.24) requires iterations over all the thermal energy groups, commonly referred to as thermal iterations [24, 17]. Finally, fixed the source term $Q_g$, Eq. (1.24) can't be easily inverted. The equation is therefore solved iteratively by progressively updating the self-scattering source through inner iterations [24, 17]. This complex system of nested iterations, which is schematized in Algorithm 1, represents the most common way of resolving energy dependence within the transport equation when multigroup formalism is adopted.

As mentioned above, one of the main drawbacks involved in multigroup formalism lies in the difficulty of calculating multigroup cross sections as in Eq. (1.17). The computation of the groups-averaged cross sections in correspondence with large resonances, in particular, requires particular care due to the sudden variations of the cross section and flux in narrow intervals. This issue, also known as energy self-Shielding, will be outlined in the following chapter, where the algorithms used by ECCO to tackle this task will be presented.

## 1.3 The collision probability method

As outlined in the previous section, the classical approach for solving the Boltzmann equation using the multigroup method involves calculating the angular neutron flux within each energy group used to discretise the energy variable. These equations are coupled together through source terms and scattering reactions. The solution is found by means of a series of nested iterations, i.e. the outer and inner iterations, and eventually the thermal iterations. The outer iterations solve the eigenvalue problem and evaluate the source terms, which provide the coupling between the energy groups. The inner iterations solve for the angular and spatial dependencies

**Algorithm 1:** Basic iterative scheme employed by deterministic code using the multi-group formalism

```
Data: Group structure, multi group cross sections
Result: Multi group fluxes, k_eff
Initialize Fission Source S_f;
Initialize Multiplication Factor k;
Initialize scattering source;
// outer iterations
do
    for g = 1, g > g_thermal, g = g + 1 do
        Solve Eq. (1.24); // inner iterations
        Compute down-scattering source in Eq. (1.23);
    end
    while Φ_g have not converged do
        forall g ∈ { thermal range } do
            // thermal iterations
            Solve Eq. (1.24); // inner iterations
            Update scattering source in Eq. (1.23);
        end
    end
    Update fission source from Eq. (1.9);
    Update multiplication factor k from Eq. (1.11) ;
while k has not converged;
```

of the angular flux in Eq. (1.24) within each energy group, for the fixed source provided by the outer iterations, thereby determining the flux distribution [13, 14, 17].

Many methods have been developed to address the angular and spatial dependencies of the neutron flux. As the Collision Probability (CP) method is the numerical method employed in the ECCO cell code, this section will examine it in detail. The CP method is based on an integral transport method. This class of methods solves for the integral form of the Boltzmann equation, which is obtained by integrating the angular dependence out of the transport equation. This technique leaves only the spatial and energy dependences of the neutron flux to be addressed [13].

The integral form of the Boltzmann equation is obtained from Eq. (1.24). After some manipulations, detailed in Appendix B, the integral form of the transport equation for the scalar flux reads

$$\Phi_g(\overline{r}) = \int dV' \frac{Q_g(\overline{r}')}{4\pi|\overline{r}-\overline{r}'|^2} e^{-\tau_g(\overline{r}'\to\overline{r})}, \tag{1.25}$$

where $Q_g(\overline{r}')$ represents the neutrons emitted isotropically by fission, scattering reactions, and eventual external sources at a given position $\overline{r}'$. This is multiplied by an exponential term, which is the Kernel of the integral transport equation [14, 24, 25, 13]. This attenuation factor gives the probability that neutrons, emitted at any location $\overline{r}'$ within the domain, reach the given location $\overline{r}$. The exponent in this term, $\tau_g(\overline{r}' \to \overline{r})$, is the optical path length [14, 24, 25, 13], defined as

$$\tau_g(\overline{r}' \to \overline{r}) = \int_0^{s'} ds'' \Sigma_{t,g}(\overline{r}_0 - s''\overline{\Omega}), \tag{1.26}$$

with $s$ being a position along the characteristic line $\overline{r} + s\overline{\Omega}$. Therefore, the scalar flux at any position in space $\overline{r}$ is given by the sum of all neutrons that, emitted isotropically at any point $\overline{r}'$ of the domain by scattering, fission reactions, and external sources, reach the specific location $\overline{r}$ without undergoing any collisions. In principle, the volume integral is performed on an infinite volume. However, integration can also be performed for finite domains by imposing

appropriate boundary conditions. For instance, the source term in Eq. (1.25) may vanish outside the boundaries [13]. Then, the volume of the domain is discretised into a set of regions, each with volume $V_j$, with $j = 1, \ldots, N$. The sources are assumed to be constant and isotropic within each region, and both sides in Eq. (1.25) are multiplied by $\Sigma_{t,g}(\overline{r})$ and integrated over $V_j$, leading to

$$\int_{V_j} dV\ \Sigma_{t,g}(\overline{r})\ \Phi_g(\overline{r}) = \int_{V_j} dV\ \Sigma_{t,g}(\overline{r}) \sum_i Q_{g,i} \int_{V_i} dV' \frac{e^{-\tau_g(\overline{r}' \to \overline{r})}}{4\pi|\overline{r} - \overline{r}'|^2}, \tag{1.27}$$

which can be expressed as

$$V_j\ \Sigma_{t,g,j}\ \Phi_{g,j} = \sum_i Q_{g,i}\ V_i\ P_{g,ij}, \tag{1.28}$$

where

$$\Phi_{g,j} = \frac{1}{V_j} \int_{V_j} dV\ \Phi_g(\overline{r}), \tag{1.29}$$

$$\Sigma_{t,g,j} = \frac{1}{V_j \Phi_{g,j}} \int_{V_j} dV\ \Sigma_{t,g}(\overline{r})\ \Phi_g(\overline{r}), \tag{1.30}$$

$$P_{g,ij} = \frac{1}{V_i} \int_{V_j} dV\ \Sigma_{t,g}(\overline{r}) \int_{V_i} dV' \frac{e^{-\tau_g(\overline{r}' \to \overline{r})}}{4\pi|\overline{r} - \overline{r}'|^2}. \tag{1.31}$$

The terms $P_{g,ij}$ are the Collision Probabilities (CPs), representing the probability that a neutron, emitted isotropically in a given region $V_j$, will have its first collision within the region $V_i$ [25, 13]. Assuming that the total cross section is uniform within each region, the reduced collision probabilities [25] can be defined as

$$p_{g,ij} = \frac{P_{g,ij}}{\Sigma_{t,g,j}} = \frac{1}{V_i} \int_{V_j} dV\ \int_{V_i} dV' \frac{e^{-\tau_g(\overline{r}' \to \overline{r})}}{4\pi|\overline{r} - \overline{r}'|^2}, \tag{1.32}$$

which are characterised by the reciprocity property, i.e.

$$p_{g,ij} V_i = p_{g,ji} V_j. \tag{1.33}$$

This property can be used in Eq. (1.28), which can be simplified further to obtain the final formulation of the CP method

$$\Phi_{g,j} = \sum_j Q_{g,j}\ p_{g,ij}. \tag{1.34}$$

The solution to the transport equation is then performed as follows: the domain is divided into $N$ regions, and the source terms (fixed from the outer iterations) and CPs are computed in each region. The CPs are then organised into a $N \times N$ matrix in Eq. (1.34) and the scalar fluxes are computed. Further details of the CPs computation will be provided in Chapter 2, where they will be applied for cross sections and flux calculations within the ECCO cell code.

## 1.4 The Monte Carlo solution of the transport equation

The Monte Carlo methods are a class of computational algorithms that solve the transport equation using a stochastic approach. In this case, systematic errors arising from the approximation of energy, angle, and space variables in deterministic solutions are replaced by statistical uncertainties [13]. This is achieved by describing the physical models without relying on approximations. For example, whereas deterministic codes require the discretisation of energy using the multigroup model, Monte Carlo methods perform energy-continuous calculations instead. The statistical nature of this method makes it highly suitable for reactor physics applications, since the behaviour of neutrons within the domain results from many random processes. In fact, the cross sections represent the probability per unit of path length of neutrons undergoing a specific reaction [13, 26, 14]. Another example is the energy of the neutron following a scattering collision, which is governed by a random process (see Appendix C).

In neutron transport theory, Monte Carlo methods describe the general behaviour of a population of neutrons by simulating the individual histories of a smaller set of neutral particles. These histories describe the frequency and type of reactions that neutrons undergo from the moment they enter the domain until they disappear, either due to capture reactions or because they exit the domain [25, 15]. The frequency and type of reactions are randomly sampled from the probability distributions that describe the physical laws, using random number generators [27, 28], which determine the stochastic nature of the method. As the laws describing the random process are reproduced exactly, the results faithfully represent the physical world. However, when the general behaviour of the population is inferred from these histories, it is subject to statistical uncertainty depending on the number of particles simulated, as described below.

### 1.4.1 The Central Limit theorem

A random variable $\xi$ is defined as the numerical outcome of a random process, e.g. the energy or the angular direction of the neutron after a scattering reaction [27, 28]. The random process can be described by a Probability Density Functions (PDF), $f(\xi)$, such that $f(\xi)d\xi$ gives the probability of the outcome of the random process being in the neighbourhood $d\xi$ [27, 28, 25]. A PDF, in order to be defined as such, must satisfy the normalisation property, i.e.

$$\int d\xi \ f(\xi) = 1, \tag{1.35}$$

where the integration runs over the range where the random variable is defined. The PDF is used to evaluate the $n-th$-order moment of the random variable [28], defined as

$$E[\xi^n] = \int d\xi \ \xi^n \ f(\xi). \tag{1.36}$$

The first-order moment, i.e. $E[\xi]$, coincides with the definition of the average value of the random variable. The second-order moment is instead associated with the variance of the random variable, i.e.

$$\sigma^2[\xi] = E[(\xi - E[\xi])^2] = \int d\xi \ (\xi - E[\xi])^2 f(\xi) = E[\xi^2] - (E[\xi])^2, \tag{1.37}$$

which represents the statistical dispersion of the random variable around its mean value [27].

The objective of statistical analysis is to determine the mean and variance of a random process from a set of sampled random variables, denoted by $\xi_1 \dots \xi_N$, which are all distributed according to the same PDF. Many techniques have been developed for sampling a random variable from its statistical distribution. However, the details of these methods are beyond the scope of this work, and the reader is referred to [27, 28]. First, the sample mean is defined as

$$\overline{\xi}_N = \frac{1}{N} \sum_{i=1}^{N} \xi_i, \tag{1.38}$$

which represents an unbiased estimator of the mean, as it can be demonstrated that $E[\overline{\xi}_N] = E[\xi]$ [28]. Defining the standard deviation $\sigma[\xi] = \sqrt{\sigma^2[\xi]}$, it can be demonstrated [13] that

$$\sigma[\overline{\xi}_N] = \frac{\sigma[\xi]}{\sqrt{N}}. \tag{1.39}$$

This result implies the following: when considering a random process with outcome $\xi$ distributed according to a PDF $f(\xi)$, the variance $\sigma^2[\xi]$ represents the distribution of $\xi$ around the mean value $E[\xi]$. If this mean value is estimated with $\overline{\xi}_N$, sampling from $f(\xi)$ a set $\xi_1 \dots \xi_N$, and this process is repeated many times, it is expected that the sample means will be distributed around the true mean with variance $\sigma^2[\overline{\xi}_N]$, which decreases as the number of sampled random

variables increases [13]. To evaluate the spread in this distribution, the unbiased estimator of the variance is defined as

$$S^2 = \frac{1}{N-1}\sum_{i=1}^{N}(\xi_i - \overline{\xi}_N)^2, \tag{1.40}$$

for which $E[S^2] = \sigma^2[\xi]$ [28].

Eqs. (1.38) and (1.40) are the formulations used to estimate the mean and variance of the random process within the Monte Carlo methods. Previous results have shown that, as $N \to \infty$, the sample mean converges to the true mean. However, simulating an infinite number of particles is evidently unfeasible. Therefore, it is necessary to quantify how far the sample mean is from the true mean for a fixed number of simulated particles, for which the central limit theorem comes into action [13, 25, 27, 28]. The theorem is formulated as follows: let $\xi_1 \dots \xi_N$ be a set of random variables sampled from a PDF $f(\xi)$ that describes a random process with mean value $\mu = E[\xi]$ and variance $\sigma^2 = \sigma^2[\xi]$. Then, as N approaches infinity, the sample mean is normally distributed, i.e.

$$f(\overline{\xi}_N) = \frac{\sqrt{N}}{\sigma\sqrt{2\pi}} \exp\left[-\frac{N(\overline{\xi}_N - \mu)^2}{2\sigma^2}\right]. \tag{1.41}$$

Another property of the PDF states that the integral of the function over the interval $[a, b]$ yields the probability that the random variable lies within that same interval. Integrating the normal distribution for the sample mean over the interval $[\mu + K\sigma/\sqrt{N}, \mu - K\sigma\sqrt{N}]$ leads to

$$P\left[|\overline{\xi}_N - \mu| \leq K\frac{\sigma}{\sqrt{N}}\right] = \int_{\mu - K\frac{\sigma}{\sqrt{N}}}^{\mu + K\frac{\sigma}{\sqrt{N}}} d\overline{\xi}_N \frac{\sqrt{N}}{\sigma\sqrt{2\pi}} \exp\left[-\frac{N(\overline{\xi}_N - \mu)^2}{2\sigma^2}\right], \tag{1.42}$$

where $K$ is a generic integer number. The result of the integral gives the probability that the sample mean lies within the interval $[\mu - K\sigma/\sqrt{N}, \mu + K\sigma/\sqrt{N}]$. This value is tabulated for several values of K [13], e.g.

$$P\left[|\overline{\xi}_N - \mu| \leq K\frac{\sigma}{\sqrt{N}}\right] = \begin{cases} 0.6826, & \text{for } K = 1 \\ 0.954, & \text{for } K = 2 \\ 0.997, & \text{for } K = 3 \end{cases} \tag{1.43}$$

The sample mean, the final result of a MC calculation, is therefore usually reported alongside its standard deviation, $\sigma/\sqrt{N}$, where the variance, $\sigma^2$, is estimated using Eq. (1.40). This indicates that there is a 68.3 % probability that the sample mean is at a distance from the true mean that is less than its standard deviation. This confidence interval, or statistical uncertainty, decreases as the number of particles increases. However, this evidently comes at the cost of high computational resources, as the standard deviation reduces proportionally to $1/\sqrt{N}$.

Variance reduction techniques have been developed to address this issues. By defining the weight function as

$$w(\xi) = \frac{f(\xi)}{f^*(\xi)}, \tag{1.44}$$

where $f^*(\xi)$ is a modified PDF [13], random variables can be sampled from this PDF instead of $f(\xi)$, and a new sample mean can be defined as

$$\overline{w\xi}_N = \frac{1}{N}\sum_{i=1}^{N} w(\xi_i)\xi_i, \tag{1.45}$$

which converges in probability to the true mean, but with a reduced variance depending on the choice of the modified PDF. Therefore, the weight function describes the statistical contribution of neutrons to the estimation of a physical variable, compensating for the modified sampling process. The process is said to be analog if the weight of the neutrons remains constantly equal to one, while it is said to be non-analog if it varies during the neutron history [25].

### 1.4.2 The random walk

As outlined in the previous section, the Monte Carlo method for neutron transport consists of randomly sampling from the PDF of the physical laws that describe the behaviour of neutrons within the medium. These random variables are then used to calculate the sample mean and sample variance. These quantities estimate the true mean and variance, and the sample mean is also subject to statistical distribution. The random variables that are sampled are the outcomes of the numerous reactions that neutrons undergo on their path through the medium. In practice, the Monte Carlo method involves tracking a neutron from the moment it appears in the domain, randomly sampling its reactions as it moves through the medium, until the moment it disappears.

Initially, the neutron source is sampled. If it is a fission source, the energy, location, and angular direction of the neutron are randomly generated [26]. Then, the free flight length is sampled from

$$f(s) = \Sigma_t(s) \exp\left[-\int_0^s \Sigma_t(s)ds\right], \tag{1.46}$$

which is the PDF describing the probability of a neutron travelling a distance $s$ between two consecutive collisions [26]. If the neutron remains within the domain, the nuclide and the type of reaction are sampled. If the reaction is an absorption, the neutron history terminates. Instead, if the reaction is of the scattering type, a new free flight length and direction are sampled, and the process is repeated until the neutron is absorbed or leaves the domain. During the random walk, various quantities are recorded, such as the number and type of collisions, the emitted particles, and so on. The sample means are then computed. These quantities are scored through mathematical constructs called tallies, which play the role of "detectors" for the system.

### 1.4.3 Criticality calculations

Monte Carlo methods can be employed for criticality calculations in reactor physics. This involves dividing the simulated particles into $N$ generations, which are usually referred to as batches of neutrons. Criticality calculations are closely related to random walks. Each time a fission event is sampled, the weight of the particle in the $n-th$ generation is updated as

$$w' = w\frac{\nu\Sigma_f}{\Sigma_a}, \tag{1.47}$$

where $w$ is the weight of the neutron prior to collision [25]. The power iteration algorithm [25] is employed by simulating $N$ batches of $M_n$ neutrons, approximately constant such that $M_n \sim M$. For each batch, neutrons have an initial weight $w_{m,n}$ approximately equal to one, such that

$$\sum_{m=1}^{M_n} w_{m,n} = M. \tag{1.48}$$

Afterwards, the random walks of $M_n$ neutrons are simulated and the multiplication factor of the $n-th$ batch is calculated as [25]

$$k_n = \frac{1}{M}\sum_{m=1}^{M_n} w'_{m,n}. \tag{1.49}$$

Each time a fission reaction takes place, the position is stored and the energy and direction of the emitted neutrons are sampled. These values are then used to initialise the random walks of the next generation of neutrons. For the first batch, the neutron source follows a user-defined distributions. Regardless of the initial distribution, the source distribution will start to converge between different batches. However, the multiplication factor of the $I_c$ batches, for which the

source distribution has not yet converged, is not representative of the real system. Therefore, the sample mean of the multiplication factor is computed by excluding these batches [25], i.e.

$$k = \frac{1}{N - I_c} \sum_{n=I_c+1}^{N} k_n. \tag{1.50}$$

When the new batch is initialised, the weight of neutrons is set to

$$w_{m,n} = \frac{w'_{m,n-1}}{k_{n-1}}, \tag{1.51}$$

as this ensure that the neutron population between different batches remain approximately constant [25].

### 1.4.4 Tallies

As mentioned above, a tally is a mathematical construct that calculates a given physical quantity in a Monte Carlo simulation, using the contributions from each individual neutron history. At each step of the random walk, the contributions to the estimators are stored depending on the event that is sampled. Different types of tallies can be defined, and their performance depends on the application. In the following, the definitions of different tallies for the estimation of the reaction rate are presented. From these, for instance, estimation of the flux can be retrieved.

An analog estimator [25] simply counts the number of collisions, taking the weights of the particles into account, i.e.

$$RR = \sum_{i=1}^{I} w_i, \tag{1.52}$$

where $I$ is the number of collisions counted. Note that for an analog calculation the estimator coincides with the number of collisions. The collision estimator [25], defined as

$$RR_x = \sum_{i=1}^{I} w_i \frac{\Sigma_x}{\Sigma_t}, \tag{1.53}$$

allows a lower variance than the analog estimator for the reaction rate of a given reaction $x$, since the contribution to the estimator also comes from collisions in which the reaction does not occur. In conclusion, recalling that the neutron flux is the path length travelled by neutrons streaming through a volume per unit of time and volume [26], this quantity can be used to define the track-length estimator [25], i.e.

$$RR = \sum_{i=1}^{T} w_i \ \Sigma_x \ l_i, \tag{1.54}$$

where $l_i$ is the length of one of the $T$ trajectories within the selected volume.

## 1.5 Perturbation theory

The perturbation theory is an extremely powerful tool in the hands of the nuclear reactor designer. This framework of methods offers its user the possibility of understanding the impact of a set of physical phenomena on the stationary state of the system. This usually involves determining relationships between some integral parameters and elementary variables, such as cross sections or geometrical data [29]. Among other possibilities, this method can be used to compute reactivity coefficients, perform parametric analysis, and uncertainty evaluations.

In general, one might be interested in computing the evolution of a stationary system by monitoring changes in the multiplication factor or reactivity coefficients, for example, following

a perturbation of the mathematical operators describing the Neutron Transport Equation. The perturbation theory offers the possibility to compute the variation of these variables of interest without having to solve again the Boltzmann equation for the perturbed state, provided that the perturbation is small. As will be outlined, this requires the solution of the adjoint equation for the reference states. The strength of this method is that, once this solution has been computed, it can be used to determine the evolution of the system following any kind of small perturbation [14].

The results of the perturbation theory provide the foundations for the Sensitivity Analysis (SA). This kind of analysis relates the perturbation on an elementary parameter $p$, with the variation generated on a variable of interest $I$, with the use of the so called Sensitivity Coefficients (SC), i.e.

$$S(I,p) = \frac{\delta I}{I} \Big/ \frac{\delta p}{p}. \tag{1.55}$$

The following sections will provide an insight into the analytical foundations of perturbation theory, and its application in computing perturbed multiplication factors and reactivity coefficients. Then, Chapter 4 will present an application of perturbation theory using the ERANOS tools. In particular, the focus will be on the first-order approximation of perturbation theory, as this enables the sensitivity coefficients to be derived independently of the perturbed state. Three different typologies of perturbation theory are possible in ERANOS [29, 30]. These are:

1. SPT - Standard Perturbation Theory, to compute perturbations on the multiplication factor.
2. GPT - Generalised Perturbation Theory, to compute perturbations on the reaction rates.
3. EGPT - Equivalent Generalised Perturbation Theory, to compute perturbations on reactivity coefficients.

The second, which is not used in the framework of this thesis, will not be addressed in the following sections. Before delving into the details of perturbation theory, the following provides an overview of the concept of the adjoint function.

### 1.5.1 The Adjoint Neutron Transport Equation

An adjoint operator $\hat{X}^\dagger$ is defined such that, for every couple of vectors $u$ and $v$, $\langle u, \hat{X}v\rangle = \langle \hat{X}^\dagger u, v\rangle$. The notation $\langle , \rangle$ denotes the multiplication of the two elements followed by integration over the entire phase space. The introduction of the adjoint operator enables an adjoint Boltzmann equation to be defined as [25, 26, 14, 18]

$$-\overline{\Omega}\cdot\nabla\phi^\dagger(\overline{r},E,\overline{\Omega}) + \Sigma_t(\overline{r},E)\phi^\dagger(\overline{r},E,\overline{\Omega}) = \oint_{4\pi} d\Omega' \int_0^\infty dE'\ \Sigma_s(\overline{r},E\to E',\overline{\Omega}\cdot\overline{\Omega}')\phi^\dagger(\overline{r},E',\overline{\Omega}') + \frac{1}{k}\frac{\nu\Sigma_f(\overline{r},E)}{4\pi}\int_0^\infty dE'\ \chi(E')\Phi^\dagger(\overline{r},E'), \tag{1.56}$$

which is solved for the adjoint angular flux, $\phi^\dagger(\overline{r},E',\overline{\Omega}')$, with BC

$$\phi^{\dagger,-}(\overline{r}_B,E,\overline{\Omega}_{in},t) = \beta(\overline{r}'_B\to\overline{r}_B,\overline{\Omega}_{out}\to\overline{\Omega}_{in})\phi^{\dagger,+}(\overline{r}'_B,E,\overline{\Omega}_{out},t) + \phi^\dagger_{in}(\overline{r}_B,E,\overline{\Omega}_{in},t). \tag{1.57}$$

In Eq. (1.56) the multiplication factor appears again, as it can be demonstrated that $k = k^\dagger$ [13, 26]. Furthermore, the removal term coincides with its expression in the Boltzmann equation for the angular flux. This operator is in fact said to be self-adjoint, as the adjoint operator is the operator itself [25, 14]. Comparing the other terms in Eq. (1.56) with those in Eq. (1.7), opposite signs for the leakage term are noticed, as well as the different angular and energy dependencies exploited in the scattering and fission operators. These differences lead to a physical interpretation of the adjoint flux. While the neutron flux, solution to Eq. (1.7), is

a measure of the contributions from scattering and fission reactions occurring throughout the entire phase space to neutrons removed at a given point in the same domain, the adjoint flux is a measure of the contributions that a neutron removed at a given point in the phase space will give to scattering and fission reactions throughout the entire domain [26].

The physical interpretation of the adjoint flux can be further detailed by defining the detector response as

$$R_i = \int dV \int dE \oint d\Omega \; \phi(\overline{r}, E, \overline{\Omega}) \Sigma_i(\overline{r}, E), \tag{1.58}$$

where $\phi(\overline{r}, E, \overline{\Omega})$ is solution to a time-dependent equation with an externally imposed source, i.e. $(\hat{T} - \hat{\theta}_s - \hat{F})\phi = Q_{ext}$ [13, 14]. By solving this equation for $Q^{\dagger}_{ext} = \Sigma_i$, the above expression can be further elaborated into [13, 14, 18]

$$R_i = \langle \phi, \Sigma_i \rangle = \langle \phi^{\dagger}, Q_{ext} \rangle, \tag{1.59}$$

from where it follows the concept of importance function. In fact, the adjoint flux can be interpreted as the importance of a neutron, i.e. a measure of the contributions that neutrons at a given point of the phase space give to the detector response [13, 14]. In the following, the adjoint solution will find wide application in perturbation theory.

### 1.5.2 SPT - Standard Perturbation Theory

The Standard Perturbation Theory (SPT) [29, 30] provides the tools to compute the variation in the multiplication factor $\delta k$, induced by a small perturbation to the mathematical operators that describes the system's stationary state, i.e.

$$\hat{M}\phi = \left(\hat{L} - \frac{1}{k}\hat{F}\right)\phi = 0, \tag{1.60}$$

where $\hat{L}\phi = (\hat{T} - \hat{\theta}_s)\phi$, and $M$ is said to be the Boltzmann operator. The Boltzmann equation is expressed with the same notation also for the adjoint solution, i.e.

$$\hat{M}^{\dagger}\phi^{\dagger} = \left(\hat{L}^{\dagger} - \frac{1}{k}\hat{F}^{\dagger}\right)\phi^{\dagger} = 0. \tag{1.61}$$

Supposing now that a small perturbation is introduced into the reference system, such that

$$\begin{cases} \hat{L} \rightarrow \hat{L}' = \hat{L} + \delta\hat{L} \\ \hat{F} \rightarrow \hat{F}' = \hat{F} + \delta\hat{F} \end{cases} \tag{1.62}$$

The perturbed system can now be described as

$$\hat{M}'\phi' = \left(\hat{L}' - \frac{1}{k'}\hat{F}'\right)\phi' = 0, \tag{1.63}$$

where $\phi' = \phi + \delta\phi$ and $k' = k + \delta k$ are the neutron flux and the multiplication factor in the perturbed state, respectively. The next step is to multiply Eq. (1.61) by $\phi'$ and integrate it over the whole phase space, and the same applies to Eq. (1.63) and $\phi^{\dagger}$. Subsequently the two results are subtracted, leading to

$$\left\langle \left(\hat{L}^{\dagger} - \frac{1}{k}\hat{F}^{\dagger}\right)\phi^{\dagger}, \phi' \right\rangle - \left\langle \phi^{\dagger}, \left(\hat{L}' - \frac{1}{k'}\hat{F}')\phi'\right)\right\rangle = 0, \tag{1.64}$$

which becomes, with some rearrangements,

$$\left\langle \phi^{\dagger}, \left(-\delta L - \frac{1}{k}\hat{F} + \frac{1}{k'}\hat{F}'\right)\phi' \right\rangle = 0. \tag{1.65}$$

Adding and subtracting the term $\left\langle \phi^\dagger, \frac{1}{k'}\hat{F}\phi' \right\rangle$ and, noting that,

$$\frac{1}{k} - \frac{1}{k'} = \frac{k' - k}{kk'} = \frac{\delta k}{kk'}, \tag{1.66}$$

it is obtained

$$\frac{\delta k}{kk'} = \frac{-\left\langle \phi^\dagger, \left(\delta\hat{L} - \frac{1}{k'}\delta\hat{F}\right)\phi' \right\rangle}{\langle \phi^\dagger, \hat{F}\phi' \rangle}. \tag{1.67}$$

Supposing that the perturbation is sufficiently small, such that $k' \approx k$, it follows that

$$\frac{\delta k}{kk'} \approx \frac{\delta k}{k^2} = \delta\rho, \tag{1.68}$$

where $\rho = 1 - \frac{1}{k}$ is the reactivity. By replacing Eq. (1.68) into Eq. (1.67), the final expression of the exact standard perturbation theory is obtained, i.e.

$$\delta\rho \approx \frac{-\left\langle \phi^\dagger, \left(\delta\hat{L} - \frac{1}{k'}\delta\hat{F}\right)\phi' \right\rangle}{\langle \phi^\dagger, \hat{F}\phi' \rangle}. \tag{1.69}$$

This expression can be further simplified by neglecting the higher order terms ($\delta\hat{L}\delta\phi = 0$, $\delta\hat{F}\delta\phi = 0$) and supposing that the perturbation is sufficiently small such that $\phi' \approx \phi$ and $k' \approx k$. These approximations leads to the expression of the first-order approximation of the SPT, which reads

$$\delta\rho = \frac{-\left\langle \phi^\dagger, \left(\delta\hat{L} - \frac{1}{k}\delta\hat{F}\right)\phi \right\rangle}{\langle \phi^\dagger, \hat{F}\phi \rangle}. \tag{1.70}$$

### 1.5.3 EGPT - Equivalent Generalised Perturbation Theory

The Equivalent Generalised Perturbation Theory (EGPT) [29, 30] is used to compute the perturbation of variables which are defined as the difference in reactivity between a reference system and a second system, here referred as modified system [29].

A typical application of EGPT is the evaluation of the perturbation of the Doppler and Coolant-voiding coefficients. The difference in reactivity between the reference system, here referred as state 1, and the modified system, referred as state 2 is defined as

$$\Delta\rho = \left(1 - \frac{1}{k_2}\right) - \left(1 - \frac{1}{k_1}\right) = \frac{1}{k_1} - \frac{1}{k_2}. \tag{1.71}$$

The perturbation on the reactivity difference reads

$$\delta(\Delta\rho) = \Delta\rho' - \Delta\rho = \left(\frac{1}{k_1'} - \frac{1}{k_2'}\right) - \left(\frac{1}{k_1} - \frac{1}{k_2}\right) = \left(\frac{1}{k_2} - \frac{1}{k_2'}\right) - \left(\frac{1}{k_1} - \frac{1}{k_1'}\right) \tag{1.72}$$

where $k_1'$ and $k_2'$ are the multiplication factors of the perturbed reference and the perturbed modified systems, respectively. The last two terms can be expressed using Eq. (1.70), i.e the SPT formulation approximated at the first-order, leading to

$$\delta(\Delta\rho) = \frac{\left\langle \phi_1^\dagger, \left(\delta\hat{L}_1 - \frac{1}{k_1}\delta\hat{F}_1\right)\phi_1 \right\rangle}{\langle \phi_1^\dagger, \hat{F}_1\phi_1 \rangle} - \frac{\left\langle \phi_2^\dagger, \left(\delta\hat{L}_2 - \frac{1}{k_2}\delta\hat{F}_2\right)\phi_2 \right\rangle}{\langle \phi_2^\dagger, \hat{F}_2\phi_2 \rangle}, \tag{1.73}$$

which is the formulation of the first-order approximated EGPT.

### 1.5.4 Sensitivity Coefficients

As will be detailed in Chapter 4, the ERANOS perturbation module allows the user to apply perturbation theory, outlined in the previous sections, to evaluate the sensitivity coefficients. For a generic variable of interest, these coefficients are defined as

$$S(I, \sigma_{r,x,g,n}) = \frac{\delta I}{I} \Big/ \frac{\delta \sigma_{r,x,g,n}}{\sigma_{r,x,g,n}}, \tag{1.74}$$

where $I$ is the variable of interest, and $\sigma_{n,r,x,g}$ is the cross section of the nuclide $n$, situated in the region $r$, for the reaction $x$ and the energy group $g$. To simplify the notation, this parameter will just be referred to using the single-index notation $\sigma_i$.

#### 1.5.4.1 Sensitivity Analysis on the multiplication factor

The sensitivity coefficient of the multiplication factor due to a perturbation of $\sigma_i$ is defined as

$$S(k, \sigma_i) = \frac{\delta k}{k} \Big/ \frac{\delta \sigma_i}{\sigma_i}. \tag{1.75}$$

By rewriting the variation of the mathematical operators of the Boltzmann Neutron Transport Equation in terms of partial derivatives with respect to the cross sections $\sigma_i$ [31, 25], i.e.

$$\delta \hat{M} = \sum_{i=1}^{n} \frac{\partial \hat{M}}{\partial \sigma_i} \delta \sigma_i, \tag{1.76}$$

and substituting Eq. (1.70) into Eq. (1.75), the sensitivity coefficient for the multiplication factor can be rewritten as

$$S(k, \sigma_i) = \frac{\delta k}{k} \Big/ \frac{\delta \sigma_i}{\sigma_i} = -k \frac{\left\langle \phi^\dagger, \left( \frac{\partial \hat{L}}{\partial \sigma_i} \sigma_i - \frac{1}{k} \frac{\partial \hat{F}}{\partial \sigma_i} \sigma_i \right) \phi \right\rangle}{\langle \phi^\dagger, \hat{F} \phi \rangle}. \tag{1.77}$$

Since $\hat{L}$ and $\hat{F}$ are integro-differential mathematical operators they are linear with respect to the cross sections [30, 31], hence

$$\frac{\partial \hat{L}}{\hat{L}} = \frac{\partial \sigma_i}{\sigma_i} \quad \text{and} \quad \frac{\partial \hat{F}}{\hat{F}} = \frac{\partial \sigma_i}{\sigma_i}. \tag{1.78}$$

These relations allow to simply Eq. (1.77) into

$$S(k, \sigma_i) = \frac{\delta k}{k} \Big/ \frac{\delta \sigma_i}{\sigma_i} = -k \frac{\left\langle \phi^\dagger, \left( \hat{L} - \frac{1}{k} \hat{F} \right)_{\sigma_i} \phi \right\rangle}{\langle \phi^\dagger, \hat{F} \phi \rangle}, \tag{1.79}$$

where the suffix $\sigma_i$ in $\left( \hat{L} - \frac{1}{k} \hat{F} \right)_{\sigma_i}$ denotes that the above equation includes only the operators in which $\sigma_i$ appears explicitly in their mathematical expression. In fact, for a generic operator $\hat{X}$ independent of $\sigma_i$, it follows that

$$\frac{\partial \hat{X}}{\partial \sigma_i} = 0. \tag{1.80}$$

The strength of this approach is that the computation of the sensitivity coefficients does not require retrieving the solution in the perturbed state, and they can be computed once for all provided that the direct and adjoint solutions of the reference system are known [7].

#### 1.5.4.2 Sensitivity Analysis on the reactivity change

Using the EGPT, it is possible to derive the sensitivity coefficients for any generic reactivity change. Using Eq. (1.73), it is possible to derive the SCs by means of the same approach used in the previous section, which leads to

$$S(\Delta\rho,\sigma_i)=\frac{\delta(\Delta\rho)}{\Delta\rho}\Big/\frac{\delta\sigma_i}{\sigma_i}=\frac{1}{\Delta\rho}\left[\frac{\left\langle\phi_1^\dagger,\left(\hat{L}_1-\frac{1}{k_1}\hat{F}_1\right)_{\sigma_i}\phi_1\right\rangle}{\langle\phi_1^\dagger,\hat{F}_1\phi_1\rangle}-\frac{\left\langle\phi_2^\dagger,\left(\hat{L}_2-\frac{1}{k_2}\hat{F}_2\right)_{\sigma_i}\phi_2\right\rangle}{\langle\phi_2^\dagger,\hat{F}_2\phi_2\rangle}\right]. \tag{1.81}$$

Again, the solution for the perturbed state is not required. It can also be noted that the EGPT sensitivity coefficients can be derived by the SCs for the SPT, since from Eq. (1.81) follows

$$S(\Delta\rho,\sigma_i)=\frac{1}{\Delta\rho}\left[-\frac{1}{k_1}S_1(k_1,\sigma_i)+\frac{1}{k_2}S_2(k_2,\sigma_i)\right]. \tag{1.82}$$

Chapter 2

# ERANOS - The ECCO cell code

The ERANOS codes and data system, mainly used for neutronic analyses of fast-spectrum reactors, includes many transport codes. Among them, the ECCO cell and lattice code is used to calculate homogenised and energy-averaged cross sections, for consequent use in full core calculations. Relying on the Collision Probability (CP) method, the code is well-suited to neutronic analyses of two-dimensional subassemblies cells. Furthermore, the code treats self-shielding effects using a fine energy group structure (1968 groups) and employing the subgroup method.

As this thesis aims to numerically validate the self-shielding module, it is necessary to gain an insight into the theory underlying the ECCO physical models, and how these are implemented in the code through different algorithms. Only by understanding the analytical models, and the approximations they introduce, can a solid procedure for code validation be developed. This enables the errors arising from the different numerical models to be identified and distinguished.

## 2.1 The ECCO cell code

ERANOS 2.3N (European Reactor ANalysis Optimized calculation System) is a system of codes and libraries developed within a European framework for performing various analyses related to fast reactors. The functions of ERANOS span between cell, lattice and core calculations, fuel depletion, shielding, perturbation analysis, and many others [32]. The ECCO code is required to prepare condensed and homogenised cross sections (typically using a broad energy structure) for subsequent use in core calculations, in accordance with the classical two-step approach [17].

The ECCO code relies on self-shielded cross sections using a fine group structure (1968 energy groups) for the resonant nuclides (or the most relevant isotopes), employing the Subgroup method. For other isotopes, a broad energy structure (33 or 172 groups) is adopted. Flux calculations are performed using various methods, depending on whether the domain is homogeneous or heterogeneous, such as P1, B1, CP and other models [33, 32]. A typical ECCO calculation consists of successive steps, each involving a separate transport calculation. The sequence of calculation steps, known as route, is defined by the user. Two main routes are recommended: the fast route and the reference route. Given the increased availability of computational resources over the past thirty years, the latter route, which is slower but more accurate, is generally preferred over the former. The main steps of the reference route are summarised in Figure 2.1 and reported below. Each time a calculation with a different group structure is required, unless energy condensations are performed, a Nuclear Data Library (NDL) is recalled as input by the code. ECCO requires NDLs to be in a specific format, known as ECCOLIB, obtained by processing the ENDF-6 tapes (Evaluated Nuclear Data File) using a series of external codes, such as NJOY and CALENDF. Chapter 3 describes the production of an ECCOLIB. The reference ECCO route consists of the steps described hereafter.

1. An initial calculation is performed in a homogeneous medium with a broad (33 or 172 groups) energy structure. This step can be considered as a kind of "initialisation", to retrieve the cross sections (for all nuclides). A buckling search is performed at this stage. This step requires an ECCOLIB as input with the data organised in the broad group structure (33 or 172 groups). The library also contains subgroup data for self-shielding treatment, as will be detailed later on.
2. The calculation of a heterogeneous medium with a broad energy structure is then performed. Here, a more accurate solution, representative of the actual geometry, is obtained by using the previously evaluated buckling. However, the group structure remains broad. As previously, an ECCOLIB in the broad structure is required as an input.
3. The solution in a heterogeneous medium with a fine energy structure (1968 groups) is obtained, with an accurate treatment of resonant nuclides. The most accurate solution is obtained at this stage. Cross sections (and subgroup data) for resonant nuclides are provided as an input in an ECCO library containing data organised within a 1968 group structure. For other isotopes, for which data are absent in the fine structure ECCOLIB, the cross sections are those evaluated in the previous step. Finally, condensation is performed from the fine structure to the broad 33-group structure.
4. A calculation with the 33-group structure is performed using the cross sections of the non-resonant nuclides produced in step two, alongside the condensed cross sections of the resonant nuclides produced in the previous step. A new buckling search is performed, and the cross sections are then homogenised.
5. A final calculation is performed in a homogeneous medium using the condensed and homogenised cross sections from the previous step.

Each transport calculation performs outer, thermal and inner iterations, resorting for each group to the subgroup module and the CP method. Figure 2.2 shows a basic scheme of this process.

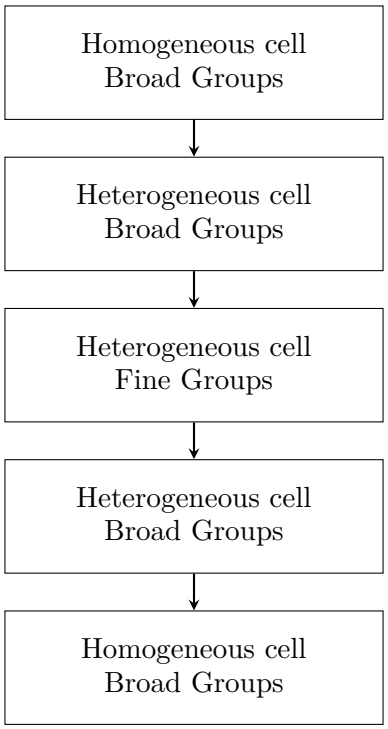


*Figure 2.1: Scheme of the reference route implemented in ECCO. At each step the transport equation is solved at the lattice level, with input data specified by the user. At the end, homogeneous and condensed cross sections are produced. The figure was adapted from [33].*

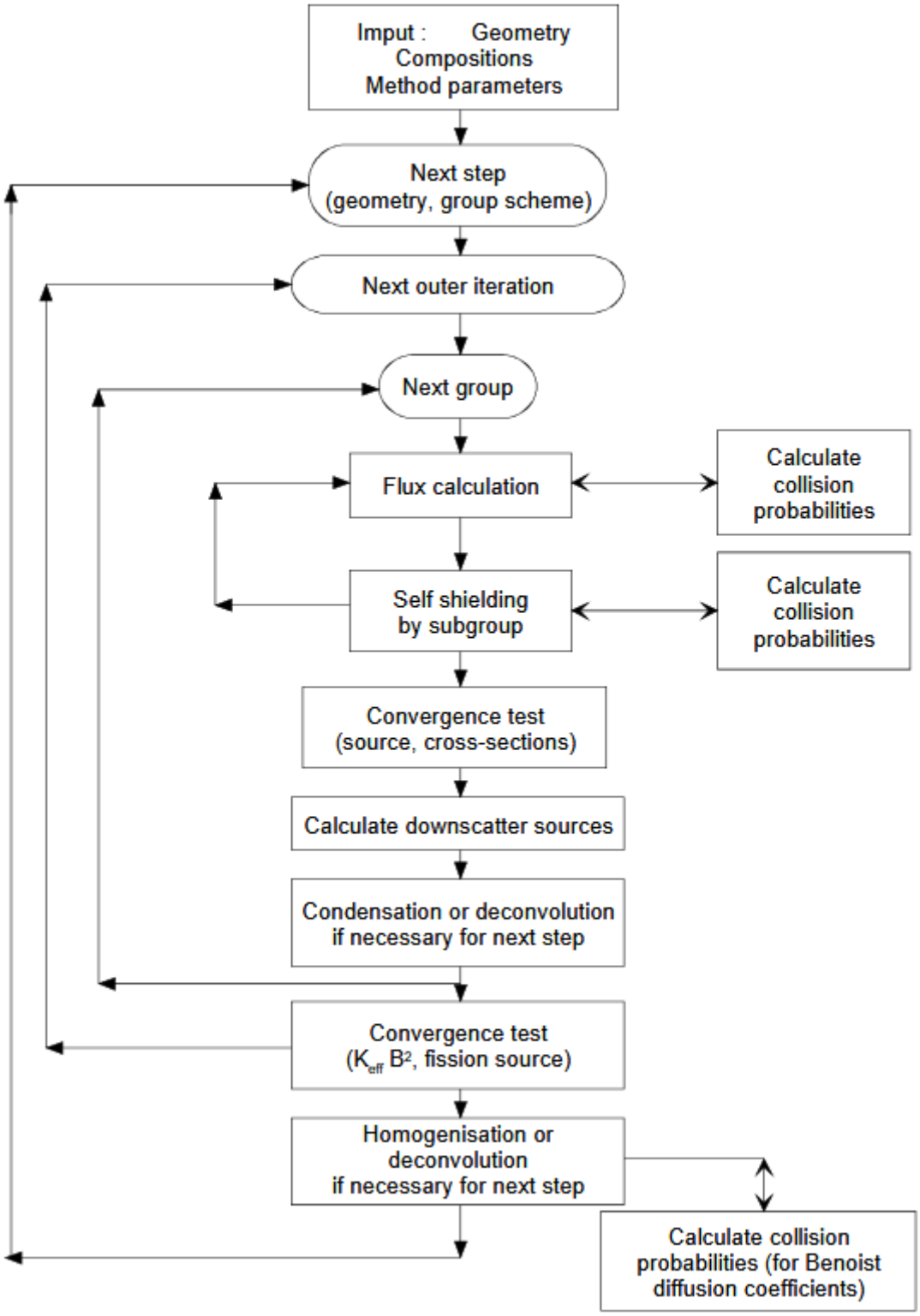


*Figure 2.2: A basic scheme of the calculations performed in the ECCO code for each of the user-defined steps. The figure was taken from [33].*

## 2.2 The approximations in the deterministic model

In the same fashion as other deterministic models, ECCO introduces a series of approximations to solve the transport equation, such as the collision probability method, or to compute resonance integrals, such as the self-shielding model. These approximations generally represent a small source of error as compared to the uncertainties in the nuclear data. However, within the

framework of a licensing process, it is necessary to precisely and independently determine these errors in order to establish whether they fall within an acceptable range. The main challenge arises from potential error compensation when only reviewing the code's overall results. It is therefore essential to distinguish the contributions of the various numerical models to the overall output in order to identify the related errors individually. The following sections will analyse these approximations from an analytical point of view, in order to understand how they can influence the accuracy of the results. Then, in the second part of this work, the source of errors related to the self-shielding module will be isolated and validated individually against Monte Carlo simulations.

### 2.2.1 The self-shielding Model

As seen in section 1.2, the multigroup formalism requires the collapsing of the cross sections within several energy groups. Assuming that the cross sections are weighted with the scalar flux (to drop the dependence on the angular direction), the equation that must be solved for a generic cross section $\sigma_{x,g}$ (where x stands for a generic reaction) reads as

$$\sigma_{x,g}(\overline{r}) = \frac{\int_{\Delta E_g} \sigma_x(\overline{r}, E)\Phi(\overline{r}, E)\, dE}{\Phi_g(\overline{r})}. \tag{2.1}$$

This operation is fundamental to prepare the cross sections used in lattice calculations and subsequently in core calculations. However, prior to the beginning of transport calculations, the knowledge of the scalar flux is unavailable. Hence, some approximations are applied [23, 22]. However, the main difficulty in computing the integral in Eq. (2.1) lies in the resonant nature of the cross section of certain nuclides, which exhibit sudden and steep variations over wide energy ranges. Within the same energy interval, the energy-dependent neutron flux tends to exhibit depressions at energy values that coincide with the cross section peaks. Figure 2.3 shows a dip in the flux coinciding with a large resonance peak in the U-238 absorption cross section [34]. As the reaction rate is given by the product of the flux and the cross section, which vary in opposite ways, it shows a weak dependence on energy [23]. This phenomenon, known as energy self-shielding, is particularly relevant for fast reactors, where the average energy variation of a neutron upon a collision is considerably lower, and the probability of falling close to a resonance is significant.

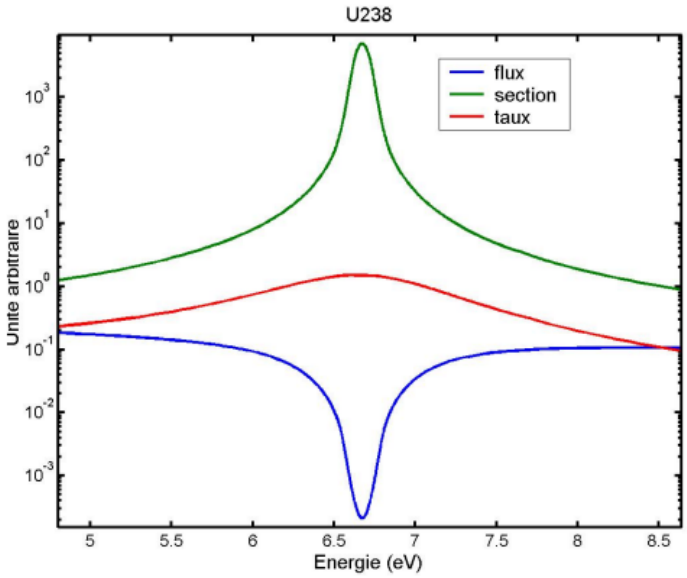


*Figure 2.3: Representation of the self-shielding effect. The flux shows depression at the energy values where peaks of the resonances are present, while the reaction rate is almost constant over the same energy interval. The figure was taken from [34].*

The resonance region of heavy nuclides, where the resonance structures are closely packed together, typically coincides with the energy interval in which the $1/E$ shape of the scalar flux is commonly assumed to solve Eq. (2.1), which turns out to be invalid due to the flux depressions induced by the energy self-shielding effect. Even if the exact shape of the flux were known, accurately resolving the integral would still require the use of thousands of points (which may not be available experimentally), due to the steep cross section variations in very narrow intervals. This would result in unacceptable computational costs and data storage requirements. Other methods are thus required to deal with the collapse of the cross sections in the resonance regions, which are commonly referred to as self-shielding models.

Several methods have been developed for producing self-shielded cross sections: these are the ultra-fine energy calculation, the equivalence theory and the subgroup method [20, 17, 25]. The first method solves the slowing-down equation in the resonance region, thus achieving an accurate solution but requiring significant computational resources. The second method solves the equation in an equivalent set of infinite homogeneous media. The third method solves Eq. (2.1) in the real medium by transforming the Riemann integral into a Lebesgue integral. Within the scope of this thesis, only the subgroup method will be discussed in depth, since this is the model implemented in ECCO for treating the self-shielding effects.

#### 2.2.1.1 The analytical model of the Subgroup Method

The Subgroup method is retrieved by starting from the transport equation and explicitly isolating a single resonant nuclide, denoted here by $re$, while all other nuclides are considered as a single non-resonant moderator element, denoted here by $nre$. By neglecting the fission sources in the slowing-down energy domain, the transport equation reads as

$$\begin{aligned} \overline{\Omega}\cdot\nabla\phi(\overline{r},E,\overline{\Omega}) + (\Sigma_t^{re}(\overline{r},E)+\Sigma_t^{nre}(\overline{r}))\phi(\overline{r},E,\overline{\Omega}) = \\ \frac{1}{4\pi}\int_E^{E/\alpha^{re}} \frac{\Sigma_s^{re}(\overline{r},E')\Phi(\overline{r},E')}{(1-\alpha^{re})E'}dE' + \frac{1}{4\pi}\int_E^{E/\alpha^{nre}} \frac{\Sigma_p^{nre}(\overline{r})\Phi(\overline{r},E')}{(1-\alpha^{nre})E'}dE', \end{aligned} \tag{2.2}$$

which is solved for energy values within a resonant energy group [20]. Within this energy interval, the cross sections of the non-resonant nuclides are assumed to be constant in energy. In addition, the scattering is assumed to be isotropic in the centre of mass and the collisions are assumed to be isotropic and elastic. This enables the maximum fraction of energy lost by a neutron upon a collision to be expressed as

$$\alpha = \left(\frac{A-1}{A+1}\right)^2, \tag{2.3}$$

where $A$ is the nuclide mass relative to the neutron mass [15]. The reader may refer to Appendix C for the full derivation of the elastic scattering term. The elastic cross section of the non-resonant nuclide is approximately constant within the resonant energy interval, and it can be assumed to coincide with the potential scattering cross section, denoted here by $\Sigma_p^{nre}$ [20]. Before going any further, it is necessary to review how the slowing down equation is commonly solved in an infinite medium. As a result of an elastic collision, a neutron having energy $E'$ is scattered within the energy interval $[\alpha E', E']$. Depending on the mass of the target nucleus, the width of this energy interval may be large or small compared to the resonance widths.

Depending on the situation, two different models have been developed: the Narrow Resonance (NR) model and the Wide Resonance (WR) model [25, 14, 16]. The reader may refer again to Appendix C for full details of these models. In the following, the main features relevant to the discussion will be provided. In the first model, the scattering interval is large compared to the width of the isolated resonances, which holds true especially for light nuclides. In this case, the scattering properties of the target nuclide are dominated by the potential scattering cross section outside the resonance interval [14], leading to

$$\int_E^{E/\alpha} \frac{\Sigma_s(\overline{r},E')\Phi(\overline{r},E')}{(1-\alpha)E'}dE' \approx \Sigma_p(\overline{r})C(E), \tag{2.4}$$

where $C(E)$ is computed as a function of the shape of the scalar flux [20]. In contrast, in the WR model the scattering interval is very small compared to the width of the resonances. This is particularly true for heavy elements, and assuming that $\alpha \to 1$, then $E' \approx E$ [20, 14], and it follows that

$$\int_E^{E/\alpha} \frac{\Sigma_s(\overline{r}, E')\Phi(\overline{r}, E')}{(1-\alpha)E'} dE' \approx \Sigma_s(\overline{r}, E)\Phi(\overline{r}, E). \tag{2.5}$$

The NR and WR models represent very peculiar cases and may not be adequate to correctly describe more complicated systems, where a mixture of nuclide is present. Therefore, the Intermediate Resonance (IR) model is introduced [25, 35, 20]. This is obtained by linearly combining the two preceding models, i.e.

$$\int_E^{E/\alpha} \frac{\Sigma_s(\overline{r}, E')\Phi(\overline{r}, E')}{(1-\alpha)E'} dE' \approx \lambda\Sigma_p(\overline{r})C(E) + (1-\lambda)\Sigma_s(\overline{r}, E)\Phi(\overline{r}, E), \tag{2.6}$$

where $\lambda$ is the Goldstein-Cohen (GC) factor. The IR model is applied for the resonant nuclide in Eq. (2.2) together with the NR model for the background nuclide. The transport equation now reads

$$\begin{aligned} &\overline{\Omega} \cdot \nabla\phi(\overline{r}, E, \overline{\Omega}) + (\Sigma_t^{re}(\overline{r}, E) + \Sigma_t^{nre}(\overline{r}))\phi(\overline{r}, E, \overline{\Omega}) = \\ &\frac{1}{4\pi}\left(\lambda\frac{\Sigma_p^{re}(\overline{r})}{E} + (1-\lambda)\Sigma_s^{re}(\overline{r}, E)\Phi(\overline{r}, E) + \frac{\Sigma_p^{nre}(\overline{r})}{E}\right), \end{aligned} \tag{2.7}$$

where the $1/E$ shape of the flux in a purely scattering medium is used to compute $C(E)$ [20]. The transport equation is then expressed in terms of the lethargy variable $u = \ln\frac{E_{ref}}{E}$, assuming that the scattering with the resonant nuclide does not change the angular direction, leading to

$$\overline{\Omega} \cdot \nabla\phi(\overline{r}, u, \overline{\Omega}) + \left(N^{re}(\overline{r})\sigma_\lambda^{re}(u) + \Sigma_t^{nre}(\overline{r})\right)\phi(\overline{r}, u, \overline{\Omega}) = \frac{1}{4\pi}\left(\lambda\Sigma_p^{re}(\overline{r}) + \Sigma_p^{nre}(\overline{r})\right), \tag{2.8}$$

where it has been made use of the fact that $\phi(u) = E\phi(E)$ [20] and

$$\sigma_\lambda^{re}(u) = \sigma_a^{re}(u) + \lambda\ \sigma_s^{re}(u), \tag{2.9}$$

remarking that

$$\sigma_t^{re}(u) = \sigma_a^{re}(u) + \sigma_s^{re}(u). \tag{2.10}$$

Observing Eq (2.9), it can be noted that when the GC factor is taken equal to 1 (i.e. the NR assumption is made for the resonant nuclide), $\sigma_\lambda^{re}(u) = \sigma_t^{re}(u)$. On contrary, when the GC factor is taken equal to 0 (i.e. using the WR approximation for the resonant nuclide), $\sigma_t^{re}(u) = \sigma_a^{re}(u)$ [25]. To address the self-shielding effect using the subgroup method in ECCO, the NR model was adopted for resonant nuclides, since it provides a more accurate description of the closely packed resonances of heavy nuclides at high and intermediate energies, where resonance widths are typically small [4, 33]. In the context of this thesis, the GC factor is therefore set to one. However, this model does not conform to the resonances of heavy nuclides at low energies, where their width is usually large. These resonances must be accurately treated using a fine energy group structure in the thermal and epithermal regions, without necessarily relying on the subgroup method. Therefore, the width of the energy intervals in the 1968 group library was chosen to correspond to a lethargy interval $\Delta u = 1/120 = 0.0083$ [4, 7]. This value corresponds to the average lethargy gain of a neutron upon collision with U-238, which can be computed as

$$\overline{\Delta u} = \overline{u - u'} = \overline{\ln\frac{E'}{E}} = \int_{\alpha E'}^{E'} \ln(\frac{E'}{E})\frac{dE}{(1-\alpha)E'} = 1 + \frac{\alpha\ln\alpha}{1-\alpha}, \tag{2.11}$$

which is approximately equal to 0.008 [15]. This implies that only a small fraction of the neutrons will remain within the same energy group for every collision (approximately one quarter of the total collisions) [7, 4].

The total cross section is then condensed in terms of the lethargy, i.e.

$$\sigma_{t,g}^{re}(\overline{r}) = \frac{\int_{\Delta u_g} \sigma_t^{re}(u)\ \Phi(\overline{r},u)\ du}{\Phi_g(\overline{r})}. \tag{2.12}$$

As mentioned above, solving this integral using the flux obtained from solving the slowing down equation would give accurate results, but it would be very computationally expensive. Instead, it can be observed in Eq. (2.8) that the lethargy dependence of the scalar flux is given only by $\sigma_\lambda^{re}(u)$ (and hence by the total cross section, for $\lambda = 1$). Thus, integration can be run over this variable to obtain

$$\sigma_{t,g}^{re}(\overline{r}) = \frac{\int_{\Delta u_g} \sigma_t^{re}(u)\ \Phi(\overline{r},\sigma_t^{re}(u))\ du}{\Phi_g(\overline{r})} = \frac{\int_{D_g} \sigma_t^{re}\ \Phi(\overline{r},\sigma_t^{re})\ \omega_g(\sigma_t^{re})\ d\sigma_t^{re}}{\int_{D_g} \Phi(\overline{r},\sigma_t^{re})\ \omega_g(\sigma_t^{re})\ d\sigma_t^{re}}, \tag{2.13}$$

where $D_g = [\min \sigma(u), \max \sigma(u)]_{u\in\Delta u_g}$ and $\omega_g(\sigma_t)$ is a probability density function, such that $\omega_g(\sigma_t)\ d\sigma_t$ gives the probability that $\sigma_t$ lies within the interval $[\sigma_t, \sigma_t + d\sigma_t]$ [34, 23]. Figure 2.4 shows this quantity as a function of a generic total cross section. The advantage here is that the previous Riemann integral has been transformed into a Lebesgue integral, which has a simpler numerical computation as the flux shows mild variations over the cross section.

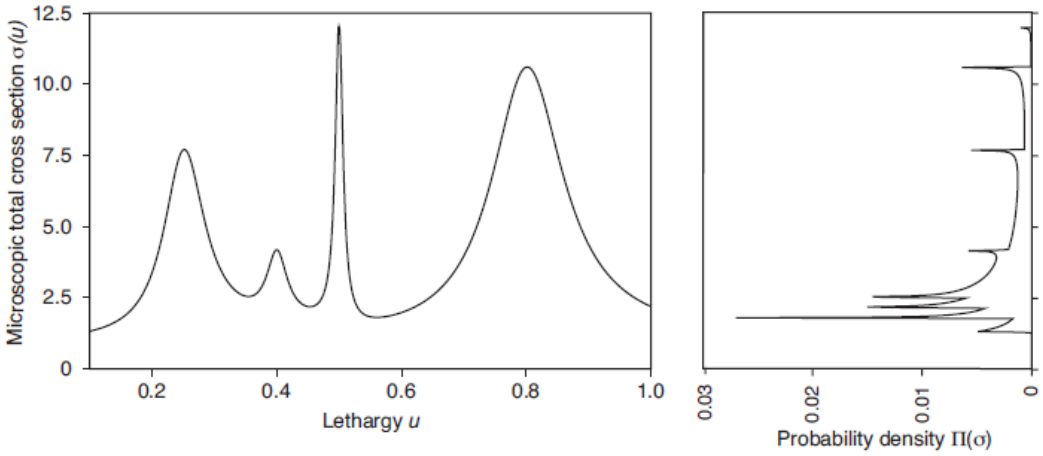


*Figure 2.4: Representation of a lethargy-dependent total cross section, alongside a probability density function showing the likelihood of the total cross section falling within an infinitesimal interval. The figure was taken from [25].*

Finally, the core of the subgroup method is to use numeric quadrature formula to solve integral (2.13), i.e.

$$\sigma_{t,g}^{re}(\overline{r}) \approx \frac{\sum_k \sigma_{t,g,k}^{re}\ \Phi(\overline{r},\sigma_{t,g,k}^{re})\ \omega_{g,k}}{\sum_k \Phi(\overline{r},\sigma_{t,g,k}^{re})\ \omega_{g,k}}, \tag{2.14}$$

where the resonant group g is divided into a number K of subgroups, hence the name of the method. The pair of values $\{\sigma_{t,k}, \omega_k\}_{g,k=1,K}$ must be provided for every resonant nuclide and for every resonant energy group [34, 23, 35]. These data makes up the so-called Probability Tables (PT), which are contained within the ECCOLIB given as an input to the ECCO code. For the partial cross section the procedure is similar, i.e.

$$\begin{aligned}\sigma_{x,g}^{re}(\overline{r}) = \frac{\int_{\Delta u_g} \sigma_x^{re}(u)\ \Phi(\overline{r},\sigma_t^{re}(u))\ du}{\Phi_g(\overline{r})} &= \frac{\int_{D_{g,t}} d\sigma_t^{re}\ \Phi(\overline{r},\sigma_t^{re}) \int_{D_{g,x}} d\sigma_x^{re}\ \sigma_x^{re}\ \omega_g(\sigma_t^{re},\sigma_x^{re})}{\int_{D_{g,t}} \Phi(\overline{r},\sigma_t^{re})\ \omega_g(\sigma_t^{re})\ d\sigma_t^{re}} \\ &= \frac{\sum_k \Phi(\overline{r},\sigma_{t,g,k}^{re}) \sum_j \tilde{\omega}_{g,jk}\ \tilde{\sigma}_{x,g,j}^{re}}{\sum_k \Phi(\overline{r},\sigma_{t,g,k}^{re})\ \omega_{g,k}} \approx \frac{\sum_k \sigma_{x,g,k}^{re}\ \Phi(\overline{r},\sigma_{t,g,k}^{re})\ \omega_{g,k}}{\sum_k \Phi(\overline{r},\sigma_{t,g,k}^{re})\ \omega_{g,k}},\end{aligned} \tag{2.15}$$

where $\omega_g(\sigma_t, \sigma_x)d\sigma_t d\sigma_x$ is the probability that for a partial cross section $\sigma_x$ lying within $[\sigma_x, \sigma_x + d\sigma_x]$, the associated total cross section $\sigma_t$ lies within $[\sigma_t, \sigma_t + d\sigma_t]$ [34, 23]. Furthermore, it has been defined

$$\sigma^{re}_{x,g,k}\ \omega_{g,k} = \sum_j \tilde{\omega}_{g,jk}\ \tilde{\sigma}^{re}_{x,g,j}, \tag{2.16}$$

which allows a set of pairs of values $\{\sigma_{x,k}, \omega_k\}_{g,k=1,K}$ to be provided to ECCO, without calculating again the probability weights [34]. Chapter 3 will present the methodology for calculating the PTs for ECCO, using the CALENDF code and the Gaussian quadrature formula theory [36, 37].

The subgroup method allows to reduce significantly the amount of points required to compute the condensed cross sections (from 80000 to 32000 for $U_{238}$, for example [4]). In addition, to take into account the broadening of the resonances due to the Doppler effect, probability tables must be provided at different levels of temperature.

#### 2.2.1.2 ECCO implementation of the Subgroups Method

The solution of Eqs. (2.14) and (2.15) requires knowledge of the scalar flux. Two approaches can be determined, depending on whether the geometry is homogeneous or heterogeneous [9, 33]. For a homogeneous medium, consisting of only one resonant and one non-resonant nuclide (result of the damping of all the other nuclides), the transport equation integrated over the solid angle is expressed assuming elastic and isotropic scattering, leading to

$$\begin{aligned}(\Sigma^{re}_t(E) + \Sigma^{nre}_t(E))\Phi(E) = \int_E^{E/\alpha} \frac{\Sigma^{re}_{s,0}(E')\Phi(E')}{(1-\alpha)E'}dE' + \int_E^{E/\alpha} \frac{\Sigma^{nre}_{s,0}(E')\Phi(E')}{(1-\alpha)E'}dE' \\ + \frac{1}{k}\chi(E)\int_0^{\infty} \nu\Sigma_f(E')\Phi(E').\end{aligned} \tag{2.17}$$

Considering a certain subgroup $k \in g$, with non-resonant cross sections assumed to be constant within the resonant group $g$, the transport equation reads

$$(\Sigma^{re}_{t,g,k} + \Sigma^{nre}_{t,g})\Phi_{g,k} = S^{re}_{g,k} + S^{nre}_g, \tag{2.18}$$

where $S^{nre}_g$ is the neutron source due to fission and scattering on the non-resonant nuclides, also assumed to be constant within the subgroup $k$, since the resonant groups are well below the energy range in which the fission sources are present. $S^{re}_{g,k}$ is instead the source due to scattering on the resonant nuclide. The Statistical (ST) model makes the hypothesis that the resonances are narrow, but in contrast to the NR model, they are not isolated but statistically distributed along the energy interval and with a spacing much smaller than the maximum lethargy variation due to scattering on the heavy nuclide [25, 23, 34]. This hypothesis, which is valid for the unresolved resonance interval, can be extended to the higher extent of the resolved range (further details about these two ranges will be provided in Chapter 3).

Therefore, for any subgroup $k$, the scattering source on the heavy nuclide is approximately the same, and it can be replaced by the mean value over the whole group $g$, i.e.

$$S^{re}_{g,k} = \int_{E_k}^{E_k/\alpha} \frac{\Sigma^{nre}_{s,0}(E')\Phi(E')}{(1-\alpha)E'}dE' \approx \frac{1}{\Delta E_g}\int_{\Delta E_g} \Sigma^{re}_{s,0}(E')\Phi(E')dE' = S^{re}_g, \tag{2.19}$$

and the scalar flux is now expressed as

$$\Phi_{g,k} = \Phi(\sigma^{re}_{t,g,k}) = \frac{S^{nre}_g + S^{re}_g}{\Sigma^{nre}_{t,g} + \Sigma^{re}_{t,g,k}} = \frac{C}{\frac{\Sigma^{nre}_{t,g}}{N^{re}} + \sigma^{re}_{t,g,k}}. \tag{2.20}$$

The numerator of this expression is constant within the group $k$, and the flux is used to compute the condensed cross section in equation Eqs. (2.14) and (2.15) as

$$\sigma^{re}_{x,g} = \frac{\sum_k \frac{\sigma^{re}_{x,g,k}\ \omega_{g,k}}{\frac{\Sigma^{nre}_{t,g}}{N^{re}} + \sigma^{re}_{t,g,k}}}{\sum_k \frac{\omega_{g,k}}{\frac{\Sigma^{nre}_{t,g}}{N^{re}} + \sigma^{re}_{t,g,k}}}. \tag{2.21}$$

The above self-shielding model has been derived by considering only one resonant nuclide, with all the others being damped in the background moderator. The derivation for the case where N resonant nuclides are considered is similar, but this time the lethargy dependence of the scalar flux in equation (2.12) is given by the cross sections of all resonant nuclides. In this case, the Lebesgue integral for the resonant nuclides $re_n$ ($n \in N$) becomes [23]

$$\sigma^{re_n}_{t,g}(\overline{r}) = \frac{\int_{D_g^{re_1}} d\sigma_t^{re_1} \cdots \int_{D_g^{re_N}} d\sigma_t^{re_N}\ \sigma_t^{re_n}\ \Phi(\overline{r}, \sigma_t^{re_1}, \ldots, \sigma_t^{re_N})\ \omega_g(\sigma_t^{re_1}, \ldots, \sigma_t^{re_N})}{\int_{D_g^{re_1}} d\sigma_t^{re_1} \cdots \int_{D_g^{re_N}} d\sigma_t^{re_N}\ \Phi(\overline{r}, \sigma_t^{re_1}, \ldots, \sigma_t^{re_N})\ \omega_g(\sigma_t^{re_1}, \ldots, \sigma_t^{re_N})}, \tag{2.22}$$

and by making use of the statistical hypothesis [23]

$$\omega_g(\sigma_t^{re_1}, \ldots, \sigma_t^{re_n}) = \prod_{i=1}^{n} \omega(\sigma_t^{re_i}), \tag{2.23}$$

equation (2.22) is expressed again with the use of quadrature formulas:

$$\sigma^{re_n}_{t,g}(\overline{r}) = \frac{\sum_{k_1} \cdots \sum_{k_N}\ \sigma^{re_n}_{t,g,k_n}\ \Phi(\overline{r}, \sigma^{re_1}_{t,g,k_1}, \ldots, \sigma^{re_N}_{t,g,k_N})\ \omega_{g,k_1} \ldots \omega_{g,k_N}}{\sum_{k_1} \cdots \sum_{k_N}\ \Phi(\overline{r}, \sigma^{re_1}_{t,g,k_1}, \ldots, \sigma^{re_N}_{t,g,k_N})\ \omega_{g,k_1} \ldots \omega_{g,k_N}}, \tag{2.24}$$

where $k_1 \ldots k_N$ are respectively the subgroups into which the group $g$ has been divided for the resonant nuclides $1 \ldots N$. Using the same approach as above, the cross section for the resonant nuclide $re_n$ is derived as

$$\sigma^{re_n}_{x,g} = \frac{\sum_{k_1} \cdots \sum_{k_N} \frac{\sigma^{re_n}_{x,g,k_n}\ \omega_{g,k_1} \ldots \omega_{g,k_N}}{\frac{\Sigma^{nre}_{t,g}}{N^{re}} + \sigma^{re_1}_{t,g,k_1} + \cdots + \sigma^{re_N}_{t,g,k_N}}}{\sum_{k_1} \cdots \sum_{k_N} \frac{\omega_{g,k_1} \cdots \omega_{g,k_N}}{\frac{\Sigma^{nre}_{t,g}}{N^{re}} + \sigma^{re_1}_{t,g,k_1} + \cdots + \sigma^{re_N}_{t,g,k_N}}}, \tag{2.25}$$

which is solved for every resonant nuclide [33]. For the heterogeneous case, the flux is computed using the collision probability method (see Eq. (1.34) in Chapter 1). Therefore, in the case of one single resonant nuclide, the self-shielded cross section is calculated for each region $i$ as

$$\sigma^{re}_{x,i,g} = \frac{\sum_j Q_{j,g} \sum_k \sigma^{re}_{x,g,k}\ p_{g,ij}(\Sigma_{t,g,k})\ \omega_{g,k}}{\sum_j Q_{j,g} \sum_k p_{g,ij}(\Sigma_{t,g,k})\ \omega_{g,k}}, \tag{2.26}$$

where $p_{i,j}$ is the reduced collision probability. Knowledge of the sources generated in others regions is required, and hence knowledge of the flux in the whole domain. Therefore, as mentioned in the introduction to this chapter, an iterative procedure is performed between the production of the self-shielded cross sections and the flux evaluation. Furthermore, since CPs also depend on the cross sections, they must be re-evaluated each time the subgroup method is employed.

In the heterogeneous medium, the implemented collision probability summations make impractical the approach used previously for the case of more than one resonant nuclide. Therefore,

ECCO adopts an iterative procedure, where a single nuclide is treated as resonant while all the others are considered as non-resonant and damped in the moderator. The self-shielded cross section is evaluated and the algorithm continues with another resonant nuclide, using the same approach, until all the nuclides have been treated. The code then repeats the cycle until convergence on the cross sections is reached [33]. The basic hypothesis of this method is that the resonances of different nuclides do not overlap within a specific energy group. This hypothesis is valid when a fine energy groups structure is adopted, but may not hold true when a broad structure or many nuclides are considered.

It is worth mentioning that this iterative process can also be used in a homogeneous medium, when many nuclides are present and the summation order in equations (2.25) increases largely [33].

In conclusion, it has been outlined how ECCO generates self-shielded partial cross sections using sets of quadrature points $Q_{x,g} = \{\sigma_{x,k}, \omega_k\}_{g,k=1,K}$. The K couple of points, for each group $g$, are provided by CALENDF using the method of moments, which yields mathematical probability tables [36, 37]. Chapter 3 will detail how these values are produced by CALENDF and integrated into the NDLs. For the production of self-shielded cross sections at different temperatures, ECCO uses interpolation laws. These are not applied between the probability tables, which may contain different numbers of subgroups at different temperatures due to Doppler broadening, but rather applied on the moments reconstructed starting from the PTs provided by CALENDF at predefined temperature levels. Afterwards, the interpolated moments at the intended temperature are used to compute the new quadrature points [33, 8].

### 2.2.2 The flux solution

As highlighted in Figure 2.2, a procedure involving iterations between the flux computation and self-shielded cross sections calculation is implemented. Since ECCO calculations are performed in homogeneous and heterogeneous geometries, the flux solution is detailed in both contexts.

#### 2.2.2.1 The collision probabilities and the Roth method

The flux solution in heterogeneous geometries is implemented in the ECCO code using the collision probability method, as detailed in Section 1.3. The CPs are implemented using different routines depending on the specific case. Some routines compute the collision probabilities analytically, provided the geometry is simple enough. Others resort instead to approximate methods to calculate the collision probabilities. Among them, the Roth method is the one customarily used within the ECCO cell code [33, 38].

This method divides complex geometries into smaller regions known as links. These regions are simpler geometries for which collision probabilities can be computed using other routines, e.g. with analytical formulations. For a generic link named $A$, let $P^A_{g,ij}$ be the CP calculated for two regions $i$ and $j$ within A. Since this approach is valid for any energy group, the group-index notation is suppressed thereafter. Then, the probability that a neutron born in the region $i$ leaves the link $A$, $P^A_{is}$, can be determined by imposing vacuum boundary conditions [33], which leads to

$$P^A_{is} = 1 - \sum_{j=1}^{n} P^A_{ij}, \tag{2.27}$$

where $n$ is the number of regions into which the link is divided. The following step is to determine how neutrons are transported between links. The quantity $N_{AB}$ gives the probability of a neutron leaving the link $A$ and arriving at the surface of link $B$. This quantity is determined by contributions from other quantities:

- $R_{AK}$ represents the number of neutrons that travel from link $A$ to link $K$ without crossing any other links. This term is generally related to the geometrical surface between the

links.

- $P_{ss}^{K}$ is the probability that a neutron crosses link $K$ without having a collision. This quantity is estimated through the reciprocity relation [33], which reads

$$P_{ss}^{A} = 1 - \sum_{i=1}^{n} \frac{4V_i \Sigma_{t,i} P_{is}^{A}}{S}, \tag{2.28}$$

  where $S$ is the surface area of the boundary and $V_i$ is the volume of the individual region.

Therefore, the number of neutrons that reach link $B$ from link $A$ is made up of two contributions: the first are the neutrons that from link $A$ reach directly link $B$, without having any collision. The second is the contribution of all neutrons born from a collision in link $A$ that reach any other link $K$, stream through this link without colliding, and then reach link $B$. This can be expressed mathematically as

$$N_{AB} = R_{AB} + \sum_{K} R_{AK}\ P_{ss}^{K}\ N_{KB}, \tag{2.29}$$

which is then arranged in a matrix form that reads

$$N = (I - RE)^{-1} R, \tag{2.30}$$

where $I$ is the identity matrix and $E$ is the transmission probability matrix, which is a diagonal matrix containing the $P_{ss}^{K}$ terms [33]. The $R$ matrix can be computed once and for all at the beginning of the calculations using the geometric data as input. Once each term in the $N$ vector is computed, the collision probabilities between links $A$ and $B$ are calculated with linear combinations of the intra-link probabilities, i.e.

$$\begin{aligned} P_{i_A j_B}^{A} &= P_{ij}^{A} + P_{is}^{A}\ N_{AB}\ P_{sj}^{B} && \text{if } A = B, \\ P_{i_A j_B}^{A} &= P_{is}^{A}\ N_{AB}\ P_{sj}^{B} && \text{if } A \neq B. \end{aligned} \tag{2.31}$$

In order to improve the accuracy of the method, Roth x4 and Roth x6 methods were developed for ECCO in rectangular and hexagonal lattices, respectively [33]. These methods calculate the intra-link probabilities accordingly to the method described above, but this time the cell is divided into its outer surfaces. The collision probabilities are then computed by taking into account the possible combinations of the cell's external surfaces. Consider, for example, a rectangular lattice in which cells are divided into four external surfaces as shown in Figure 2.5.

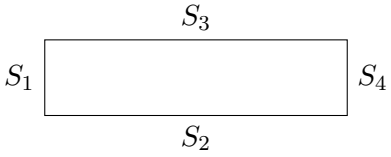


*Figure 2.5: Roth x 4 method. The rectangular cell is divided into four external surfaces. The figure was taken from [33].*

The probability of a neutron born by collision in $i$ escaping the link $A$ through the surface $S_\alpha$ is calculated as [33]

$$P_{iS_\alpha}^{A} = \frac{S_\alpha}{S} P_{is}^{A}. \tag{2.32}$$

Similarly, the probability that a neutron entering the link $A$ crosses surface $S_\alpha$, streams without colliding, and exits the link through surface $S_\beta$ is

$$\begin{aligned} P_{S_\alpha S_\beta}^{A} &= \frac{\max\{S_\beta, 2S_\beta - T_\alpha\}}{\max\{2S_1 + S_2, 2S_2 + S_1\}} && \text{if } \alpha \neq \beta, \\ P_{S_\alpha S_\beta}^{A} &= 0 && \text{if } \alpha = \beta, \end{aligned} \tag{2.33}$$

where $T_1 = T_4 = S_2 = S_3$ and $T_2 = T_3 = S_1 = S_4$. Then, the formulation of Eq. (2.30) remains unchanged, but this time the $R$ matrix will have a larger dimension as it contains information on neutron transport across different surfaces [33].

#### 2.2.2.2 The fundamental mode solution in the homogeneous medium

The flux solution in a homogeneous medium can be derived from the transport equations under the multigroup approximation, as derived in Section 1.2, which reads

$$\overline{\Omega} \cdot \nabla \phi_g(\overline{r}, \overline{\Omega}) + \Sigma_{t,g}\phi_g(\overline{r}, \overline{\Omega}) = \sum_{g'=1}^{G} \sum_{l=0}^{\infty} \Sigma_{s,l,gg'} \sum_{\beta=-l}^{l} Y_l^{\beta}(\overline{\Omega}) \phi_{l,g'}^{\beta}(\overline{r}) + \frac{S_g(\overline{r})}{4\pi}, \tag{2.34}$$

where $S_g$ is the sum of the fission source and an eventual external source, which are both assumed to be isotropic. If the medium is infinite, the flux will be isotropic and spatially uniform [33], which leads to the trivial solution

$$\phi_g = \frac{S'_g}{\Sigma_{r,g}}, \tag{2.35}$$

where $S'_g$ is the fission and scattering source (from higher energy groups), and $\Sigma_{r,g}$ is the removal scattering cross section (result of the total cross section minus the intra-group scattering cross sections) [33]. In a finite domain, the Fundamental Mode (FM) method is employed for the flux solution. For simplicity, the derivation will be detailed for a 1D geometry, but the methodology can be extended to 2D and 3D geometries. The fundamental mode consists of separating the angular and spatial dependencies in the neutron flux and source, i.e.

$$\phi_g(x, \mu) = \phi_g(\mu) e^{iBx}, \tag{2.36}$$

$$S_g(x) = S_g e^{iBx}, \tag{2.37}$$

where $B^2$ is said to be the Buckling [33, 8]. Substituting these terms in Eq. (2.34) and dividing everything by the exponential term, it is obtained

$$(iB\mu + \Sigma_{t,g})\phi_g(\mu) = \sum_{g'=1}^{G} \sum_{l=0}^{\infty} \Sigma_{s,l,gg'} \sum_{\beta=-l}^{l} Y_l^{\beta}(\overline{\Omega}) \phi_{l,g'}^{\beta} + \frac{S_g}{4\pi}, \tag{2.38}$$

where the moments of the angular flux are evaluated in a 1D geometry as

$$\phi_{l,g'}^{\beta} = \oint d\Omega' \phi_{g'}(\mu')\ Y_l^{\beta *}(\overline{\Omega}') = \int d\varphi' \int d\mu' \phi_{g'}(\mu') \left( \frac{2l+1}{4\pi} \frac{(l-\beta)!}{(l+\beta)!} \right)^{\frac{1}{2}} P_l^{\beta}(\mu') e^{-i\beta\varphi'}. \tag{2.39}$$

Because of the presence of the exponential factor, all terms except $\beta = 0$ vanish, and it follows

$$\begin{aligned} \phi_{l,g'}^{0} = 2\pi \int d\mu'\ \phi_{g'}(\mu') \left( \frac{2l+1}{4\pi} \right)^{\frac{1}{2}} P_l^0(\mu') = \\ 2\pi \left( \frac{2l+1}{4\pi} \right)^{\frac{1}{2}} \int d\mu' \phi_{g'}(\mu') P_l(\mu') = 2\pi \left( \frac{2l+1}{4\pi} \right)^{\frac{1}{2}} \phi_{l,g'} \end{aligned} \tag{2.40}$$

Therefore, Eq. (2.38) now becomes

$$(iB\mu + \Sigma_{t,g})\phi_g(\mu) = \sum_{g'=1}^{G} \sum_{l=0}^{\infty} \frac{2l+1}{2}\ \Sigma_{s,l,gg'}\ \phi_{l,g'}\ P_l(\mu) + \frac{S_g}{4\pi}. \tag{2.41}$$

Then, the flux on the LHS is also expanded on the Legendre polynomials, and both sides are multiplied by $P_m(\mu)$ and integrated over $\mu$ to obtain

$$\begin{aligned} iB \sum_{l=0}^{\infty} \frac{2l+1}{2} \phi_{l,g} \int d\mu\ \mu\ P_l(\mu)\ P_m(\mu) + \Sigma_{t,g} \sum_{l=0}^{\infty} \frac{2l+1}{2} \phi_{l,g} \int d\mu\ P_l(\mu)\ P_m(\mu) = \\ \sum_{g'=1}^{G} \sum_{l=0}^{\infty} \frac{2l+1}{2}\ \Sigma_{s,l,gg'}\ \phi_{l,g'} \int d\mu\ P_l(\mu)\ P_m(\mu) + \frac{S_g}{4\pi} \int d\mu\ P_m(\mu). \end{aligned} \tag{2.42}$$

Then, using the recursive relation of the Legendre polynomials [14], i.e.

$$\mu P_l(\mu) = \frac{1}{2l+1}[(l+1)P_{l+1}(\mu) + lP_{l-1}(\mu)], \tag{2.43}$$

together with the orthogonality property [14], i.e.

$$\int d\mu \; P_l(\mu) \; P_m(\mu) = \frac{2\delta_{lm}}{2l+1}, \tag{2.44}$$

an equation for each projection of the neutron flux is obtained [8], which reads

$$\frac{l+1}{2l+1} iB\phi_{l+1,g} + \frac{l}{2l+1} iB\phi_{l-1,g} + \Sigma_{t,g}\phi_{l,g} = \sum_{g'=1}^{G} \Sigma_{s,l,gg'}\phi_{l,g'} + \frac{2}{2l+1}\frac{S_{g,lo}}{4\pi}, \tag{2.45}$$

where $l$ ranges between 0 and $N+1$, $N$ being the truncation order. The set of $N+1$ equations is solved by eliding the term $\phi_{l+1}$ assuming that this term vanishes, which leads to the $P_N$ approximation [8, 33, 13, 25]. Then, in the $P_1$ approximation [8, 33] the equations for the first two moments assume the shape

$$iB\phi_{1,g} + \Sigma_{t,g}\phi_{0,g} = \sum_{g'=1}^{G} \Sigma_{s,0,gg'}\phi_{0,g'} + \frac{S_{g,0}}{2\pi}, \tag{2.46}$$

$$\frac{iB}{3}\phi_{0,g} + \Sigma_{t,1,g}\phi_{1,g} = \sum_{g'=1}^{G} \Sigma_{s,1,gg'}\phi_{1,g'}, \tag{2.47}$$

where $\Sigma_{t,1,g}$ is the total cross section weighted on the current instead of the scalar flux. The first two orders of the flux are related to two well known physical quantities, which are the scalar flux and the neutron current, respectively [33, 14]. In $P_1$ approximation, the equations are solved for these two quantities, which leads to

$$\Phi_g = \phi_{0,g} = \frac{S_g - \dfrac{B^2 S_{1,g}}{\Sigma_{t,1,g} - \Sigma_{s,1,gg}}}{\Sigma_{r,g} + \dfrac{B^2}{3(\Sigma_{t,1,g} - \Sigma_{s,1,gg})}}, \tag{2.48}$$

$$J_g = i\phi_{1,g} = \frac{|B|\dfrac{\Phi_g}{3} + S_{1,g}}{\Sigma_{t,1,g} - \Sigma_{s,1,gg}}, \tag{2.49}$$

where $S_g$ is the neutron source in group $g$ originating from fission and scattering in other groups, and $S_{1,g}$ is the first-order scattering neutron source. For higher orders, the consistent $P_N$ solution uses the extended transport approximation [8, 33]. In this approximation, it is assumed that strongly anisotropic scattering does not change the neutron energy, leading to an expression for the scattering term that reads

$$\sum_{g'=1}^{G} \Sigma_{s,l,gg'}\phi_{l,g'} \approx \sum_{g'=1}^{G} \int dE \int dE' \Sigma_{s,l}(E' \to E)\phi_l(E') \approx \tag{2.50}$$

$$\sum_{g'=1}^{G} \int dE \int dE' \Sigma_{s,l}(E \to E')\phi_l(E) \approx \phi_{l,g} \sum_{g'=1}^{G} \Sigma_{s,l,g'g} = \phi_{l,g}\Sigma^S_{s,l,g} \quad \text{for} \quad l \geq 2. \tag{2.51}$$

Then, the higher-order projections of the neutron flux are

$$\phi_{l,g} = \frac{l}{2l+1}\frac{i|B|\phi_{g,l-1}}{A_l} \quad \text{for} \quad l = 2 \cdots N, \tag{2.52}$$

where the term $A_l$ is defined as [33]

$$A_l = b_{l-1} + \cfrac{a_l}{b_l + \cfrac{a_{l+1}}{b_{l+1} + \cdots + \cfrac{a_{N-1}}{b_{N-1}}}}, \tag{2.53}$$

for $l$ that ranges from 1 to $N-1$ and for $N=1$, $A_N = b_{N-1}$, where

$$a_l = \frac{(l+1)^2 B^2}{(2l+1)(2l+3)}, \tag{2.54}$$

$$b_0 = \Sigma_{t,1,g}, \tag{2.55}$$

$$b_l = \Sigma_{t,1,g} - \Sigma_{s,gg,l+1}. \tag{2.56}$$

In the inconsistent $P_N$ solution the extended transport approximation is applied also for the $l=1$ order, which leads to the solution

$$\Phi_g = \frac{S_g}{\Sigma_{r,g} + \cfrac{B^2}{3A_1}}, \tag{2.57}$$

$$J_g = |B| \frac{\Phi}{3A_1}, \tag{2.58}$$

$$\phi_{l,g} = \frac{l}{2l+1} \frac{i|B|\phi_{g,l-1}}{A_l} \quad \text{for} \quad l = 2 \cdots N, \tag{2.59}$$

with $b_0$ this time equal to

$$b_0 = \Sigma_{t,1,g} - \Sigma_{s,gg,l+1}. \tag{2.60}$$

Chapter 3

# The nuclear data libraries and the ECCOLIB

The Nuclear Data Library (NDL) is the cornerstone of every deterministic or stochastic code. This set of files contains all the information about the nuclides' cross sections, properties and reactions required for transport and shielding calculations in everyday practice. Generally, the uncertainties in the nuclear data have a greater impact on the accuracy of the final results of a neutronic code, compared to the approximations introduced by the solving algorithms. During a numerical validation process, the results of the deterministic code are usually compared with reference values, such as the results of Monte Carlo (MC) simulations. During a validation process, it is essential to ensure consistency and coherency between the NDLs in the deterministic and MC codes. If this is not the case, the differences between the NDLs may be non-negligible and overshadow the errors arising from the deterministic models, making the validation process impractical.

During the processing of NDLs, the data are not only manipulated to make them accessible to the codes, but also integrated with additional information. For example, this applies to the PTs, which are generated by CALENDF and implemented in ECCO, as outlined in Chapter 2. In the second part of this work, the ECCO self-shielding model will be validated using the ENDF/B-VIII.0 ECCO library that is used for ERANOS calculations within *new*cleo , taking as a reference the results of the OpenMC Monte Carlo code [39, 40]. Recognising the possible differences between the libraries produced for ECCO and OpenMC will lay a solid foundation for any future validation work, which will only be possible if the error sources are isolated from those eventually generated by discrepancies in the NDLs.

Processing Evaluated Nuclear Data Files (ENDF), contained in the NDLs, requires the precise concatenation of operations performed by external codes. Along the chain of procedures, the user must make physical assumptions and perform the necessary informatics operations to process the raw experimental data. This applies to the NDLs that are generated for both ECCO and OpenMC, although they require two different workflows. Beyond the difference in the NDL preparation routine, eventual incoherence in the physical assumptions may lead to further discrepancies. The following chapter will provide the reader with the fundamental knowledge about the production of the NDLs, leading to a better understanding of the eventual discrepancies found when analysing the ECCO library.

## 3.1 ENDF/B Cross section Representations

The ENDF/B libraries are the result of the collaboration between the U.S.'s Cross Section Evaluation Working Group (CSEWG) and the international community [41]. These files contain data on neutron and charged-particle reactions, activation, decay processes, and so on. The latest

versions of the libraries, namely from version VI up to version VIII, follow the ENDF-6 format (also shared by the European JEFF libraries [42, 43]). In this format, the NDL is divided into several ENDF files (tapes), containing information for a single incident particle and other data types. Each tape is subdivided into different materials (MAT), which contain several files (MF). Each of the MF contains sections (MT), which include data (records) about the reaction and its products between the material and the particle specified in the tape [41, 22]. A schematic representation of this structure is reported in figure 3.1.

In the context of this thesis only incident-neutron data will be examined. In this tape, the MF=1 file contains the description of the tape and general data characterizing the material, e.g. the atomic mass, the energy and neutrons released per fission reaction for fissionable isotopes, and so forth. The MF=2 file contains resolved and, if present, unresolved resonance parameters. This data enables the reconstruction of resonant cross sections, as tabulating the pointwise data would require excessive storage memory. File MF=3 contains the tabulations of the energy-continuous cross sections, also called the dilute-average cross sections. Files MF=4,5 and 6 contain the energy and angle distribution of emitted neutrons, reaction products, and other particles. Other files outside the intended focus of this work are also present [41].

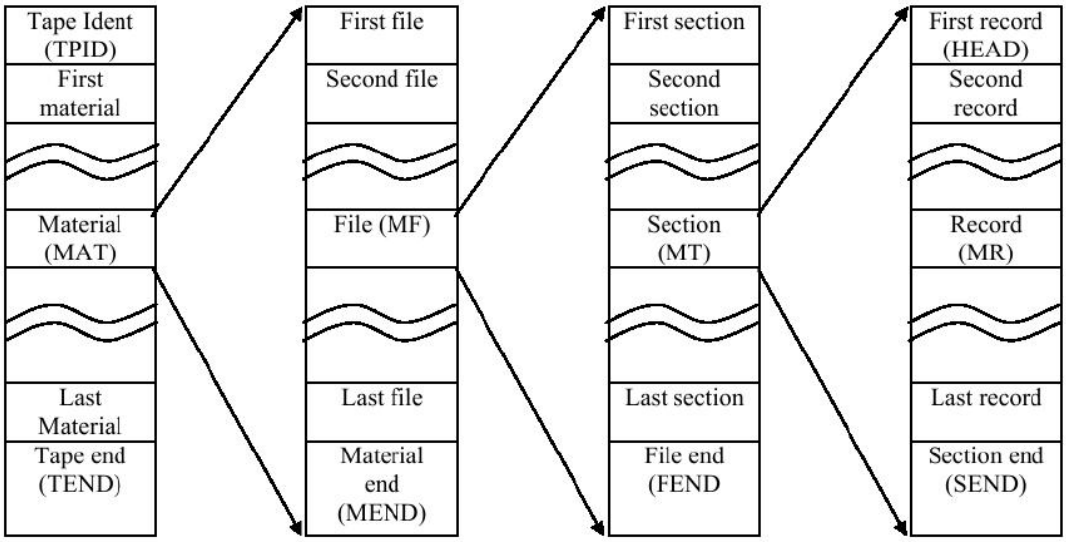


*Figure 3.1: Representation of the structure of and ENDF data tape in the ENDF-6 format. The data are subdivided into materials (MAT), files (MF) and sections (MT). The latter contains the sets of data (records). The figure was taken from [41].*

For resonant materials, the cross sections are reconstructed by summing the background (BG) cross sections from file MF=3 with the resonances computed from the parameters in file MF=2 [41, 22]. Figure 3.2 shows the variation in the total cross section of U-238 throughout the entire energy range, which has been partitioned in three groups: the Resolved Resonance Range (RRR), the Unresolved Resonance Range (URR), and the Continuum.

In the RRR, the cross section resonances are sufficiently spaced that the experimental resolution can determine their individual widths and distributions. In the context of this thesis, the RRR has been extended to the thermal range, where the cross section is smooth again, which is generally referred to as the Low Energy Region (LER) [41]. In the URR, although the resonances are still not overlapping, they are so closely packed together that the experimental resolution cannot determine their individual parameters. Therefore, the resonance parameters given for this range in the MF=2 file are coefficients that describe the statistical distribution of the width and spacing of the resonances [41]. In the Continuum, or the High-Energy Region (HER), the resonances overlap and the cross section is smooth again [41]. Typically, the lighter the isotope, the more the resonances shift towards higher energies. Therefore, for these elements,

the evaluator can omit the URR data if it corresponds to energy values that are of no interest in practical calculations. For the lightest isotopes, even resolved data can be omitted [22].

The cross section reported in figure 3.2 is therefore the result of the union of the background cross section with the resonances outside the URR; in the latter interval, as will be detailed later on, the resonance generation follows a stochastic process. Beyond the statistical approach, the reconstruction of the resonances itself differs between the RRR and the URR. In the RRR, different formalism can be used to reconstruct the cross sections, namely the Single-Level Breit-Wigner (SLBW), the Multilevel Breit-Wigner (MLBW), the Reich-Moore (RM), and the Adler-Adler (A-A) [41, 22]. The ENDF-6 tape includes indication from the evaluator regarding the formalism that has to be used to reconstruct the resonances. In the URR, only the SLBW is allowed [41, 22].

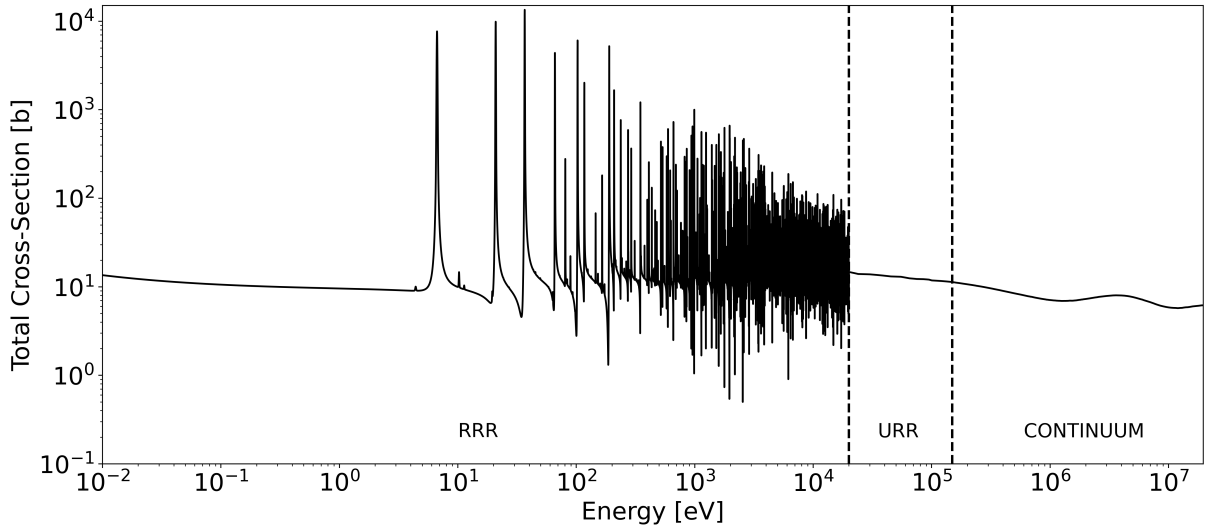


*Figure 3.2: Plot of the energy-dependent total cross section of U-238 at 294K. The energy range has been divided into three intervals: the URR,the RRR, and the Continuum. The represented cross section is given by the sum of the background cross sections and the resonances reconstructed outside the URR.*

## 3.2 ECCO library production workflow

In this section, the workflow required to produce an ECCO library (usually referred to as ECCOLIB) will be outlined. Throughout the process, the ENDF-6 file must be converted into a format that is accessible to ECCO. This involves processing the pointwise ENDF (PENDF) into multigroup (1968, 172, 33) and subgroup data for ECCO calculations [44, 45]. This is achieved using two codes, NJOY and CALENDF [22, 36], together with two interface codes, namely MERGE [46] and GECCO [47]. Figure 3.3 depicts the basic scheme used to process the NDLs in the ECCO 1968 groups library. The final output of the process is a multigroup file (GENDF), which is the actual ECCOLIB used within ECCO. The 33 and 172 groups ECCO libraries are then produced by the CONDENA code, which condenses the 1968 PTs for the resonant nuclides into broader group structures and merges them with the multigroup data produced for the non-resonant nuclides [48, 44].

The NJOY and CALENDF codes work in a complementary way to process the NDLs. The former is responsible for preparing the multigroup cross section data, scattering matrices, and for the thermal scattering treatment. The latter produces multigroup cross sections and probability tables, using a Gaussian quadrature, for the treatment of self-shielding in ECCO (for the resonant nuclides). The MERGE interface then checks, makes consistent, and joins the multigroup cross sections and PTs in a unique GENDF* file. The new file is then fed as input

to the GECCO code, which converts it to a format that can be read by ECCO. In the following, each step is briefly described.

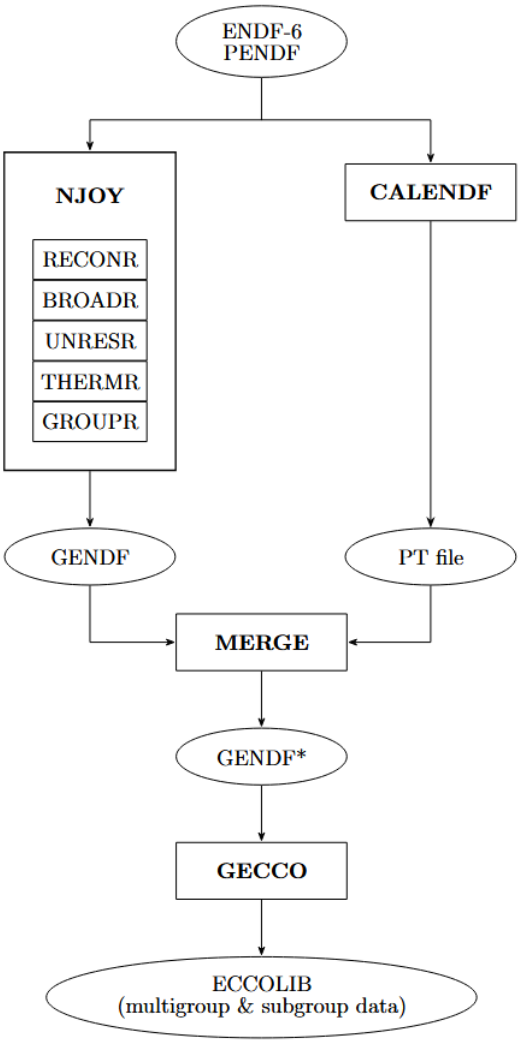


*Figure 3.3: Workflow representation of the production of a 1968 groups ECCO library. Throughout the process, the PENDF (which contains pointwise data) is elaborated into a GENDF (which contains multigroup data). The output from the NJOY code (multigroup cross sections) is merged with PTs produced by the CALENDF code, using the MERGE code. Finally, GECCO converts the GENDF* file into the ECCOLIB. The figure was adapted from [45].*

### 3.2.1 The NJOY code

NJOY is the code used to elaborate the pointwise cross sections and resonance parameters in the ENDF-6 format into a set of multigroup cross sections. NJOY is a multi-modular programme, and each module must be executed in the prescribed order to manipulate the library correctly. The modules are presented below in the order in which they are called for the processing of ECCO-compatible NDLs. Unless otherwise specified , all information in this section refers to the NJOY2016 manual [22].

#### 3.2.1.1 RECONR

The RECONR module reads the ENDF-6 input and produces pointwise cross sections which are then stored in a PENDF output. The cross sections are computed at 0 K on a common energy grid, starting from the BG values in file MF=3 and the resonance parameters in file MF=2.

NJOY uses linear interpolation schemes to reconstruct the cross sections at intermediate energies between two neighbouring points. This makes it possible to compute summation cross sections (elastic, fission, etc.) as the sum of their constituent partial cross sections. However, not all the interpolation schemes in the ENDF-6 tape are linear. Starting from the input tape, RECONR creates a union grid for all the cross sections, enabling linear interpolation while ensuring an acceptable level of accuracy.

Then, RECONR computes the cross sections on this grid in the resolved and unresolved ranges. In the resolved range, the module uses one of the following formalism: SLBW, MLBW, RM or A-A. In the URR, the SLBW computes the cross section using the statistical distribution and average parameters in the MF=2 file. These data will eventually be overwritten by the self-shielded values in the UNRESR module.

#### 3.2.1.2 BROADR

The BROADR module is used to apply Doppler broadening to cross sections within the resolved range. This is particularly important for reactions that exhibit resonances, such as elastic scattering, capture, and fission. This is achieved by conserving the reaction rates between the stationary state and the states at different temperatures. Then, the module computes a new energy grid able to accommodate the Doppler-broadened cross sections.

#### 3.2.1.3 UNRESR

The UNRESR module computes self-shielded effective cross sections on the BROADR energy grid within the URR. Due to the statistical uncertainty of the resonance distributions within this range, energy-averaged cross sections can only be defined as

$$\sigma_x(\overline{E}) = \frac{\int_{E_1}^{E_2} \sigma_x(E)\Phi(E)dE}{\int_{E_1}^{E_2} \Phi(E)dE} \quad \text{for } \overline{E} \in [E_1, E_2], \tag{3.1}$$

where $x$ stands for a generic reaction and the interval $[E_1, E_2]$ should be sufficiently small, compared to the smooth variations in $\Phi(E)$, but should also contain a significant number of resonances. To account for dips in the scalar neutron flux, UNRESR adopts the Bondarenko method [49], which assumes that its shape can be described as

$$\Phi(E) = \frac{C(E)}{\sigma_t(E) + \sigma_0}, \tag{3.2}$$

where $C(E)$ is a slowly varying function of energy, $\sigma_t$ is the total cross section of the nuclide and $\sigma_0$ is the background cross section, assumed to be constant within $[E_1, E_2]$, which results from the lumping together of the total cross sections of the other isotopes in the surrounding medium. This term controls the effect on self-shielding of the isotope dilution in a material containing more nuclides; for small values of $\sigma_0$, the flux develops dips in correspondence of the peaks in the total cross section $\sigma_t(E)$ and self-shielding is accounted for. Conversely, for large values of $\sigma_0$ the flux is dominated by this parameter alone and self-shielding effects are not taken into account. When $\sigma_0$ tends to infinity, the effective cross section is said to be infinitely diluted.

The effective cross section is finally expressed as

$$\sigma_x(\overline{E}) = \frac{\displaystyle\int_{E_1}^{E_2} \frac{\sigma_x(E)\ C(E)}{\sigma_t(E) + \sigma_0} dE}{\displaystyle\int_{E_1}^{E_2} \frac{C(E)}{\sigma_t(E) + \sigma_0} dE} \quad \text{for } \overline{E} \in [E_1, E_2], \tag{3.3}$$

which is further elaborated within the UNRESR module and solved at different temperatures. The dilution choice is a free parameter that must be specified by the user. The parameter is not known *a priori*, and it is common practice to provide a grid of values exploring the sensitivity of the cross section to these values.

#### 3.2.1.4 THERMR

Within the thermal range (at energies lower than 1 eV) the scattering reactions cannot be simply described by considering the target nucleus as free to recoil. The kinetic energy transferred in each collision is comparable to the thermal motion of the nucleus and the excitation energy of the atoms in crystalline and other molecular structures [14]. Therefore, the RECONR module takes into account these effects by applying several models and writing the results in new MT sections.

#### 3.2.1.5 GROUPR

The task of the GROUPR module is to compute energy-averaged cross sections for use in the multigroup method, i.e.

$$\sigma_{x,g} = \frac{\int_{E_g}^{E_{g-1}} dE\ \sigma_x(E)\Phi(E)}{\Phi_g}. \tag{3.4}$$

As outlined in Chapter 1, computing these quantities requires knowledge of the scalar flux. Several options are available in the GROUPR module. For typical applications, the thermal Maxwellian distribution, the $1/E$ shape, and the fission spectrum are employed in the thermal, epithermal and fast regions, respectively. Where resonances are present, and the usual flux shapes cannot be used, GROUPR produces multigroup Self-Shielded cross sections by applying the Bondarenko model, as outlined in the UNRESR section. In this case too, the choice of the background cross section $\sigma_0$ determines how self-shielding is taken into account in the final results.

Moreover, GROUPR elaborates scattering matrices, energy-angle distribution, prompt and delayed fission spectrums, and the average number of neutrons emitted by fission into multigroup structures.

### 3.2.2 CALENDF

CALENDF is the code, complementary to NJOY, used for the production of multigroup averaged cross sections and probability tables for ECCO [36] (and other applications, such as TRIPOLI [50, 51, 52]). For each nuclide and each resonant energy group, the probability tables are used in the subgroup method to solve Eqs. (2.25) and (2.26). As described in the previous chapter, a probability table consists of a set of pairs of values $Q_{x,g} = \{\sigma_{x,k}, \omega_k\}_{g,k=1,K}$ for each $k-th$ subgroup within the energy group $g$, and for a generic reaction ($x$ can stand for total, fission, capture, etc.). The value $\omega_{g,k}$ represents the discretisation of a continuous probability density function representing the probability that the microscopic total cross section lies within an infinitesimal interval, as shown in Figure 3.4. These pairs of values make up quadrature points that can be used to solve the Lebesgue integral. The process of generating the discrete values starting from the continuous total cross sections and PDF $\omega$ is performed using the method of moments [23, 37, 53] , which is discussed in the following section.

#### 3.2.2.1 The Method of Moments

This method is based on the definition of the $l-th$ order moment of the total cross section, and its subsequent expression in terms of a Lebesgue integral. This leads to

$$\mathcal{M}_{l,g} = \frac{1}{\Delta u_g}\int_{\Delta_{u_g}} \sigma_t^l(u)\ du = \int_{D_g} \sigma_t^l\ \omega(\sigma_t)\ d\sigma_t, \tag{3.5}$$

which can be computed by CALENDF reading from the MF=2 and MF=3 files in the ENDF-6 libraries. The $l-th$ moment can be expressed approximately in terms of the $K$ doublets of

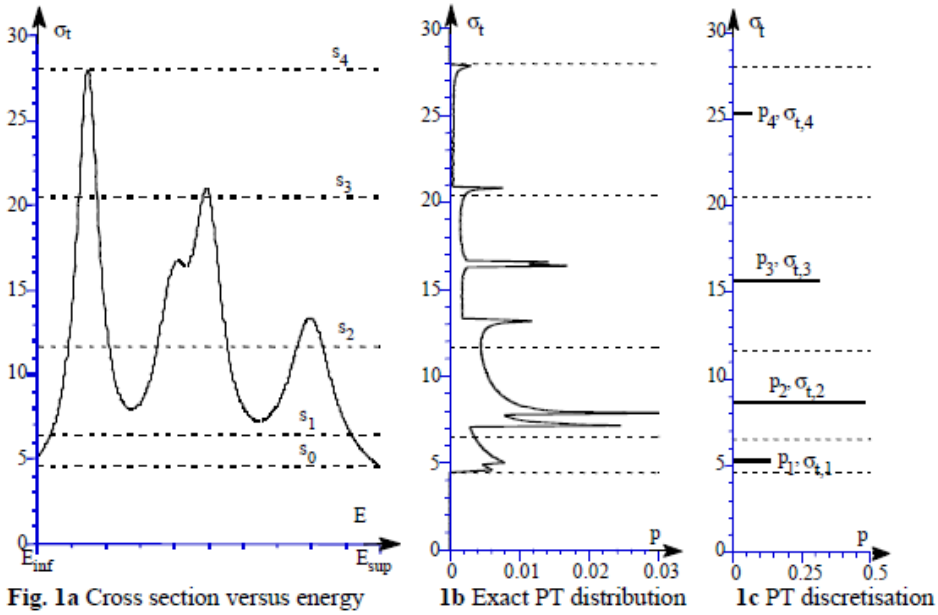


*Figure 3.4: Graphical representation of a probability table. The value p (in the context of this thesis, referred to as ω) is the probability that the total cross section lies within an infinitesimal interval. The figure was taken from [53].*

points $Q_{t,g} = \{\sigma_{t,k}, \omega_k\}_{g,k=1,K}$ as

$$\tilde{M}_{l,g}(Q_{t,g}) = \sum_{k=1}^{K} \omega_{g,k}\ \sigma^l_{t,g,k}, \tag{3.6}$$

where the right-hand side represents a Gauss quadrature and, therefore, benefits from the mathematical strength of this type of quadrature. This includes the uniqueness of the quadrature for each moment, as well as the generation of positive values of $\omega_{g,k}$ [23, 8, 53]. In fact, this purely mathematical approach generates the so-called mathematical probability tables, which differ from those generated by other approaches such as the physical probability tables, for example [20]. The computation of the $2K$ values $\{\sigma_{t,k}, \omega_k\}_{g,k=1,K}$ is performed by equating $2K$ exact and approximated $l-th$ order moments, i.e.

$$\mathcal{M}_{l,g} \approx \tilde{M}_l(Q_{t,g}) \quad \text{for } L \leq l \leq L + 2K - 1, \tag{3.7}$$

which represents a system of nonlinear equations with $2K$ unknowns. Due to the properties of Gauss quadrature, this system has a unique solution [53]. Furthermore, the system of $2K$ equations results in a system of $2K-1$ equations, as the PDF normalization condition constraint requires

$$\sum_{k=1}^{K} \omega_{g,k} = 1, \tag{3.8}$$

which coincides with the preservation of the $0-th$ order moment. Further details on the solution to the system of nonlinear equations (3.7) can be found in Appendix D.

Once the quadrature for the total cross section has been derived, the quadrature for the partial cross sections can be derived by conserving their moments [53, 23] , which leads to

$$\mathcal{M}_{l,x,g} = \frac{1}{\Delta u_g} \int_{\Delta u_g} \sigma_x(u)\ \sigma^l_t(u) du = \int_{D_{g,t}} d\sigma_t \int_{D_{g,x}} d\sigma_x\ \sigma_x\ \sigma^l_t\ \omega^*(\sigma_t, \sigma_x) \tag{3.9}$$

$$\approx \sum_{k=1}^{K} \omega_{g,k}\ \sigma^l_{t,g,k}\ \sigma_{x,g,k} \quad \text{for } L \leq l \leq L + K - 1, \tag{3.10}$$

which represents a system of $K$ linear equations. Once the probability tables have been retrieved, the effective cross section at a given dilution can be computed as

$$\sigma_{x,g}(\sigma_0) = \frac{\sum_{k=1}^{K} \frac{\omega_{g,k}\sigma_{x,g,k}}{\sigma_{t,g,k}+\sigma_0}}{\sum_{k=1}^{K} \frac{\omega_{g,k}}{\sigma_{t,g,k}+\sigma_0}}. \tag{3.11}$$

By default, CALENDF produces the PTs for the partial reactions grouped into five main MT numbers:

- Elastic scattering (MT=2)
- Capture (MT=101, sum of MT 102 to 117)
- Fission (MT=18)
- Inelastic scattering (MT=4)
- N,xn, i.e. any process emitting several neutrons, except fission (MT=16,17,24,25,30,37,41,42)

with the sum of the five reactions that yields the total cross section (MT=1) [53]. The accuracy of the PT depends on the choice of the term $K$, while the term $L$ represents the only remaining degree of freedom. Preserving negative moments has been shown to generally yield more accurate results [37, 54], providing a better numerical representation of the wide fluctuations in the cross sections [53]. Within CALENDF, the moments to be conserved are determined by default depending on the order of the table (and, therefore, on the accuracy). For the total cross section, $L$ takes values between $1-K$ and $K$, while it ranges between $(1-K)/2$ and $(K-1)/2$ for the partial cross sections [53]. In the code, the maximum allowed table order is $K = 11$.

#### 3.2.2.2 Computation of the moments in the resolved and unresolved ranges

As mentioned above, CALENDF computes the moments by reading the data from the ENDF-6 tape. In the resolved range, calculating the moments is straightforward once the microscopic cross section has been computed by adding the resonances, reconstructed from the parameters in the MF=2 file, to the background cross sections read from the MF=3 file. The computation of the BG cross section is performed by the code using cubic interpolation laws, which provide a more accurate representation than other codes (such as NJOY, which uses linear laws).

In the RRR, CALENDF reconstructs the resonances using by default the formalism recommended by the evaluator [53]. This is, in some sense, similar to what has already been outlined for the NJOY module RECONR. Furthermore, CALENDF has an additional feature that allows it to determine the most suitable formalism that best fits the resonance parameters. In the URR, different formalisms are allowed within the code, but only the SLBW is recommended in the ENDF-6 format for this interval. Within this range, the ENDF-6 provides mean values and statistical distributions, including the Wigner distribution [25] for the resonance spacings and the $\chi^2$ distribution for the partial widths [22, 41]. Although the parameters are energy averaged, the energy dependence is given by their subdivision into intervals [41]. The code then computes the moments using a stochastic approach. First, energy values are sampled from the eigenvalues of a random matrix [53]. Random ladders of resonances are then generated using the above statistical distributions, and cross sections are derived from the resonances using a fine energy grid [55, 56]. Finally, $\chi - \psi$ Doppler broadening [25] is applied to produce the PTs at the intended temperature [55, 56]. Once the procedure has been terminated, the code can evaluate the moments and compute the PT.

### 3.2.3 MERGE

The MERGE code [46] receives the NJOY and CALENDF output files (multigroup cross sections, matrices and PTs). First, the code performs some consistency tests, e.g. it checks that the outputs contain the same isotopes, temperatures, group structure, etc. For the total and the five main partial reactions, MERGE then compares the NJOY infinitely diluted group-averaged cross sections with those produced by CALENDF, using the latter's subgroup data.

By default, preference is given to the CALENDF values. In fact, the subgroup data can represent the resonance fluctuations whether the NJOY provides only group-averaged values (particularly in the URR) [45]. This means that the NJOY multigroup and scattering matrices are corrected to match CALENDF, and the results are printed in a new GENDF* file. In this file, the probability tables are printed in the MF=50 section. The NJOY multigroup values are kept in the file wherever the CALENDF subgroup data are not present.

However, due to the mathematical approach implemented in CALENDF, it can occur that some of the subgroup data are negative, and they are included in the final library. This is not an issue, as long as the multigroup cross sections remain positive. However, in some cases, it can occur that negative cross sections are produced for some groups, particularly when the shape of the partial cross section differs significantly from the total cross section [45]. For these specific groups, the NJOY values are used as a reference instead of the CALENDF ones, and the PTs are scaled accordingly and printed in the MF=50 file [46, 45, 44].

### 3.2.4 GECCO

Although the MERGE code carries out a series of consistency tests before writing the data in the GENDF*, the results of the comparison are limited to cross-checking the CALENDF and NJOY values. The GECCO code [47] performs additional consistency checks, such as ensuring that the main partial reactions sum up the total and that the response functions sum to the main partial reaction [47, 57, 58]. For instance, this applies to the capture cross section, which is obtained from several other response functions, such as $(n,\gamma), (n,\alpha), (n,p)$ and so on. The code also verifies that the group-averaged fission spectrum sums to unity and that the inelastic levels sum to the total inelastic, among other checks [47, 58]. Then, corrective factors are applied to the cross sections.

Finally, GECCO inverts the energy grid establishing the standard ordering of the energy groups, and prints the data in the ECCOLIB format.

## 3.3 OpenMC library production workflow

The previous sections provided a basic overview of the processing workflow that, starting from an ENDF-6 tape, produces a NDL for the ECCO code, with multigroup data in a fine structure (1968 groups) and subgroup data for the resonant nuclides. This procedure was applied to generate the JEFF-3.1 and JEFF-3.1.1 ECCO libraries, which are included in the ERANOS distribution, as well as the ENDF/B-VIII.0 ECCOLIB, which results from an independent evaluation. The focus of the second part of this work will be the assessment of the self-shielding capabilities of the latter library, by comparing the calculation results with a MC reference provided by the OpenMC code [39, 40].

Similarly to the ECCO code, OpenMC requires the ENDF-6 raw data to be processed into a format that the MC code can handle. The raw data are processed in the ACE format using NJOY and subsequently further elaborated and stored in the HDF5 format [59, 60]. The final library will contain the PENDF data that have been processed at different temperatures. This is one of the main advantages of using a MC code, as it avoids the approximations introduced by the multigroup method.

The ACE files, produced using NJOY, contain the cross sections interpolated on common energy grids, probability tables in the URR, probability and cumulative density functions for energy-angle distributions, etc. [61]. In addition to the RECONR, BROADR, and UNRESR modules, which have been previously described for the ECCOLIB generation, additional modules are also used: namely HEATR, GASPR, and PURR [22]. As the latter is the most relevant in the context of this thesis, its functionalities are briefly described below.

PURR is the module used in place of UNRESR for the treatment of data in the unresolved range, where the Bondarenko method employed in the latter module is not suitable for energy-continuous MC methods [22]. At first, the PURR module generates ladder of resonances starting from the resonance data in the MF=2 file, analogously to what is done in the CALENDF code. The width and spacing of the resonances are sampled from the statistical distributions, and the SLBW model is used to reconstruct the cross sections. Finally, PURR applies the $\chi - \psi$ model to produce Doppler-broadened cross sections at the intended temperature.

To compute PTs, PURR applies the Levitt method [62], which significantly reduces the storage resource requirement for MC applications. This method is based on the NR assumption that the resonances are so close together that a scattered neutron can randomly enter any resonance without this being correlated with the resonances at higher energies [62, 22]. As shown in Figure 3.5, the total cross section is divided into several monotonically increasing discrete bands. For each resonance ladder, the cross section points in each band are counted. Then, the average cross section for each band is computed, and the associated discrete probability is obtained by taking the ratio of the band entries to the total number of cross section values [62]. This process is repeated, generating several ladders of resonances, until convergence is reached [22].

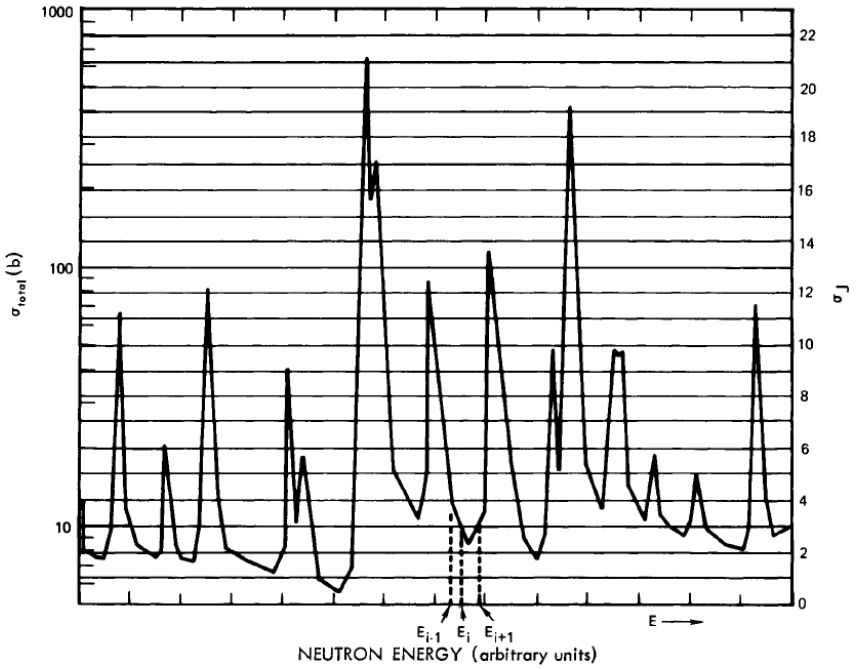


*Figure 3.5: In the Levitt method, the total cross section is discretized into a number of intervals called bands. For each band, the number of cross section points are counted, allowing to compute the average value and the associated discrete probability. The figure was taken from [62].*

The values of the partial reactions are associated with each total cross section point. Therefore, probability tables for these partial reactions can be generated by computing the average values of the partial cross sections associated with the total cross section in each discrete band. However, it should be noted that this process only generates monotonically increasing PTs for the total cross section.

Within OpenMC, the PTs are then used for the cross section sampling [63]. Whenever a neutron has an energy value $E$ within the URR, the code determines two neighbouring values $E_i$ and $E_{i+1}$. Afterward, a band $j$ is sampled from the cumulative distribution of the PT and the cross section is computed by linear interpolation, i.e.

$$\sigma(E) = \sigma_{i,j} + \frac{E - E_i}{E_{i+1} - E_i}(\sigma_{i+1,j} - \sigma_{i,j}), \tag{3.12}$$

where $\sigma_{i,j}$ is the average cross section in the band $j$ of the PT at energy $E_i$.

In conclusion, Figure 3.6 shows a visual representation of the PTs produced for Pu-239 using NJOY and a JEFF-3.1 NDL. Together with the background cross sections, these form the data set used by the OpenMC code in the URR.

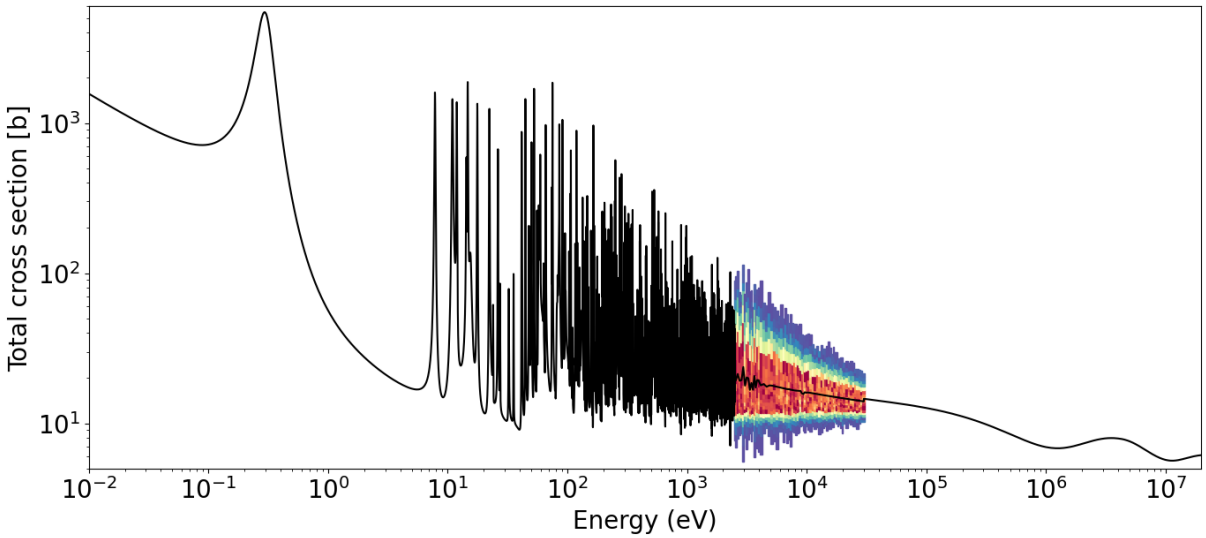


*Figure 3.6: Graphic visualization of the PTs produced by PURR for Pu-239 in a JEFF-3.1 NDL. The PTs are plotted with OpenMC starting from the HDF-5 files.*

# Part II

# Validation of ECCO self-shielding module with the ENDF/B-VIII.0 ECCOLIB

Chapter 4

# Sensitivity analysis of an LFR core

The primary function of the ECCO cell code is to prepare self-shielded, condensed, and homogenised cross sections for subsequent core calculations. As this thesis aims to numerically validate the self-shielding model, in Chapter 5 the results of ECCO calculations will be compared with those of the Monte Carlo reference. However, since an LFR cell is composed of many nuclides, comparing the cross sections of each of them with those calculated using the MC reference would require excessive time and computational resources.

Therefore, the first-order perturbation theory described in Section 1.5 will be applied to derive Sensitivity Coefficients (SCs) for a representative LFR case, namely the Nuclear Energy Agency (NEA) lead-cooled fast reactor benchmark, which is based on the ALFRED reactor core design [12, 64, 65, 66]. To achieve this, the ENDF/B-VIII.0 ECCO library will be used alongside the tools provided by ERANOS. Within the code, the perturbation module offers the possibility of breaking down the sensitivity coefficients into the contribution of each type of partial cross section for each nuclide, as well as for specific regions and energy groups [30]. These sensitivity coefficients will determine which nuclides and their specific reactions have the greatest impact on a selected variable of interest. Therefore, the SCs will enable a smaller set of isotopes to be selected for monitoring during the numerical validation of the ECCO cell code using the same ENDF/B-VIII.0 NDL.

The variables of interest are usually selected at the beginning of any validation work. These are the quantities influenced by the physical phenomena under consideration [6]. As this thesis aims to numerically validate the ECCO self-shielding module, the variables of interest selected were the effective multiplication factor and the Doppler reactivity change[1]. The former is one of the most important parameters in neutronic analysis, and it is clearly impacted by the group-averaged cross sections and thus by self-shielding effects. The latter quantifies the reactivity change between two states at different temperatures. As this is related to the broadening of the cross sections resonances, it is expected to be significantly influenced by self-shielding effects.

## 4.1 ERANOS setup

Due to ERANOS current limitations, it is not possible to perform sensitivity analysis using the 3D nodal transport solver implemented in the code, namely VARIANT. Instead, the user must employ finite difference flux solvers, based on diffusion or transport theory [29, 30]. In the framework of this thesis, the transport theory will be applied with the BISTRO $S_N$ solver [67, 68], as this avoids the issue of evaluating the perturbation of the material-dependent diffusion coefficient[1], i.e. $\delta D$ [69], and enables retrieving more accurate results.

The BISTRO module is a finite difference $S_N$ solver for 2D geometries, i.e. X-Y and R-Z. Given the significant variation in materials along the axial direction, the R-Z solver was se-

[1] Gérald Rimpault, private communication

lected. Therefore, the hexagonal-lattice model of the reactor core was converted to a cylindrical-equivalent model. For details of the reactor geometry design, the reader can refer to the benchmark specifications provided by NEA [12]. Figure 4.1 shows the results of the cylindrisation process, carried out with the precise objective of conserving volumes, and therefore masses. Along the radial direction, the hexagonal lattice has been replaced by a series of regions composed of materials from the same sub-assemblies, but with a cylindrical geometry. The alternation of the materials was designed with the aim of conserving as much as possible the distribution of the sub-assemblies in the hexagonal lattice. The cylindrical R-Z description of the core was then replicated within ERANOS.

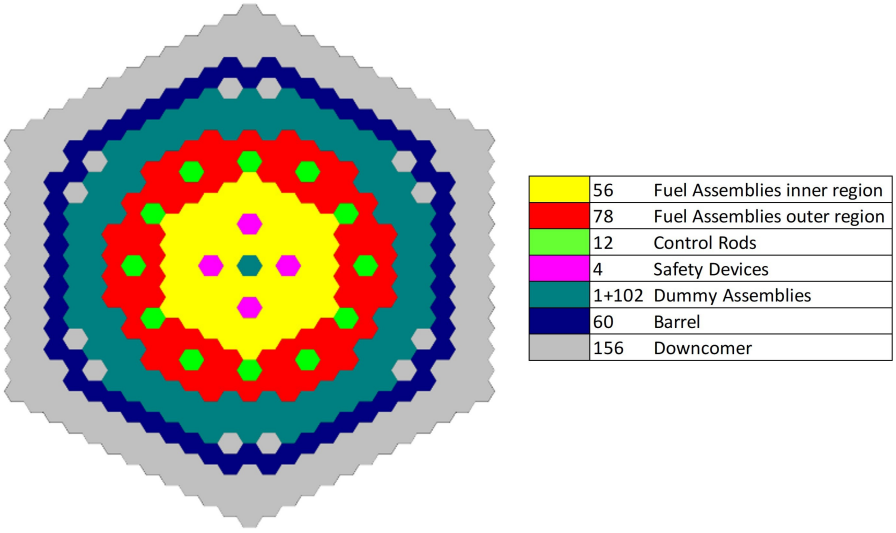


*(a) Hexagonal distribution of the sub-assemblies in the 3D NEA LFR benchmark model. The figure was adapted from [12].*

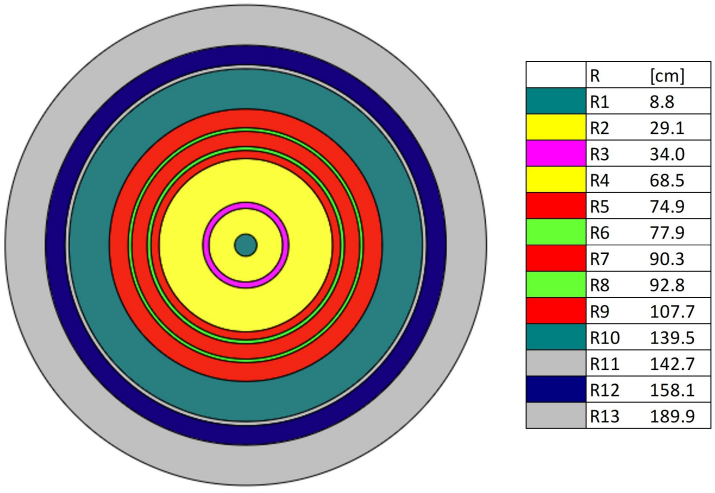


*(b) Cylindrisation of the 3D model in the radial direction.*

*Figure 4.1: Cylindrisation of the NEA LFR benchmark core. While the axial composition has remained intact, the hexagonal lattice has been converted into a series of concentric cylinders in the radial direction.*

Figure 4.2 shows the axial description of the sub-assemblies in the core. These are made up of different components, each of which presents a different material composition. This distribution remains unchanged in the R-Z geometry. The control rods were simulated for Beginning of Cycle (BoC) conditions, while the shutdown rods were modelled as fully retracted. Each

medium was simulated separately[2] in ECCO, according to the NEA benchmark specifications (geometry, composition, temperature, etc. at hot full power conditions and BoL) [12], resulting in the production of cell-homogenised cross sections, condensed into the ECCO 33 groups structure. For the derivation of the SCs for the Doppler reactivity change, a temperature increase of 300 K in the MOX region was applied in both FINN and FOUT (internal and external fuel assemblies, respectively).

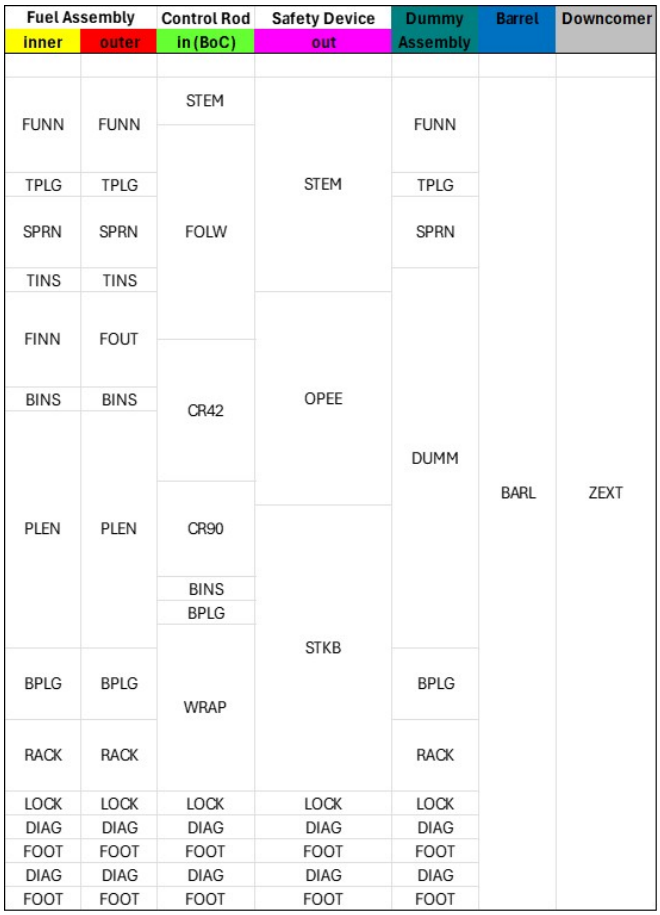


*Figure 4.2: Axial distribution of the materials composing the sub-assemblies in the 3D NEA LFR benchmark model, at BoC conditions with the shutdown rods fully retracted. Each of the section that axially compose one assembly represents a different medium. The names of the media are the ones provided in the benchmark specifications. The figure was adapted from [12].*

When deriving the SCs, it should be noted that the impact of each nuclide will depend not only on its cross sections but also on its relative concentration. Figure 4.3, for example, shows the relative isotopic concentrations of the internal fuel sub-assembly FINN. This heterogeneous medium is made of three materials: the MOX material (fuel), the AIM1 (structural material), and the lead coolant.

Listing 4.1 shows the settings adopted for the BISTRO R-Z solver. This solver uses the same 33-group structure that will be employed to derive the SCs. The integral convergence criterion (on the multiplication factor) was set to 1 pcm, while the local convergence criterion was set to $10^{-4}$ for most groups. A milder convergence criterion was set for a few groups in the epithermal region to improve the convergence of the ERANOS solver's transport iterations. However, as it will be seen below, the impact of low-energy groups in LFR applications is minimal. The $10^{-3}$ criterion was set for the inner iterations, which account for up-scattering phenomena.

[2]Credits to Matteo Falabino (*new*cleo) for the ECCO simulations of the NEA LFR benchmark cells.

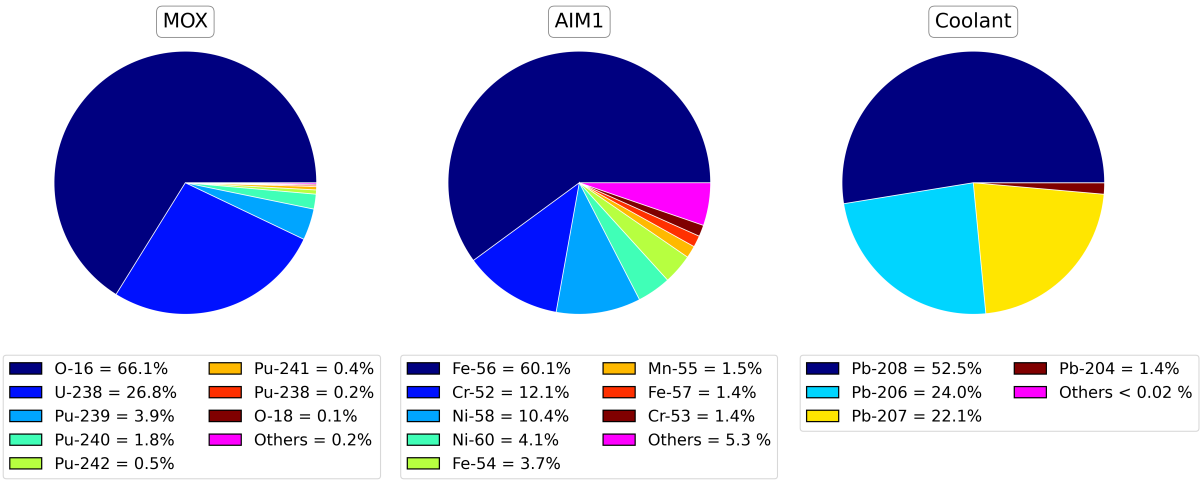


*Figure 4.3: The internal fuel medium (FINN) has been conceptually subdivided into three macro materials: MOX, AIM1 and coolant. The isotopic composition of each material is reported in relative terms.*

```
FD_DIFFUSION_MATRIX_COEFFICIENT -> COEFF_SET
   GEOMETRY (GEO_RZ)  ! EDL storing geometry data
   MACRO    (MACRO_SET)  ! EDL storing (macroscopic) cross section data
   HORIZONTAL_MESH 1 1
   TRANSPORT;  ! Option for transport

FD_DIFFUSION_METHOD -> METHOD_SET
   COEFFICIENT (COEFF_SET)
   PLANE SUCCESSIVE_LINE_OVER_RELAXATION CALCULATION ;

DIRECTION_COSINE_AND_WEIGHT_CREATION ->PESI
   SECTION_SET 'S4_SYMETRIQUE' ;

RECTANGULAR_SN_TRANSPORT_ITERATION -> FLUX_TR
                      ANGULAR_FLUX -> FLUX_ANG_TR
   METHOD (METHOD_SET)
   COEFFICIENT (COEFF_SET)
   DIRECTION (PESI)
   AREA_OF_INTEREST  1 46 28 48  !  RZ Coordinates of fuel region
   DIFFERENCING_SCHEME DIAMANT_TETA 0.9
   CALCULATIONAL_PARAMETER
      OUTER_ITERATION
         MAXIMUM_NUMBER       200
         INTEGRAL_CONVERGENCE 1.E-05
         LOCAL_CONVERGENCE    REP(25,1.E-04) 5.E-03 REP(3,1.E-03) REP(4,1.E-04)
         TCHEBYCHEFF          4
      INNER_ITERATION
         MAXIMUM_NUMBER       30
         LOCAL_CONVERGENCE    1.E-03
   K_EFFECTIVE -> K_EFF_DIR_REF
   ACCELERATION DIFFUSION ITERATION_DIFFUSION 20
   SPECTRUM VARIABLE
   CALCULATION DIRECT
   MOMENT_STORAGE YES ;
```

*Listing 4.1: Setting of the $S_N$ BISTRO R-Z solver in ERANOS*

## 4.2 Sensitivity analysis results for the multiplication factor

As described above, ERANOS breaks down the sensitivity coefficients according to nuclide, reaction, energy group, and spatial region. Due to the linearity of the SCs, which allows their summation, the sensitivity analysis will be approached by looking at the global coefficients and then progressively refining the description by looking at the single constitutive parts. This procedure is described in the following.

The SA was performed using the ERANOS tools distinguishing between the contributions coming from all nuclides present in the LFR benchmark core. First, the SCs for the effective multiplication factor for the entire reactor were assessed, using first-order Standard Perturbation Theory (SPT) as described in Section 1.5. The SC is given by the sum of the contributions from each region. For instance, the impact of the perturbed U-238 cross sections on the effective multiplication factor is given by the sum of the contributions from all media containing U-238, i.e. the internal and external fuel assemblies (FINN and FOUT in Figures 4.1 and 4.2). The SCs were then summed over the contribution of each energy group. The obtained SCs for each partial reaction (capture, fission, elastic and inelastic scattering, and (n,xn)) were then summed in absolute value. The figure of merit that is obtained, i.e.

$$\mathcal{S}_n = \sum_x \left| \sum_g \sum_r S(k, \sigma_{r,g,x,n}) \right| \ , \tag{4.1}$$

is not strictly a sensitivity coefficient. However, the advantage is that it allows the impact of each nuclide to be ranked, avoiding compensations between large sensitivity coefficients of opposite sign. This enables the identification of the nuclides with the greatest influence on the $k_{eff}$.

Figure 4.4 shows the results of $\mathcal{S}_n$ for a fraction of nuclides that account for 98.7 % of the total impact. As expected, the largest contribution comes from the nuclides that compose the MOX fuel (heavy fissile isotopes and oxygen). Next, a significant contribution is made by Fe-56 and Pb-208. These are the two most abundant nuclides in the cladding and coolant materials, respectively (as shown in Figure 4.3). However, it can be concluded that these two materials have a much lower impact on the multiplication factor than the fuel does. B-10, which is present mainly in the control rods, also impacts the multiplication factor.

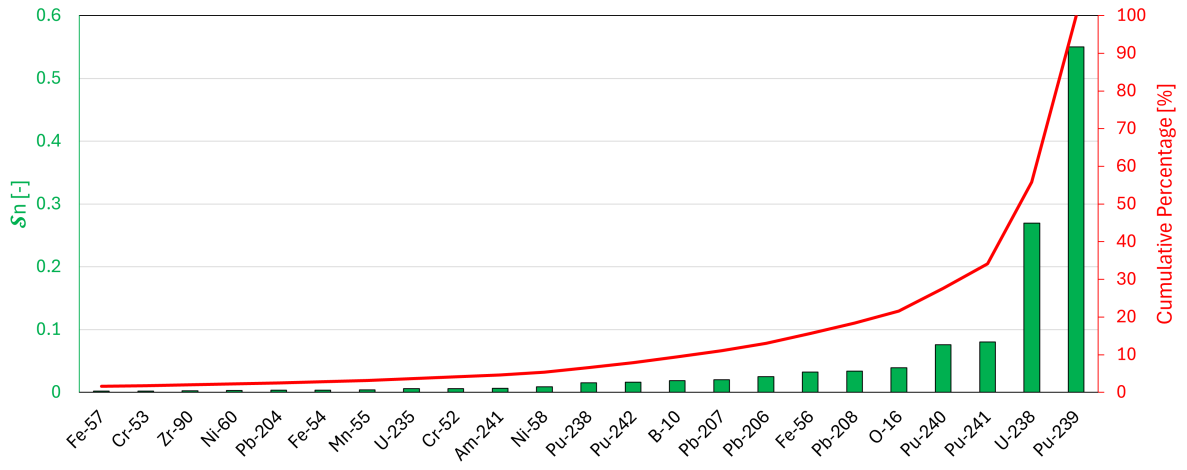


*Figure 4.4: NEA LFR benchmark core. Ranking of the nuclides' contributions to the effective multiplication factor. The ranking is based on the values obtained by summing the energy-integrated SCs of the partial reactions in absolute values, for the entire core.*

However, the same nuclide can be present at different concentrations in different regions of the domain, having a different impact on the effective multiplication factor depending on the

location. Therefore, the analysis was further detailed by looking at the two different fuel media, namely FINN and FOUT. Figure 4.5 shows the FOM $\mathcal{S}_n$ broken down by medium and nuclide, denoted here with $\mathcal{S}_{n,r}$. The internal fuel, where the neutron flux is at its maximum, has a greater impact than the external fuel. Furthermore, despite having half the concentration of Pb-208, Pb-206 has a greater impact than the latter within the internal fuel. This can possibly be attributed to the larger capture and inelastic cross sections of Pb-206.

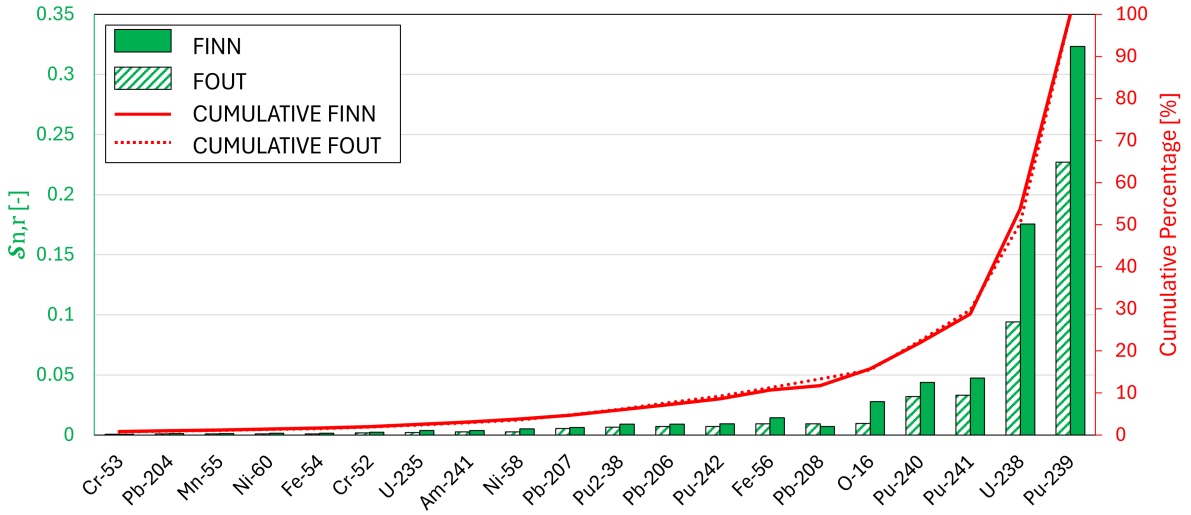


*Figure 4.5: NEA LFR benchmark core. Ranking of the nuclides' contributions to the effective multiplication factor, subdivided between the contributions of FINN and FOUT. The SCs are energy-integrated.*

Once the ranking of the most important nuclides was established, the impact of each reaction on the effective multiplication factor could be determined. This time, the SCs are reported with their actual sign in order to assess the different impacts of each reaction. Figure 4.6 shows the SCs for the three macro materials, with a focus on the nuclides that have the greatest impact within each of them, as determined by the previous ranking. Once again, the dominant role played by Pu-239 and U-238 is evident. In particular, the fission reaction of the former has the opposite sign to the capture reaction of the latter. This is to be expected, as an increase in the fission cross section of Pu-239 would result in an increase in the number of neutrons produced, and thus an increase in the multiplication factor. Conversely, an increase in the capture cross section of U-238 would determine a reduction in the neutron population, and thus a decrease in the multiplication factor.

Furthermore, for the lead isotopes, particularly Pb-207 and Pb-206, the SA results in non-negligible SCs of opposite signs. This supports the introduction of the FOM $S_n$, obtained by summing the absolute values of the SCs, in order to perform the previous ranking. Indeed, if SCs for the lead isotopes had been summed over all reactions with their actual signs, opposite contributions would have cancelled each other out, resulting in overall little impact of the nuclide, although these were non-negligible in absolute value. Instead, using this methodology to approach the ranking allows the importance of each nuclide to be appreciated, as a variation in one of the partial reaction cross sections would have a significant impact on the multiplication factor. Looking at the graphs, it can also be concluded that the (n,xn) reactions do not significantly contribute to the multiplication factor for any of the nuclides in the three materials.

The analysis was further refined by accounting for the energy dependence of the SCs. Figure 4.7 shows the variation in energy of SCs for the most important nuclides (for each material) and reactions. In the same graphs, the URR bounds (on the 33 groups structure) for U-238 and Pu-239 are also reported. In Appendix E, the values of the SCs for some of the most important nuclides are reported.

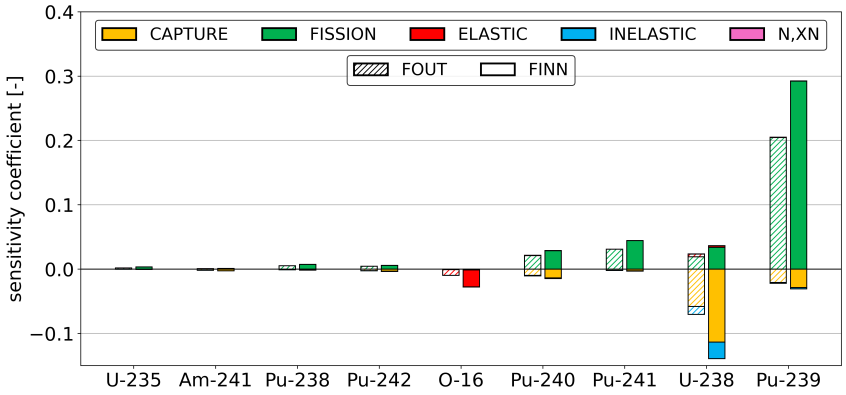


*(a) MOX*

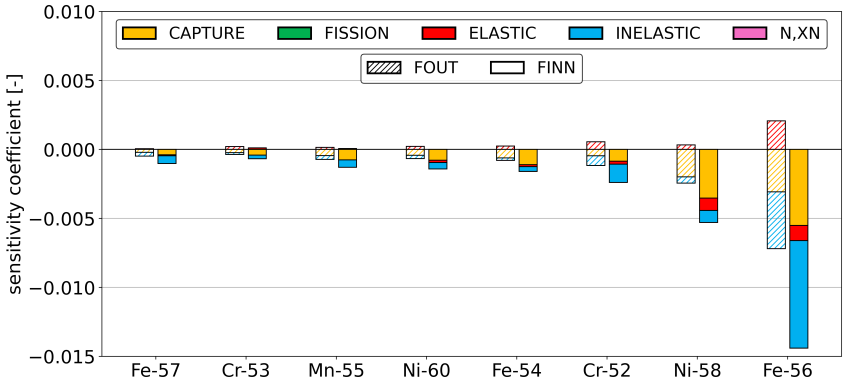


*(b) AIM1*

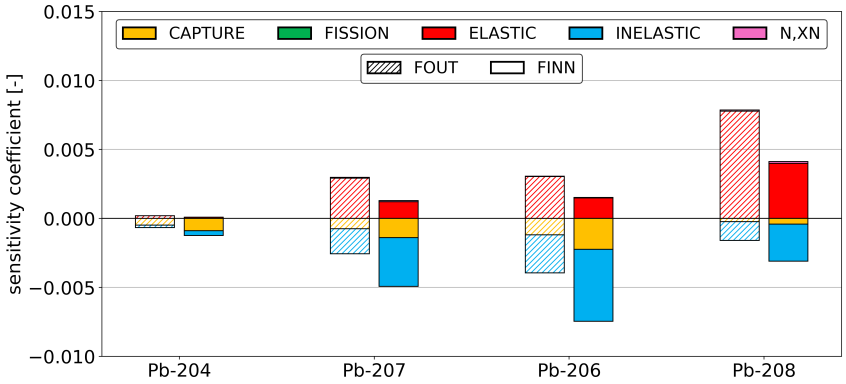


*(c) Coolant*

*Figure 4.6: NEA LFR benchmark core. Energy-integrated SCs for the effective multiplication factor, broken down according to the five main partial reactions for the most important nuclides in FINN and FOUT. The SCs are ulteriorly divided according to the three macro materials.*

## 4.3 Sensitivity analysis results for the Doppler reactivity change

Similarly to what was done in the previous section, the SCs were derived using first-order Equivalent Generalised Perturbation Theory (EGPT) for the Doppler reactivity change (see Section 1.5). This term refers to the change in the system's reactivity following an increase or a decrease in fuel temperature, which causes the resonances of the cross sections to broaden or to narrow, respectively, and thereby altering the probability of a neutron interacting with the medium. For the purposes of this work, the reactivity change following a 300 K temperature increase (from 1200 K to 1500 K) in the MOX of FINN and FOUT was analysed. As outlined in Section 1.5, the SCs are computed in ERANOS by a linear combination of those derived using the SPT for the reference (1200 K) and modified (1500 K) systems.

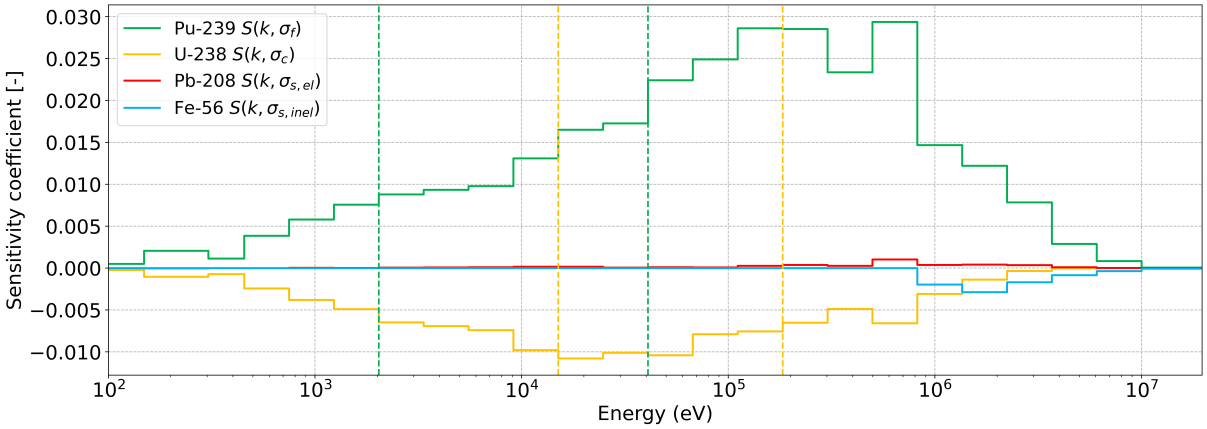


*Figure 4.7: NEA LFR benchmark core. Energy dependence of the SCs for the effective multiplication factor, expressed using the ECCO 33 energy groups structure. The URR bounds of U-238 (yellow) and Pu-239 (green) are reported in dashed lines.*

Figure 4.8 shows the FOM $\mathcal{S}_n$ computed for the entire core using the SCs of the Doppler reactivity change in absolute values. Unlike in the previous ranking, where the impact of O-16 was smaller than that of the fuel isotopes (see Figures 4.4 and 4.5), it can be observed that this nuclide plays a predominant role in the case of the Doppler reactivity change, having a greater impact than U-238. This can be attributed to the large concentration of oxygen in the MOX fuel and the non-negligible presence of O-16 resonances in the high-energy region. A significant contribution is also given by the isotopes of the cladding, particularly Fe-56 and Ni-58. The remaining contribution is mainly provided by the lead isotopes of the coolant.

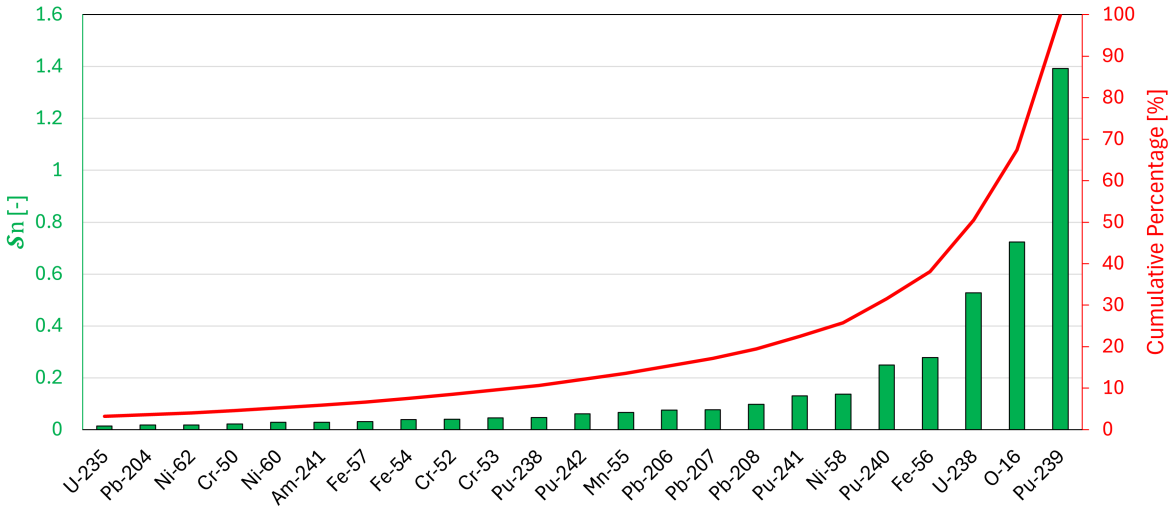


*Figure 4.8: NEA LFR benchmark core. Ranking of the nuclides contribution to the Doppler reactivity change. The ranking is made on the basis of the values obtained by summing the energy-integrated SCs of the partial reactions in absolute values, for the entire core.*

The FOM $\mathcal{S}_n$ was then broken down according to the contributions of the FINN and FOUT fuel assemblies, as shown in figure 4.9. With respect to the SA for the effective multiplication factor, the results revealed a more pronounced variation between the two fuel assemblies. This is particularly evident for O-16, Fe-56, and the lead isotopes, for which the contribution of the inner assemblies is approximately twice that of the outer assemblies. For lead isotopes in particular, the chart shows that the contribution to the reactor is almost entirely provided by the inner assemblies. Given that the increase in temperature is only imposed on the fuel isotopes, for nuclides outside the MOX the SCs are mainly influenced by the different shapes of the direct

and adjoint fluxes, between the reference and modified states (see the EGPT formulation in Section 1.5). Thus the SCs could be influenced by more pronounced variations of the neutron flux in the inner regions, than in the outer regions.

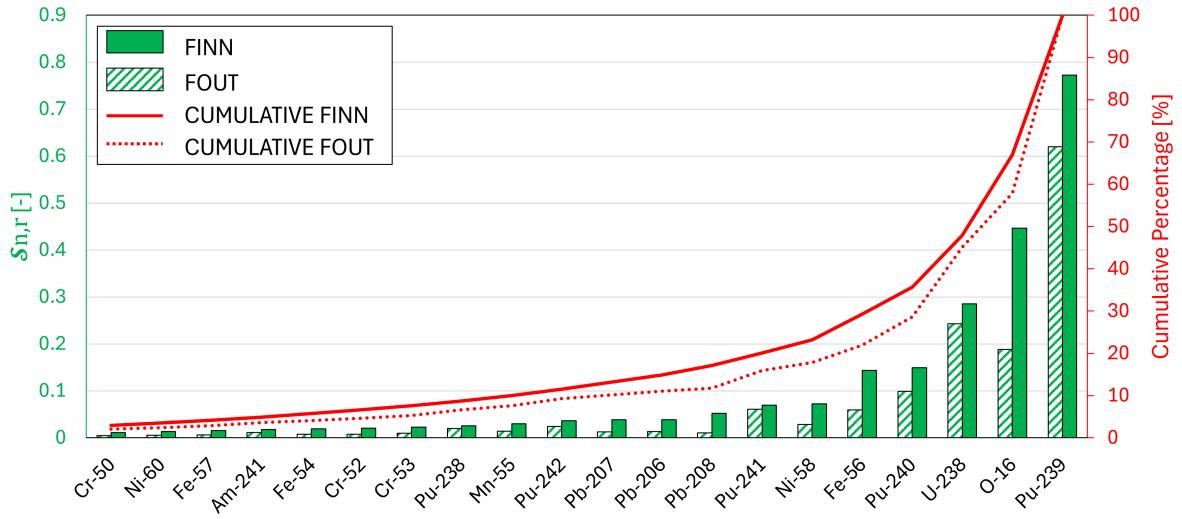


*Figure 4.9: NEA LFR benchamrk core. Ranking of the nuclides impact to the Doppler reactivity change, with a subdivision between the contributions of FINN and FOUT. The SCs are energy-integrated.*

As it was done for the multiplication factor, Figure 4.10 shows the SCs for the Doppler reactivity change, broken down according to the five main partial reactions. These are shown for the most important isotopes in the three materials, as determined by the previous ranking. Looking at the fuel isotopes, it can be seen once again that the predominant effect comes from fission and capture reactions. However, this time, the elastic scattering of O-16 also plays a predominant role, accounting for the total contribution observed in the previous ranking. As the neutron flux in the inner assemblies shifts towards higher energies, the predominant effect of the scattering (both elastic and inelastic) of O-16 and the lead isotopes may explain the greater impact of FINN than that of FOUT. Indeed, these lighter isotopes tend to exhibit resonances at higher energies, where the greater neutron flux of FINN could enhance neutron scattering interactions. Additionally, since they affect the transport of neutrons towards lower-energy regions where fuel isotopes' capture resonances are located, the scattering reactions of the structural and coolant materials can be expected to influence the Doppler effect [70].

Moreover, the opposite sign of the SCs for the capture reaction can be seen, which are negative for the plutonium isotopes and U-235, and positive for U-238. To better understand the consequence of opposite coefficients' signs, consider the perturbation on the Doppler reactivity change computed with the sensitivity coefficient, following a 1% relative variation in the capture cross section, which reads

$$\delta(\Delta\rho_T) = S(\Delta\rho_T, \sigma_c)\Delta\rho_T, \tag{4.2}$$

where $\Delta\rho_T$ is the difference in reactivity between the states at different temperatures, which is negative for a temperature increase, and $S(\Delta\rho_T, \sigma_c)$ is the sensitivity coefficient for the Doppler reactivity change (see Section 1.5). Then, from the moment that

$$\delta(\Delta\rho_T) = \Delta\rho' - \Delta\rho = (\rho'_2 - \rho'_1) - (\rho_2 - \rho_1), \tag{4.3}$$

where $\Delta\rho'$ is the change in reactivity in the perturbed states, it follows

$$(\rho'_2 - \rho'_1) < (\rho_2 - \rho_1) \quad \text{for } S(\Delta\rho_T, \sigma_c) > 0 \tag{4.4}$$

or, alternatively,

$$(\rho'_2 - \rho'_1) > (\rho_2 - \rho_1) \quad \text{for } S(\Delta\rho_T, \sigma_c) < 0. \tag{4.5}$$

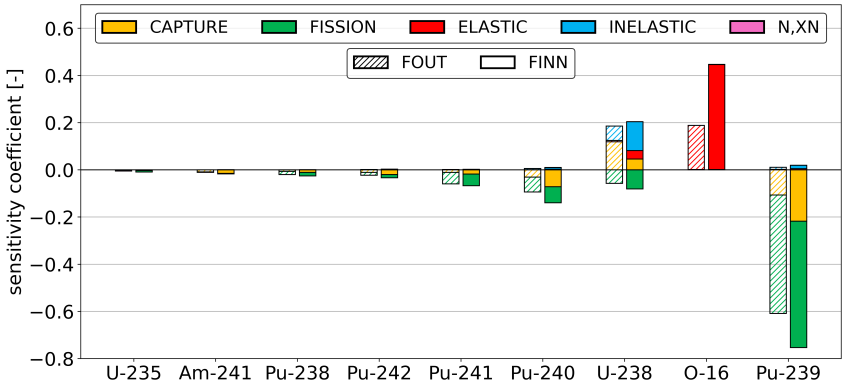


*(a) MOX*

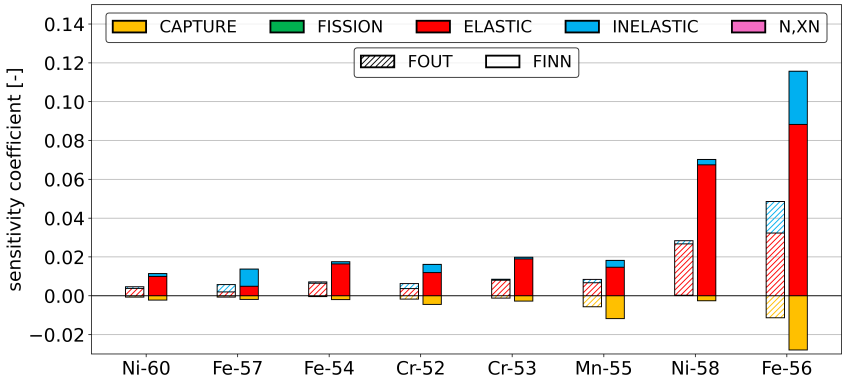


*(b) AIM1*

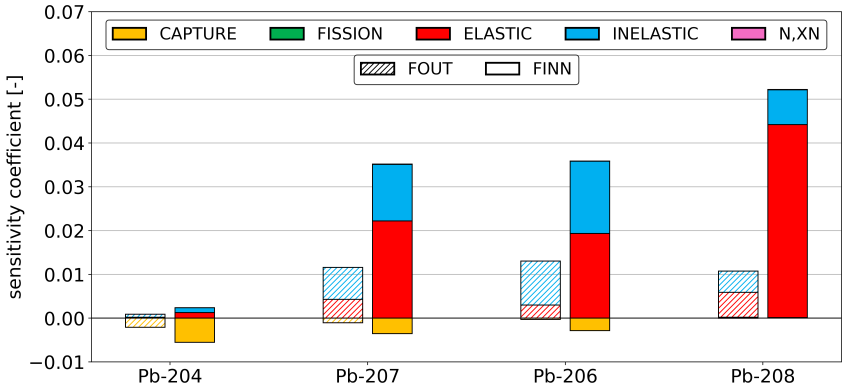


*(c) Coolant*

*Figure 4.10: NEA LFR benchmark core. Energy-integrated SCs for the Doppler reactivity change, broken down according to the five main reactions for the most important nuclides of FINN and FOUT. The SCs are ulteriorly divided according to the three macro materials.*

Since the reactivity decreases with temperature, both terms on each side are negative. Therefore, it follows that in the case of U-238 (which has an overall positive SC), the magnitude of the perturbed Doppler reactivity change between the reference and modified states will be greater than between the non-perturbed states, as from expression (4.4) is determined

$$|\rho_2' - \rho_1'| > |\rho_2 - \rho_1|. \tag{4.6}$$

This is a desirable effect, meaning that an increment in the concentration of U-238 increases the negative reactivity span that follows a positive variation in temperature. This improves the control of power excursions in nuclear reactors. When power, and thus temperature, increases, the negative reactivity feedback is stronger and helps to restore the original configuration.

From expression (4.5) it follows instead that

$$|\rho_2' - \rho_1'| < |\rho_2 - \rho_1|, \tag{4.7}$$

and therefore the magnitude of the perturbed Doppler reactivity change decreases with an increase in the concentration of Pu-239 or U-235, since their coefficients are overall negative. This is an undesirable effect, as greater negative reactivity variations are desirable for controlling power excursions. In fact, the reduction in the magnitude of the Doppler coefficient with increasing U-235 or MOX fuel enrichment has been the subject of several studies [71, 72, 73]. In conclusion, the sensitivity coefficients for the capture reaction of U-238 and Pu-239 can be expected to have the opposite sign for the LFR benchmark core [74]. In the referenced work, the EGPT formulation has the opposite sign to that in Eq. (1.81). Therefore, the SCs also have the opposite sign.

Figure 4.11 shows the energy dependence of SCs for the Doppler reactivity change, evaluated for the entire reactor. For U-238, the capture SCs have a significant impact within the RRR and URR of U-238. This is to be expected, given that the Doppler effect is mainly associated with the broadening of capture cross sections resonances, which are absent at higher energies. For Pu-239, however, fission SCs also have a strong impact on the Doppler reactivity change in the continuum range. As the cross sections outside the resonance intervals are less affected by changes in temperature, these SCs are likely to be the result of indirect effects.

According to the EGPT formulation, these indirect effects arise from variations in the direct and adjoint neutron fluxes between the reference and modified states (as already discussed for the structural and coolant materials). These variations in the neutron flux at higher energies could result from variations in the elastic scattering resonances of O-16, which was shown to have a significant impact on the Doppler reactivity change. This nuclide is indeed affected by the imposed temperature variation. Furthermore, variations in the Pu-239 fission cross section can influence the transport of neutrons from high-energy regions to regions where capture resonances are located [70]. Similar trends of the Pu-239 SCs for the Doppler reactivity change outside the resonance intervals can be observed in the study by Fiorito et al. [75]. Furthermore, the SCs for the Doppler reactivity change can be significantly impacted by the imposed temperature variation [76].

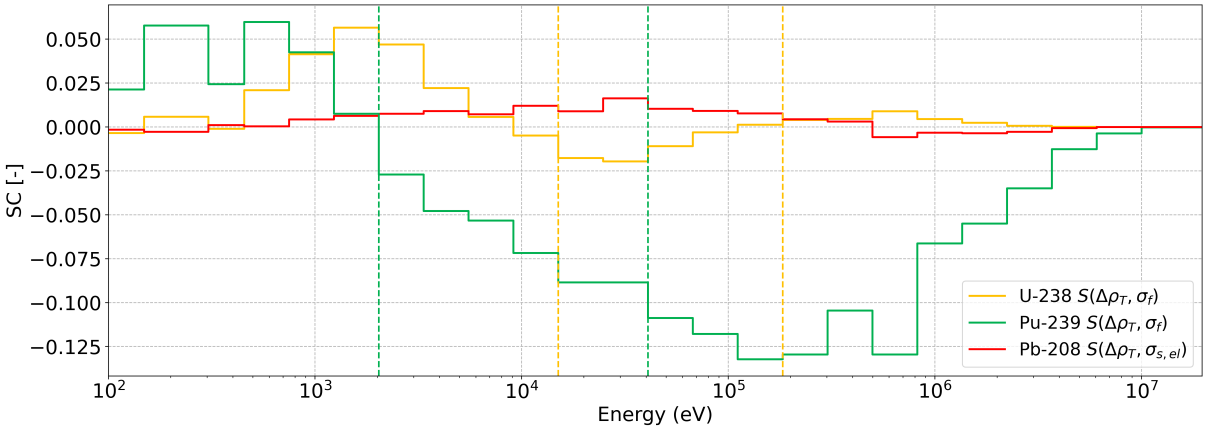


*Figure 4.11: NEA LFR benchmark core. Energy dependence of the SCs for the Doppler reactivity change, expressed using the ECCO 33 energy groups structure. The URR bounds of U-238 (yellow) and Pu-239 (green) are reported.*

## 4.4 Comparison against Monte Carlo results

In addition to deterministic tools, stochastic MC codes can also be used to derive sensitivity coefficients [74]. The main drawback of deriving SCs with MC codes is that the reactions with a very low impact on the integral parameters are associated with very high statistical uncertainty. However, the advantage is that SCs can be derived for an exact 3D description of the core geometry. Within the *new*cleo *C&M* team, sensitivity analyses have been performed on different reactor cores using the Serpent2 [77] MC code [3].

Therefore, the ERANOS SCs have been compared with those produced by MC simulations. For Pu-239, figure 4.12 shows a comparison of the effective multiplication factor SCs of the partial reactions and $\nu$, i.e. the average number of neutrons produced by fission.

The relative errors of ERANOS with respect to Serpent2 were defined as

$$\text{Rel. Err.} = \frac{\text{SC}^{ERANOS} - \text{SC}^{Serpent}}{\text{SC}^{Serpent}}. \tag{4.8}$$

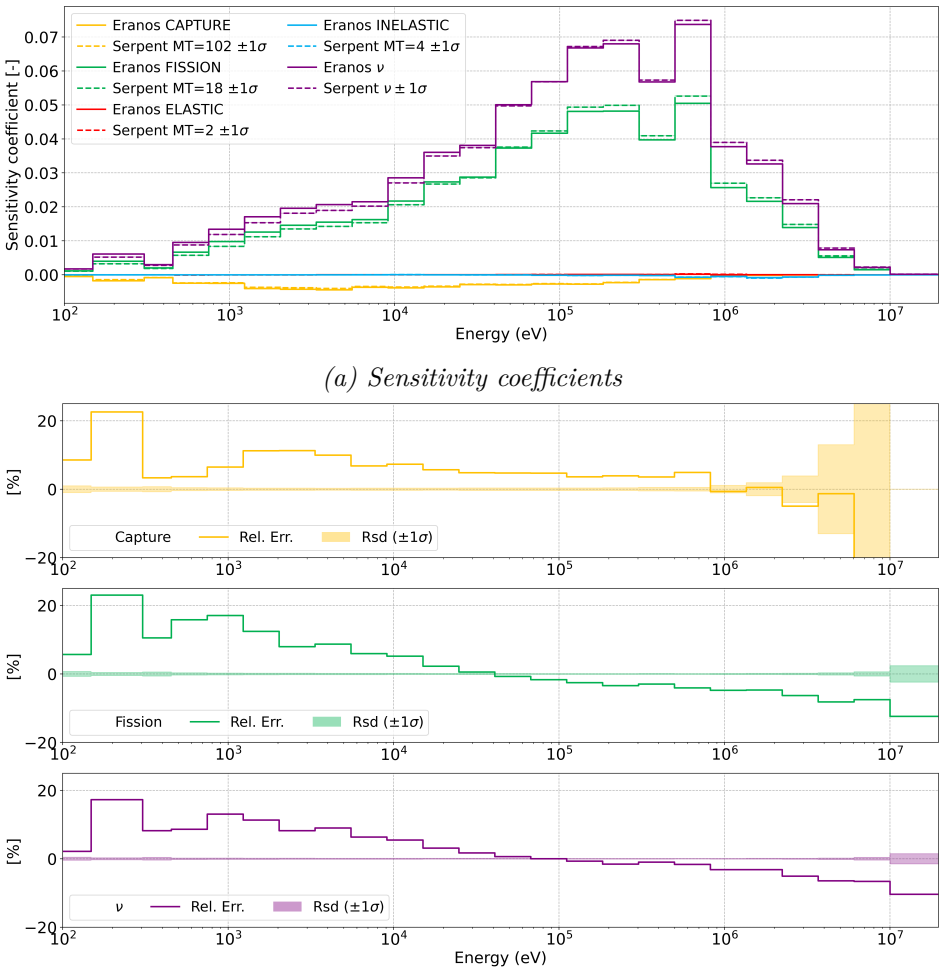


*(a) Sensitivity coefficients*

*(b) Relative errors*

*Figure 4.12: NEA LFR benchmark core. Comparison between the effective multiplication factor SCs produced by ERANOS and Serpent2 for Pu-239, using the 33 group structure for the entire core. Above, the SCs are reported for both the codes and compared for the main partial reactions and $\nu$. Below, the relative errors are reported with the relative standard deviation.*

[3] Credits to Darian Andreas Olivares (*new*cleo) for the Serpent2 simulations of the NEA LFR benchmark core.

The relative errors of the elastic and inelastic reactions are not reported, since the statistical noise does not permit comparison. The same assessment was made for U-238, shown in figure 4.13. It can be noticed that, at lower energies, the relative errors are of the same order of magnitude as the relative standard deviation, preventing any meaningful comparison in this range. Despite this, in the energy range where they are comparable, the SCs are generally in agreement. Even though the errors are not negligible, they can be considered acceptable given the deterministic approximations within ERANOS and the different geometries (R-Z vs. 3D). In Appendix E, the comparison for other nuclides is shown.

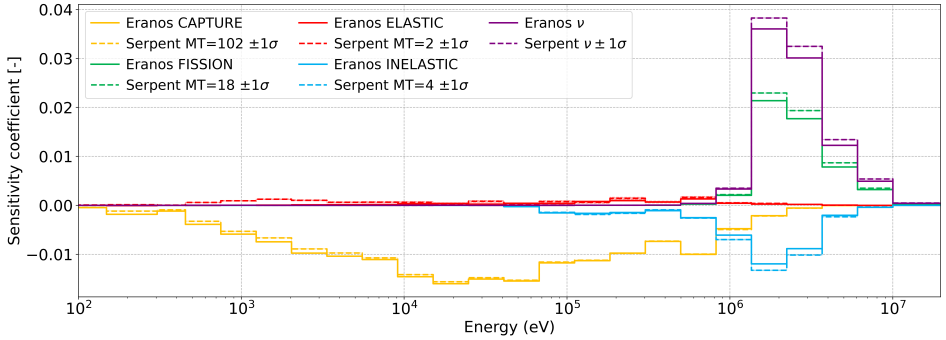


*(a) Sensitivity coefficients*

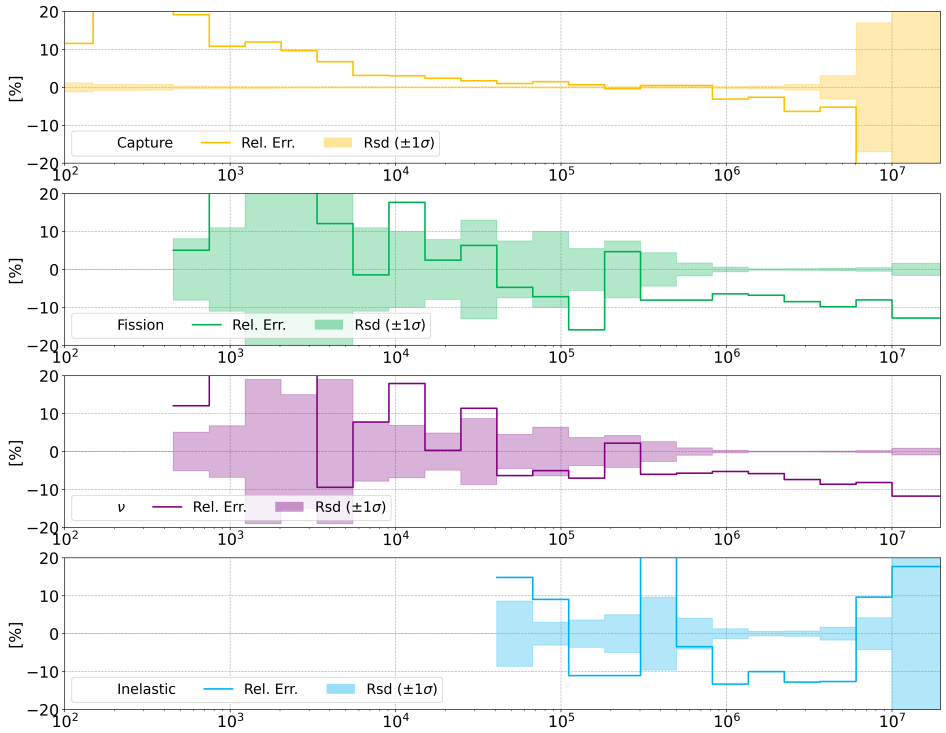


*(b) Relative errors*

*Figure 4.13: NEA LFR benchmark core. Comparison between the effective multiplication factor SCs produced by ERANOS and Serpent2 for U-238, using the 33 group structure. For ν and the inelastic scattering, the very low statistics at low energies does not produce any output in Serpent2. In this range, the relative error is undefined. The comparison in made between the SCs derived for the entire core.*

Then, an attempt was made to produce SCs for the Doppler reactivity change using Serpent2, applying Eq. (1.82) and the methodology outlined in Section 1.5.3.2. Figure 4.14 shows the results of a comparison between ERANOS and Serpent2 for Pu-239 and U-238. Despite the low statistical uncertainty of the SCs for the effective multiplication factor, the difference between the SCs for a 300 K temperature increase is considerably small and of the same order of magnitude as the standard deviation of the SCs for the multiplication factor. Conse-

quently, as it can be seen in the figure, the SCs for the Doppler reactivity change are associated with large statistical uncertainties, preventing any meaningful conclusion about the validity of these results. However, as these SCs are the result of a purely algebraic manipulation of the SCs for the effective multiplication factor, for which a reasonable accuracy was determined at both temperatures, the ERANOS results can be considered valid. Further support for the reliability of the ERANOS SCs could be obtained by comparing larger temperature increases, which would allow a greater variation in the coefficients to be determined, thus leading to smaller statistical uncertainties.

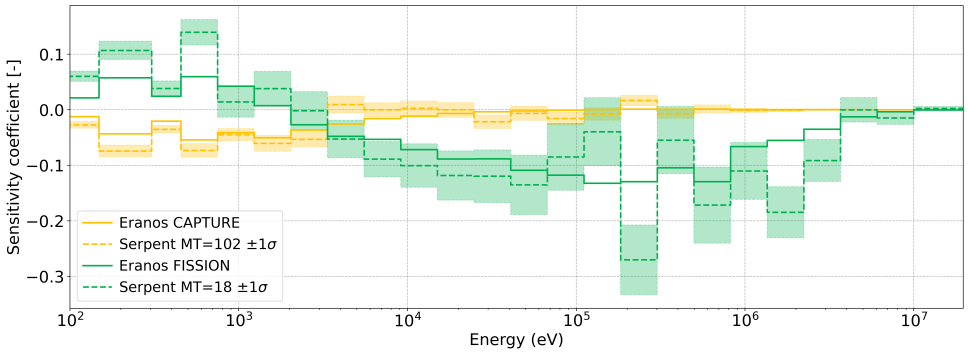


*(a) Pu-239*

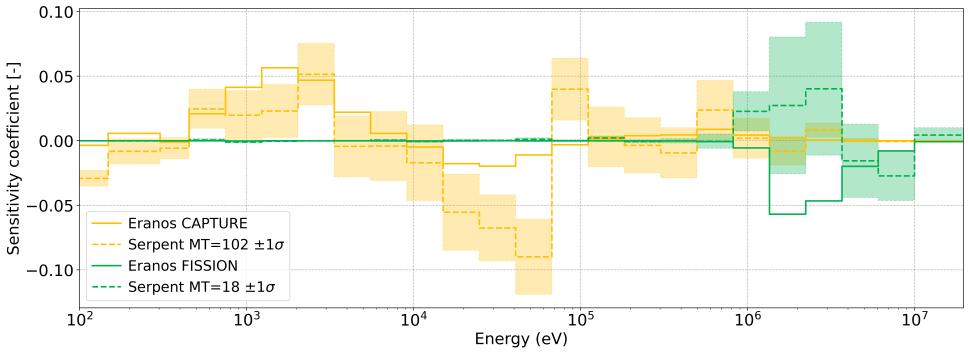


*(b) U-238*

*Figure 4.14: NEA LFR benchmark core. Comparison between the U-238 and Pu-239 SCs for the Doppler reactivity change produced by ERANOS and Serpent2, using the EGPT formulation.*

## 4.5 Impact assessment of the first-order approximation

As described in the opening sections of this chapter, the SCs for both the effective multiplication factor and the Doppler reactivity change were derived using first-order approximated SPT and EGPT. This approach is based on the assumption that the perturbations are computed following small variations in the local parameters. In the following chapters, the SCs that have been derived will be used to transpose the discrepancies in the cross sections, evaluated with deterministic and stochastic codes, into discrepancies in integral parameters. However, these discrepancies may not be small. Therefore, the error associated with the SCs due to the use of the first-order approximation was assessed.

For this reason a second core calculation using the BISTRO solver was performed. In this calculation, the media of the inner and outer fuel assemblies were originated with the Pu-239 atomic density increased by 1%. This second system is here denoted as perturbed state. The relative variation in the effective multiplication factor between the two states $\Delta k/k$ was computed and reported in table 4.1. This value was then compared with $\delta k/k$, obtained by multiplying the SC for $k_{eff}$ of Pu-239 for the entire core and all the reactions and energy groups, by a 1% relative variation of the cross section. Increasing the atomic density by 1% is,

in fact, equivalent to increasing by the same amount the microscopic total cross section over the entire energy range. With this approach, it was possible to compare a value obtained using the first-order approximated SPT ($\delta k/k$), with a value obtained by a direct calculation ($\Delta k/k$).

The same approach was adopted to assess the impact of the first-order approximation on the EGPT. This time, the reference and modified (with a +300 K fuel temperature) states were perturbed once again with a 1% increase in the Pu-239 atomic density. The relative variation $\Delta(\Delta\rho)/\Delta\rho$ was compared with $\delta(\Delta\rho)/\Delta\rho$, which was obtained from the SC for the Doppler reactivity change. The results are reported in table 4.1. The results in both cases are similar, with a discrepancy between the direct and the approximated calculations of less than 10%.

| **Assessment for $k_{eff}$** | | | **Assessment for $\Delta\rho_T$** | | | | |
|---|---|---|---|---|---|---|---|
| | **Reference** | **Perturbed** (+1% $N_{Pu-239}$) | | **Reference** | **Modified** (+300K) | **Perturbed** (+1% $N_{Pu-239}$) | **Modified & Perturbed** (+300K) (+1% $N_{Pu-239}$) |
| $k$ | 1.02988 | 1.03403 | $k$ | 1.02988 | 1.02846 | 1.03403 | 1.03261 |
| $\Delta k$ | 415 [pcm] | | $\Delta\rho$ | −134.36 [pcm] | | −132.73 [pcm] | |
| $\frac{\Delta k}{k}$ | 403 [pcm] | | $\frac{\Delta(\Delta\rho)}{\Delta\rho}$ | −1213 [pcm] | | | |
| $S_{Pu-239}$ | 0.44485 [-] | | $S_{Pu-239}$ | −1.33137 [-] | | | |
| $\frac{\delta k}{k}$ | 445 [pcm] | | $\frac{\delta(\Delta\rho)}{\Delta\rho}$ | −1331 [pcm] | | | |
| **Rel. Diff.** | −9.6 [%] | | **Rel. Diff.** | −9.8 [%] | | | |

*Table 4.1: NEA LFR benchmark core. Results of the impact assessment of the first-order approximation, on both the effective multiplication factor and the Doppler reactivity change. The values obtained by direct calculations are compared with those produced by first-order approximated SPT and EGPT, multiplying the SCs of Pu-239 for the entire core and all reactions and energy groups, by a 1% relative variation in the cross section.*

## 4.6 Conclusions about the sensitivity analysis

The sensitivity analysis was performed on the NEA lead-cooled fast reactor benchmark [12], using the ERANOS tools. This analysis involves computing sensitivity coefficients, which are defined as the relative variation in an integral parameter resulting from a relative variation in the nuclear data. This enables determining which nuclides and their reactions are the most impactful on a representative LFR system. Due to code limitations, the BISTRO $S_N$ solver was used to derive the SCs for a cylindrical equivalent geometry of the reactor core. The sensitivity analysis was performed for the effective multiplication factor and the Doppler reactivity change, using fist-order SPT and EGPT formulations. The latter parameter was examined by increasing the temperature of the MOX fuel by 300 K, in both the internal and external fuel assemblies.

The ERANOS tools enable the SCs to be broken down by region, nuclide, reaction, and group, exploiting the linearity of these coefficients. The absolute values of the SCs for the entire core were summed, and then the analysis was refined by distinguishing between contributions from the internal and external fuel assemblies. This allowed the nuclides to be ranked according to their impact on lead fast reactor applications. A further refinement was performed by assessing the SCs for each nuclide and reaction, with their actual sign.

This revealed the predominant roles of U-238 capture and Pu-239 fission. Compared to other nuclides, these reactions have the greatest impact on both the effective multiplication factor and Doppler reactivity change. Other fuel isotopes have been shown to significantly influence LFR systems. For example, the elastic scattering reaction of O-16 substantially impacts the Doppler

effect, and Pu-241 fissions significantly influence the multiplication factor. U-235 was found to have very little impact on either parameter, which was attributed to the nuclide's very low concentration in the fuel material of the numerical benchmark. Nevertheless, given that it is widely recognised as one of most important nuclides in nuclear reactors, this nuclide could be of great interest for other applications.

Regarding the coolant isotopes, the elastic scattering is more predominant, with Pb-208 generally being the most influent nuclide. In fact, this isotope constitutes over half of the coolant in the fuel assemblies. Similarly, the elastic scattering reaction of Fe-56 was found to be the most noteworthy reaction for the cladding material. Finally, the analysis was refined by assessing the SCs for the most significant nuclides and reactions using the ECCO 33 energy group structure.

The accuracy of the SCs was then assessed by comparing them with Serpent2 simulation results available internally to *new*cleo. In fact, Monte Carlo calculations can be exploited to perform sensitivity analyses with an accurate description of the reactor geometry. However, the main drawback is that SCs for reactions with minimal influence are associated with large statistical uncertainty. In fact, it was only possible to draw meaningful conclusions for the most significant reactions of some of the fuel isotopes. For U-238 and Pu-239, for example, good agreement was generally found with Monte Carlo simulations of SCs for the effective multiplication factor. Given the large approximation introduced by the cylindrical description of the reactor core in ERANOS, the accuracy of the SCs for the multiplication factor was deemed satisfactory for the purposes of this thesis. Instead, according to the EGPT formulation, the SCs for the Doppler reactivity change result from the difference in the SCs for the multiplication factor between two states, and thus a 300 K variation in the MOX fuel is too small to assess them with an acceptable statistical uncertainty. Nevertheless, since the SCs for the multiplication factor are reasonably accurate at both temperatures, those for the Doppler reactivity change can also be considered to be sufficiently reliable, as they result from a purely algebraic manipulation.

Finally, the impact of using a first-order approximation was assessed. This was achieved by comparing the SCs with the results of a direct calculation. The direct calculation involved increasing by 1% the concentration of Pu-239 in the MOX fuel and then computing the variation in the effective multiplication factor and Doppler reactivity change. The comparison revealed that using a first-order approximation offsets the results obtained by the SCs from those obtained by direct calculation by approximately 10%. For the purposes of this study, this difference was deemed acceptable.

Chapter 5

# Validation of the ECCO self-shielding model with the ENDF/B-VIII.0 library

The ECCO cell code, together with the ENDF/B-VIII.0 based ECCO library used within the *new*cleo team, aims to provide an accurate treatment of self-shielding effects. Since this study focusses on analysing the performance of the ECCO self-shielding module, described in Section 2.2.1.2, the main challenge lies in isolating the errors generated by the deterministic approximations of the code from those introduced during the manipulation of the ENDF-6 data in the ECCOLIB production process. Also, to separate the error related to the ECCO self-shielding module from the error sources due to other models, e.g. cross section homogenisation and condensation, leakage model, Doppler broadening and so forth, the approach adopted by P. Jacquet in his Ph.D. thesis [9] will be initially followed. Jaquet followed this approach for the numerical validation of the ECCO cell code for the analysis of Sodium Fast Reactors (SFR).

Consistently with his approach, both spatially homogeneous and heterogeneous systems will be considered. As described in the second chapter of this work, the computation of the self-shielded cross section differs, in fact, in the two cases. Moreover, the heterogeneous case poses the challenge of distinguishing errors related to the self-shielding model from those arising from the use of collision probabilities. In the following sections, a first attempt will be made to replicate the results obtained by Jacqet for SFR problems, in order to verify the consistency of the workflow. Then, a case representative of an LFR system will be addressed.

## 5.1 Validation of self-shielding module in the homogeneous medium

To assess the self-shielding performance of ECCO, using the ENDF/B-VIII.0 ECCOLIB, the reference route described in Chapter 2 was not followed. Indeed, this route is intended for the homogenisation of heterogeneous cross sections, which is unnecessary in this case since the medium is already homogeneous. Instead, only two steps were adopted within the code: the first using a broad structure (33 or 172 groups) and the second using the fine 1968 energy group structure. The cross sections were then condensed from the 1968 energy mesh to a broader group structure. Listing 5.1 provides a description of the two steps within the code. In both steps, the buckling was set equal to zero. This enabled an infinite medium to be simulated, thereby avoiding any errors originating from the leakage model.

To avoid other error sources, additional simplifications were made. In line with Jacquet, the cell temperature was set to 293 K, which is one of the temperatures at which nuclear data are stored in the ECCOLIB. This choice avoids the need for cross-section interpolation between neighbouring temperatures. Finally, it should be noted that the resonances are narrower at lower temperatures. This should lead to a more pronounced self-shielding effect, and thus the numerical model should encounter more difficulty with this problem than with one at a higher

temperature. Furthermore, all geometry dilatations were neglected. The composition of the homogeneous, infinite cell is detailed in the following sections.

```
      ->STEP_1_FUEL_IN
      GEOMETRY HOMOGENEOUS
      ELEMENTS ALL ! Self-shielding applied to all isotopes in cell
      GROUP STRUCTURE OTHER 33 ! Or 172
      INPUT LIBRARY 'ECCOLIB_ENDFB_80.33' ! Or ECCOLIB_ENDFB_80.172
      FLUX SOLUTION FM P1 CONSISTENT ORDER 1 ! Flux solution fundamental mode
      BUCKLING 0.0;
      ->STEP_2_FUEL
      GEOMETRY HOMOGENEOUS
      GROUP STRUCTURE FINE   ! 1968 group structure
      INPUT LIBRARY 'ECCOLIB_ENDFB_80.1968'
      ELEMENTS ALL
      FLUX SOLUTION FM P1 CONSISTENT ORDER 1
      BFROM 1
      CONDENSE 33 ! Condense 1968 XS into 33 group structure
         1 82 142 202 262 322 382 442 502 564        !boundaries of 33 groups
         624 686 746 808 868 928 988 1048 1108 1168  !in the 1968 structure
         1228 1288 1336 1422 1480 1516 1579 1648 1708 1768
         1837 1919 1952 ;
      PRINT DATA FLUXES CROSS SECTIONS MICROSCOPIC VECTORS ;
```

*Listing 5.1: Two-steps calculation scheme adopted in ECCO for the evaluation of self-shielding performance with the ENDF/B-VIII.0 library. The scheme differs from the reference route because cross sections are not homogenised and a leakage model is not used. At the end of the second step, the cross sections are condensed into a 33 group structure.*

### 5.1.1 Analysis of the Sodium Fast Reactor homogeneous fuel pin

The results of the sensitivity analysis, performed in Chapter 4, revealed the importance of nuclides U-238 and Pu-239, highlighting the need to properly calculate their cross sections. Eventual errors in the computation of these quantities, for example due to incorrect treatment of the self-shielding, would result in significant errors in the multiplication factor or Doppler reactivity change. In his work, Jacquet assessed the numerical accuracy of the self-shielding treatment of these nuclides considering three different media, whose compositions are reported in Table 5.1 [9]. His approach consisted of analysing the impact of the resonances of the two isotopes separately, and then when they are mixed together. The third case is used to determine the impact of mutual self-shielding between the two heavy nuclides.

| **Concentration [atom/(b-cm)]** | | | |
|---|---|---|---|
| **Isotope** | **A** | **B** | **C** |
| U-238 | - | 8.359E-03 | 7.040E-03 |
| Pu-239 | 8.324E-03 | - | 1.313E-03 |
| O-16 | | 1.657E-02 | |
| Na-23 | | 8.410E-03 | |
| Fe-56 | | 2.101E-02 | |

*Table 5.1: The nuclides and their respective atomic concentrations in the SFR cells considered by Jacquet [9]. The concentrations of the nuclides O-16, Na-23, and Fe-56 are common to all media. Medium A contains Pu-239, medium B contains U-238, and the third medium C contains both nuclides.*

#### 5.1.1.1 Check of internal reproducibility

In his work, Jacquet used the JEFF-3.1 ECCO library and compared its results with those of the TRIPOLI-4® MC code [51, 52, 50], which used the same JEFF-3.1 NDL. In the present analysis, the OpenMC Monte Carlo code was used as a reference for validation [40]. Due to its high flexibility and fidelity, this open-source code is widely used within the international community [39]. User-code interactions are greatly simplified through the support of a Python API, enhancing the manageability of the input files. As described in Chapter 3, the code uses NDLs in HDF5 format, which are generated from ACE files. Therefore, it benefits from the suite of codes (e.g. NJOY) that have been developed for other well-established MC codes, such as MCNP and Serpent [78, 77]. For these reasons, this code was adopted for the validation purposes of this work.

Using an ECCOLIB based on the JEFF-3.1 and the same ECCO route (first step with 33 groups) the Jacquet's infinite multiplication factor was replicated exactly with ECCO [9]. Table 5.2 shows the results of a comparison between ECCO, OpenMC, and TRIPOLI-4® results. A significant discrepancy was found between OpenMC and ECCO results for case C, which was considerably greater than the Jacquet reference result. However, the multiplication factor is an integral parameter and is insufficient alone to identify the origin of this discrepancy. To refine the investigation, the group-averaged cross sections computed with ECCO, OpenMC, and TRIPOLI-4® were compared. The microscopic cross sections calculated using the 1968 structure were condensed into the RRR, URR, and continuum of U-238 and Pu-239, in both the ECCO and OpenMC codes. The energy bounds of these intervals vary for each nuclide and even between different nuclear data evaluations, as shown in Table 5.3.

| $k_\infty$ Homogeneous SFR fuel pin | | | | | |
|---|---|---|---|---|---|
| | | | | Abs. Diff. [pcm] | |
| Medium | TRIPOLI-4® | OpenMC | ECCO | ECCO vs. TRIPOLI-4® | ECCO vs. OpenMC |
| A | 2.72051(9) | 2.72032(∼1) | 2.71902 | -149 | -130 |
| B | 0.14741(5) | 0.14744(∼1) | 0.14737 | -4 | -7 |
| C | 1.40152(9) | 1.40002(1) | 1.40250 | 98 | 248 |

*Table 5.2: SFR homogeneous fuel pin. The infinite multiplication factor is computed using ECCO and OpenMC and the JEFF-3.1 library, in each of the three media. The values are compared with Jacquet's ECCO and TRIPOLI® results [9], which were obtained using the same JEFF-3.1 NDL. As Jacquet's results were exactly replicated, the ECCO values are reported only once. The standard deviations of both Monte Carlo reference values are reported in parenthesis (in pcm).*

Table-5.4 illustrates the capture cross section of U-238 ($\sigma_c^{^{238}\mathrm{U}}$) and the fission cross section of Pu-239 ($\sigma_f^{^{239}\mathrm{Pu}}$), computed in the three-group structure using ECCO and OpenMC, and compared with those calculated by Jacquet in the same energy mesh [9]. Furthermore, also the cross sections condensed in the total energy range (from $10^{-5}$ eV to 1.96 MeV) were compared. Once again, Jacquet's ECCO cross sections were exactly replicated. Consistently with his work, the relative error was defined as

$$\text{Rel. Err.} = \frac{\sigma^{ECCO} - \sigma^{MC}}{\sigma^{MC}}. \tag{5.1}$$

As it can be seen in the table, some discrepancies between the OpenMC and ECCO results were found for Pu-239 in the unresolved resonance range. These errors may be due to differences in the way the libraries have been processed for OpenMC and TRIPOLI-4®. The latter indeed shares the URR treatment with ECCO, using mathematical Probability Tables (PTs) generated by the

| Pu-239 JEFF-3.1 & ENDF/B-VIII.0 | | | | | |
|---|---|---|---|---|---|
| Interval | Energy [eV] | 33 Groups | 295 Groups | 1968 Groups | Energy ECCO 33 [eV] |
| RRR | [1.00e-05, 2.50e+03] | 19 - 33 | 207 - 295 | 1108 - 1968 | [1.00e-05, 2.034684e+03] |
| URR | [2.50e+03, 3.00e+04] | 13 - 18 | 165 – 206 | 746 – 1107 | [2.034684e+03,4.086771e+04] |
| Continuum | [3.00e+04, 2.00e+07] | 1 - 12 | 1 - 164 | 1 – 745 | [4.086771e+04,1.96403e+07] |
| **U-238 ENDF/B-VIII.0** | | | | | |
| Interval | Energy [eV] | 33 Groups | 295 Groups | 1968 Groups | Energy ECCO 33 [eV] |
| RRR | [1.00e-05, 2.00e+04] | 15 - 33 | 183 - 295 | 868 - 1968 | [1.00e-05, 1.503439e+04] |
| URR | [2.00e+04,1.50e+05] | 10 - 14 | 141 - 182 | 564 - 867 | [1.503439e+04,3.01974e+05] |
| Continuum | [1.50e+05, 2.00e+07] | 1 - 9 | 1 - 140 | 1 - 563 | [3.01974e+05,1.96403e+07] |
| **U-238 JEFF-3.1** | | | | | |
| Interval | Energy [eV] | 33 Groups | 295 Groups | 1968 Groups | Energy ECCO 33 [eV] |
| RRR | [1.00e-05, 2.00e+04] | 15 - 33 | 183 - 295 | 868 - 1968 | [1.00e-05, 1.503439e+04] |
| URR | [2.00e+04,3.00e+05] | 9 - 14 | 129 - 182 | 502 - 867 | [1.503439e+04,1.831564e+05] |
| Continuum | [3.00e+05, 2.00e+07] | 1 - 8 | 1 - 128 | 1 - 501 | [1.831564e+05,1.96403e+07] |

*Table 5.3: The energy bounds (second column) of the three energy intervals used for the cross sections condensation have been condensed are reported for U-238 and Pu-239, in the JEFF-3.1 and ENDF/B-VIII.0 library. Columns three, four and five express the same energy intervals in terms of discrete groups in the 33, the 295 (see AppendixF), and the 1968 groups structures, respectively. The final column reports the energy values of the boundaries mapped in the ECCO 33-group structure.*

CALENDF code for the Monte Carlo sampling, while the former uses the PTs generated by the PURR module of NJOY. In contrast, good agreement was found with Jacquet's TRIPOLI-4® reference values for U-238 within the other energy intervals and media. This supports the validity of OpenMC simulations. Therefore, it was decided to proceed with the ENDF/B-VIII.0 NDL to determine whether the discrepancy between ECCO and OpenMC was also present with this library. The switch to this library was already planned, as the final aim of this work is to assess the performance of the ECCO self-shielding module with a more recent NDL.

#### 5.1.1.2 ECCO self-shielding validation in a Sodium Fast Reactor cell with the ENDF/B-VIII.0 library

For the same SFR cells, Table 5.5 shows the results for the infinite multiplication factor, compared between ECCO and OpenMC, using in both codes the ENDF/B-VIII.0 NDL.

| $k_\infty$ Homogeneous SFR fuel pin | | | |
|---|---|---|---|
| Medium | OpenMC | ECCO | Abs. Diff. |
| A | 2.70463(∼1) | 2.70274 | -189 |
| B | 0.14462(∼1) | 0.14440 | -22 |
| C | 1.39514(1) | 1.39225 | -289 |

*Table 5.5: SFR homogeneous fuel pin. Infinite multiplication factor computed for the three different media, using OpenMC and ECCO with the ENDF/B-VIII.0 NDL. The standard deviations of Monte Carlo reference values are reported in parenthesis (in pcm).*

| **Homogeneous infinite SFR fuel pin** | | | | **A** | **B** | **C** | |
|---|---|---|---|---|---|---|---|
| | | | | $\sigma_f^{^{239}\mathrm{Pu}}$ | $\sigma_c^{^{238}\mathrm{U}}$ | $\sigma_f^{^{239}\mathrm{Pu}}$ | $\sigma_c^{^{238}\mathrm{U}}$ |
| CONTINUUM | | TRIPOLI-4® | [b] | 1.6547 | 0.1007 | 1.5899 | 0.0980 |
| | | OpenMC | [b] | 1.6547 | 0.1007 | 1.5899 | 0.0980 |
| | | ECCO | [b] | 1.6542 | 0.1007 | 1.5898 | 0.0981 |
| | R.S.D. | TRIPOLI-4® | [%] | 0.002 | 0.011 | 0.003 | 0.005 |
| | | OpenMC | [%] | 0.002 | 0.005 | $\sim 0.001$ | 0.005 |
| | Rel. Err. | ECCO vs. TRIPOLI-4® | [%] | -0.034 | -0.005 | -0.004 | 0.082 |
| | | ECCO vs. OpenMC | [%] | -0.034 | -0.025 | -0.008 | 0.048 |
| URR | | TRIPOLI-4® | [b] | **1.6746** | 0.2643 | **1.8254** | 0.2514 |
| | | OpenMC | [b] | **1.6683** | 0.2644 | **1.8144** | 0.2515 |
| | | ECCO | [b] | **1.6751** | 0.2644 | **1.8284** | 0.2515 |
| | R.S.D. | TRIPOLI-4® | [%] | 0.009 | 0.004 | 0.005 | 0.004 |
| | | OpenMC | [%] | 0.008 | 0.001 | $\sim 0.001$ | 0.002 |
| | Rel. Err. | ECCO vs. TRIPOLI-4® | [%] | **0.025** | 0.034 | **0.164** | 0.046 |
| | | ECCO vs. OpenMC | [%] | **0.406** | -0.020 | **0.772** | -0.013 |
| RRR | | TRIPOLI-4® | [b] | 3.9239 | 0.9260 | 5.9155 | 0.7712 |
| | | OpenMC | [b] | 3.9222 | 0.9261 | 5.9152 | 0.7712 |
| | | ECCO | [b] | 3.9232 | 0.9228 | 5.9542 | 0.7681 |
| | R.S.D. | TRIPOLI-4® | [%] | 0.054 | 0.005 | 0.013 | 0.007 |
| | | OpenMC | [%] | 0.046 | 0.003 | 0.007 | 0.004 |
| | Rel. Err. | ECCO vs. TRIPOLI-4® | [%] | -0.018 | -0.354 | 0.654 | -0.403 |
| | | ECCO vs. OpenMC | [%] | 0.025 | -0.365 | 0.660 | -0.400 |
| Total energy range | | TRIPOLI-4® | [b] | 1.6581 | 0.4017 | 1.8036 | 0.2826 |
| | | OpenMC | [b] | 1.6577 | 0.4019 | 1.8014 | 0.2827 |
| | | ECCO | [b] | 1.6576 | 0.4014 | 1.8058 | 0.2823 |
| | R.S.D. | TRIPOLI-4® | [%] | 0.002 | 0.003 | 0.003 | 0.003 |
| | | OpenMC | [%] | 0.002 | 0.002 | 0.002 | 0.002 |
| | Rel. Err. | ECCO vs. TRIPOLI-4® | [%] | -0.030 | -0.081 | 0.124 | -0.110 |
| | | ECCO vs. OpenMC | [%] | -0.009 | -0.136 | 0.248 | -0.166 |

*Table 5.4: SFR homogeneous fuel pin. The microscopic cross sections, calculated using OpenMC and ECCO with the 1968 group structure, are condensed in the RRR, URR and continuum intervals of U-238 and Pu-239, as well as in the total energy range. For each medium, the values are compared with those obtained by Jacquet in the same energy structure [9]. In each code the JEFF-3.1 NDL is used. As the ECCO values were replicated exactly , they are reported only once in the table.*

When the absolute differences between the two codes are compared with Jacquet's reference values in Table 5.2, larger discrepancies are evident in each medium. In relative terms, this is particularly significant for cases B and C, with the ECCO simulations underestimating the infinite multiplication factor.

Once again, to find the origin of those discrepancies, the analysis was refined by comparing the microscopic cross sections. The cross sections were condensed again into the three-group structure and the entire energy range and they are shown in Table 5.6. In contrast to the previous

case, $\sigma_f^{^{239}\mathrm{Pu}}$ was properly calculated within the URR, with very good agreement between the MC and ECCO simulations. For $\sigma_c^{^{238}\mathrm{U}}$, instead, large discrepancies were found in the URR. This difference is considerably higher than that found by Jacquet in his work, as it can be observed in Table 5.4. Looking at the resolved range, it seems that mild but significant errors are also present in this interval. However, these values are comparable with Jacquet's reference values [9]. Moreover, the low-energy range is in general of little interest for fast reactor applications, since the number of neutrons that slow down to these energies is extremely low. This is also reflected in the difficulty of properly calculating this range in MC calculations, since the associated statistical uncertainty is generally significant [9]. Since an energy mesh of three groups only may hide information about the origin of these discrepancies, in the following sections cross sections condensed into finer group structures will be compared.

| **Homogeneous infinite SFR fuel pin** | | | **A** | **B** | **C** | |
|---|---|---|---|---|---|---|
| | | | $\boldsymbol{\sigma_f^{^{239}\mathrm{Pu}}}$ | $\boldsymbol{\sigma_c^{^{238}\mathrm{U}}}$ | $\boldsymbol{\sigma_f^{^{239}\mathrm{Pu}}}$ | $\boldsymbol{\sigma_c^{^{238}\mathrm{U}}}$ |
| CONTINUUM | OpenMC | [b] | 1.6518 | 0.1035 | 1.5951 | 0.1013 |
| | ECCO | [b] | 1.6509 | 0.1035 | 1.5948 | 0.1013 |
| | Rel. Err. | [%] | -0.057 | 0.021 | -0.023 | 0.081 |
| | R.S.D. | [%] | 0.002 | 0.003 | 0.003 | 0.005 |
| URR | OpenMC | [b] | 1.7227 | **0.2939** | 1.8584 | **0.2830** |
| | ECCO | [b] | 1.7240 | **0.3006** | 1.8595 | **0.2884** |
| | Rel. Err. | [%] | 0.075 | **2.283** | 0.059 | **1.910** |
| | R.S.D. | [%] | 0.008 | **0.001** | 0.003 | **0.001** |
| RRR | OpenMC | [b] | 3.8447 | 0.9103 | 5.8051 | 0.7626 |
| | ECCO | [b] | 3.8437 | 0.9071 | 5.8482 | 0.7600 |
| | Rel. Err. | [%] | -0.026 | -0.351 | 0.742 | -0.343 |
| | R.S.D. | [%] | 0.043 | 0.003 | 0.007 | 0.001 |
| Total energy range | OpenMC | [b] | 1.6588 | 0.3997 | 1.8120 | 0.2824 |
| | ECCO | [b] | 1.6581 | 0.4014 | 1.8131 | 0.2843 |
| | Rel. Err. | [%] | -0.045 | 0.414 | 0.061 | 0.657 |
| | R.S.D. | [%] | 0.002 | 0.002 | 0.001 | 0.002 |

*Table 5.6: SFR homogeneous fuel pin. The fission cross section of Pu-239 and the capture cross section of U-238 are calculated using ECCO with the ENDF/B-VIII.0 NDL, and then condensed from the 1968 groups structure into the RRR, URR, and continuum (and total energy range) of their respective isotopes.*

#### 5.1.1.3 Pu-239 fission cross section

The Pu-239 fission cross section, computed using the 1968 group structure, was condensed into 33 and 295 group structures, as shown in Figure 5.1 for Case A. The energy bounds of the latter structure are reported in Appendix F. The dashed vertical lines represent the energy boundaries of the URR in the three-group structure. Hereafter, the focus will be on energies above 100 eV, since this is the range of practical interest for fast reactor applications. Looking at the figure, the considerably low relative error (ECCO vs. OpenMC) within the continuum range is evident. However, resonances are not present in this interval and the self-shielding model is not applied. In the resolved range, the error is also small, but it is of the same magnitude as the statistical uncertainty. Therefore, it is not possible to draw any significant conclusion about the numerical accuracy of the self-shielding model. Nevertheless, the cross sections computed with OpenMC and ECCO are generally in good agreement.

In the unresolved range, large errors of opposite sign are present. These errors are to be expected [9], as the generation of resonances in this range is a stochastic process, and the energy grids used in CALENDF and the PURR module of NJOY may differ. However, when these errors are condensed into broader group structures, they tend to decrease significantly. Moreover, because of errors of the same magnitude and opposite sign in different energy groups, they compensate each other and therefore do not appear when the cross sections in the 1968 group structure are condensed into the three-group structure. This results in the negligible errors observed in the URR in Table 5.6. In conclusion, the computation of the cross section for this nuclide with the ENDF/B-VIII.0 library can be considered to yield satisfactory results, since the relative errors are generally low in the broad structure and are consistent with those observed by Jacquet with the JEFF-3.1 NDL [9]. Furthermore, adopting the ENDF/B-VIII.0 NDL leads to a better agreement with OpenMC compared to the JEFF-3.1 ECCOLIB, which, as shown in Section 5.1.1.1, may account for the ECCO overestimation of the Pu-239 fission cross section.

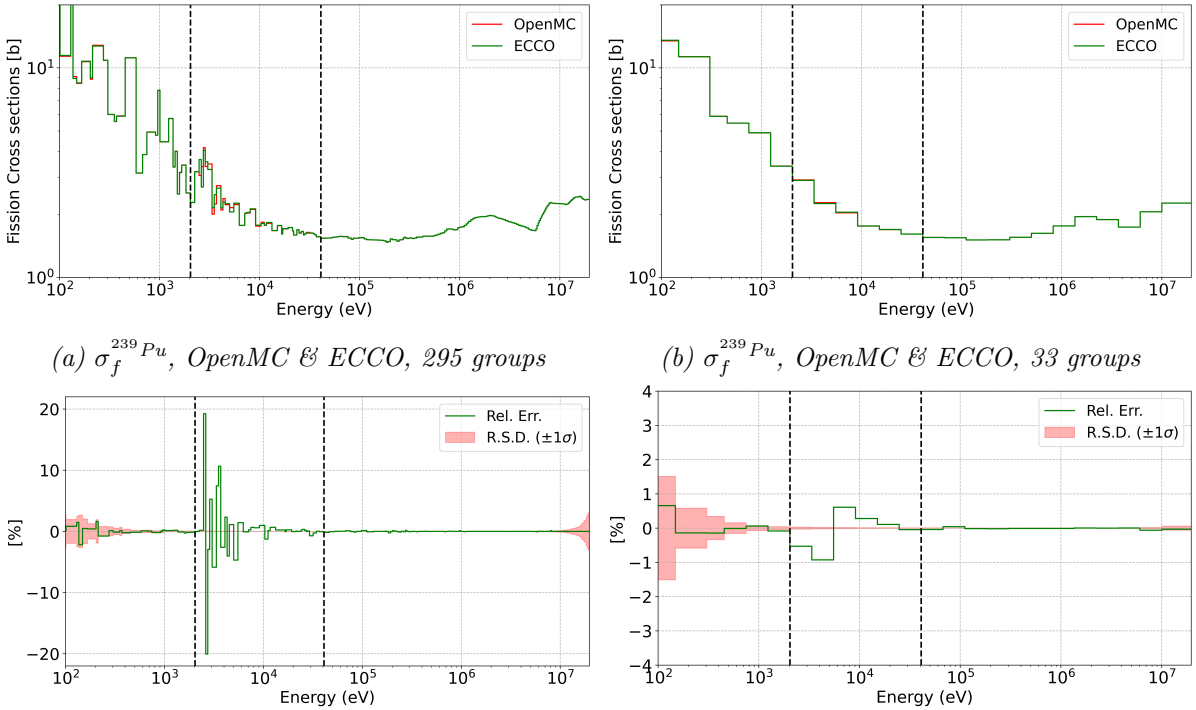


*(a)* $\sigma_f^{^{239}Pu}$*, OpenMC & ECCO, 295 groups*

*(b)* $\sigma_f^{^{239}Pu}$*, OpenMC & ECCO, 33 groups*

*(c)* $\sigma_f^{^{239}Pu}$*, relative error, 295 groups*

*(d)* $\sigma_f^{^{239}Pu}$*, relative error, 33 groups*

*Figure 5.1: SFR homogeneous fuel pin, case A. Above, the Pu-239 fission cross section is computed using the ENDF/B-VIII.0 NDL and compared between OpenMC and ECCO, using 33 and 295 group structures. Below, the relative errors for both group structures are reported. The black vertical dashed lines indicate the URR energy bounds for Pu-239.*

#### 5.1.1.4 U-238 capture cross section

Figure 5.2 shows a comparison of the U-238 capture cross section between OpenMC and ECCO for Case B, as well as the relative error in the 33 and 295 group structures. In this case, the larger statistical uncertainty is associated with the high-energy region. In fact, this zone coincides with the interval where the cross section has the lowest values. As the errors measured in this region are smaller than the statistical uncertainty, they are meaningless. In the thermal region, the errors are not negligible, but they are of less concern because of the low interest in this region for fast reactor applications.

The errors in the URR pose instead a greater concern. In fact, this energy range is relevant in LFR applications, since the capture cross section of U-238 in this interval significantly impacts

the multiplication factor (as highlighted by the sensitivity analysis presented in Chapter 4). Although these errors are smaller than those for Pu-239, they all have a positive sign. This means that they will not cancel each other out when the cross section is condensed into the three-group structure, leading to the non-negligible errors observed in Table 5.6.

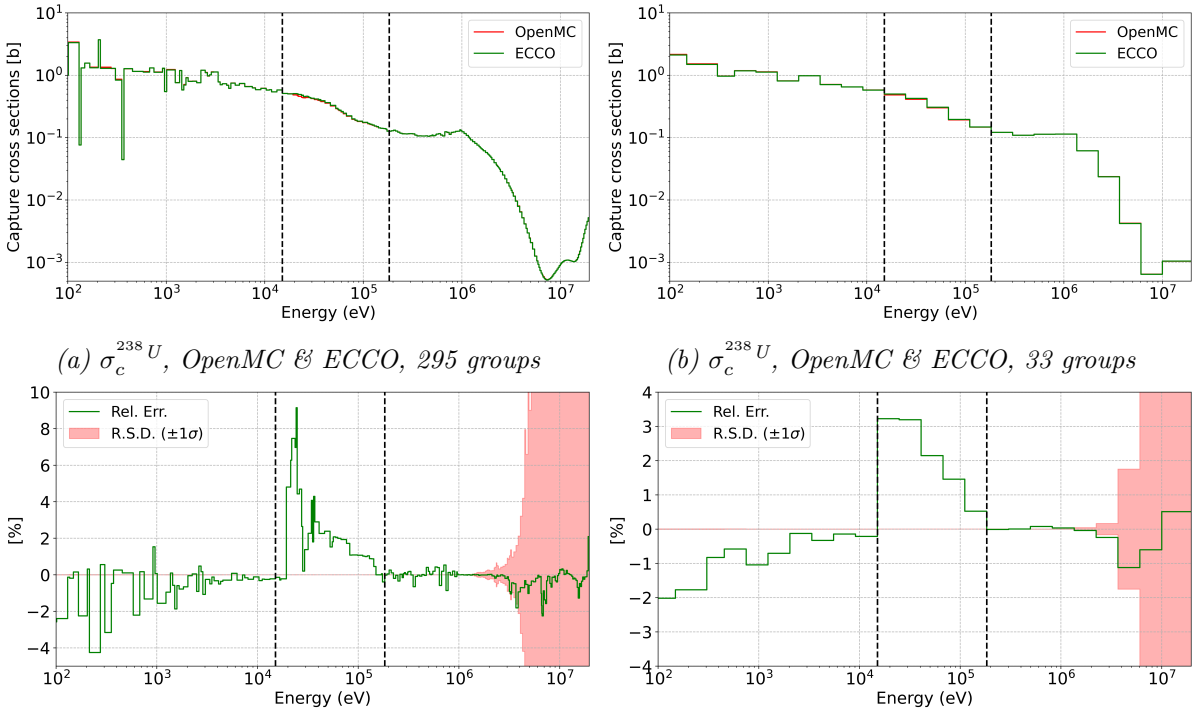


*(a)* $\sigma_c^{^{238}U}$*, OpenMC & ECCO, 295 groups*

*(b)* $\sigma_c^{^{238}U}$*, OpenMC & ECCO, 33 groups*

*(c)* $\sigma_c^{^{238}U}$*, relative error, 295 groups*

*(d)* $\sigma_c^{^{238}U}$*, relative error, 33 groups*

*Figure 5.2: SFR homogeneous fuel pin, case B. Above, the capture cross section of U-238 is computed using the ENDF/B-VIII.0 NDL and compared between OpenMC and ECCO, using 33 and 295 group structures. Below, the relative errors for both group structures are reported. The black vertical dashed lines indicate the URR energy bounds for U-238.*

Figure 5.3 shows a comparison of the U-238 normalised microscopic capture reaction rate, calculated for Case B taking the product between $\sigma_c^{^{238}U}$ and the normalised neutron flux. This is a necessary check, as preserving the reaction rate is at the core of the multigroup model. Therefore, the errors in the capture cross section may originate from errors in the flux, which could possibly be influenced by other nuclides and which would be compensated for by U-238 in order to preserve the reaction rate. However, it can be seen that the error in the capture reaction rate fully reflects the errors in the cross section. Thus the error on the reaction rate seems not affected by the error on the flux, which is shown in Figure 5.4. This suggests that the errors may arise from an erroneous calculation of the cross sections within the ECCO code.

#### 5.1.1.5 Probability tables evaluation

The errors observed in the capture cross section of U-238 in the URR suggest an incorrect data treatment in this energy interval. As described in Chapter 3, both ECCO and OpenMC treat the unresolved range using probability tables produced by CALENDF and the NJOY PURR module, respectively. Using an ERANOS built-in procedure, it was possible to access the PTs data in the libraries. This enabled the identification of energy groups in the 1968 ECCOLIB that contain the PTs data. The procedure was applied to both the JEFF-3.1 and ENDF/B-VIII.0 ECCO libraries. For each library, the relative error in the fission cross sections of Pu-239 and the relative error in the capture cross sections of U-238 were computed with respect to the OpenMC references. Results are displayed in Figures 5.5 and 5.6 where the energy groups of the 1968 structure containing the PTs have been coloured in purple.

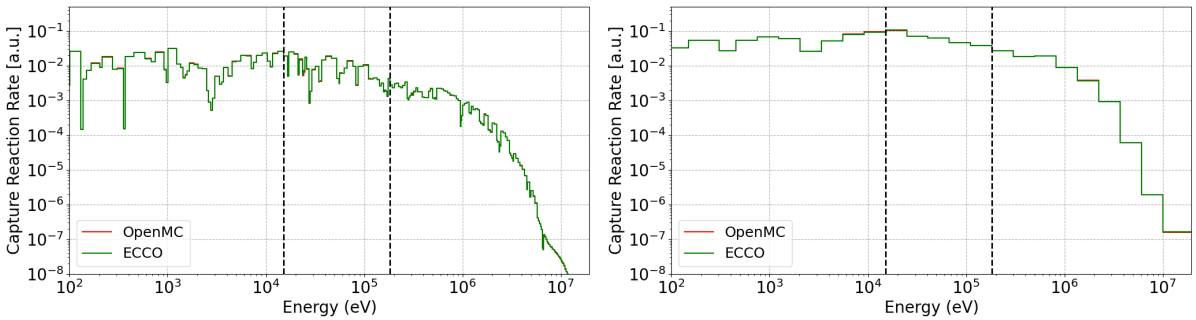


*(a) Normalized $RR_c$, OpenMC&ECCO, 295 groups* *(b) Normalized $RR_c$, OpenMC&ECCO, 33 groups*

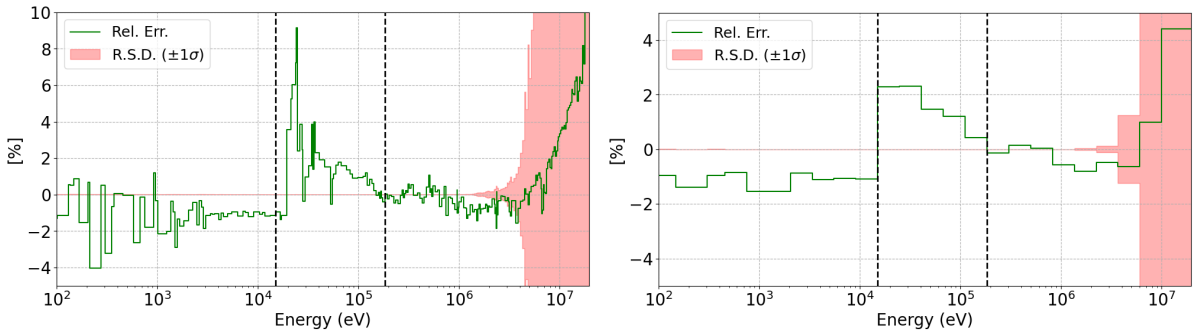


*(c) Normalized $RR_c$, relative error, 295 groups* *(d) Normalized $RR_c$, relative error, 33 groups*

*Figure 5.3: SFR homogeneous fuel pin, case B. Using the ENDF/B-VIII.0 NDL, The normalised capture reaction rate of U-238 is computed using ECCO and OpenMC, taking the product between the microscopic capture cross section and the normalised neutron flux.*

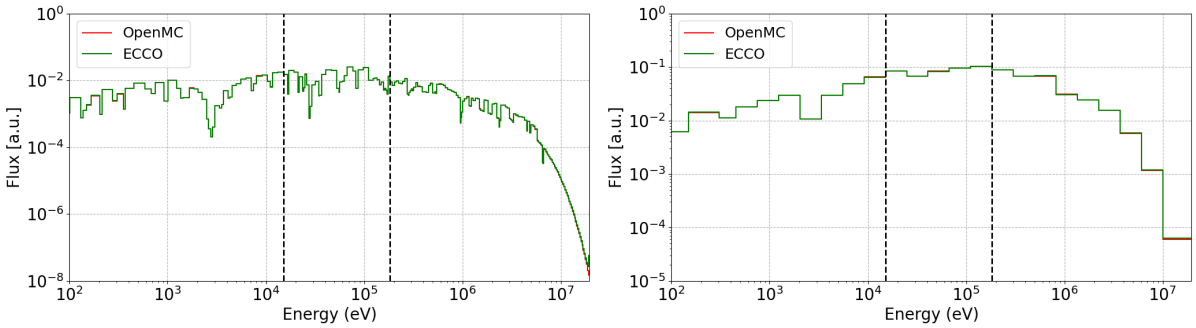


*(a) Normalized $\phi$, OpenMC & ECCO, 295 groups* *(b) Normalized $\phi$, OpenMC & ECCO, 33 groups*

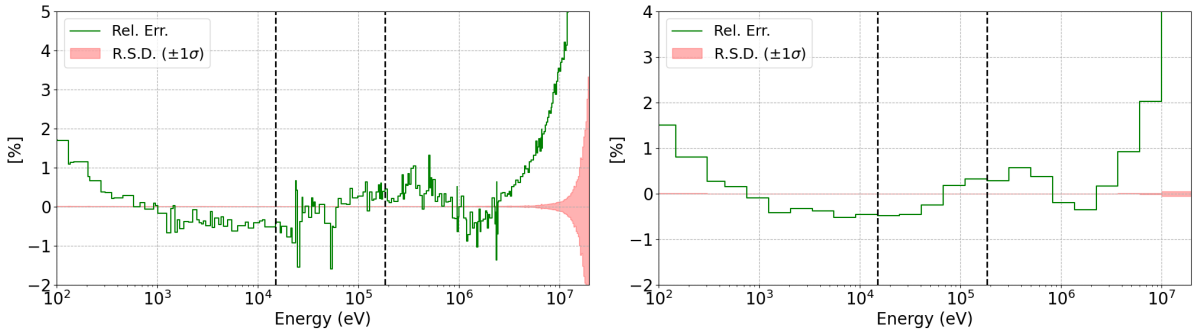


*(c) Normalized $\phi$, relative error, 295 groups* *(d) Normalized $\phi$, relative error, 33 groups*

*Figure 5.4: SFR homogeneous fuel pin, case B. Normalised neutron flux are calculated with the ENDF/B-VIII.0 NDL.*

In both NDLs the energy groups belonging to the 1968 structure fully cover the resolved and unresolved ranges with PTs for the Pu-239 fission cross section. The discrepancies found in the URR for Pu-239 when using JEFF-3.1, already mentioned above, may in this case be due to

inconsistencies in the NDL processing between PURR for OpenMC and CALENDF for ECCO. However, these discrepancies do not occur when using the ENDF/B-VIII.0 NDL.

In the ENDF/B-VIII.0 ECCO library, on the contrary, the PTs for the U-238 capture cross section are not fully covering the URR. In the JEFF-3.1 NDL, where the PTs are present in the URR, the cross section errors are much smaller and cancel each other out within the energy range, as already observed for Pu-239. For the ENDF/B-VIII.0 NDL, instead, errors arise in the URR where the PTs are missing.

To confirm that the lack of PTs is causing the discrepancies in the URR, two simulations of the same medium (Case B) were performed using the Serpent2 MC code [77]. This code allows the user either to enable (consistently with OpenMC) or to disable the sampling from the PTs in the URR, which is equivalent to sampling from the energy distribution of the average values of the cross sections, calculated by the RECONR module of NJOY (as outlined in Chapter 3). Within ECCO, since the URR of U-238 lacks the PTs, the cross sections used in the calculations are the multigroup averaged ones produced by the GROUPR module of NJOY, based on the values produced by the RECONR and UNRESR modules. As the multigroup data used by ECCO in energy regions where PTs are not present are produced consistently with the nuclear data used by Serpent2 when the sampling from PTs is disabled, similar results are expected between these two calculations.

Figure 5.7 shows the capture cross section values of U-238 calculated in the URR using OpenMC, Serpent2 and ECCO. When the PTs sampling is enabled in Serpent2, the result matches that produced by OpenMC. Conversely, when PTs sampling is disabled, the Serpent2 result matches that produced by ECCO. On the one hand, this provides confirmation of the reliability of the OpenMC results, since the MC results match when the same URR treatment methodology is applied. On the other hand, these results provide an evidence that the error in the U-238 capture cross section is mainly due to the absence of PTs in the ENDF/B-VIII.0 ECCO library.

Figure 5.8 shows a comparison of the relative error between ECCO vs. OpenMC and ECCO vs. Serpent2 without the PTs sampling, for the 33 and 295 group structures. As before, disabling the PTs sampling yields lower errors in the URR, since ECCO and Serpent2 use similar data in the unresolved range. However, this evidently yields an incorrect value compared to the OpenMC reference solution. Outside the URR, the relative errors are identical, meaning that the methodologies applied in OpenMC and Serpent2 are equivalent in these intervals.

### 5.1.2 Analysis of the LFR homogeneous fuel pin

The analysis of the SFR fuel pin showed the impact of missing PTs for U-238 in the URR. However, this impact may be amplified by the fact that the investigation focused on very simple media containing only a few nuclides, in which U-238 and Pu-239 play a predominant role. Although these two nuclides are in general the most relevant, as demonstrated in the sensitivity analysis in Chapter 4, the presence of many other nuclides could determine a different impact on the overall behaviour of the medium.

For this reason, the same analysis was repeated but in a case representative of LFR applications, i.e. the Nuclear Energy Agency (NEA) lead-cooled fast reactor benchmark, based on the ALFRED design, which was introduced in Chapter 4 [12, 64, 65, 66]. In particular, the LFR fuel pin was examined. As before, the system was modelled as an infinite homogeneous medium, obtained by smearing the nuclides present in the fuel pin materials (MOX, cladding and coolant). In this case, more nuclides are present in the medium, and a larger error can be expected due to mutual self-shielding effect between heavy isotopes. To treat the non-resonant nuclides more accurately, the first step of the ECCO route used a 172 groups structure. Table 5.7 shows a comparison of the infinite multiplication factor estimated with ECCO and OpenMC, highlighting the significant underestimation of ECCO with respect to the MC reference. The

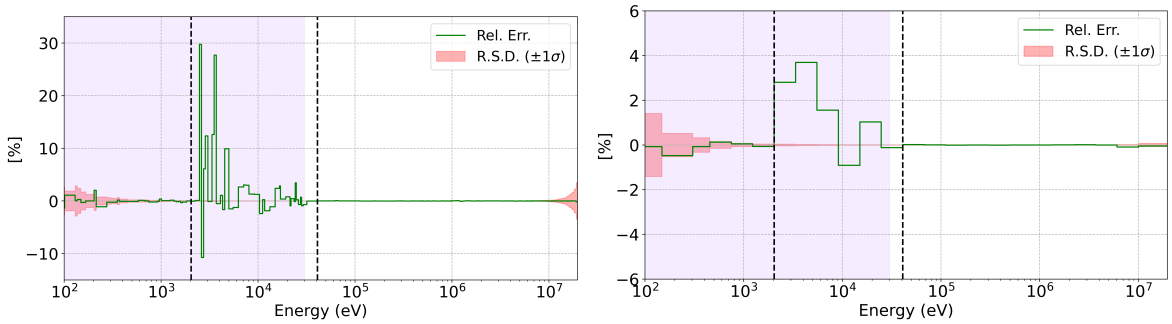


(a) $\sigma_f^{^{239}Pu}$, *JEFF-3.1, 295 groups*




(b) $\sigma_f^{^{239}Pu}$, *JEFF-3.1, 33 groups*

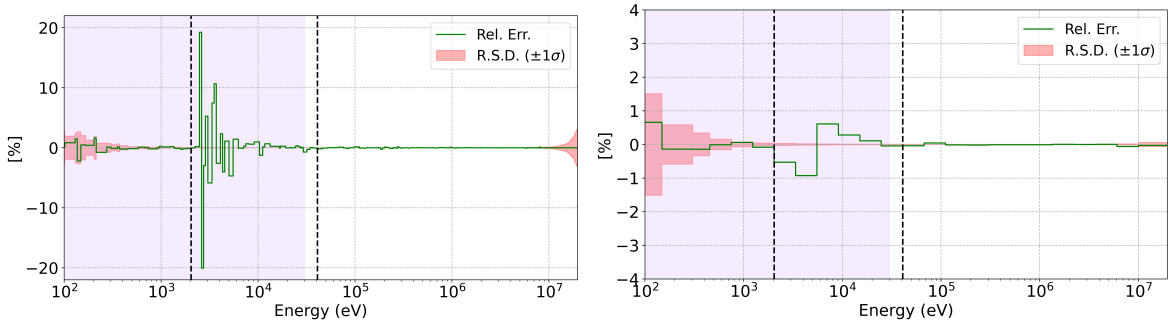


(c) $\sigma_f^{^{239}Pu}$, *ENDF/B-VIII.0, 295 groups*




(d) $\sigma_f^{^{239}Pu}$, *ENDF/B-VIII.0, 33 groups*

*Figure 5.5: SFR homogeneous fuel pin, case A. Relative error in the $\sigma_f^{^{239}Pu}$ (ECCO vs. OpenMC) computed using the JEFF-3.1 NDL above and the ENDF/B-VIII.0 below. Results are compared using both the 33 and the 295 energy structures. The energy groups of the ECCOLIB containing the PTs are indicated with purple colour.*

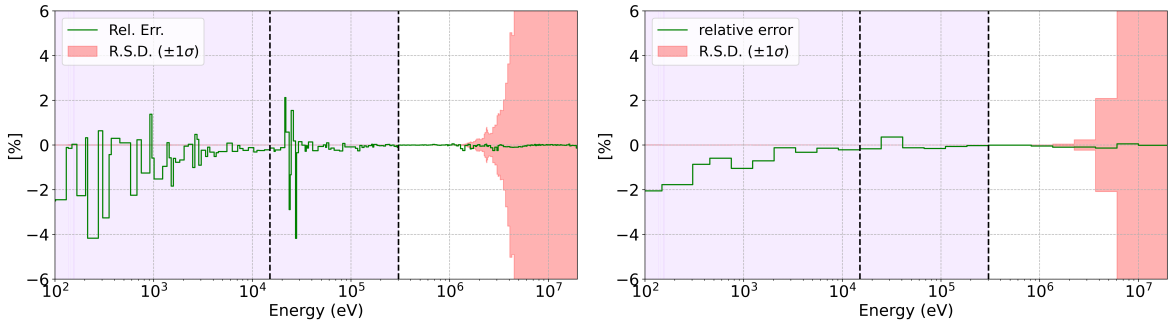


(a) $\sigma_c^{^{238}U}$, *JEFF-3.1, 295 groups*




(b) $\sigma_c^{^{238}U}$, *JEFF-3.1, 33 groups*

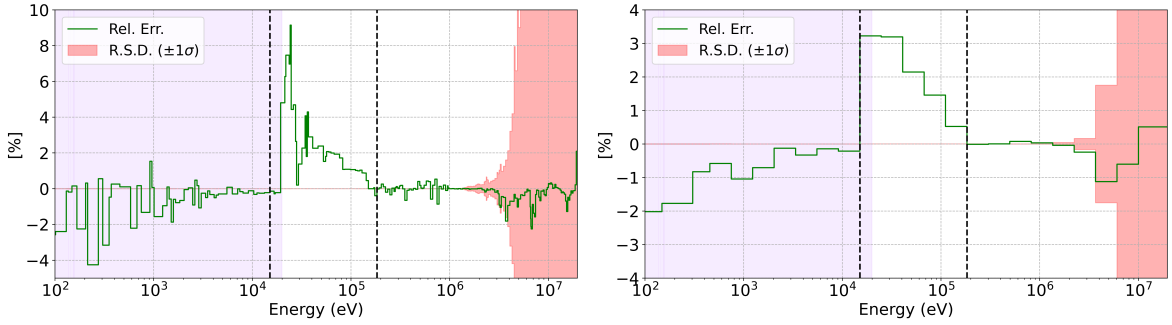


(c) $\sigma_c^{^{238}U}$, *ENDF/B-VIII.0, 295 groups*




(d) $\sigma_c^{^{238}U}$, *ENDF/B-VIII.0, 33 groups*

*Figure 5.6: SFR homogeneous fuel pin, case B. Relative error in the $\sigma_c^{^{238}U}$ (ECCO vs. OpenMC) computed using the JEFF-3.1 NDL above and the ENDF/B-VIII.0 below. Results are compared using both the 33 and the 295 energy structures. The energy groups of the ECCOLIB containing the PTs are indicated with purple colour.*

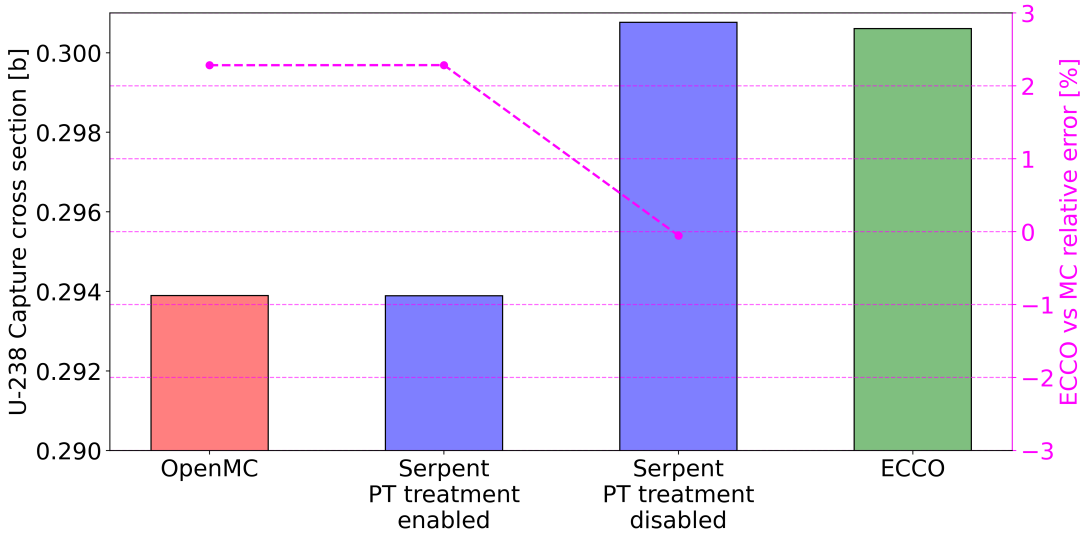


*Figure 5.7: SFR homogeneous fuel pin, case B. The $\sigma_c^{^{238}U}$ values in the URR are computed using the ENDF/B-VIII.0 NDL and compared between OpenMC, Serpent2, and ECCO. The R.S.D. of the MC simulations is 0.001 %. Two simulations have been performed using Serpent2, disabling in one of them the PTs sampling in the URR.*

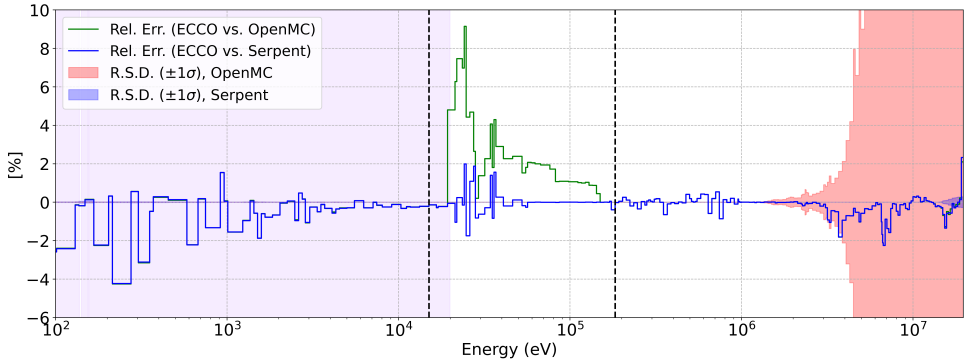


*(a) $\sigma_c^{^{238}U}$, relative error, 295 groups*

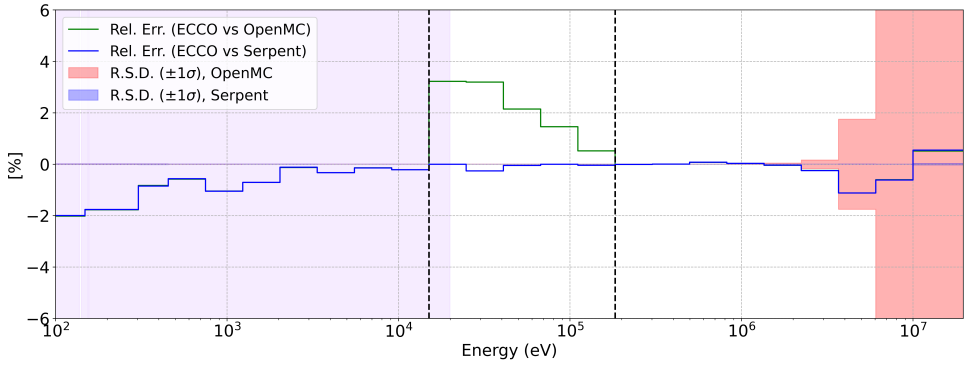


*(b) $\sigma_c^{^{238}U}$, relative error, 33 groups*

*Figure 5.8: SFR homogeneous fuel pin, case B. Using the ENDF/B-VIII.0 NDL with 33 and 295 group structures, the relative error in the $\sigma_c^{^{238}U}$ is compared between ECCO vs. OpenMC and ECCO vs. Serpent2 without the PT sampling.*

computed difference is close to the effective delayed neutron fraction of the ALFRED core [66, 79], i.e. about 315 pcm, highlighting the necessity of taking counteractive measures to reduce this error. A similar discrepancy was found in a previous work on the ECCO validation in fuel cells of the NEA LFR benchmark [11].

| $k_\infty$ Homogeneous LFR fuel pin | | |
|---|---|---|
| **OpenMC** | **ECCO** | **Abs. Diff. [pcm]** |
| 1.36428(1) | 1.36148 | -280 |

*Table 5.7: LFR NEA benchmark, homogeneous fuel pin. Comparison of the infinite multiplication factor evaluated using OpenMC and ECCO with the ENDF/B-VIII.0 NDL. The standard deviation of the Monte Carlo reference value is reported in parenthesis (in pcm).*

As in the previous case, the cross sections produced using the 1968 group structure were condensed into the three-group structure and reported in Table 5.8. In this case, the comparison between ECCO and OpenMC is based on more nuclides, which were selected according to their relevance, as highlighted by the sensitivity analysis performed in Chapter 4. Since the URR does not exist for Pb-208, Fe-56, and O-16 (as all the resonances are resolved across the entire energy range), it was decided to condense their cross sections within the same energy bounds of U-238.

| **Homogeneous infinite LFR fuel pin** | | | | | | | | | |
|---|---|---|---|---|---|---|---|---|---|
| | | | $\sigma_f^{^{239}\mathrm{Pu}}$ | $\sigma_c^{^{238}\mathrm{U}}$ | $\sigma_f^{^{235}\mathrm{U}}$ | $\sigma_f^{^{241}\mathrm{Pu}}$ | $\sigma_{s,el}^{^{56}\mathrm{Fe}}$ | $\sigma_{s,el}^{^{208}\mathrm{Pb}}$ | $\sigma_{s,el}^{^{16}\mathrm{O}}$ |
| CONTINUUM | OpenMC | [b] | 1.5948 | 0.1028 | 1.3823 | 1.8552 | **2.9016** | **6.3253** | 3.6264 |
| | ECCO | [b] | 1.5947 | 0.1029 | 1.3820 | 1.8542 | **2.9088** | **6.5500** | 3.6242 |
| | Rel. Err. | [%] | -0.011 | 0.063 | -0.021 | -0.053 | **0.251** | **3.553** | -0.060 |
| | R.S.D. | [%] | 0.001 | 0.003 | 0.001 | 0.001 | **0.001** | **0.001** | 0.001 |
| URR | OpenMC | [b] | 1.9206 | **0.2807** | 2.8275 | 4.0122 | 5.0341 | 10.7297 | 3.6336 |
| | ECCO | [b] | 1.9194 | **0.2846** | 2.8275 | 4.0142 | 5.0418 | 10.7820 | 3.6334 |
| | Rel. Err. | [%] | -0.059 | **1.392** | -0.001 | 0.048 | 0.152 | 0.488 | -0.004 |
| | R.S.D. | [%] | 0.003 | **0.002** | 0.003 | 0.004 | 0.002 | 0.002 | 0.002 |
| RRR | OpenMC | [b] | 5.1432 | 0.7397 | 8.3074 | 27.2650 | 5.5010 | 11.2409 | 3.7780 |
| | ECCO | [b] | 5.1882 | 0.7386 | 8.2910 | 27.5704 | 5.5015 | 11.2415 | 3.7780 |
| | Rel. Err. | [%] | 0.874 | -0.145 | -0.197 | 1.120 | 0.009 | 0.005 | $< 0.001$ |
| | R.S.D. | [%] | 0.011 | 0.005 | 0.011 | 0.165 | 0.005 | 0.005 | 0.005 |
| Total energy range | OpenMC | [b] | 1.7325 | 0.2638 | 1.8487 | 2.4184 | 4.1805 | 8.9081 | 3.6491 |
| | ECCO | [b] | 1.7325 | 0.2652 | 1.8473 | 2.4172 | 4.1856 | 9.0247 | 3.6481 |
| | Rel. Err. | [%] | 0.004 | 0.547 | -0.074 | -0.051 | 0.121 | 1.309 | -0.028 |
| | R.S.D. | [%] | 0.002 | 0.002 | 0.002 | 0.002 | 0.002 | 0.001 | 0.001 |

*Table 5.8: LFR NEA benchmark, homogeneous fuel pin. The cross sections of some of the most relevant nuclides in the fuel pin, calculated with ECCO, the 1968 groups structure and the ENDF/B-VIII.0 NDL, are condensed from into the RRR, URR, and continuum (and total energy range) of their respective isotopes. For convention, the cross sections of Pb-208, Fe-56, and O-16 have been condensed in the same energy bound of U-238.*

Similarly to the SRF fuel pin case, outlined in Section 5.1.1.2, ECCO overestimates the capture cross section of U-238 compared to OpenMC. This is most likely the main reason behind the underestimation of the infinite multiplication factor, which will find confirmation in Chapter 6 through a decomposition analysis. However, it can be noticed that the error is lower compared to the previous SFR case. This is the beneficial effect of diluting a nuclide within a mixture that contains a large number of other nuclides. In fact, as more nuclides are present, the impact of each nuclide on the energy dips of the flux (which depend on the total cross section

of the medium) decreases. Therefore, the self-shielding phenomenon for the nuclide in question is attenuated to some extent. Furthermore, analysis of the LFR fuel pin revealed significant errors in the elastic scattering cross sections of Pb-208 and Fe-56 in the continuum energy range of U-238. Non-negligible errors for the Pu-239 and Pu-241 fission can also be observed in the resolved region. However, as in the previous case, larger errors in this range are to be expected and are generally of lower concern. In the next sections, the differences between ECCO and OpenMC will be analysed again with finer energy group structures. For each nuclide, purple colour bands will be used again to represent the energy groups containing PTs.

#### 5.1.2.1 U-238 & Pu-239 cross sections

Figure 5.9 shows a comparison of the U-238 and Pu-239 cross sections, computed using ECCO and OpenMC with 33 and 295 energy group structures. The behaviour of the cross sections relative errors is the same as in the SFR case. As already observed in the three-group structure, the error in the U-238 capture cross section decreased in the homogeneous LFR fuel pin, due to the nuclide smearing. This can be visually appreciated by comparing the U-238 capture cross sections in Figure 5.2 and 5.9, which are calculated in the homogeneous SFR and LFR fuel pins, respectively.

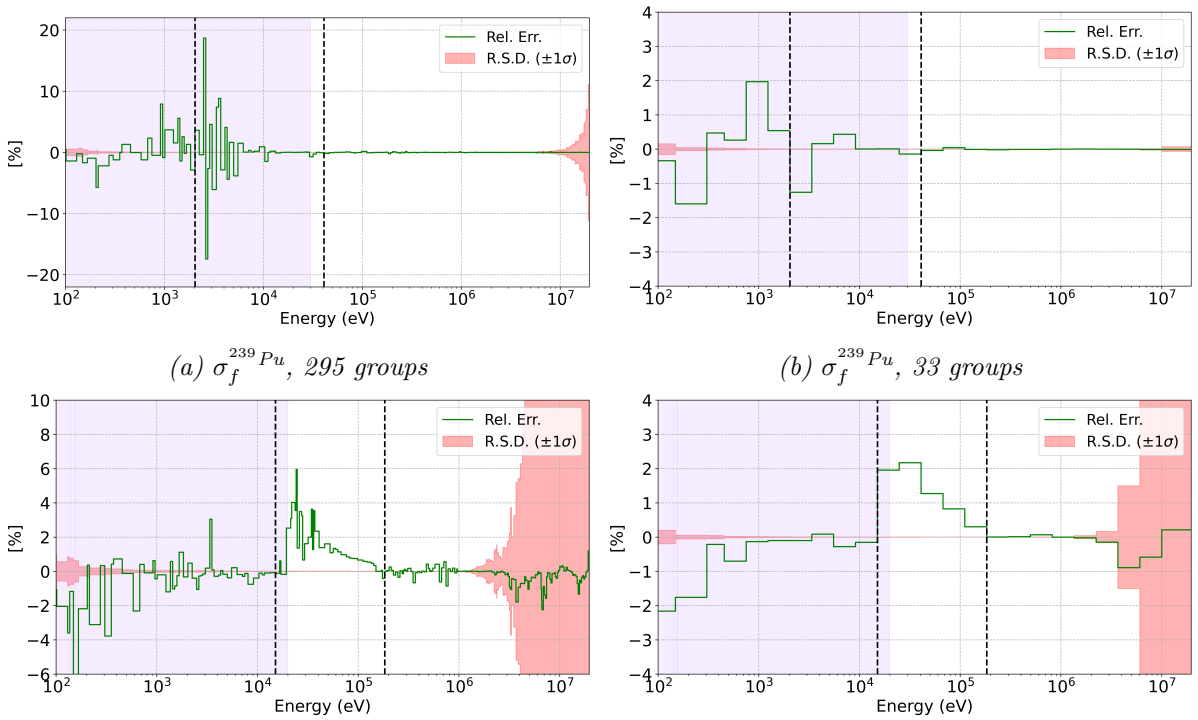


*(a)* $\sigma_f^{^{239}Pu}$*, 295 groups*

*(b)* $\sigma_f^{^{239}Pu}$*, 33 groups*

*(c)* $\sigma_c^{^{238}U}$*, 295 groups*

*(d)* $\sigma_c^{^{238}U}$*, 33 groups*

*Figure 5.9: LFR NEA benchmark, homogeneous fuel pin. The* $\sigma_c^{^{238}U}$ *and* $\sigma_f^{^{239}Pu}$ *are computed using ECCO and OpenMC with the ENDF/B-VIII.0 NDL. The comparison is made using the 33 and the 295 groups structures.*

#### 5.1.2.2 U-235, Pu-241 and O-16 cross sections

Figure 5.10 shows a comparison of the U-235, Pu-241, and O-16 cross sections. Although PTs lack for the former nuclide in the URR, the errors within this range are much smaller than those of U-238. There are two possible explanations for this effect. First, the resonances of U-235 are orders of magnitude lower than those of U-238. The second and most likely explanation is that the concentration of U-235 in the numerical benchmark fuel pin is extremely low. Consequently, the significant dilution of the nuclide in a mixture primarily composed of other isotopes makes it

incapable of determining significant energy dips in the neutron flux, and the classical approach used to prepare the cross sections in the NJOY code turns out to be sufficient to properly compute the energy-averaged cross sections. However, this suggests that using the same library in media with a higher concentration of U-235 would probably result in errors similar to the ones observed for U-238.

Once again, Pu-241 fission shows very similar results to the ones of Pu-239 fission: although the errors are large, they cancel each other out within the URR. Also, the excellent self-shielding performance of the ENDF/B-VIII.0 ECCOLIB for O-16 is observed, as the PTs produce negligible errors for the nuclide in both group structures.

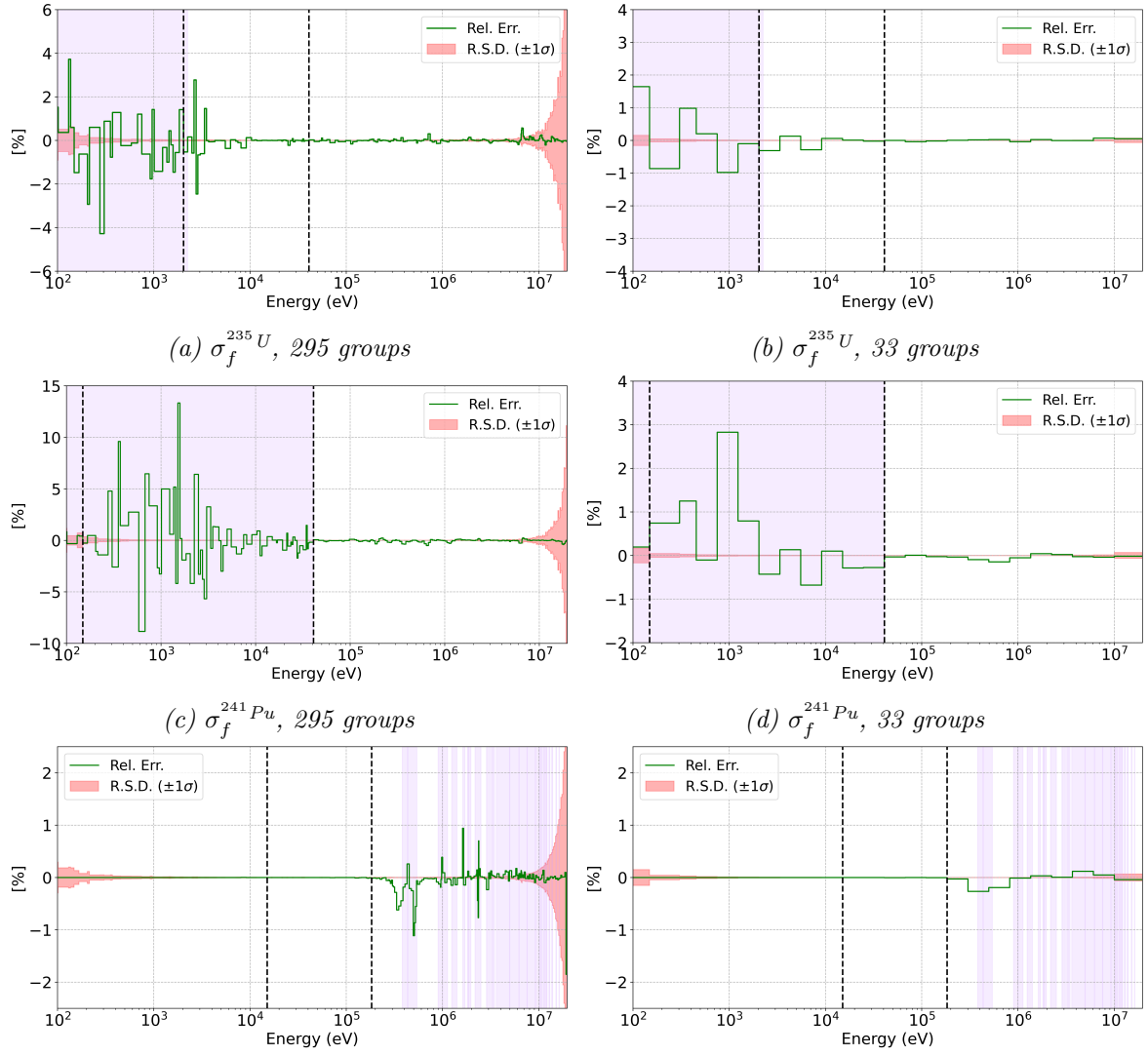


*(a)* $\sigma_f^{^{235}U}$*, 295 groups*

*(b)* $\sigma_f^{^{235}U}$*, 33 groups*

*(c)* $\sigma_f^{^{241}Pu}$*, 295 groups*

*(d)* $\sigma_f^{^{241}Pu}$*, 33 groups*

*(e)* $\sigma_{s,el}^{^{16}O}$*, 295 groups*

*(f)* $\sigma_{s,el}^{^{16}O}$*, 33 groups*

*Figure 5.10: LFR NEA benchmark, homogeneous fuel pin. The* $\sigma_f^{^{235}U}$*,* $\sigma_f^{^{241}Pu}$*, and* $\sigma_{s,el}^{^{16}O}$ *are computed using ECCO and OpenMC with the ENDF/B-VIII.0 NDL. The cross sections are condensed into the 33 and the 295 groups structures. For O-16, black vertical dashed lines indicate the URR energy bounds of U-238.*

#### 5.1.2.3 Fe-56 and lead isotopes cross sections

The analysis with the three group structure revealed significant differences between ECCO and OpenMC in the elastic scattering cross sections of Pb-208 and Fe-56 in the high-energy region. These cross sections are compared between ECCO and OpenMC in Figures 5.11 and 5.12. Looking at the relative error for Fe-56 in the 33 groups energy structure, it can be seen that this

increases in correspondence of the large cross section dip and at energy values larger than 0.85 MeV, where PTs are not present. In fact, as it can be seen in Figure 5.13, the energy-continuous cross section has several spikes in this region. These spikes are described by pointwise data in the MF = 3 file of the ENDF-6 tape, and no resonance parameters are given in this energy range. However, such abrupt variations in the cross sections could still provide self-shielding effects, affecting the accuracy of group-averaged cross sections.

The same also holds for Pb-208, but in this case the largest discrepancies between ECCO and OpenMC are found in the energy groups with PTs. Since all resonances are resolved for Pb-208, these errors cannot be attributed to discrepancies between the PURR module of NJOY and CALENDF. Eventually, all of these errors originate from the differences between the ENDF-6 tape manipulations performed by CALENDF and the RECONR module of NJOY.

The errors observed in the elastic scattering cross sections of Pb-208 are the highest among the ones that were examined. These errors are particularly relevant for LFR, where lead acts as a coolant, potentially leading to large impacts on neutronic calculations. For this reason, the other isotopes that make up most of the coolant, namely Pb-206 and Pb-207, have also been analysed. The errors in the elastic scattering cross sections, computed again by condensing the 1968 group structure into the 33 and 295 group structures, are shown in Figure 5.14. The figure displays large errors also in the cross sections of these two nuclides, especially for Pb-207, where the errors have the opposite sign to those of Pb-208.

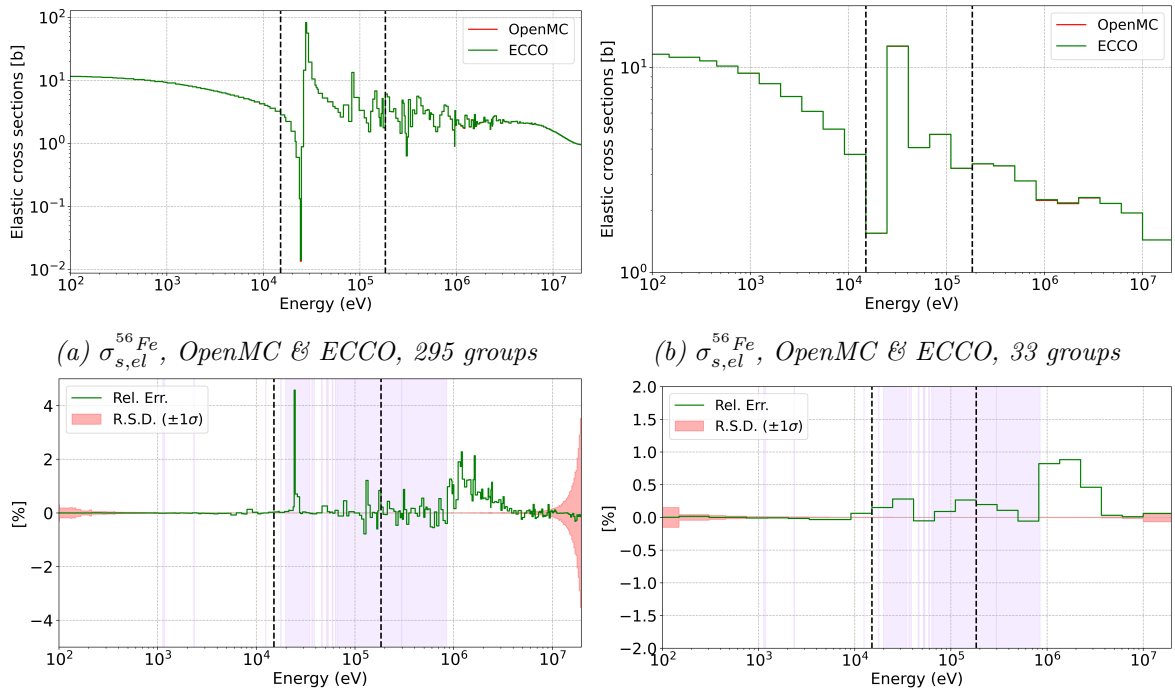


*(a) $\sigma_{s,el}^{^{56}Fe}$, OpenMC & ECCO, 295 groups*

*(b) $\sigma_{s,el}^{^{56}Fe}$, OpenMC & ECCO, 33 groups*

*(c) $\sigma_{s,el}^{^{56}Fe}$, relative error, 295 groups*

*(d) $\sigma_{s,el}^{^{56}Fe}$, relative error, 33 groups*

*Figure 5.11: LFR NEA benchmark, homogeneous fuel pin. The $\sigma_{s,el}^{^{56}Fe}$ is computed using ECCO and OpenMC with the ENDF/B-VIII.0 NDL. The cross sections are condensed into the 33 and the 295 groups structures. The black dashed lines represent the URR energy bounds of U-238.*

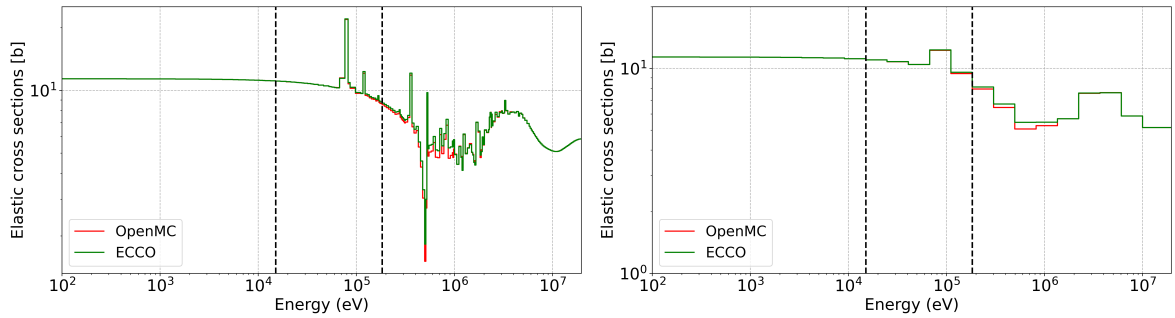


*(a)* $\sigma_{s,el}^{^{208}Pb}$*, OpenMC & ECCO, 295 groups*




*(b)* $\sigma_{s,el}^{^{208}Pb}$*, OpenMC & ECCO, 33 groups*

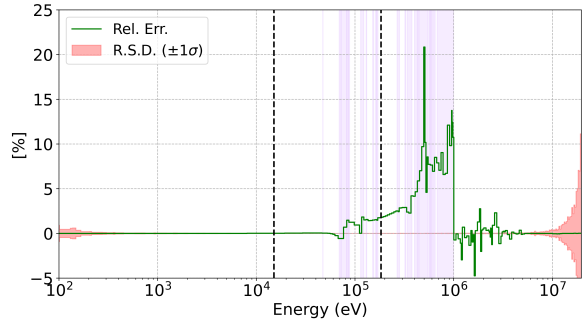


*(c)* $\sigma_{s,el}^{^{208}Pb}$*, relative error, 295 groups*

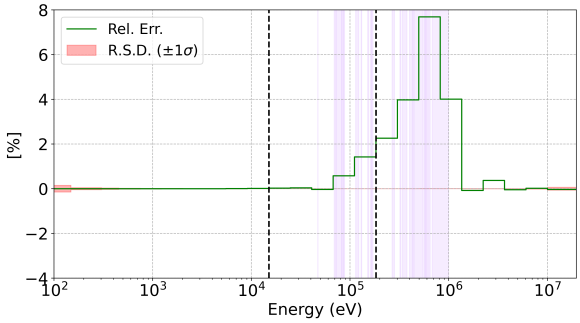


*(d)* $\sigma_{s,el}^{^{208}Pb}$*, relative error, 33 groups*

*Figure 5.12: LFR NEA benchmark, homogeneous fuel pin. The* $\sigma_{s,el}^{^{208}Pb}$ *is computed using ECCO and OpenMC with the ENDF/B-VIII.0 NDL. The cross sections are condensed into the 33 and the 295 groups structures. The black dashed lines represent the URR energy bounds of U-238.*

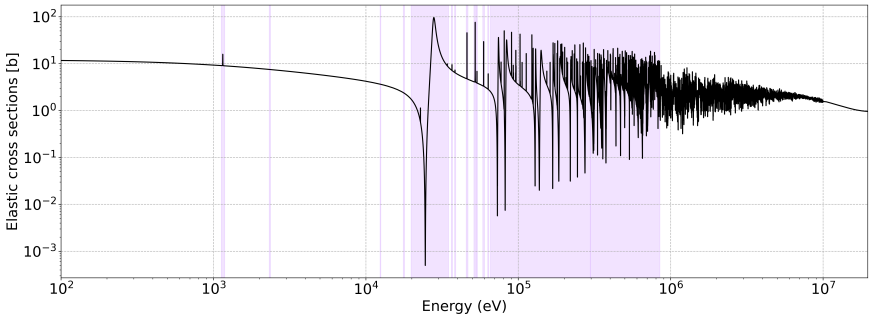


*(a)* $\sigma_{s,el}^{^{56}Fe}$*, OpenMC*

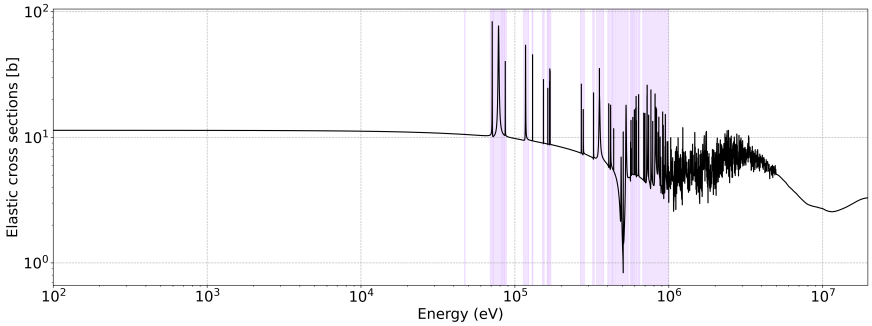


*(b)* $\sigma_{s,el}^{^{208}Pb}$*, OpenMC*

*Figure 5.13: The elastic scattering cross sections of Fe-56 and Pb-206 are plotted with OpenMC from the HDF5 tapes. The spikes at energies larger than 1 MeV are not properly resonances, thus they are not covered with PTs.*

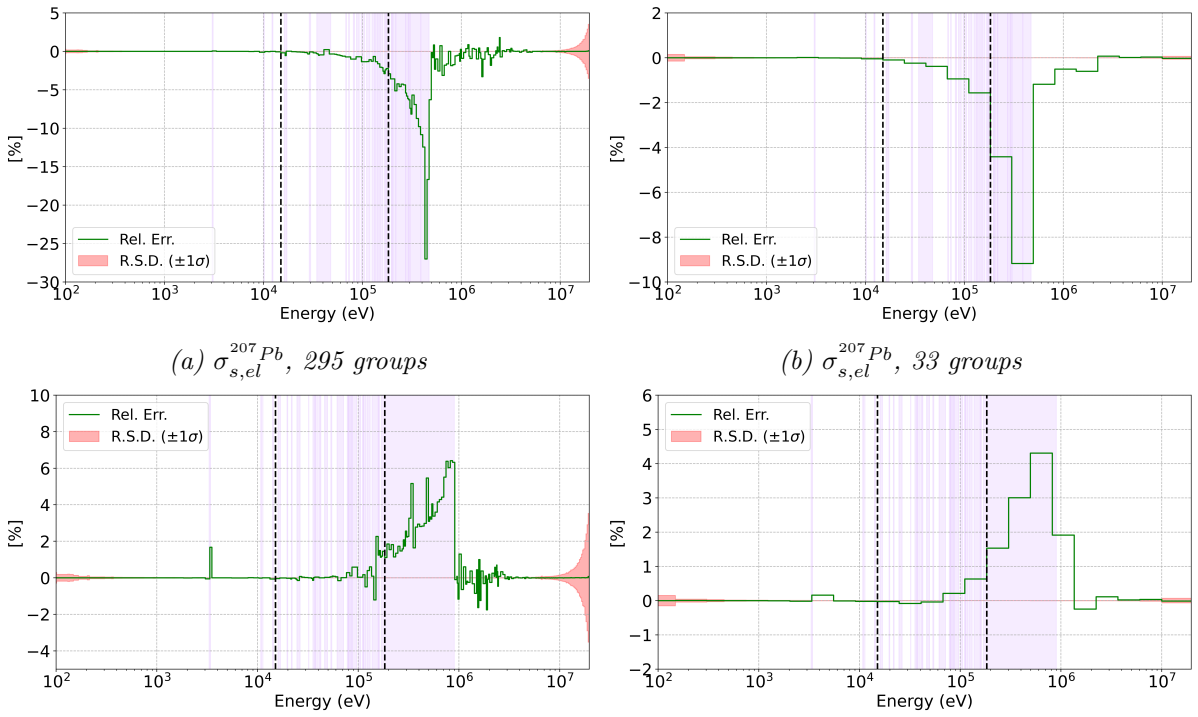


(a) $\sigma_{s,el}^{^{207}Pb}$, 295 groups

(b) $\sigma_{s,el}^{^{207}Pb}$, 33 groups

(c) $\sigma_{s,el}^{^{206}Pb}$, 295 groups

(d) $\sigma_{s,el}^{^{206}Pb}$, 33 groups

*Figure 5.14: LFR NEA benchmark, homogeneous fuel pin. The $\sigma_{s,el}^{^{207}Pb}$ and $\sigma_{s,el}^{^{206}Pb}$ are computed using ECCO and OpenMC with the ENDF/B-VIII.0 NDL. The cross sections are condensed into the 33 and the 295 groups structures. The black dashed lines represent the URR energy bounds of U-238.*

### 5.1.3 Probability tables for LFR pin nuclides

The analysis of the ENDF/B-VIII.0 ECCOLIB in the homogeneous, infinite LFR fuel pin revealed the absence of PTs data within the URR of U-238 and U-235. In order to obtain a complete overview of the library, the built-in procedure of ERANOS was employed again to determine the energy groups containing the PTs for all of the NEA benchmark fuel pin nuclides with an unresolved range contained within the 1968 ECCOLIB. As a reference, these groups have been compared with those of the same nuclides in the JEFF-3.1 ECCOLIB. The results of this comparison are shown in Figure 5.15 for the groups within the URR of each nuclide. The lack of PTs data in the thermal region would be of lower concern for LFR applications.

The figure highlights the absence of PT data for U-238 and U-235 once again. Moreover, the absence of the data for Zr-91 can be seen, even though this is of less concern given that this isotope is present in only small quantities in the LFR benchmark fuel pin. Furthermore, it can be seen that in the ENDF/B-VIII.0 ECCO library some nuclides have PTs that are otherwise lacking in the JEFF-3.1 ECCOLIB. Among them, PTs are present for nuclides such as U-236 and Am-243, which are potentially relevant isotopes for fuel evolution calculations.

In conclusion, in light of the above results, it is possible to say that the lack of PTs within the ENDF/B-VIII.0 ECCOLIB is only a concern for U-238 and U-235, and it does not occur for any other relevant isotopes. However, limiting the analysis to missing data only, particularly in the unresolved range, does not rule out eventual errors arising from the handling of the ENDF-6 data during the PTs generation, as it was observed for lead isotopes.

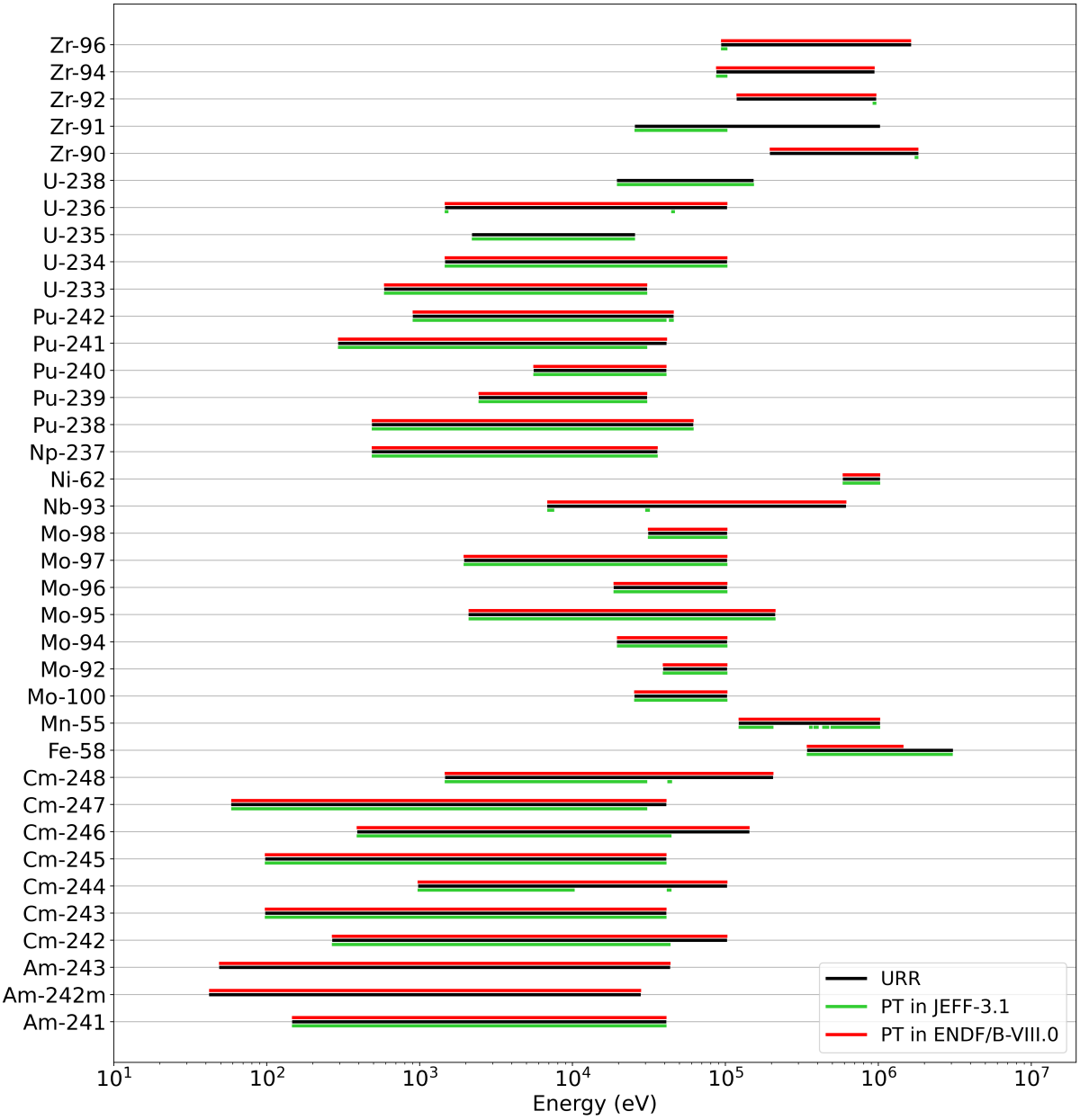


*Figure 5.15: For the nuclides of the NEA LFR fuel pin which have an unresolved range and are present in the 1968 ENDF/B-VIII.0 ECCOLIB, the energy groups containing PT data in the URR are compared with the corresponding groups in the JEFF-3.1 ECCOLIB.*

### 5.1.4 ENDF/B-VIII.0 comparison with JEFF-3.1

The comparison of the PTs for several nuclides revealed the crucial importance of the handling of raw nuclear data contained in ENDF-6 tapes. In fact, producing the ECCOLIB is a very delicate procedure, and the final results can easily be influenced by either the evaluator's choices or the raw data themselves. In Chapter 7, the influence that the settings adopted in the ECCOLIB production workflow have on the errors observed in the lead isotopes will be discussed.

To conclude the analysis of the homogeneous LFR fuel pin, the relative errors obtained using NDLs based on ENDF/B-VIII.0 in both ECCO and OpenMC were compared with those obtained when using NDLs based on JEFF-3.1 in both codes. Figure 5.16 shows the results of a comparison for six nuclides using a 33 group structure. Focusing on U-238, it is evident the reduction in the cross section errors within the URR when using the JEFF-3.1 NDL. This decrease of the error was also observed in the SFR fuel pin case, which was simulated using

both libraries to assess the impact of the absence of PTs in the ENDF/B-VIII.0 ECCOLIB (see Figure 5.6). Similarly, the difference in the relative errors of the LFR fuel pin when using the JEFF-3.1 and the ENDF/B-VIII.0 NDLs is due to the latter library's lack of PTs data.

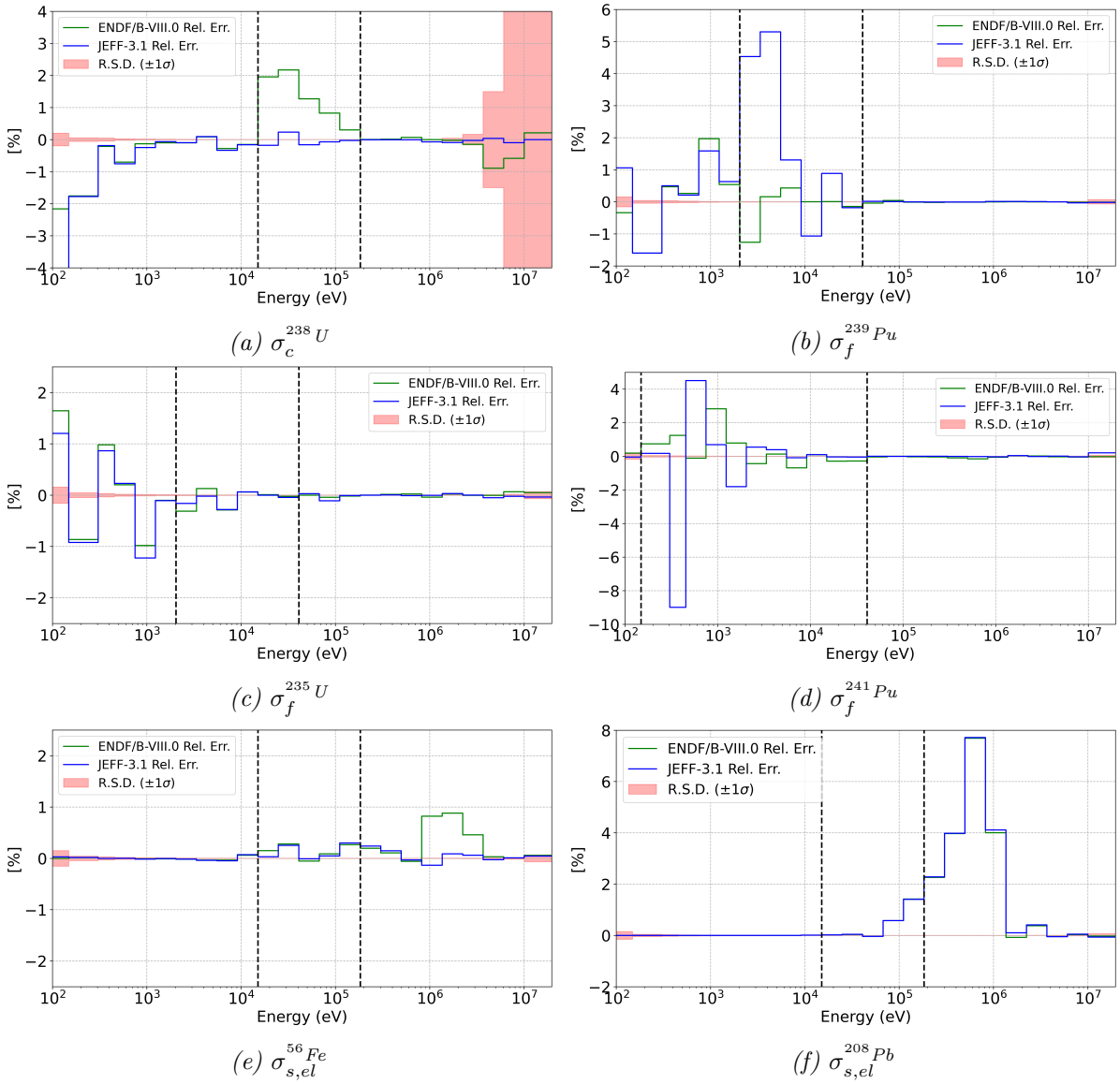


(a) $\sigma_c^{^{238}U}$ (b) $\sigma_f^{^{239}Pu}$

(c) $\sigma_f^{^{235}U}$ (d) $\sigma_f^{^{241}Pu}$

(e) $\sigma_{s,el}^{^{56}Fe}$ (f) $\sigma_{s,el}^{^{208}Pb}$

*Figure 5.16: LFR NEA benchmark, homogeneous fuel pin. Comparison, with the 33 group structure, of the relative errors (ECCO vs. OpenMC) evaluated using ENDF/B-VIII.0 and JEFF-3.1 NDL for both codes. For brevity, only the R.S.D. of the ENDF/B-VIII.0 simulations are reported for reference. For each nuclide, the black dashed lines separate the three energy regions, according to ENDF/B-VIII.0. For Fe-56 and Pb-208, the URR energy bounds are those of U-238.*

Moreover, it can be seen that, in the case of JEFF-3.1, the errors in the fission cross section of the plutonium isotopes are slightly higher in the unresolved ranges. A similar trend for Pu-239 was observed in Section 5.1.1.1 during the reproduction of the Jacquet's TRIPOLI-4® results with OpenMC. These discrepancies may, in fact, be caused by differences in data handling within the URR between CALENDF and the PURR module of NJOY. Additionally, the JEFF-3.1 ECCOLIB provides a better treatment, for Fe-56, of the energy intervals where cross sections spikes are present, as described in Figure 5.13, and PTs are not included in the ENDF/B-VIII.0 ECCOLIB. It is fundamental to note that the errors in the elastic cross section of Pb-208 are almost identical in the two libraries. In fact, when the raw data on the ENDF-6 tapes are compared, the evaluations of this nuclide are in very good agreement. This suggests

that if consistency is maintained between the two ECCOLIB production workflows, the issue that affects the handling of the JEFF-3.1 data will also persist in the case of ENDF/B-VIII.0. As mentioned above, in Chapter 7 a deeper investigation on this topic will be conducted.

## 5.2 Validation of the self-shielding module in the heterogeneous medium

The analysis performed in the previous section revealed that the observed errors in the cross sections are primarily due to the nuclear data contained in the ECCOLIB rather than to the numerical schemes and approximations employed in the ECCO cell code. However, as outlined in Chapter 2, the computation of the cross sections differs between homogeneous and heterogeneous media when using the subgroup method. Additionally, the flux solution is different too, with the fundamental mode method and the collision probability method, respectively.

To exclude that the errors in the cross sections are influenced by the deterministic models, a simulation of a heterogeneous medium was performed. As described in Chapter 2, the computation of cross sections in the heterogeneous medium makes use of both collision probabilities and subgroup data. Once again, to reduce the numerical errors that arise from the numerical schemes, only two calculation steps are performed within ECCO. These steps are reported in Listing 5.2. The main differences with respect to the homogeneous medium are the geometry and flux-solution input data. The remaining input data set remains unchanged from the homogeneous case. Once again, the two-step resolution does not involve the spatial homogenisation of the cross sections across the entire geometry.

```
->STEP_1_FUEL_IN
     GEOMETRY ORIGINAL
     ELEMENTS ALL
     GROUP STRUCTURE OTHER 172
     INPUT LIBRARY 'ECCOLIB_ENDFB_80.172'
     FLUX SOLUTION CP P1 CONSISTENT ORDER 1 ! Flux solution collision
    probability
     BUCKLING 0.0
     SELF SHIELDING NODBBSH; ! DBBSH option, used for CP in subcritical media,
    is not used
->STEP_2_FUEL
     GEOMETRY ORIGINAL
     GROUP STRUCTURE FINE ! 1968 group structure
     INPUT LIBRARY 'ECCOLIB_ENDFB_80.1968'
     FIND_ELEMENTS_IN_LIST  ! Apply self-shielding to elements in list
        'U238' ... 'Pb208' ! Isotopes on the 1968 ENDF/B-VIII.0 ECCOLIB
     FLUX SOLUTION CP P1 CONSISTENT ORDER 1
     SELF SHIELDING NODBBSH
     BFROM 1
     CONDENSE 33 ! Condense 1968 XS into 33 group structure
        1 82 142 202 262 322 382 442 502 564        !boundaries of 33 groups
        624 686 746 808 868 928 988 1048 1108 1168  !in the 1968 structure
        1228 1288 1336 1422 1480 1516 1579 1648 1708 1768
        1837 1919 1952 ;
     PRINT DATA FLUXES CROSS SECTIONS MICROSCOPIC VECTORS ;
```

*Listing 5.2: Two steps calculation implemented in ECCO for the evaluation of ENDF/B-VIII.0 self-shielding performances in a heterogeneous medium. In this case, collision probabilities are implied for both the computation of the cross sections and the flux-solution. The buckling is set equal to zero to simulate an infinite medium.*

### 5.2.1 Analysis of the LFR heterogeneous fuel pin

The analysis of the heterogeneous medium was conducted again on the LFR fuel pin. This time, however, the three different regions - the MOX fuel, the cladding, and the coolant - were

distinguished and described separately in the ECCO code. These regions and their geometrical arrangement are described in Figure 5.17. As it can be seen in the figure, the hexagonal fuel pin was converted to an equivalent cylindrical shape. The equivalence was achieved by conserving the volumes of the three regions for two main reasons: first, this eliminates the vacuum space in the fuel pin, which is smeared with the fuel pellet, adjusting its density accordingly, to avoid issues with the code; second, it avoids the numerical error associated with the collision probabilities. In fact, using a cylindrical geometry allows to use CPs that are computed analytically, thus increasing the numerical accuracy. This approach is equivalent to that adopted by P. Jacquet for the validation of ECCO in heterogeneous SFR fuel pins [9].

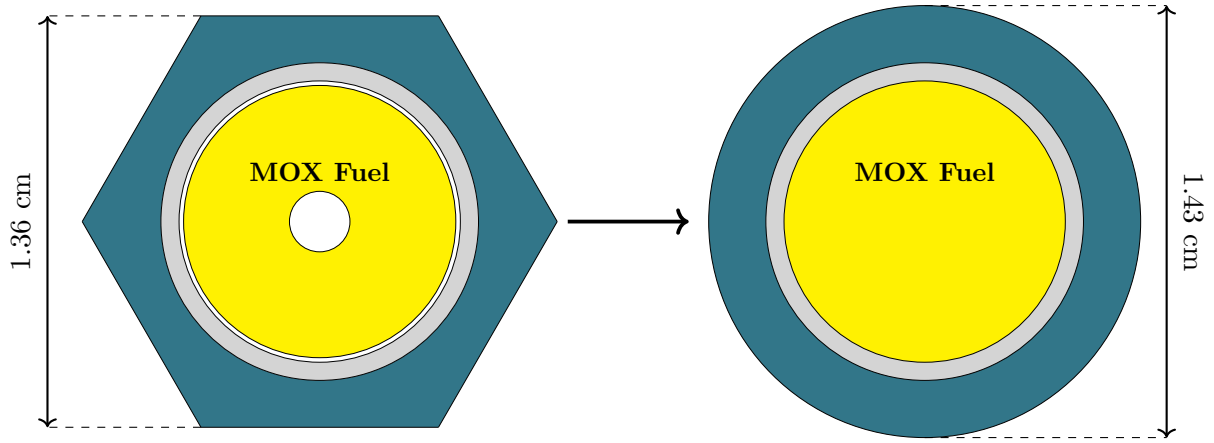


*Figure 5.17: The heterogeneous LFR fuel pin cell is reshaped into a cylindrical cell, conserving the volumes of the MOX fuel (yellow), cladding (grey), and coolant (blue) regions, and removing the void region. The geometrical configuration is described according to the NEA benchmark [12].*

For simplicity, the temperature was set equal to 293 K for the three regions, and the material dilatations were not considered. To simulate an infinite cell, white boundary conditions were set on the outer edge of the coolant region. The same materials and geometry were modelled within OpenMC, and the results of a comparison for the infinite multiplication factor are shown in Table 5.9 and compared with the ECCO result. The discrepancy observed between the two simulations is approximately of the same magnitude as that observed for the homogeneous medium. Once again, this difference is consistent with results found in Ref. [11].

| $k_\infty$ **Heterogeneous LFR fuel pin** | | |
|---|---|---|
| **OpenMC** | **ECCO** | **Abs. Diff. [pcm]** |
| 1.36799(1) | 1.36503 | -296 |

*Table 5.9: LFR NEA benchmark, heterogeneous fuel pin. The infinite multiplication factor is computed using OpenMC and ECCO with the ENDF/B-VIII.0 NDL. The standard deviation of the Monte Carlo reference values is reported in parenthesis (in pcm).*

Table 5.10 shows a comparison, between OpenMC and ECCO, of the cross sections of the most important nuclides , condensed in the three and one group structures. In both codes, cross sections were condensed using the flux of the region containing the specific isotope. Therefore, cross sections are not homogenised over the entire fuel pin, but rather in the three materials composing the fuel pin, namely the MOX fuel, cladding, and coolant (e.g. the U-238 capture cross section is homogenised in the MOX material). Once again, significant errors can be observed for the cross sections of U-238 in the URR, and the cross section of Pb-208 at high-energies, analogously to what observed in the homogeneous cell. This is further highlighted in Table 5.11, where the relative errors in the cross sections are compared between the homogeneous and heterogeneous media.

| Heterogeneous infinite LFR fuel pin | | | | | | | | | |
|---|---|---|---|---|---|---|---|---|---|
| | | | $\sigma^{239\text{Pu}}_{f-MOX}$ | $\sigma^{238\text{U}}_{c-MOX}$ | $\sigma^{235\text{U}}_{f-MOX}$ | $\sigma^{241\text{Pu}}_{f-MOX}$ | $\sigma^{56\text{Fe}}_{s,el-CLAD}$ | $\sigma^{208\text{Pb}}_{s,el-COOL}$ | $\sigma^{16\text{O}}_{s,el-MOX}$ |
| CONTINUUM | OpenMC | [b] | 1.5950 | 0.1027 | 1.3822 | 1.8551 | 2.8910 | **6.3197** | 3.6238 |
| | ECCO | [b] | 1.5948 | 0.1028 | 1.3819 | 1.8541 | 2.8984 | **6.5449** | 3.6216 |
| | Rel. Err. | [%] | -0.010 | 0.063 | -0.022 | -0.054 | 0.256 | **3.563** | -0.061 |
| | R.S.D. | [%] | 0.001 | 0.004 | 0.001 | 0.001 | 0.002 | **0.002** | 0.002 |
| URR | OpenMC | [b] | 1.9205 | **0.2802** | 2.8293 | 4.0279 | 4.9994 | 10.7206 | 3.6336 |
| | ECCO | [b] | 1.9193 | **0.2845** | 2.8295 | 4.0301 | 5.0069 | 10.7726 | 3.6335 |
| | Rel. Err. | [%] | -0.058 | **1.523** | 0.007 | 0.054 | 0.151 | 0.485 | -0.004 |
| | R.S.D. | [%] | 0.003 | **0.002** | 0.003 | 0.004 | 0.002 | 0.002 | 0.002 |
| RRR | OpenMC | [b] | 5.1577 | 0.7267 | 8.3596 | 27.2733 | 5.5208 | 11.2416 | 3.7781 |
| | ECCO | [b] | 5.2003 | 0.7254 | 8.3402 | 27.5450 | 5.5193 | 11.2421 | 3.7781 |
| | Rel. Err. | [%] | 0.827 | -0.183 | -0.232 | 0.996 | -0.027 | 0.005 | <0.001 |
| | R.S.D. | [%] | 0.011 | 0.005 | 0.011 | 0.120 | 0.005 | 0.005 | 0.004 |
| Total energy range | OpenMC | [b] | 1.7344 | 0.2621 | 1.8533 | 2.4237 | 4.1661 | 8.9068 | 3.6481 |
| | ECCO | [b] | 1.7344 | 0.2637 | 1.8517 | 2.4224 | 4.1705 | 9.0226 | 3.6471 |
| | Rel. Err. | [%] | 0.001 | 0.594 | -0.082 | -0.052 | 0.106 | 1.299 | -0.028 |
| | R.S.D. | [%] | 0.002 | 0.002 | 0.002 | 0.004 | 0.002 | 0.002 | 0.002 |

*Table 5.10: LFR NEA benchmark, heterogeneous fuel pin. The cross sections of the most important nuclides are computed using OpenMC and ECCO with the ENDF/B-VIII.0 NDL. These have been then condensed into the three and one group structures. For each nuclide, the cross section is computed with both codes in the same region (MOX, cladding, and coolant) where the isotope is located. For convention, the cross sections of Pb-208, Fe-56, and O-16 have been condensed in the same energy bound of U-238*

| Heterogeneous & homogeneous, infinite LFR fuel pins | | | | | | | | | | |
|---|---|---|---|---|---|---|---|---|---|---|
| $k_\infty$ | Abs. Diff. | [pcm] | Homogeneous | -280 | | | | | | |
| | | | Heterogeneous | -296 | | | | | | |
| | | | | $\sigma_f^{239\text{Pu}}$ | $\sigma_c^{238\text{U}}$ | $\sigma_f^{235\text{U}}$ | $\sigma_f^{241\text{Pu}}$ | $\sigma_s^{56\text{Fe}}$ | $\sigma_s^{208\text{Pb}}$ | $\sigma_s^{16\text{O}}$ |
| CONTINUUM | Rel. Err. | [%] | Homogeneous | -0.011 | 0.063 | -0.021 | -0.053 | 0.251 | **3.553** | -0.060 |
| | | | Heterogeneous | -0.010 | 0.063 | -0.022 | -0.054 | 0.256 | **3.563** | -0.061 |
| URR | Rel. Err. | [%] | Homogeneous | -0.059 | **1.392** | -0.001 | 0.048 | 0.152 | 0.488 | -0.004 |
| | | | Heterogeneous | -0.058 | **1.523** | 0.007 | 0.054 | 0.151 | 0.485 | -0.004 |
| RRR | Rel. Err. | [%] | Homogeneous | 0.874 | -0.145 | -0.197 | 1.120 | 0.009 | 0.005 | < 0.001 |
| | | | Heterogeneous | 0.827 | -0.183 | -0.232 | 0.996 | -0.027 | 0.005 | <0.001 |
| Total energy range | Rel. Err. | [%] | Homogeneous | 0.004 | 0.547 | -0.074 | -0.051 | 0.121 | 1.309 | -0.028 |
| | | | Heterogeneous | 0.001 | 0.594 | -0.082 | -0.052 | 0.106 | 1.299 | -0.028 |

*Table 5.11: The relative errors (ECCO vs. OpenMC) in the cross section of the seven most relevant nuclides are calculated using the ENDF/B-VIII.0 NDL, and compared between the homogeneous and heterogeneous LFR fuel pins.*

As the errors are similar in both cases, it can be concluded that the discrepancies of the cross sections with respect to the MC references are poorly influenced by the ECCO solution schemes. At the same time, their dependence on the nuclear data themselves is once again confirmed. The same holds for finer group structures, as it can be seen in Figure 5.18 where the relative errors for U-238 and Pb-208 in the heterogeneous case are shown. In this case, they exhibit the same energy profile as that of the homogeneous medium, as visible in Figures 5.9 and 5.12.

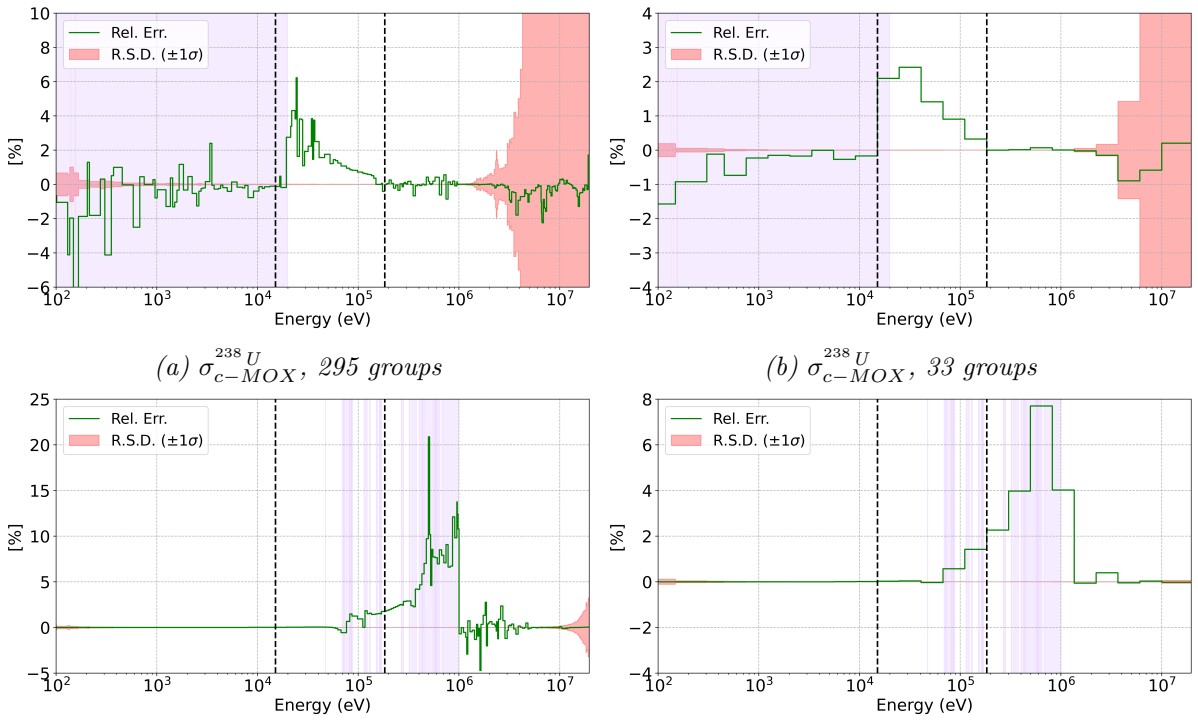


(a) $\sigma^{^{238}U}_{c-MOX}$, *295 groups*

(b) $\sigma^{^{238}U}_{c-MOX}$, *33 groups*

(c) $\sigma^{^{208}Pb}_{s,el-COOL}$, *295 groups*

(d) $\sigma^{^{208}Pb}_{s,el-COOL}$, *33 groups*

*Figure 5.18: LFR NEA benchmark, heterogeneous fuel pin. Relative errors in the* $\sigma^{^{238}U}_{c-MOX}$ *and* $\sigma^{^{208}Pb}_{s,el-COOL}$ *are computed using ECCO and OpenMC with the ENDF/B-VIII.0 NDL. The comparison is made with the 33 and the 295 group structures. The black dashed lines represent the URR energy bounds of U-238.*

## 5.3 Validation of the self-shielding module in the LFR fuel assembly

In the previous sections, the homogeneous and heterogeneous LFR fuel pins were analysed, highlighting the significant influence of the raw ENDF-6 data treatment, during the ECCOLIB generation, on the final accuracy of the ECCO code. However, this analysis was conducted with the precise aim of isolating as much as possible the numerical errors arising from the numerical schemes implemented in ECCO. Therefore, the physical conditions set during the pin modelling (e.g., the room temperature) differ greatly from the actual LFR operating conditions. Moreover, adopting a two-step approach inside ECCO is different from the "reference" route, which is the usual routine applied for the preparation of homogenised and condensed cross sections for successive core calculations.

Therefore, in this section, the self-shielding performances of the ENDF/B-VIII.0 ECCO library are assessed within a framework that more closely resembles actual standard procedures used in typical core design calculations. Consequently, production of the condensed and homogenised cross sections will be replicated, under operating conditions, on a lattice level within a fuel assembly. As mentioned in Chapter 2, these would be the cross sections used in successive calculations in the classical two-step approach. However, in order to assess the numerical accuracy of the procedure, a slightly modified "reference route" will be adopted, as shown in Listing 5.3.

As the validation regards a lattice calculation, the only deviation from the reference route is that the buckling is set equal to zero, thus simulating an infinite lattice of fuel assemblies. This enabled ECCO simulation to be replicated exactly in OpenMC by applying reflective boundary conditions to the outer edge of the assembly.

```
->STEP_1_FUEL
    GEOMETRY HOMOGENEOUS
    ELEMENTS ALL
    GROUP STRUCTURE OTHER 172
    INPUT LIBRARY 'ECCOLIB_ENDFB_80.172'
    FLUX SOLUTION FM P1 INCONSISTENT ORDER 1
    BUCKLING 0.0 ;
->STEP_2_FUEL
     GEOMETRY ORIGINAL
     GROUP STRUCTURE OTHER 172
     INPUT LIBRARY 'ECCOLIB_ENDFB_80.172'
     FLUX SOLUTION CP P1 INCONSISTENT ORDER 1
     BFROM 1
     SELF SHIELDING NODBBSH ! DBBSH option, used for CP in subcritical media, is
    not used
     PROFILE COLLISION PROBABILITIES ROTH 6 ; ! Apply Roth method with hexagonal
    lattice
->STEP_3_FUEL
      GEOMETRY ORIGINAL
      GROUP STRUCTURE FINE
      INPUT LIBRARY 'ECCOLIB_ENDFB_80.1968'
     FIND_ELEMENTS_IN_LIST  ! Apply self-shielding to elements in list
        'U238' ... 'Pb208' ! Isotopes on the 1968 ENDF/B-VIII.0 ECCOLIB
      FLUX SOLUTION CP P1 INCONSISTENT ORDER 1
      BFROM 1
      SELF SHIELDING NODBBSH
      PROFILE COLLISION PROBABILITIES ROTH 6
      CONDENSE 33 ! Condense 1968 XS into 33 group structure
        1 82 142 202 262 322 382 442 502 564        !boundaries of 33 groups
        624 686 746 808 868 928 988 1048 1108 1168  !in the 1968 structure
        1228 1288 1336 1422 1480 1516 1579 1648 1708 1768
        1837 1919 1952 ;
->STEP_4_FUEL
     GEOMETRY ORIGINAL
     GROUP STRUCTURE OTHER 33
     FLUX SOLUTION CP P1 INCONSISTENT ORDER 1
     SELF SHIELDING NODBBSH
     PROFILE COLLISION PROBABILITIES ROTH 6
     BUCKLING 0.0  ;
-> STEP_5_FUEL
      HOMOGENISE  ! Homogenise cross sections
      GEOMETRY HOMOGENEOUS
      GROUP STRUCTURE OTHER 33
      FLUX SOLUTION FM P1 INCONSISTENT ORDER 1
      BFROM 4
      PRINT DATA FLUXES CROSS SECTIONS MICROSCOPIC VECTORS ;
```

*Listing 5.3: The usual "reference route" adopted in ECCO is slightly revised by applying the buckling equal to zero in each step. This guarantees coherence when the infinite fuel assembly simulation is replicated in OpenMC. The flux-solution model adopted in the hexagonal geometry is the collisional probability using the Roth method.*

The analysis was performed on the internal fuel assembly of the LFR core, which is shown in Figure 5.19. As for the heterogeneous fuel pin, since the vacuum regions are generally not modelled in ECCO, the gap space was smeared with the fuel pellet, and the density of the MOX material was corrected to conserve the fuel mass. The same approach was taken for the internal channel, by modelling an entire fuel pin made of steel material with a reduced density. In OpenMC, instead, the original geometry was preserved, and the void gaps in the central channel and fuel pins are modelled. This time, as the aim was to model a scenario that resembles realistic operating conditions, the fuel temperature was set at 1200 K while the cladding and coolant temperatures were set at 600 K, according to the numerical benchmark specifications [12]. It is expected that these settings have a significant impact on the cross sections, due to Doppler

broadening of the resonances. However, the thermal expansions of the materials were neglected according with the benchmark specifications.

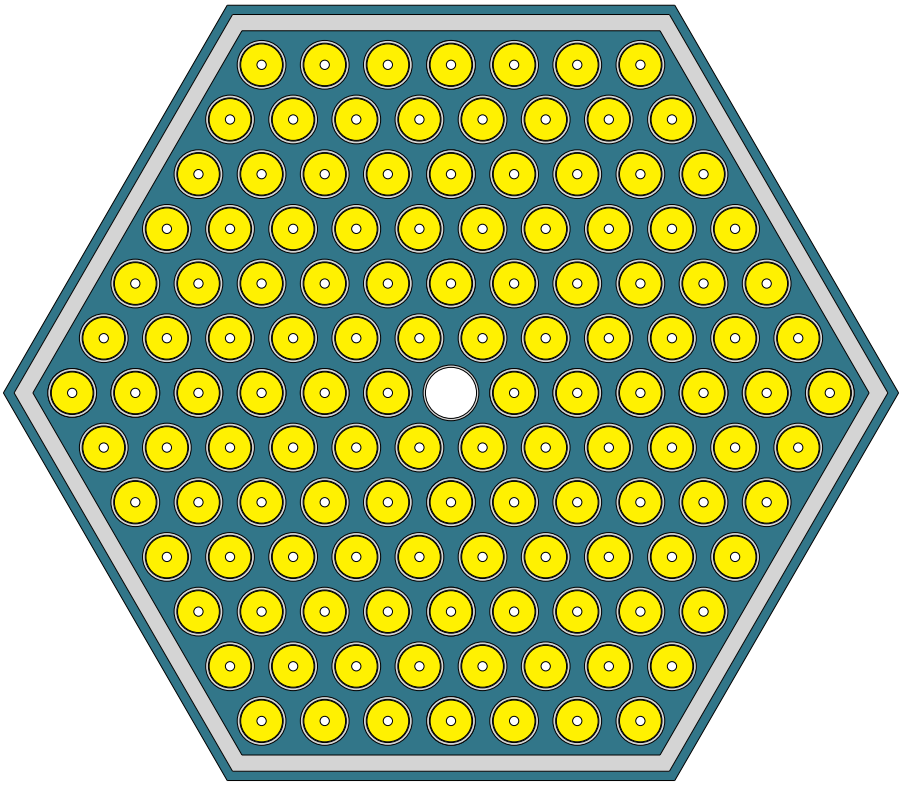

*Figure 5.19: Sketch of the NEA LFR benchmark inner fuel assembly. Three materials are distinguished: the MOX fuel (yellow), the fuel pin and external wrapper steel (grey) and the coolant (blue). The geometrical configuration is described according to the NEA benchmark [12].*

Table 5.12 shows a comparison of the infinite multiplication factor between ECCO and OpenMC. Although it decreased, the difference between the two values remains similar to that observed for the LFR fuel pin. Also for this geometry, the results are consistent with those in Ref. [11].

| **$k_\infty$ LFR internal fuel assembly** | | |
|---|---|---|
| **OpenMC** | **ECCO** | **Abs. Diff. [pcm]** |
| 1.28690(1) | 1.28463 | -227 |

*Table 5.12: LFR NEA benchmark, heterogeneous fuel assembly. Infinite multiplication factor computed using OpenMC and ECCO with the ENDF/B-VIII.0 NDL. The standard deviation of the Monte Carlo reference value is reported in parenthesis (in pcm).*

Within the standard usage of ECCO, it is common practice to compute homogenised and condensed cross sections, by using the 33 group structures, on a lattice level, for the successive core calculations within ERANOS. Therefore, the homogenised microscopic cross sections produced by ECCO were compared with those computed in OpenMC using the same group structure. Microscopic cross section homogenisation, for a nuclide $n$ located in a cell with volume $V_n$, is performed by weighting the macroscopic cross sections across the entire domain and

then dividing by the expanded nuclide density throughout the whole region, i.e.

$$\overline{\sigma}_{n,x,g} = \frac{V_n}{N_n V_{tot}} \frac{\int dV \; \Sigma_{n,x,g}(\overline{r}) \; \Phi_g(\overline{r})}{\int dV \; \Phi_g(\overline{r})} \approx \frac{V_n}{N_n V_{tot}} \frac{\sum_{r=1}^{R} \Sigma_{x,g,r} \; \Phi_{g,r} \; V_r}{\sum_{r=1}^{R} \Phi_{g,r} \; V_r}, \tag{5.2}$$

where $x$ stands for the partial reaction, $g$ is the energy group, $V_{tot}$ is the volume of the entire domain, $N_n$ is the nuclide density in the cell, and $r$ is any of the $R$ regions in which the domain is subdivided within ECCO. The latter determines the ECCO approximation in the above equation. In OpenMC, instead, the homogenised microscopic cross sections are evaluated by numerical integration, computing the reaction rates and fluxes across the entire domain (without applying any spatial filter). This avoids incurring in spatial approximations.

Figure 5.20 shows a comparison of the condensed and homogenised cross sections between OpenMC and ECCO for the six most important nuclides. Unlike in the previous cases, the relative errors change in both sign and magnitude in the thermal region. This could be a possible result of the use of CPs, which introduce an additional source of error. In fact, these are calculated applying the Roth X 6 model which represents an additional approximation with respect to the fuel pin case where the CPs computation is analytical. Moreover, the geometry modelled in ECCO is approximated with respect to OpenMC.

Notably, it is possible to see that significant errors are still evident for U-238 and Pb-208 in the same energy interval as before. However, it can be seen that the magnitude of the error in the capture cross section of the former nuclide has decreased significantly. This can be expected as a result of the change in the operating conditions, i.e. the effect of the temperature on the cross sections, which could partially reduce self-shielding effects, mitigating the consequences of the lack of PTs. For Pb-208, however, the magnitude of the errors has not decreased significantly. This suggests that the PT generation could be affected by a systematic issue that persists at different temperatures.

In conclusion, the analysis of the LFR fuel assembly revealed that the errors in the cross section result from two independent sources: discrepancies arising from incongruences in the self-shielding treatment between ECCO and OpenMC, and errors originating from CPs and geometry approximations. As discussed in the previous sections, the former are related to differences in the NDLs of the deterministic and Monte Carlo codes. These provide the predominant contribution to the error observed in the high-energy regions (typically the URR and continuum) in the homogenised and condensed cross sections of the fuel assemblies. The error trends are consistent with those observed for the LFR fuel pin, and eventually they decrease in magnitude due to a change in operating conditions, as in the case of U-238.

In the RRR, however, significant errors that did not appear in the previous analysis of the fuel pin are evident. This could be attributed to the CPs model having a predominant effect over the self-shielding model, although the two contributions are not clearly distinguishable. Furthermore, these errors are of less concern due to the limited interest in the low-energy region for LFR applications. Nevertheless, the analysis could be extended in future by assessing the individual contributions of the two error sources in the ECCO code, by numerically validating the ECCO CPs model in addition to the self-shielding model, isolating both from discrepancies arising from the NDLs. This would enable the simultaneous impact of the two error sources to be determined.

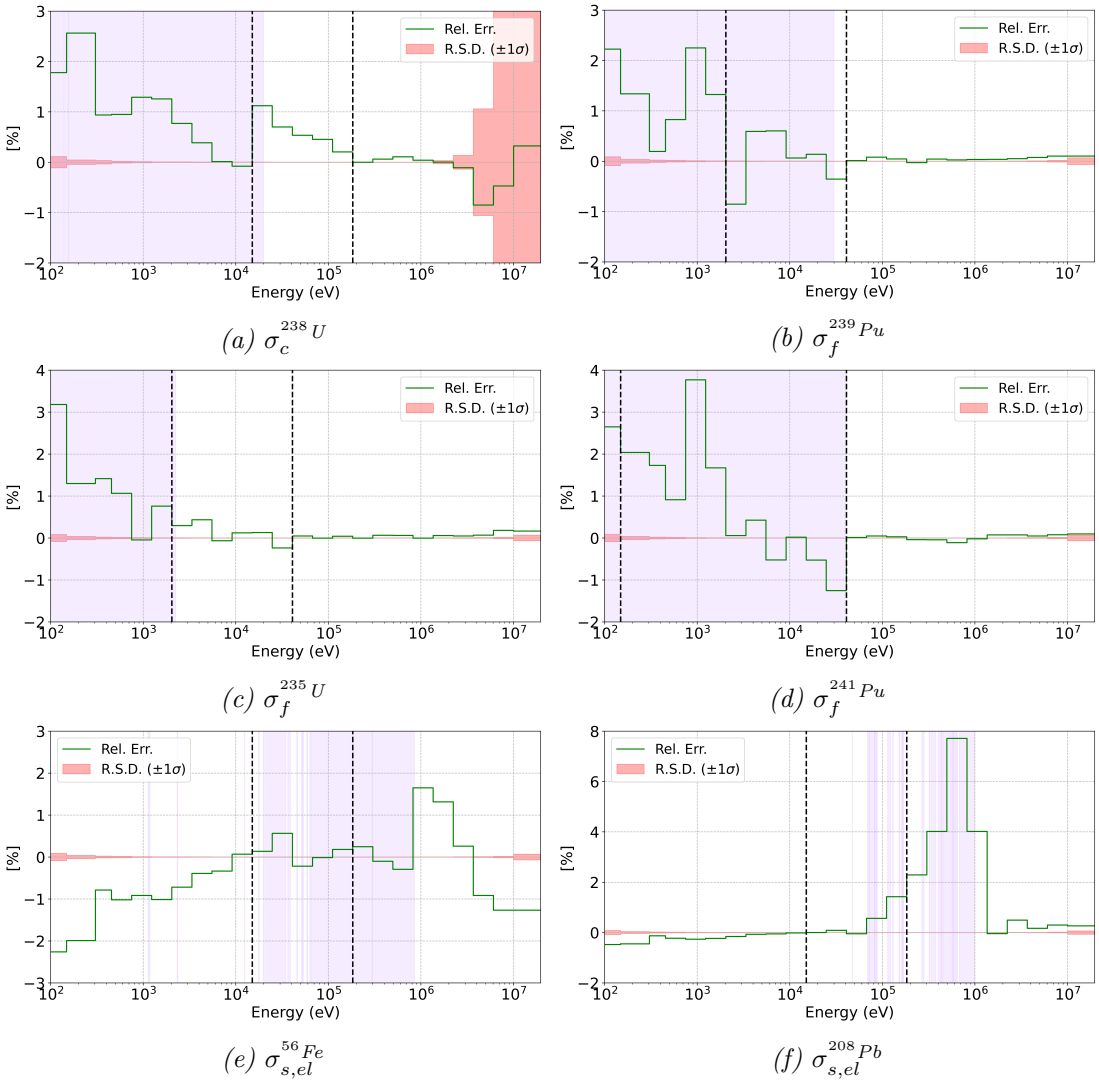


(a) $\sigma_c^{^{238}U}$ (b) $\sigma_f^{^{239}Pu}$

(c) $\sigma_f^{^{235}U}$ (d) $\sigma_f^{^{241}Pu}$

(e) $\sigma_{s,el}^{^{56}Fe}$ (f) $\sigma_{s,el}^{^{208}Pb}$

*Figure 5.20: LFR NEA benchmark, heterogeneous fuel assembly. Relative errors (ECCO vs. OpenMC) in the homogenised and condensed microscopic cross sections of the six most important nuclides. The relative errors are shown using the 33 group structure.*

## 5.4 Conclusions

Building on the analysis conducted by P. Jacquet in his PhD thesis [9], the ECCO self-shielding model was numerically validated for LFR cells. Since the computation of self-shielded cross sections differs in homogeneous and heterogeneous media (see Chapter 2), both scenarios were analysed. For each medium, the cross sections calculated using ECCO were compared with those calculated using the OpenMC Monte Carlo code. First, an attempt was made to replicate Jacquet's results for simplified SFR cells. In his work, Jacquet used the TRIPOLI-4® Monte Carlo code as a reference for the validation, alongside the JEFF-3.1 NDL. Therefore, the same library was used for the internal reproducibility tests in ECCO and OpenMC. While the ECCO calculations for the infinite multiplication factor and cross sections matched Jacquet's results exactly, discrepancies were found in the fission cross section of Pu-239 within the URR between OpenMC and TRIPOLI-4®. However, the good agreement between OpenMC and TRIPOLI-4® for the capture cross section of U-238 supported the validity of OpenMC simulations. Such discrepancies were therefore deemed to arise from incongruences in the NDL generation between OpenMC and TRIPOLI-4®. The latter indeed shares with ECCO the same methodology to generate PT within the URR, which could explain why such discrepancies do not appear between the two codes.

Consequently, the analysis proceeded using the more modern ENDF/B-VIII.0 NDL, which is adopted by the *new*cleo company for designing its LFR units. Using this library in both ECCO and OpenMC produced consistent results for Pu-239, whereas significant discrepancies were found in the U-238 capture cross section, once again within the URR. A refined analysis of the ECCO library revealed that PTs are absent within the URR for this nuclide. This explains the errors in the cross sections, as supported by additional calculations using the Serpent2 Monte Carlo code. Therefore, the analysis was performed on a case representative of LFR applications such as the NEA lead-cooled fast reactor benchmark [12]. The heterogeneous and homogeneous fuel pins were simulated using ECCO and OpenMC, with a temperature of 293 K imposed in the medium. The self-shielding effect is in fact expected to be more pronounced at low temperatures, where the resonances are narrower. As the LFR benchmark fuel pin is a more complex mixture than the simplified SFR fuel pin, more nuclides were monitored.

In both geometries, significant discrepancies were again found in the U-238 capture cross sections within the URR, due to the lack of PTs data. The same issue was found for U-235, but this had minimal impact on the accuracy of the cross section due to the nuclide's high dilution in the benchmark medium. Nevertheless, the lack of PTs for U-235 could produce non-negligible effects in different mixtures. Furthermore, large errors were found in the elastic scattering cross sections of the lead isotopes, which turned out to be the greatest among the errors evaluated for all nuclides. In particular, the discrepancies were found in energy groups where PTs are present in the ECCOLIB. Therefore, these errors were deemed to arise from inconsistencies in the preparation of the cross section data for the OpenMC and ECCO NDLs, performed by the NJOY RECONR module for the former and the CALENDF code for the latter. For other nuclides, such as O-16, Pu-241, and Fe-56, good agreement was found between OpenMC and ECCO.

The analysis was then repeated on the LFR benchmark fuel assembly. This context is of interest because it is closer to the purpose of the ECCO cell code in a design framework, which is the preparation of condensed and homogenised cross sections at the lattice level. In order to resemble a realistic design procedure, the assembly was modelled with temperature and geometries according to the numerical benchmark [12]. In particular, the higher temperatures are expected to significantly impact the self-shielding effects, compared to the previous case of a fuel pin at room temperature. The validation process identified two main sources of error: the self-shielding module (related, as described above, to the NDLs) and the CPs module. The former was found to be the predominant error source in the URR and continuum ranges of several nuclides. The latter instead showed to significantly affect the low-energy region. Furthermore, changing the operating conditions notably reduced the magnitude of the error for U-238, whereas it remained unchanged for the lead isotopes.

In light of the above results, it can be concluded that validating the ECCO self-shielding module, using the ENDF/B-VIII.0, is complicated by errors primarily arising from inconsistencies in the NDLs between ECCO and OpenMC. While it was possible to assess the errors related to the self-shielding module for a set of isotopes, such as Pu-239, Pu-241, and O-16, the same could not be achieved for U-238 and lead isotopes, due to errors arising from the NDLs overshadowing those from the self-shielding treatment. Similar issues also emerged for plutonium isotopes when calculations were performed using the JEFF-3.1 NDL, which were not found by Jacquet due to the uniformity of the nuclear data for the URR treatment between ECCO and TRIPOLI-4®. This analysis therefore highlights the crucial requirement for consistency in the generation of NDLs for deterministic and stochastic codes in order to ensure an accurate validation activity. Achieving this would enable the validation to be extended to the CPs module in future work. This would allow the simultaneous impacts of self-shielding and CPs approximations in heterogeneous geometries, such as fuel assemblies, to be assessed individually.

Chapter 6

# Impact of the cross sections discrepancies on the multiplication factor and Doppler reactivity change

The numerical validation of the ECCO self-shielding module with the ENDF/B-VIII.0 ECCOLIB, as detailed in Chapter 5, revealed significant discrepancies between the self-shielded cross sections, evaluated using ECCO and OpenMC. Analysis of the errors showed that they primarily originate from the data contained in the ECCO library for the treatment of the self-shielding effect. These discrepancies were observed in very simple media, such as a homogeneous and infinite LFR fuel pin, as well as in more realistic cases, such as an LFR fuel assembly. While simple media were analysed to isolate the errors related to the NDL from those originating from other modules, the fuel assembly was studied to resemble actual applications of the ECCO cell code, although the errors could not be isolated from those arising from the collision probabilities module.

The validation process requires identifying and quantifying all potential sources of error with the aim of minimising them as much as possible. Although errors in the cross sections have been identified and quantified, their influence on the neutronic design variables of interest has yet to be determined. This chapter therefore aims to assess the impact of the observed differences in two distinct cases: the LFR fuel pin and core of the NEA lead-cooled fast reactor benchmark [12, 64, 65, 66], respectively. While the former is of interest for validation purposes and was indeed used in Chapter 5 to isolate the numerical errors in the self-shielding module, the latter represents a typical design framework. Specifically, the objective is to evaluate the impact of errors in the cross sections originating from the NDL on the multiplication factor and on the Doppler reactivity change. This is achieved by means of a Decomposition Analysis (DA), as outlined below.

## 6.1 Principles of a Decomposition Analysis

The DA is a procedure that employs the sensitivity coefficients to determine the impact of differences in the nuclear data on the integral parameters. The definition of the SC in (1.75) can be rearranged as

$$\frac{\Delta k}{k} \approx S(k, \sigma_i) \frac{\Delta \sigma_i}{\sigma_i}, \tag{6.1}$$

where the approximation is derived from the fact that the SCs obtained using a first-order approximation are used alongside discrete variations in the cross sections. In fact, the first-order approximated SPT only derives SCs for small perturbations in the elementary parameters. However, the intention here is to apply this equation to discrepancies in the cross sections

between ECCO and OpenMC. As observed in Chapter 5, these differences are significant for specific nuclides and reactions. For example, the errors peaked at approximately 2% and 8% for the capture and elastic scattering cross sections of U-238 and Pb-208, respectively, in the LFR heterogeneous and infinite fuel pin (with the ECCO 33 group structure, see Figure 5.18). Nevertheless, this approach enables the multiplication factor discrepancy between ECCO and OpenMC to be broken down into the contributions of the differences observed between the two codes in the cross sections for each reaction and nuclide. Individual contributions can be estimated (subject to the limitations of the first-order approximation) by making the terms in the above equation explicit, which leads to

$$\Delta k = k - k_{ECCO} = S(k, \sigma_i^{ECCO}) \frac{\sigma_i^{OpenMC} - \sigma_i^{ECCO}}{\sigma_i^{ECCO}} k_{ECCO}. \tag{6.2}$$

The above equation provides an estimate of the variation in the ECCO multiplication factor that could be expected if the ECCO reference system were to be perturbed using the OpenMC cross sections. By excluding the contributions of other numerical modules to the multiplication factor and repeating this process for each nuclide and reaction, the sum of the contributions would be consistent with the discrepancy observed between ECCO and OpenMC. Analogously, the same analysis can be conducted on the Doppler reactivity change between two states at different temperatures, leading to

$$\Delta(\Delta\rho) = \Delta\rho - \Delta\rho_{ECCO} = S(\Delta\rho, \sigma_i^{ECCO}) \frac{\sigma_i^{OpenMC} - \sigma_i^{ECCO}}{\sigma_i^{ECCO}} \Delta\rho_{ECCO}. \tag{6.3}$$

## 6.2 Decomposition Analysis in the LFR fuel pin

The decomposition analysis started with the LFR fuel pin of the NEA benchmark [12]. This geometry was analysed in Chapter 5 for the validation of the ECCO self-shielding module, and the observed errors in the cross sections were deemed to originate from the nuclear data in the ECCOLIB. However, these errors were amplified by unphysical operating conditions, particularly with regard to temperature. In the following, the impact of these discrepancies on the infinite multiplication factor and Doppler reactivity change is assessed.

### 6.2.1 Decomposition Analysis of the infinite multiplication factor in the LFR fuel pin

The analysis performed in Section 5.2.1 on the heterogeneous fuel pin revealed a difference of 296 pcm in the infinite multiplication factor between OpenMC and ECCO. As the U-238 capture cross section calculated by ECCO in the URR was overestimated compared to that calculated using OpenMC, this was considered the cause of the underestimation of the infinite multiplication factor. To quantify this assumption, the DA based on Eq. (6.2) was conducted.

This required the use of ERANOS tools to derive the SCs for the infinite multiplication factor of the LFR fuel pin. The same methodologies employed in Chapter 4 were used to derive the SCs using the first-order SPT and the BISTRO R-Z solver on the equivalent cylindrical fuel pin, which was described in Section 5.2.1. The SCs for some of the most relevant nuclides are shown in Figure 6.1. As it was done for the LFR core, these SCs were integrated over all the 33 energy groups and broken down into the five main partial reactions. Once again, the predominant impact of U-238 and Pu-239 is evident. The figure also illustrates the negligible contributions of Fe-56 and Pb-208.

Consequently, the 33-group SCs were multiplied by the cross section relative errors (OpenMC vs. ECCO) in each group. As outlined in the introduction of this chapter, the result of this operation is the relative variation in the infinite multiplication factor with respect to the ECCO

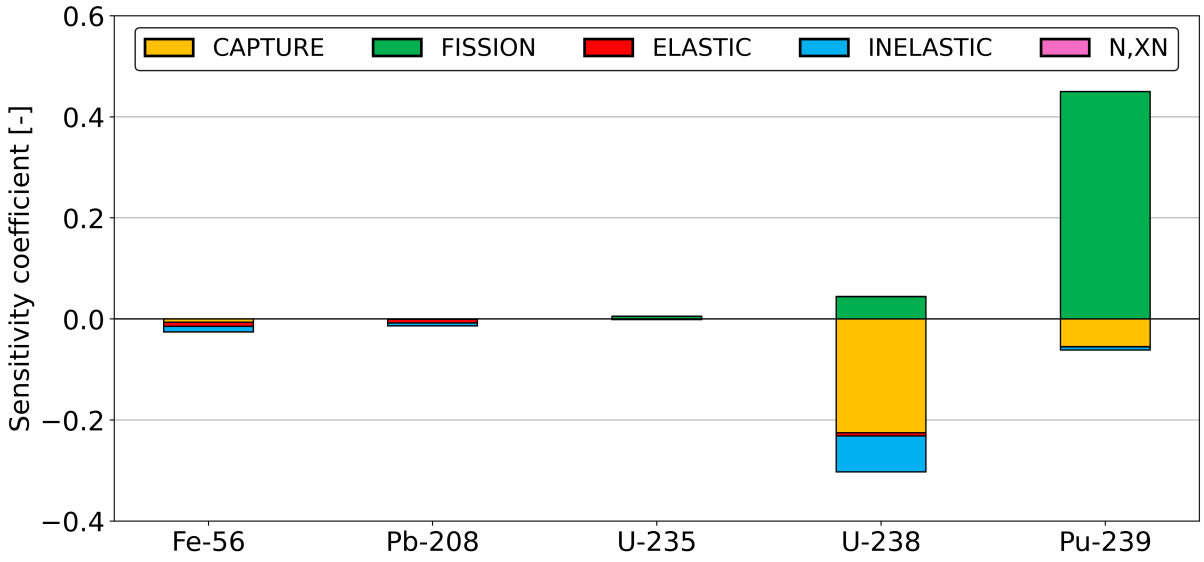


*Figure 6.1: LFR NEA benchmark, heterogeneous fuel pin at 294 K. The energy-integrated sensitivity coefficients for the infinite multiplication factor are shown for the most important nuclides and reactions.*

reference state ($\Delta k/k_{ECCO}$), as if it were perturbed using the OpenMC cross sections. The relative variation of the infinite multiplication factor due to U-238 captures and Pb-208 scattering is shown in Figure 6.2, alongside the corresponding cross sections relative errors.

Since the SCs for both U-238 captures and Pb-208 scattering are negative, the variation in the infinite multiplication factor has opposite sign to the cross section error. Furthermore, the difference in magnitude of the U-238 and Pb-208 SCs clearly determine a different effect on the infinite multiplication factor. In the former case, large SCs enhance the variation in the infinite multiplication factor induced by the errors in the capture cross section within the URR. Conversely, although the errors in the elastic scattering cross section of Pb-208 are larger than those of U-238, the variation in the infinite multiplication factor is much smaller in magnitude. Therefore, the effect of the discrepancies in the Pb-208 isotope is, to a certain extent, damped.

Finally, the $k_\infty$ relative variation due to the error on the self-shielded cross sections were summed within the three-group structure of U-238 and multiplied by the infinite multiplication factor calculated using ECCO. As a result, the absolute impact $\Delta k$ of U-238 and Pb-208 in the RRR, URR, and continuum of the former isotope could be computed. The results are shown in Figure 6.3. The largest contribution comes from the U-238 capture cross section within the URR. Chapter 5 showed that errors in the U-238 capture cross section are primarily due to a lack of PTs data within the URR in the ENDF/B-VIII.0 ECCO library. Given the current DA, it can be concluded that the absence of these data accounts for 213 pcm, approximately two-thirds of the 296 pcm discrepancy in the $k_\infty$ of the LFR fuel pin, observed between OpenMC and ECCO. Therefore, it would be suggested to revise the ENDF/B-VIII.0 ECCOLIB production workflow to refine the URR treatment of U-238. Using properly evaluated data containing PTs (such as those in OpenMC) would reduce the difference in the infinite multiplication factor between OpenMC and ECCO by more than 200 pcm. Otherwise, the validation activity performed using the ENDF/B-VIII.0 ECCO library would be complicated by the fact that errors in the NDL would overshadow the errors in the solution schemes.

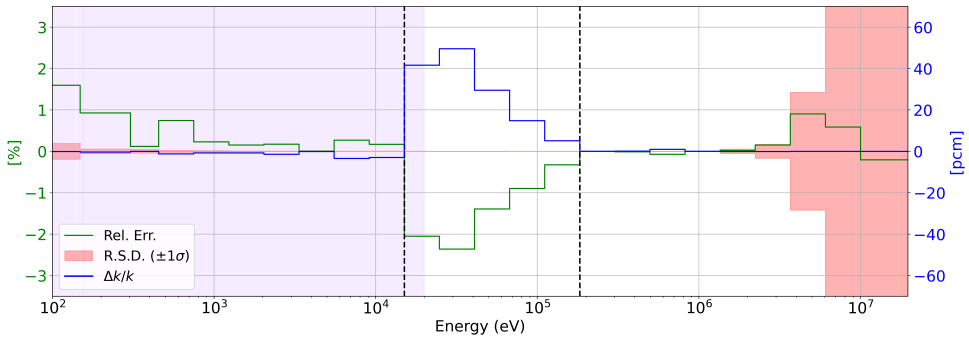


(a) $\sigma_c^{^{238}U}$

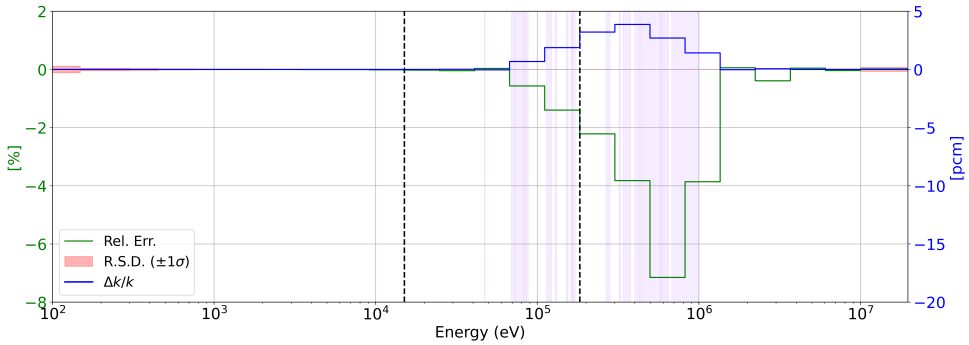


(b) $\sigma_s^{^{208}Pb}$

*Figure 6.2: LFR NEA benchmark, heterogeneous fuel pin at 294 K. The relative impact (blue line) on the infinite multiplication factor, $\Delta k/k_{ECCO}$, is assessed using a 33 group structure and the ENDF/B-VIII.0 NDL, taking the product between SCs for the fuel pin and the relative errors (OpenMC with respect to ECCO, green line) in the U-238 capture cross section, $\sigma_c^{^{238}U}$, and in the Pb-208 elastic scattering cross sections, $\sigma_s^{^{208}Pb}$. The black dashed lines indicate the URR bounds of U-238.*

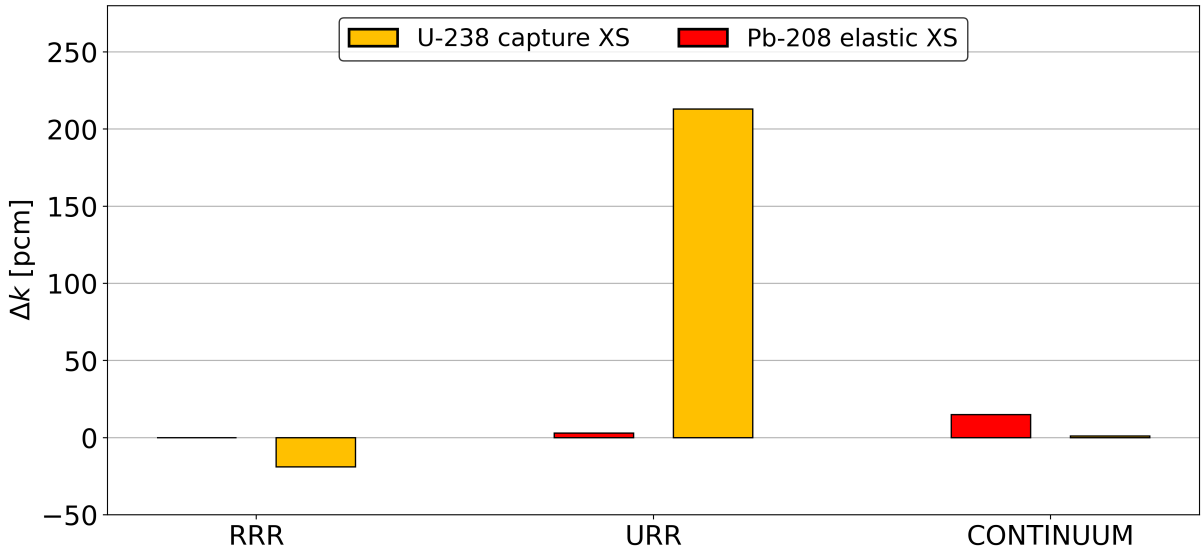


*Figure 6.3: LFR NEA benchmark, heterogeneous fuel pin at 294 K. The absolute variation in the infinite multiplication factor is assessed in the RRR, URR, and continuum of U-238, by summing the contributions from errors in the cross sections obtained using a 33 group structure and the ENDF/B-VIII.0 NDL.*

### 6.2.2 Decomposition Analysis of the Doppler reactivity change in the LFR fuel pin

Building on the previous analysis, the impact on the Doppler reactivity change of the LFR fuel pin was assessed. Since the choice of the temperature interval can influence the Doppler reactivity change [76] four different fuel temperature values were examined. These values correspond to those at which the NDL was generated for OpenMC. However, this means that errors resulting from temperature interpolation in ECCO cannot be ruled out. Nevertheless, it has been shown in the work of S. Rahlfs [8] that the impact of temperature interpolations on the reactivity is generally small.

Table 6.1 shows the infinite multiplication factor evaluated using ECCO and OpenMC with the ENDF/B-VIII.0 NDL, for each of the four temperature values. For each pair of temperatures, the reactivity change between the higher and lower temperature states is computed using both codes. The absolute and relative differences between the results of the two codes (OpenMC with respect to ECCO) are shown in Table 6.2. As it can be seen, the discrepancies between ECCO and OpenMC vary for each pair of temperatures. This suggests that there could be other sources of numerical error in addition to those originating from discrepancies in the NDLs.

Therefore, a decomposition analysis was performed on the 1200-2500 K states, where the relative difference is at its minimum, and the 600-900 K states, where it is at its maximum. However, it should be noted that the difference in the reactivity change between 1200 K and 2500 K is comparable to the statistical uncertainty. The SCs were derived using the first-order EGPT for both pairs of states. However, when Eq. (6.3) is applied, it is not determined *a priori* in which state the relative variation in the cross sections should be computed. For the purposes of this study, the relative differences were computed in the lower-temperature state. In fact, discrepancies coming from the resonance self-shielding treatment are expected to be larger at lower temperatures, thus leading to a conservative approach.

Furthermore, since the Doppler effect is related to the broadening of cross sections resonances, the SCs for the Doppler reactivity change can have a non-negligible impact at lower energies, compared to the case of the SCs for the multiplication factor. Consequently, the impact of other isotopes, especially the heavier ones, should not be ruled out. As observed in Chapter 5, the ECCO code tends to exhibit larger discrepancies with respect to OpenMC in the thermal and epithermal regions. Although is not possible to determine a priori whether these discrepancies are related to NDLs, they could still have a non-negligible influence on the Doppler reactivity change, even though they occur in a region of low influence in LFR applications.

| | | | | $k_\infty$ **LFR heterogeneous fuel pin** | | | | | |
|---|---|---|---|---|---|---|---|---|---|
| | | | | **900 K** | | **1200 K** | | **2500 K** | |
| | | | | ECCO | OpenMC | ECCO | OpenMC | ECCO | OpenMC |
| | | | | 1.35546 | 1.35767 (± 1) | 1.35329 | 1.35540 (± 1) | 1.34818 | 1.35026 (± 1) |
| $k_\infty$ | **600 K** | ECCO | 1.35864 | -172.55 | | -290.85 | | -571.14 | |
| | | OpenMC | 1.36104 (± 1) | | -182.37 (± 2) | | -305.73 (± 2) | | -586.58 (± 2) |
| | **900 K** | ECCO | 1.35546 | | | -118.30 | | -398.58 | |
| | | OpenMC | 1.35767 (± 1) | | | | -123.36 (± 2) | | -404.21 (± 2) |
| | **1200 K** | ECCO | 1.35329 | | | | | -280.28 | |
| | | OpenMC | 1.35540 (± 1) | | | | | | -280.85 (± 2) |

*Table 6.1: LFR NEA benchmark, heterogeneous fuel pin. The infinite multiplication factor is evaluated using ECCO and OpenMC with the ENDF/B-VIII.0 NDL at four different MOX fuel temperatures. The Doppler reactivity change, between the higher and lower temperature states, is computed and reported (in pcm) in the central part of the table for each pair of temperature values. The statistical uncertainty of the MC results is reported in pcm between brackets.*

| $\Delta(\Delta\rho)$ LFR heterogeneous fuel pin | | | | | |
|---|---|---|---|---|---|
| | | | **900 K** | **1200 K** | **2500 K** |
| **600 K** | Abs. Diff. | [pcm] | 9.82 | 14.88 | 15.44 |
| | Rel. Diff. | [%] | 5.69 | 5.12 | 2.70 |
| **900 K** | Abs. Diff. | [pcm] | | 5.06 | -5.63 |
| | Rel. Diff. | [%] | | 4.28 | -1.39 |
| **1200 K** | Abs. Diff. | [pcm] | | | -0.57 |
| | Rel. Diff. | [%] | | | -0.20 |

*Table 6.2: LFR NEA benchmark, heterogeneous fuel pin. The absolute and relative differences in the Doppler reactivity change are computed for OpenMC with respect to ECCO, using the ENDF/B-VIII.0 NDL.*

Therefore, the DA was performed including several isotopes, as shown in Figure 6.4. The isotopes for which the DA was performed are only a small selection of those that have the greatest influence on the Doppler reactivity change, as determined by the ranking made in Chapter 4. Other isotopes, such as O-16, Fe-56, and Pu-240, were intentionally omitted, since Chapter 5 showed that the errors in their cross sections are generally small. Therefore, these isotopes are expected to have a negligible influence in the current DA. The absolute variation in the Doppler reactivity change, $\Delta(\Delta\rho)$, is broken down into the contributions from the cross sections errors in the RRR, URR, and continuum of their respective nuclides. It can be seen that Pu-241 has a significant impact in the URR. This could be explained by the energy bounds of the unresolved range of Pu-241 being in the epithermal region, which is where ECCO produces largest errors. Lead isotopes, which are lighter elements with resonances at higher energies than fissile isotopes, contribute more in the continuum energy range (considering the three energy regions of U-238), where the errors in the cross sections are also larger. The impact of U-238 capture cross section discrepancies is once again grater in the URR than in the other regions.

However, when the absolute variations in the Doppler reactivity change, as determined by the errors in the cross sections, are summed across all energy intervals and nuclides, the sum is relatively small for both pairs of temperatures. This variation, in the order of 1 pcm, is consistent with the value shown in Table 6.2 for the 1200-2500 K variation, although comparable to the statistical uncertainty, but less than the value for the 600-900 K variation. This suggests that the difference in the reactivity change, between ECCO and OpenMC, varies between pairs of temperatures due to other sources of numerical error, rather than errors originating from the self-shielding treatment using the PTs data in the ECCOLIB. Indeed, errors in the cross sections determine a variation in the Doppler reactivity change that remains negligible and approximately constant across different temperature intervals. Determining these other sources of error requires further investigation. Nevertheless, variations of the order of pcm can be considered considerably small for typical neutronic applications, especially given that the statistical uncertainty is of a similar order of magnitude.

However, the requirements for a validation process differ significantly from those for a design activity. The DA conducted on the fuel pin aimed to assess the impact of the errors in the cross sections on the infinite multiplication factor. This geometry was modelled to simulate a highly simplified medium, which enabled the errors originating from the self-shielding module to be isolated from those related to other solution schemes. Nevertheless, the infinite multiplication factor of the fuel pin is of little interest to neutronic analyses, which focus on parameters relevant to the entire reactor system instead. Moreover, errors in the cross section are exacerbated by low temperature values, which enhance the effect of self-shielding, but are not realistic for actual design frameworks. The next sections therefore analyse a case study representative of realistic LFR neutronic design applications, such as the LFR benchmark core [66, 12].

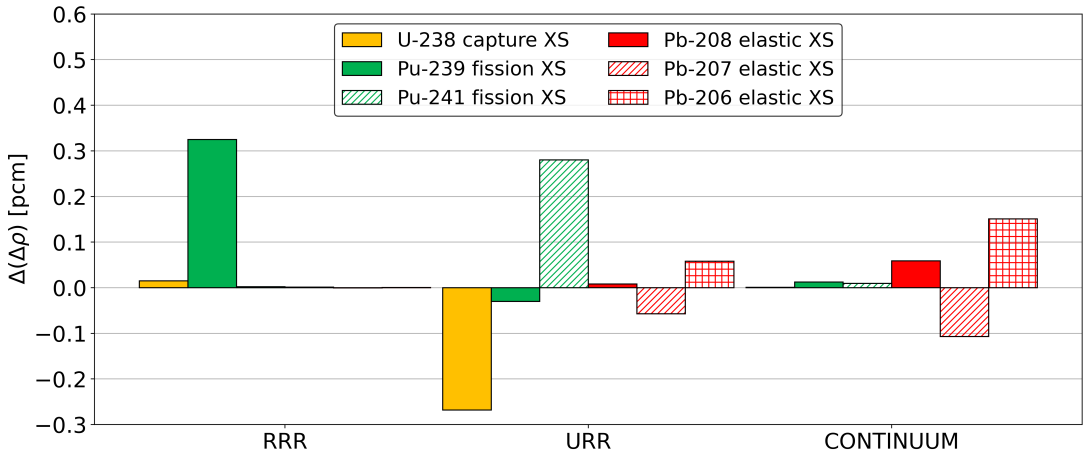


*(a) 600 K - 900 K*

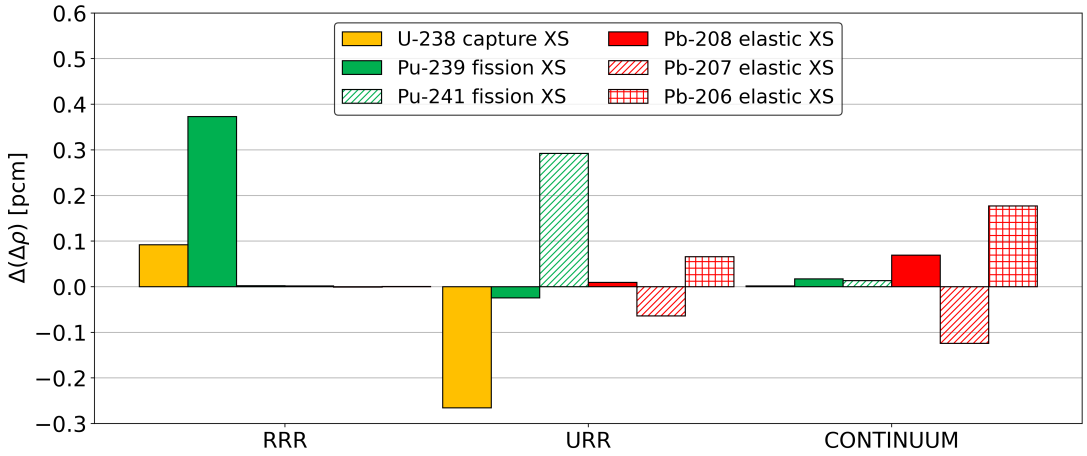


*(b) 1200 K - 2500 K*

*Figure 6.4: LFR NEA benchmark, heterogeneous fuel pin. The absolute variation in Doppler reactivity change due to cross section errors is broken down into the contributions from the RRR, URR, and continuum of their respective nuclides. For the lead isotopes, the energy intervals follow the usual U-238 convention used for this study. The impact on the Doppler reactivity change is assessed between two pairs of fuel temperature values: 600-900 K above and 1200-2500 K below.*

## 6.3 Decomposition Analysis in the LFR core

In Chapter 5 was observed that the errors in the cross section decreased when moving from a toy-model made of a few resonant isotopes to a realistic LFR fuel element. Building on this analysis, the impact of the discrepancies in the ECCO library was assessed within a framework relevant for design applications: the LFR reactor core of the NEA numerical benchmark [12]. In this case, the SCs derived in Chapter 4 for the same geometry and operating conditions will be employed.

### 6.3.1 Decomposition Analysis of the effective multiplication factor in the LFR core

In the classical two-step approach, the homogenised and condensed cross sections, which are evaluated at the lattice level, are used in subsequent core calculations. A rigorous DA would require the use of the relative errors in these quantities, within Eqs. (6.2) and (6.3), to assess the impact on the LFR core.

However, performing a DA with discrepancies in these quantities would include the impact of other error sources, such as the ones introduced by homogenisation, condensation, CPs, and leakage models. It would be impossible to determine whether the relative variations in the variables of interest are caused by errors in the cross sections arising from the self-shielding module and the ECCO NDL, or by errors in the cross sections originating from other modules. Therefore, the DA will be performed using relative errors in the microscopic cross sections of the infinite, heterogeneous LFR fuel pin under the operating conditions specified in the numerical benchmark (1200 K for the fuel and 600 K for the cladding and coolant). It is assumed that the errors in the self-shielding module affecting the fuel pin will persist identically in the fuel assembly and could potentially be shadowed by the errors in other modules (CPs, condensation, leakage, etc.), making this a conservative approach. This was partially observed in Chapter 5, when the heterogeneous fuel pin and fuel assembly were evaluated. However, in that case, a significant change in the magnitude of the cross section errors resulted from the change in the operating conditions.

Nevertheless, it should be noted that this approach does not allow the impact of the self-shielding module to be distinguished from that of the Doppler broadening and the temperature interpolation. However, the result obtained is more representative than considering the fuel pin at room temperature. Furthermore, it has been shown in the work of S. Rahlfs [8] that the errors due to the temperature interpolation tend to be confined to the thermal region, where the relative difference between ECCO and OpenMC is less significant due to greater statistical uncertainty.

In order to quantify the discrepancies between OpenMC and ERANOS, the effective multiplication factor of the LFR benchmark core was evaluated using both codes. Table 6.3 shows the results obtained using the 3D Nodal Variational Transport VARIANT code, which is implemented in ERANOS [4], and the Monte Carlo code. Of the other transport codes available in ERANOS, the VARIANT module was chosen as it provides the most accurate estimation of the effective multiplication factor. Therefore, additional numerical errors unrelated to the nuclear data in the ENDF/B-VIII.0 ECCOLIB are, in principle, ruled out.

| | VARIANT | OpenMC | Abs. Diff. [pcm] |
|---|---|---|---|
| $\boldsymbol{k_{eff}}$ | 1.04549 | 1.04778(2) | 229 |

*Table 6.3: LFR core under operating conditions according to the numerical benchmark specifications [12]. The effective multiplication factor is evaluated using the the VARIANT flux solver for the 3D geometry. The results are compared with the OpenMC result for the same core geometry. The ENDF/B-VIII.0 NDL is used. The standard deviation of the Monte Carlo reference value is reported in parenthesis (in pcm).*

Consequently, as it was done in the LFR fuel pin case, the DA was performed taking the product between the relative variation in the cross sections of the heterogeneous pin and the sensitivity coefficients derived for the entire core. These latter were described in Chapter 4. As mentioned above, the cross sections and SCs were calculated this time by imposing the temperatures in the various media according to the numerical benchmark specifications.

Figure 6.5 shows the relative impact on the effective multiplication factor of the reactor core, broken down into the 33 group structure. As it can be seen, the relative errors in the cross sections of U-238 and Pb-208 (OpenMC with respect to ECCO), evaluated for the heterogeneous fuel pin under operating conditions according to the numerical benchmark specifications, are not significantly different to those observed in Section 5.3 (ECCO with respect to OpenMC) for the heterogeneous fuel assembly, under the same operating conditions. This supports the initial hypothesis in the introduction to this section, which implied that errors in the NDL and the self-shielding module, evaluated in the fuel pin, would persist in the fuel assembly when the

same operating conditions were imposed.

Secondly, it can be seen that the relative variation in the core effective multiplication factor, caused by errors in the cross sections of both isotopes, differs considerably from that of the fuel pin case. For U-238, this is a consequence of the decrease in the magnitude of the relative errors. Therefore, the relative variation in the effective multiplication factor also decreases. For Pb-208, for which the magnitude of the relative errors has not decreased, the relative variation in the effective multiplication factor of the core is significantly higher in modulus than for the fuel pin. Furthermore, this variation has the opposite sign to that of the infinite multiplication factor of the fuel pin. This is due to the change in the magnitude and sign of the SCs for the lead isotopes, which differ notably between the fuel pin and the core. This result could be interpreted physically as follows. In the fuel pin, the smaller OpenMC estimate of the Pb-208 elastic scattering cross section results in decreased neutron transfer towards lower energies. This hardens the neutron spectrum of the infinite cell. Consequently, higher-energy neutrons can exploit more fissions in the heavy nuclides, and the relative errors in the scattering cross section can increase the infinite multiplication factor. In the LFR benchmark core, where vacuum boundary conditions are imposed, the smaller Pb-208 elastic scattering cross section values could enhance the neutron leakage. Therefore, negative discrepancies in the scattering cross section can lead to negative variations in the effective multiplication factor.

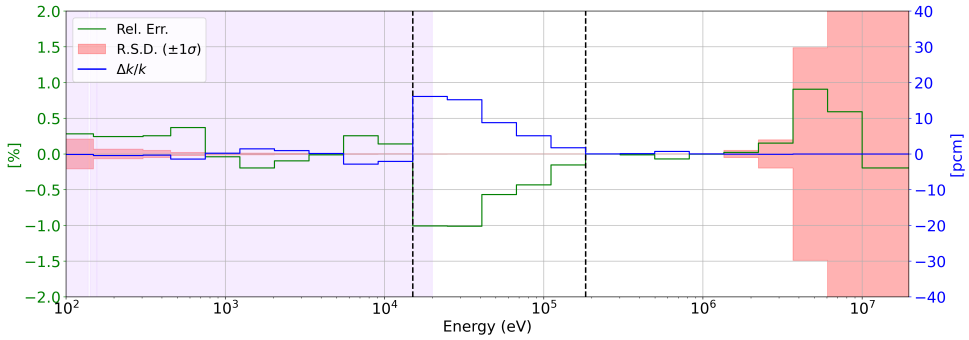


*(a)* $\sigma_c^{^{238}U}$

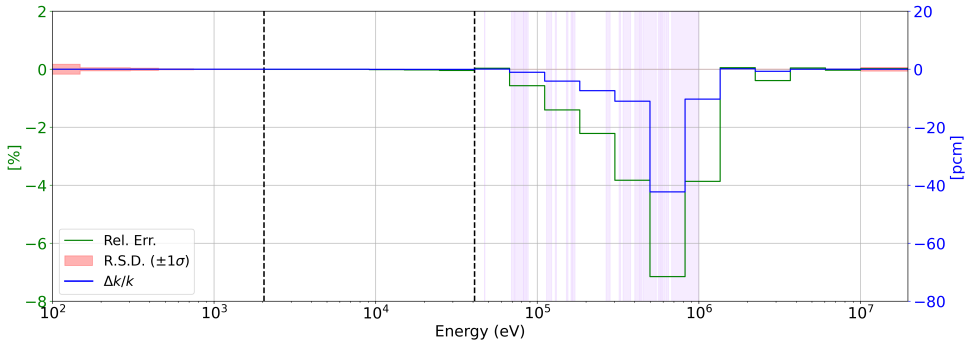


*(b)* $\sigma_s^{^{208}Pb}$

*Figure 6.5: LFR core under operating conditions according to the numerical benchmark specifications [12]. The relative variation in the effective multiplication factor (blue line) is assessed using a 33 groups structure and the ENDF/B-VIII.0 NDL, taking the product between SCs for the reactor core and the relative errors (OpenMC with respect to ECCO, green line) in the U-238 capture cross section, $\sigma_c^{^{238}U}$, and in the Pb-208 elastic scattering cross sections, $\sigma_s^{^{208}Pb}$. The black dashed lines indicate the URR bounds of U-238.*

This is made more evident in Figure 6.6, where the absolute variation in the effective multiplication factor, induced by the cross sections relative errors, is broken down again into the contributions of each isotope in the three-group energy structure of U-238. Absolute variation is obtained by multiplying the relative variation by the effective multiplication factor calculated

using the VARIANT module (see Table 6.3). In this case, the impact of U-238 within the URR is considerably smaller than in the fuel pin case and, in magnitude, it is even smaller than the impact of Pb-208 at high energies. Moreover, the two impacts have the opposite signs, and therefore they partially cancel each other out. The same applies to Pb-206 and Pb-207, whose contributions of opposite sign compensate each other within the continuum. When the contributions of all nuclides are summed together, the impact on the effective multiplication factor of the LFR benchmark core is considerably smaller than the discrepancy observed in Table 6.3 between VARIANT and OpenMC. Given the compensation of the errors generated in the NDLs discrepancies, it can be concluded that this difference is due to other sources of numerical error.

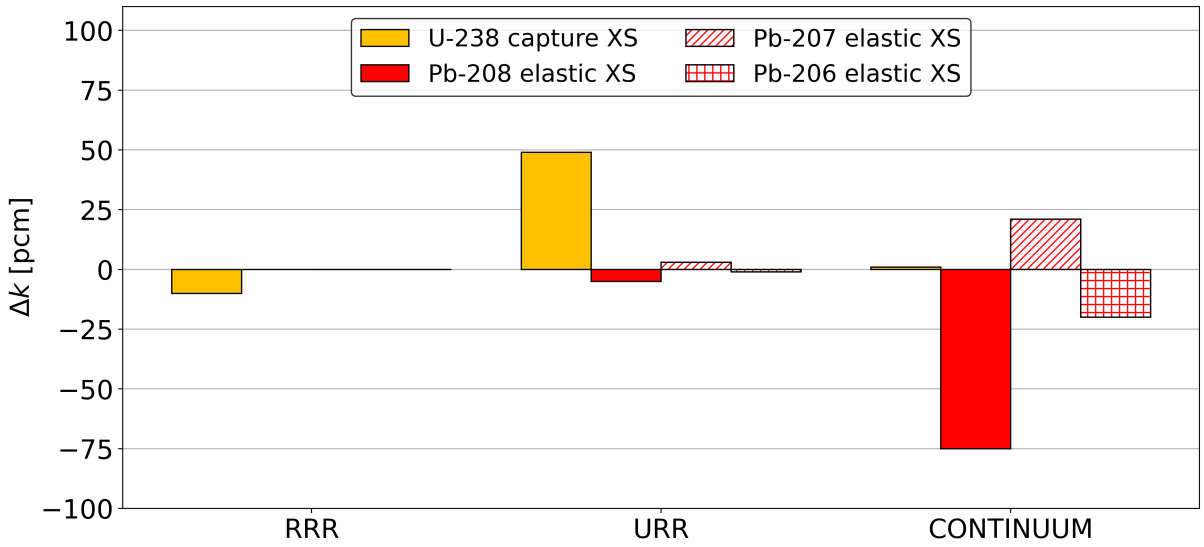


*Figure 6.6: LFR core under operating conditions according to the numerical benchmark specifications [12]. The absolute variation in the effective multiplication factor is assessed in the RRR, URR, and continuum of U-238, summing the contributions from errors in the cross sections obtained using a 33 group structure and the ENDF/B-VIII.0 NDL.*

### 6.3.2 Decomposition Analysis of the Doppler reactivity change in the LFR core

As with the fuel pin case, the DA of the LFR benchmark core was concluded with the assessment of the impact on the Doppler reactivity change. In line with Table 6.1, Table 6.4 shows the effective multiplication factor calculated using the VARIANT module and OpenMC for the same four MOX fuel temperature values (applied to both internal and external fuel assemblies, i.e. FINN and FOUT). Additionally, both values of the reactivity change are calculated for each pair of temperatures, between the higher and lower temperature states. Then, Table 6.5 shows the absolute and relative variation between the Monte Carlo and ERANOS results. Once again, the comparison is made between OpenMC and the VARIANT module, since the latter excludes potential numerical errors arising from the approximations in other modules.

Unlike in the fuel pin case, where the relative difference was at its minimum for the 1200-2500 K variation, in the LFR benchmark core it is at its maximum. The minimum relative difference occurs for the 900-1200 K variation instead. However, in this case too, the absolute difference between the two states is comparable to the statistical uncertainty. In line with the analysis of the fuel pin, the decomposition analysis was performed for the Doppler reactivity change between these two pairs of temperatures.

| | | | | $k_{eff}$ LFR benchmark core | | | | | |
|---|---|---|---|---|---|---|---|---|---|
| | | | | 900 K | | 1200 K | | 2500 K | |
| | | | | VARIANT 1.04742 | OpenMC 1.04970 (± 2) | VARIANT 1.04549 | OpenMC 1.04778 (± 2) | VARIANT 1.04077 | OpenMC 1.04328 (± 2) |
| $k_{eff}$ | 600 K | VARIANT | 1.05019 | -251.82 | | -428.07 | | -861.84 | |
| | | OpenMC | 1.05242 (± 2) | | -246.22 (± 3) | | -420.78 (± 3) | | -832.45 (± 3) |
| | 900 | VARIANT | 1.04742 | | | -176.24 | | -610.02 | |
| | | OpenMC | 1.04970 (± 2) | | | | -174.57 (± 3) | | -586.23 (± 3) |
| | 1200 | VARIANT | 1.04549 | | | | | -433.78 | |
| | | OpenMC | 1.04778 (± 2) | | | | | | -411.66 (± 3) |

*Table 6.4: LFR NEA benchmark core. The effective multiplication factor is evaluated using the VARIANT module and OpenMC at four different MOX fuel temperatures (in both the internal and external fuel assemblies). The ENDF/B-VIII.0 NDL is used. The Doppler reactivity change, between the higher and lower temperature states, is computed and reported (in pcm) in the central part of the table for each pair of temperature values. The statistical uncertainty of the MC results is reported in pcm in brackets.*

| **$\Delta(\Delta\rho)$ LFR benchmark core** | | | | | |
|---|---|---|---|---|---|
| | | | **900 K** | **1200 K** | **2500 K** |
| **600 K** | Abs. Diff. | [pcm] | 5.61 | 7.28 | 29.40 |
| | Rel. Diff. | [%] | -2.23 | -1.70 | -3.41 |
| **900 K** | Abs. Diff. | [pcm] | | 1.68 | 23.79 |
| | Rel. Diff. | [%] | | -0.95 | -3.90 |
| **1200 K** | Abs. Diff. | [pcm] | | | 22.12 |
| | Rel. Diff. | [%] | | | -5.10 |

*Table 6.5: LFR NEA benchmark core. The absolute and relative differences in the Doppler reactivity change are computed for OpenMC with respect to the VARIANT module, using the ENDF/B-VIII.0 NDL.*

Figure 6.7 shows the absolute impact on the Doppler reactivity change for the same nuclides analysed in the fuel pin case. Looking at the picture, it can be seen the change in the sign of contributions of some nuclides, such as Pb-206, Pb-208, and Pu-239. Moreover, the variation in the magnitude of the contributions between the two pairs of temperatures is more pronounced than in the fuel pin case, with the errors impact being slightly larger for the 1200-2500 K variation. This is also the interval in which the VARIANT-OpenMC variation is greatest. However, as in the fuel pin case, the absolute impact of the discrepancies in the NDLs on the Doppler reactivity change is negligible. As it was concluded for the fuel pin case, discrepancies in the reactivity change can be attributed to other sources of numerical error.

## 6.4 Conclusions about the Decomposition Analysis

In order to assess the impact of the discrepancies observed in Chapter 5 between ECCO and OpenMC, particularly for U-238 and the lead isotopes, a decomposition analysis was performed. This type of analysis is performed by multiplying the sensitivity coefficients by the relative errors in the cross sections. Thanks to the definition of the SCs, it is possible to individually determine the contribution of these discrepancies to the differences observed between the two codes for a given variable of interest. The dissimilarities in the ENDF/B-VIII.0 NDLs, between OpenMC and ECCO, were deemed to be the main cause of the cross sections errors. Therefore, by means of the DA, it was possible to determine how the quality of the ECCO results would improve if these inconsistencies were corrected.

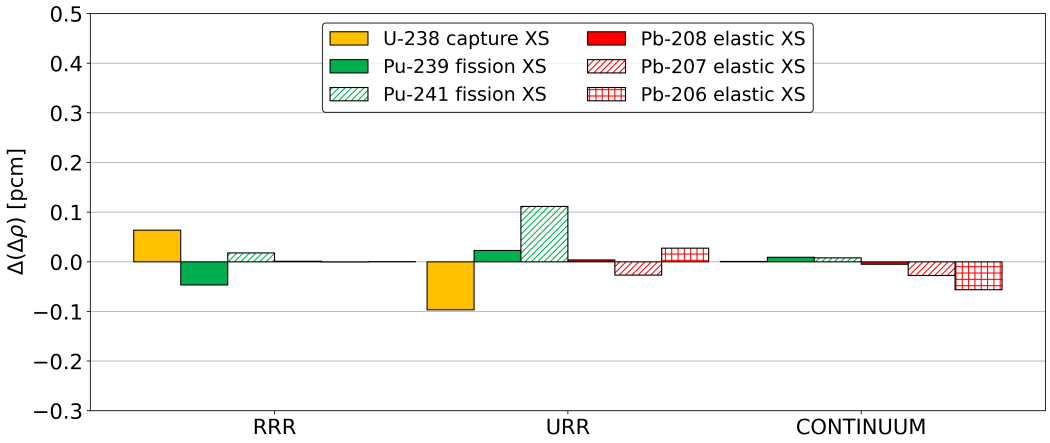


*(a) 900 K - 1200 K*

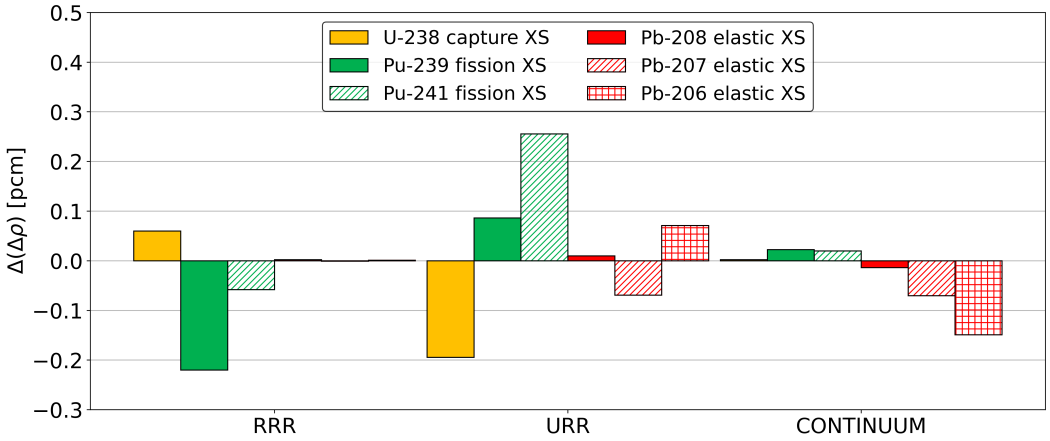


*(b) 1200 K - 2500 K*

*Figure 6.7: LFR NEA benchmark core. The absolute variation in the Doppler reactivity change due to errors in the cross sections is broken down into the contributions from the RRR, URR, and continuum of their respective nuclides. For the lead isotopes, the energy intervals follow the usual U-238 convention of this study. The impact on the Doppler reactivity change is assessed between two pairs of fuel temperature values: 900-1200 K above and 1200-2500 K below.*

Chapter 5 showed that, although the errors in the cross sections originate mainly from differences in the NDLs, they can be significantly influenced by the operating conditions applied, particularly with regard to temperature. This was a concern, as unrealistic temperature values (293 K) were required to isolate numerical errors during the validation process. Furthermore, when the ECCO cell code is used in more realistic frameworks, such as assembly-level calculations, additional solution schemes may cause numerical errors that overshadow those arising from the NDLs. Therefore, the DA was performed for two representative cases: the heterogeneous LFR fuel pin, at room temperature, and the LFR reactor core, under operating conditions in accordance with the NEA numerical benchmark specifications [12]. In both cases, the analysis was performed by multiplying the relative errors in the cross sections (calculated for the fuel pin) by the respective SCs. These were derived following the methodologies described in Chapter 4 for both geometries and operating conditions. As the SCs were derived for the multiplication factor and Doppler reactivity change, the DA was performed for these quantities. The variations in these quantities were first assessed using a 33 group structure, and then by summing the contributions in each of the usual three-groups structure (RRR, URR, and continuum). However, using SCs derived with the first-order approximation in conjunction with discrepancies in the cross-sections that are not small can negatively impact the accuracy of the analysis. Another limitation arises from the fact that the SCs are derived using the BISTRO solver for an R-Z geometry, whereas the comparisons of the integral parameters are made for the actual the reactor

core geometry.

Different trends are observed in the fuel pin and the reactor core with regard to the multiplication factor. In the former, errors in the cross sections tend to be higher, particularly for U-238 within the URR, due to the lower applied temperature. Moreover, the impact of lead isotopes SCs is minimal. Consequently, 213 out of 296 pcm difference observed between OpenMC and ECCO for the infinite multiplication factor originate from the errors in the capture cross section of U-238 within the URR, while the impact of Pb-208 is negligible. These errors in the capture cross section of U-238 were attributed to the lack of PTs within the URR in the ENDF/B-VIII.0 ECCOLIB. This suggests that adding these data to the library would reduce the discrepancy observed between ECCO and the Monte Carlo code by approximately two-thirds. In the reactor core instead, the increase in the temperature values significantly decreases the errors for U-238. Furthermore, the relative concentration of U-238 in relation to the total amount of materials is much smaller in the reactor core than in the fuel pin. Therefore, the effect of lead on neutron leakage could predominate, with the coolant significantly influencing the effective multiplication factor. This could potentially explain the variation in the sensitivity coefficients for the infinite and effective multiplication factors of the fuel pin and reactor core, respectively. Thus, at high energies, the impact of Pb-208 is greater than that of U-238 within the URR, and they partially compensate each other due to contributions of opposite signs. The same applies to Pb-206 and Pb-207. Therefore, the discrepancy observed in the core effective multiplication factor, between ERANOS and OpenMC, can be attributed to other sources of error. Furthermore, this analysis only considered a limited number of reactions and nuclides located in the internal and external fuel assemblies. Future work should extend the DA to include nuclides present in other regions of the reactor. If significant discrepancies were to occur between ECCO and OpenMC for nuclides and reactions in regions not included here, this could potentially explain the discrepancy observed between ERANOS and OpenMC in the effective multiplication factor. In that sense, influence on neutron leakage of discrepancies in the lead self-shielding treatment in different regions of the reactor should be investigated.

Regarding the impact on the Doppler reactivity change, this was evaluated at different MOX fuel temperatures. In the case of the reactor, the fuel temperature was set for both the internal and external fuel assemblies. Considerably small differences between ECCO (or ERANOS) and OpenMC Doppler reactivity change are generally observed in both the fuel pin and the reactor core. In particular, the DA revealed that the impacts of the errors in the cross sections of each nuclide tend to be mild, and they usually cancel each other out. For pairs of temperatures for which the discrepancies between the two codes are greater, the differences can be attributed to other sources of numerical error. To determine these sources, further investigations are required.

In conclusion, it can be claimed that the errors in the cross sections, generated from inconsistencies in the NDLs do not have a significant impact on the ECCO and ERANOS calculations during standard procedures, typical of design calculations, employed for the LFR numerical benchmark. However, it must be emphasised that a single case may not be fully representative of any kind of LFR system and that further investigation of other configurations may be required. Indeed, the impact on the LFR benchmark core is of little concern due to errors compensation effects, which may not occur in other systems. Nevertheless, the DA revealed that the inconsistencies in the NDLs can excessively complicate the validation process, as the errors they generate tend to overshadow those originating from the numerical schemes. Therefore, it is suggested that the discrepancies in the NDLs be addressed in order to determine their origin and correct them accordingly. This would facilitate the numerical validation of the ECCO cell code with a modern set of data, such as the ENDF/B-VIII.0 NDL.

Chapter 7

# Analysis of discrepancies origin within the ECCOLIB production workflow

The previous part of this work delved into the analysis of an ENDF/B-VIII.0 based ECCO library, which is used by the *new*cleo team and which is the result of an independent evaluation. The study has highlighted some issues with U-238 and the lead isotopes, and a decomposition analysis was performed assessing the impact of these differences. Furthermore, a comparison with the JEFF-3.1 ECCOLIB, which is part of the ERANOS code distribution [44], has revealed that the lead isotopes are affected by a common issue in both libraries.

Following the conclusion of the Super-Phénix experience, the ERANOS distribution has not undergone significant developments [69]. This also applies to the system of codes, described in Chapter 3, for creating an ECCO NDL. In contrast, more recent NDLs have been developed following the release of the JEFF-3.1 and JEFF-3.1.1 ECCO libraries [80, 44]. Meanwhile, only a few studies dealt with the production of ECCO libraries using modern data [81, 82]. Therefore, the final part of this work aims at doing the root causes of the discrepancies previously described within the ECCOLIB production workflow. This will clarify whether any further modernisation work is required on the ECCOLIB production workflow.

## 7.1 Manipulation of the ECCOLIB production workflow for the handling of the lead isotopes errors

In the work of W.F.G. van Rooijen [82] new ECCO libraries were produced based on the JENDL-4.0 [83], JEFF-3.1.2 [84], and ENDF/B-VII.0 [85] NDLs. ERANOS calculations were then performed using the new libraries and the results were compared with those of the ZEBRA MOZART numerical benchmark [86]. The benchmark values were obtained using the Monte Carlo code MCNP [78].

As described in Chapter 3, the MERGE code allows the user to prioritise either the NJOY or CALENDF multigroup cross section values, adjusting the output values of one of the two codes to match those of the preferred code. Generally, it is a standard procedure to prioritise the CALENDF values [46, 44]. However, in his study van Rooijen pointed out that the ERANOS results were in better agreement with those of the MCNP code when preference was given to the NJOY values [82]. This can be expected, as the MCNP code uses NJOY to produce its NDL, employing the same methodologies for Doppler broadening, resonance reconstruction, and linear interpolation, among others, as those described in Chapter 3 for OpenMC. Therefore, the discrepancies observed in Chapter 5 between ECCO and OpenMC, particularly for the lead isotopes, may similarly be caused by discrepancies between NJOY and CALENDF.

### 7.1.1 Replica of the original JEFF-3.1 ECCOLIB

In order to conduct a detailed investigation, the suite of codes for the generation of ECCO libraries described in Chapter 3 was revised and put to good use to generate ECCOLIB files for selected isotopes. The NJOY, CALENDF, MERGE, and GECCO codes were set in place using input files according to the CEA JEFF-3.1 ECCOLIB specifications [44]. The aim was to replicate the existing JEFF-3.1 ECCOLIB, for the target isotope, to validate the production workflow and the set of input data used to generate the new library. However, it must be remarked that for the generation of the original CEA JEFF-3.1 ECCOLIB the NJOY-99.90 and CALENDF-2005 versions of the codes were used [44]. For this work, instead, the more recent and up-to-date versions of the codes, namely NJOY-2016 and CALENDF-2010, were used. Therefore, some minor discrepancies could be expected. Regarding the other codes, in line with the original libraries, the MERGE-3.8 and GECCO-1.4 versions were used.

Using the codes mentioned above, separate ECCOLIB files were generated for all the nuclides present in the JEFF-3.1 ECCOLIB of the ERANOS distribution. The following focusses on Pb-206, Pb-207, and Pb-208. The input files used for the generation of a library for Pb-208, in the 1968 group structure, are given in Appendix G. Using the ERANOS procedure shown in Listing 7.1, the infinite diluted energy-averaged cross sections were exported from the internally produced library and the original JEFF-3.1 ECCOLIB, using the same group structure.

```
1 ECCO_FILE_EDITION
2       REFERENCE_FILE 'NEWCLEO.REF' ! Or ECCOLIB_JEFF_31.REF
3       FILE 'NEWCLEO.1968' ! Or ECCOLIB_JEFF_31.1968
4       ISOTOPE 'Pb208' 1 2 1 1968 ; ! Same for Pb-207 and Pb-206
```

*Listing 7.1: ERANOS routine used to print the values of the infinite diluted cross sections with the 1968 group structure, stored in the ECCOLIB files.*

Once infinite diluted cross sections were obtained, for both libraries, the ratio within each of the 1968 groups was taken. Figure 7.1 shows the results of a comparison between the two libraries for Pb-208 at 293 K. Looking at the picture, it can be noted that the two data sets are in excellent agreement, with the discrepancy between the two being negligible for most of the group and reactions. For the capture reaction only, non-negligible discrepancies occur in the low-energy region. However, given the very small values of the capture reaction in this range, these differences are of low concern and could be attributed to the numerical precision of the codes.

As a further step in the internal validation of the libraries, these were tested within the ECCO cell code. A simple, infinite, and homogeneous medium at 293 K was simulated, consisting only of the tested isotope. As this medium contains only the lead isotopes and no fissile isotopes, this had to be treated as a sub-critical medium within ECCO. The external imposed flux was taken from the homogeneous, infinite LFR fuel pin analysed in Chapter 5. Listing 7.2 shows the single-step calculation performed within the code using the 1968 group structure. Then, the cross sections were condensed into the 33 group structure.

Table 7.1 shows a comparison of the group-averaged cross sections, calculated using the original CEA and the *new*cleo JEFF-3.1 ECCO libraries, for a homogeneous medium made of pure Pb-208. Once again, significant discrepancies are present only in the capture cross section, but as before, the very small values of the cross section make these discrepancies negligible. As a good agreement was also found for the other lead isotopes, the replica of the original JEFF-3.1 ECCOLIB for these nuclides can be considered successful.

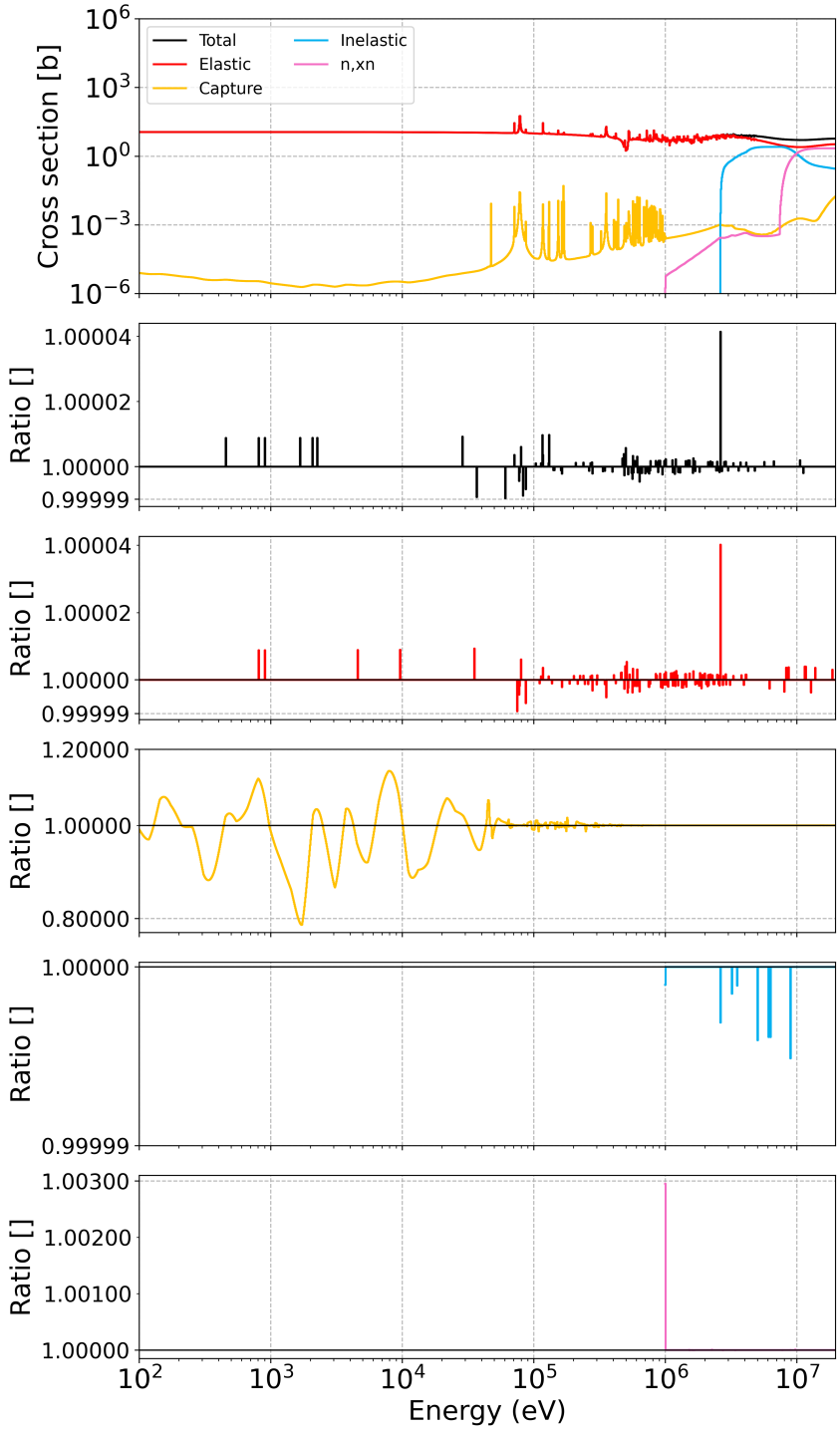


*Figure 7.1: The 1968-group infinite diluted cross sections of Pb-208 are printed as stored in the ECCOLIB produced internally at newcleo. Below, the ratio with the CEA original JEFF-3.1 ECCOLIB is taken for the main partial reactions.*

```
->STEP_1_FUEL_IN
GROUP STRUCTURE OTHER 1968
FLUX SOLUTION FM P1 CONSISTENT ORDER 1
GEOMETRY HOMOGENEOUS
FIND_ELEMENTS_IN_LIST 'Pb208' ! Or Pb-207 or Pb-206
INPUT LIBRARY 'NEWCLEO.1968' ! Or ECCOLIB_JEFF_31.1968
SUBCRITICAL FLUXB 'FLUX1968' ! From LFR homogeneous fuel pin
BUCKLING 0.0
SELF SHIELDING DBBSH
CONDENSE 33 ! Condense 1968 XS into 33 group structure
   1 82 142 202 262 322 382 442 502 564        !boundaries of 33 groups
   624 686 746 808 868 928 988 1048 1108 1168  !in the 1968 structure
   1228 1288 1336 1422 1480 1516 1579 1648 1708 1768
   1837 1919 1952 ;
PRINT DATA FLUXES CROSS SECTIONS MICROSCOPIC VECTORS;
```

*Listing 7.2: Single-step calculation performed within the ECCO cell code with an external imposed flux.*

### 7.1.2 Analysis of NJOY and CALENDF discrepancies

The JEFF-3.1 ECCOLIB replica for the lead isotopes ensured that the internal processing workflow was correct and that no errors were made when handling the raw data. As mentioned above, the findings of van Rooijen suggest that using NJOY as a reference to adjust accordingly the CALENDF PTs within the MERGE code could decrease the discrepancy between ERANOS and a Monte Carlo code that uses NDLs processed with NJOY. Since it is a standard procedure to normalise the NJOY values instead, using those of CALENDF as a reference, eventual incoherences between NJOY and CALENDF could generate the discrepancies observed in Chapter 5 between ECCO and OpenMC. Therefore, the internally produced output files of NJOY and CALENDF were analysed. Figure 7.2 shows a comparison of the elastic scattering cross sections generated by CALENDF and NJOY for Pb-208 using the JEFF-3.1 NDL, before the MERGE and GECCO codes manipulate the data and apply the correcting factors. Two sets of data at 293 K were compared: the pointwise data in the PENDF file, which are reconstructed by CALENDF and the NJOY RECONR module, and the multigroup data in the 1968 and 295 group structures. The latter are the infinite diluted energy-averaged cross sections calculated by the GROUPR module for NJOY, and the infinite diluted cross sections calculated from the probability tables as described in Chapter 3, for CALENDF. The NJOY and CALENDF input files used to generate the multigroup cross section in the 295 group structure are given in Appendix G.

Looking at the pictures, it can be seen that the discrepancies in the 295 group structure have the identical shape to that observed in Section 5.1.2.3, where the Pb-208 elastic scattering cross section produced by ECCO was compared with that of OpenMC for the homogeneous LFR fuel pin. Although these discrepancies were observed when using the ENDF/B-VIII.0 NDL, it was observed in Section 5.1.4 that the Pb-208 elastic scattering cross section exhibited similar discrepancies in the JEFF-3.1 NDL. Moreover, the discrepancies between the two codes are evident in the same energy interval for the pointwise data. This suggests that the discrepancies observed in the group-averaged cross sections originate from the two codes performing a different reconstruction of the pointwise data, starting from the raw ENDF-6 tapes. Such discrepancies, outside the URR, are generally not observed for other isotopes [87].

Figure 7.3 shows a comparison of the elastic scattering cross sections of Pb-206 and Pb-207 produced using the 295 group structure, as calculated by NJOY and CALENDF. Also in this case, the shape of the differences is similar to that observed between ECCO and OpenMC for the LFR fuel pin (see Figure 5.14).

| Group | Original JEFF-3.1 ECCOLIB | | | | *newcleo* JEFF-3.1 ECCOLIB | | | | | Relative Difference [%] | | | | |
|---|---|---|---|---|---|---|---|---|---|---|---|---|---|---|
| | TOTAL | ELASTIC | N,XN | INELASTIC | CAPTURE | TOTAL | ELASTIC | N,XN | INELASTIC | CAPTURE | TOTAL | ELASTIC | N,XN | INELASTIC | CAPTURE |
| 1 | 5.4131E+00 | 2.8523E+00 | 2.0555E+00 | 5.0087E-01 | 4.3442E-03 | 5.4130E+00 | 2.8522E+00 | 2.0554E+00 | 5.0101E-01 | 4.3448E-03 | -0.002 | -0.005 | -0.006 | 0.027 | 0.013 |
| 2 | 5.6262E+00 | 3.0427E+00 | 3.0673E-01 | 2.2758E+00 | 9.8853E-04 | 5.6261E+00 | 3.0425E+00 | 3.0678E-01 | 2.2758E+00 | 9.8863E-04 | -0.003 | -0.005 | 0.015 | -0.002 | 0.010 |
| 3 | 7.5668E+00 | 5.6138E+00 | 3.7469E-04 | 1.9521E+00 | 4.9435E-04 | 7.5669E+00 | 5.6139E+00 | 3.7469E-04 | 1.9521E+00 | 4.9435E-04 | 0.001 | 0.002 | -0.001 | -0.002 | 0.001 |
| 4 | 7.4116E+00 | 7.2250E+00 | 2.3895E-04 | 1.8549E-01 | 8.7301E-04 | 7.4116E+00 | 7.2249E+00 | 2.3896E-04 | 1.8554E-01 | 8.7300E-04 | 0.001 | 0.000 | 0.003 | 0.026 | -0.001 |
| 5 | 5.4196E+00 | 5.4191E+00 | 4.8148E-05 | 1.0000E-20 | 4.6304E-04 | 5.4196E+00 | 5.4191E+00 | 4.8149E-05 | 1.0000E-20 | 4.6304E-04 | -0.001 | -0.001 | 0.003 | 0.000 | 0.001 |
| 6 | 5.1743E+00 | 5.1737E+00 | 6.0875E-06 | 1.0000E-20 | 5.3483E-04 | 5.1743E+00 | 5.1737E+00 | 6.0875E-06 | 1.0000E-20 | 5.3484E-04 | 0.000 | 0.000 | -0.001 | 0.000 | 0.002 |
| 7 | 4.6048E+00 | 4.6037E+00 | 0.0000E+00 | 8.1903E-21 | 1.1540E-03 | 4.6049E+00 | 4.6037E+00 | 0.0000E+00 | 8.1904E-21 | 1.1540E-03 | 0.001 | 0.001 | 0.000 | 0.002 | 0.000 |
| 8 | 6.0387E+00 | 6.0383E+00 | 0.0000E+00 | 6.7744E-21 | 4.3463E-04 | 6.0389E+00 | 6.0385E+00 | 0.0000E+00 | 6.7742E-21 | 4.3464E-04 | 0.003 | 0.003 | 0.000 | -0.003 | 0.004 |
| 9 | 8.1106E+00 | 8.1105E+00 | 0.0000E+00 | 1.1469E-21 | 6.3040E-05 | 8.1106E+00 | 8.1105E+00 | 0.0000E+00 | 1.1469E-21 | 6.3071E-05 | 0.000 | 0.000 | 0.000 | 0.005 | 0.049 |
| 10 | 9.4733E+00 | 9.4724E+00 | 0.0000E+00 | 3.5186E-21 | 8.6739E-04 | 9.4733E+00 | 9.4724E+00 | 0.0000E+00 | 3.3530E-21 | 8.6743E-04 | 0.000 | 0.000 | 0.000 | -4.708 | 0.005 |
| 11 | 1.1095E+01 | 1.1094E+01 | 0.0000E+00 | 3.8778E-21 | 6.2568E-04 | 1.1095E+01 | 1.1094E+01 | 0.0000E+00 | 3.8778E-21 | 6.2573E-04 | 0.000 | 0.000 | 0.000 | 0.000 | 0.008 |
| 12 | 1.0454E+01 | 1.0454E+01 | 0.0000E+00 | 1.6564E-22 | 1.6320E-04 | 1.0454E+01 | 1.0454E+01 | 0.0000E+00 | 1.6564E-22 | 1.6333E-04 | 0.000 | 0.000 | 0.000 | 0.000 | 0.081 |
| 13 | 1.0801E+01 | 1.0801E+01 | 0.0000E+00 | 0.0000E+00 | 8.6795E-06 | 1.0801E+01 | 1.0801E+01 | 0.0000E+00 | 0.0000E+00 | 8.5553E-06 | 0.000 | 0.000 | 0.000 | 0.000 | -1.431 |
| 14 | 1.1021E+01 | 1.1021E+01 | 0.0000E+00 | 0.0000E+00 | 5.2048E-06 | 1.1021E+01 | 1.1021E+01 | 0.0000E+00 | 0.0000E+00 | 5.2661E-06 | 0.000 | 0.000 | 0.000 | 0.000 | 1.178 |
| 15 | 1.1157E+01 | 1.1157E+01 | 0.0000E+00 | 0.0000E+00 | 3.5863E-06 | 1.1157E+01 | 1.1157E+01 | 0.0000E+00 | 0.0000E+00 | 3.3390E-06 | 0.000 | 0.000 | 0.000 | 0.000 | -6.894 |
| 16 | 1.1241E+01 | 1.1241E+01 | 0.0000E+00 | 0.0000E+00 | 2.7655E-06 | 1.1241E+01 | 1.1241E+01 | 0.0000E+00 | 0.0000E+00 | 2.9632E-06 | 0.000 | 0.000 | 0.000 | 0.000 | 7.149 |
| 17 | 1.1292E+01 | 1.1292E+01 | 0.0000E+00 | 0.0000E+00 | 2.4031E-06 | 1.1292E+01 | 1.1292E+01 | 0.0000E+00 | 0.0000E+00 | 2.3351E-06 | 0.000 | 0.000 | 0.000 | 0.000 | -2.831 |
| 18 | 1.1323E+01 | 1.1323E+01 | 0.0000E+00 | 0.0000E+00 | 2.3477E-06 | 1.1323E+01 | 1.1323E+01 | 0.0000E+00 | 0.0000E+00 | 2.2540E-06 | 0.000 | 0.000 | 0.000 | 0.000 | -3.994 |
| 19 | 1.1342E+01 | 1.1342E+01 | 0.0000E+00 | 0.0000E+00 | 2.5182E-06 | 1.1342E+01 | 1.1342E+01 | 0.0000E+00 | 0.0000E+00 | 2.1493E-06 | 0.000 | 0.000 | 0.000 | 0.000 | -14.652 |
| 20 | 1.1354E+01 | 1.1354E+01 | 0.0000E+00 | 0.0000E+00 | 2.9255E-06 | 1.1354E+01 | 1.1354E+01 | 0.0000E+00 | 0.0000E+00 | 2.9897E-06 | 0.000 | 0.000 | 0.000 | 0.000 | 2.192 |
| 21 | 1.1361E+01 | 1.1361E+01 | 0.0000E+00 | 0.0000E+00 | 3.5710E-06 | 1.1361E+01 | 1.1361E+01 | 0.0000E+00 | 0.0000E+00 | 3.6879E-06 | 0.000 | 0.000 | 0.000 | 0.000 | 3.274 |
| 22 | 1.1365E+01 | 1.1365E+01 | 0.0000E+00 | 0.0000E+00 | 4.3378E-06 | 1.1365E+01 | 1.1365E+01 | 0.0000E+00 | 0.0000E+00 | 3.9758E-06 | 0.000 | 0.000 | 0.000 | 0.000 | -8.344 |
| 23 | 1.1367E+01 | 1.1367E+01 | 0.0000E+00 | 0.0000E+00 | 5.6261E-06 | 1.1367E+01 | 1.1367E+01 | 0.0000E+00 | 0.0000E+00 | 5.6920E-06 | 0.000 | 0.000 | 0.000 | 0.000 | 1.171 |
| 24 | 1.1369E+01 | 1.1369E+01 | 0.0000E+00 | 0.0000E+00 | 7.4778E-06 | 1.1369E+01 | 1.1369E+01 | 0.0000E+00 | 0.0000E+00 | 7.4714E-06 | 0.000 | 0.000 | 0.000 | 0.000 | -0.085 |
| 25 | 1.1370E+01 | 1.1370E+01 | 0.0000E+00 | 0.0000E+00 | 9.0392E-06 | 1.1370E+01 | 1.1370E+01 | 0.0000E+00 | 0.0000E+00 | 9.2492E-06 | 0.000 | 0.000 | 0.000 | 0.000 | 2.324 |
| 26 | 1.1371E+01 | 1.1371E+01 | 0.0000E+00 | 0.0000E+00 | 1.1096E-05 | 1.1371E+01 | 1.1371E+01 | 0.0000E+00 | 0.0000E+00 | 1.1440E-05 | 0.000 | 0.000 | 0.000 | 0.000 | 3.098 |
| 27 | 1.1371E+01 | 1.1371E+01 | 0.0000E+00 | 0.0000E+00 | 1.4579E-05 | 1.1371E+01 | 1.1371E+01 | 0.0000E+00 | 0.0000E+00 | 1.4571E-05 | 0.000 | 0.000 | 0.000 | 0.000 | -0.059 |
| 28 | 1.1371E+01 | 1.1371E+01 | 0.0000E+00 | 0.0000E+00 | 1.9032E-05 | 1.1371E+01 | 1.1371E+01 | 0.0000E+00 | 0.0000E+00 | 1.8774E-05 | 0.000 | 0.000 | 0.000 | 0.000 | -1.356 |
| 29 | 1.1371E+01 | 1.1371E+01 | 0.0000E+00 | 0.0000E+00 | 2.4419E-05 | 1.1371E+01 | 1.1371E+01 | 0.0000E+00 | 0.0000E+00 | 2.4976E-05 | 0.000 | 0.000 | 0.000 | 0.000 | 2.279 |
| 30 | 1.1372E+01 | 1.1371E+01 | 0.0000E+00 | 0.0000E+00 | 3.3353E-05 | 1.1372E+01 | 1.1372E+01 | 0.0000E+00 | 0.0000E+00 | 3.5786E-05 | 0.000 | 0.001 | 0.000 | 0.000 | 7.294 |
| 31 | 1.1372E+01 | 1.1372E+01 | 0.0000E+00 | 0.0000E+00 | 6.8753E-05 | 1.1372E+01 | 1.1372E+01 | 0.0000E+00 | 0.0000E+00 | 5.6242E-05 | -0.002 | -0.003 | 0.000 | 0.000 | -18.198 |
| 32 | 1.1377E+01 | 1.1377E+01 | 0.0000E+00 | 0.0000E+00 | 2.1689E-04 | 1.1373E+01 | 1.1373E+01 | 0.0000E+00 | 0.0000E+00 | 1.2170E-04 | -0.033 | -0.032 | 0.000 | 0.000 | -43.887 |
| 33 | 1.1401E+01 | 1.1401E+01 | 0.0000E+00 | 1.8853E-22 | 4.6174E-04 | 1.1387E+01 | 1.1386E+01 | 0.0000E+00 | 3.3434E-23 | 3.4341E-04 | -0.126 | -0.125 | 0.000 | -82.266 | -25.626 |

*Table 7.1: Original CEA and newcleo JEFF-3.1 ECCO libraries comparison. The cross sections for the total and main partial reactions are calculated within ECCO, simulating an infinite and homogeneous medium containing only Pb-208, using both libraries. The cross sections are condensed into the 33 group structure, and the relative difference (newcleo with respect to CEA original library) is computed. Relative error values are highlighted in green when below 0.1 %, in orange between 0.1 % and 0.5 %, and in red when above 0.5 %.*

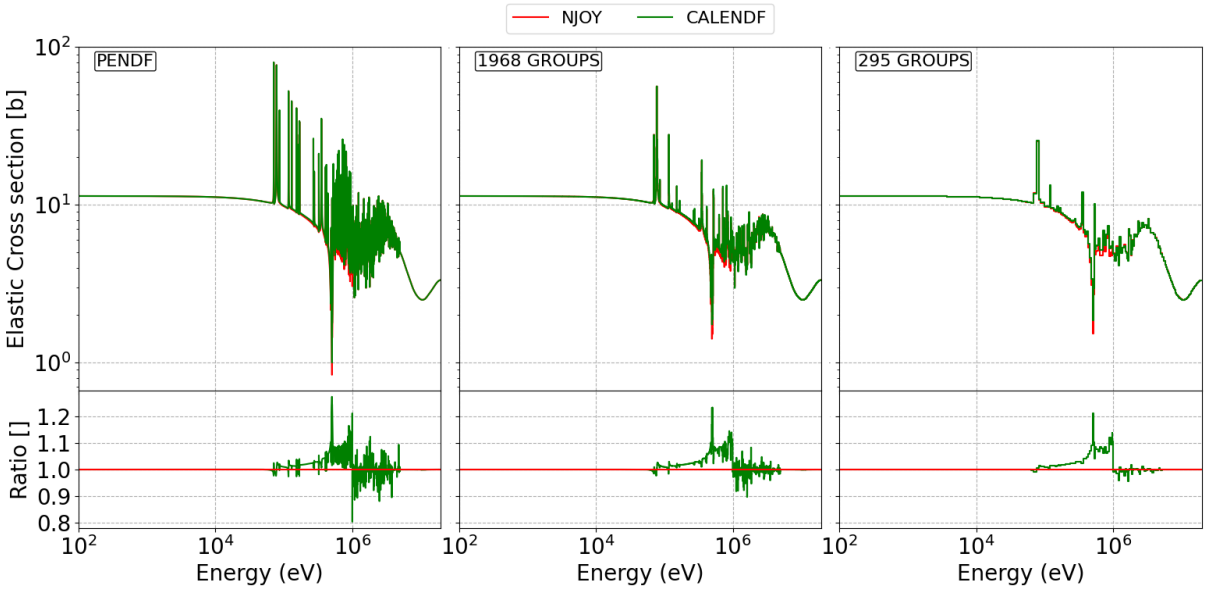


*Figure 7.2: Pb-208, NJOY and CALENDF reconstruction and group-averaging of the elastic scattering cross sections. The JEFF-3.1 ENDF-6 tapes are used. The picture on the left shows the cross sections in the PENDF produced by both codes, starting from the ENDF-6 tapes. The middle and right pictures show the infinite diluted cross sections in the 1968 and 295 group structures. In each case, the ratio of CALENDF with respect to NJOY is taken.*

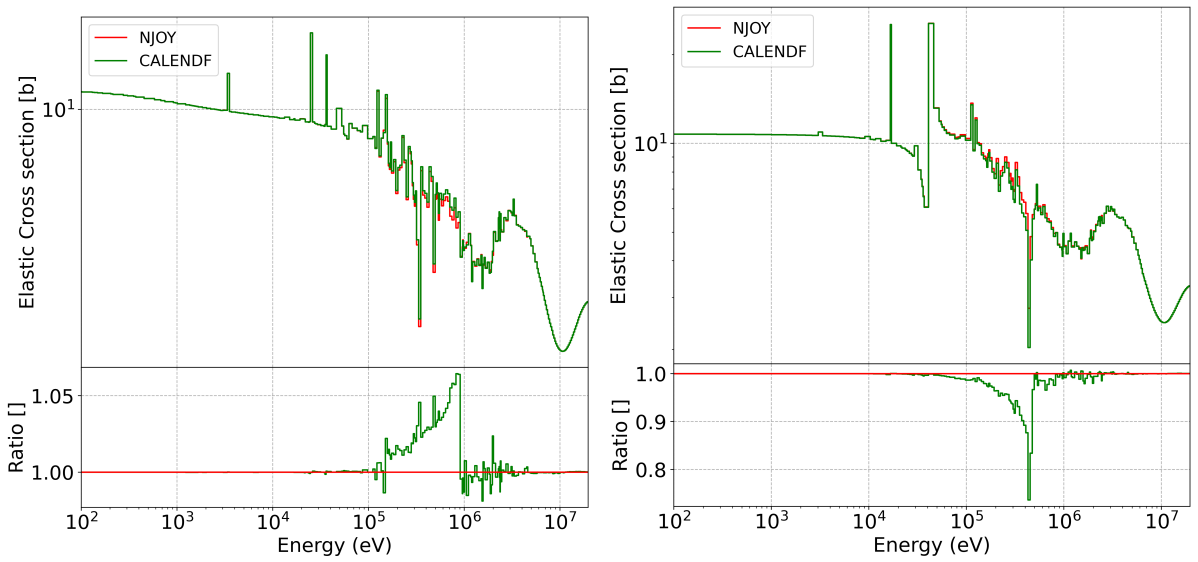


*(a)* $\sigma_s^{^{206}Pb}$*, 295 groups*

*(b)* $\sigma_s^{^{207}Pb}$*, 295 groups*

*Figure 7.3: Pb-206 and Pb-207, NJOY and CALENDF group-averaging of the elastic scattering cross sections. The JEFF-3.1 ENDF-6 tapes are used. The cross sections are calculated using both codes with the 295 group structure. In each case, the ratio of CALENDF with respect to NJOY is taken.*

### 7.1.3 Generation and testing of a new ECCOLIB with NJOY values as a reference

The discrepancies observed between NJOY and CALENDF provide an explanation for the discrepancies observed between OpenMC and ECCO. The standard procedure in the MERGE code is to use the CALENDF values as a reference, applying correction factors to the NJOY cross sections and scattering matrices to match the CALENDF infinite diluted multigroup cross sections.

Therefore, the ECCO code uses PTs produced by CALENDF to treat the self-shielding effect, and these remain unchanged in MERGE. The NJOY multigroup cross sections and scattering matrices, which are corrected by MERGE, are stored and used only for energy groups where the CALENDF values have been removed (e.g. due to negative values being produced). Conversely, Monte Carlo codes such as OpenMC and MCNP use pointwise data in the RRR and PT data in the URR to treat the self-shielding effect. Both of these are processed exclusively with NJOY. Eventual inconsistencies between NJOY and CALENDF therefore induce discrepancies between the deterministic and stochastic results.

In line with the work of van Rooijen [82], new ECCOLIB files were generated for the lead isotopes using the JEFF-3.1 ENDF-6 tapes, this time giving preference to the NJOY values and applying the correction factors to the CALENDF PTs. Thanks to the built-in "MISE A JOUR BIBLIOTHEQUES ECCO" procedure of ERANOS, it was possible to replace the data for the lead isotopes in the original CEA JEFF-3.1 ECCOLIB with the newly generated ECCOLIB files that used the NJOY values as a reference.

Consequently, the LFR homogeneous and infinite fuel pin was simulated again within ECCO, using both the original and the new JEFF-3.1 ECCO libraries. Figure 7.4 shows a comparison of the relative error in the Pb-208, Pb-206, and Pb-207 elastic scattering cross sections (ECCO with respect to OpenMC), obtained using both libraries and the JEFF-3.1 NDL also for the Monte Carlo code. The comparison was made using the 33 and 295 group structures. As it can be seen, using the newly generated ECCOLIB significantly reduces discrepancies between the two codes, with negligible errors in both group structures.

In conclusion, the origin of the discrepancies in the lead isotope cross sections was found to be the different cross section reconstructions performed by NJOY and CALENDF. However, although the relative differences have decreased significantly when using NJOY as a reference in MERGE, this does not necessarily imply that the NJOY-processed data are more accurate than those of CALENDF. In fact, the decrease in the discrepancies is a consequence of consistency being achieved between the NDLs of the deterministic and stochastic codes. Only by comparing the results with experimental benchmarks can it be determined which of the two nuclear data processing codes provides higher accuracy.

## 7.2 Causes of missing Probability Tables in the unresolved resonance range

The analysis performed for the lead isotopes does not apply to U-238 and U-235, for which the PT data are missing within the entire unresolved resonance range. To determine the cause of the absence of PTs, the CALENDF code was used to generate PTs for U-238 using both the JEFF-3.1 and ENDF/B-VIII.0 NDLs. Analysis of the output files revealed that CALENDF generated PTs data within the URR for both libraries.

Subsequent investigation of the MERGE code revealed that it determines which PTs are included in the final version of the ECCOLIB. This selection is based on a threshold defined by the lowest energy group containing PT data for the (n,xn) reactions. The code prints only PTs corresponding to energy groups below this threshold in the MF=50 file of the GENDF*. Conversely, energy groups above the threshold, which contain subgroup data for (n,xn) reactions, are excluded. As a result, PTs for all the reactions are not stored in the ECCOLIB at energy values higher than the (n,xn) threshold.

Listing 7.3 shows the probability tables produced by CALENDF for U-238, focusing on the the 833th and 834th energy groups, using the ENDF/B-VIII.0 tape. The first two columns are reserved to the probability weights (first column) and the quadrature points for the total reaction (second column). The subsequent columns contain the quadrature points for the partial reactions. These partial reactions are grouped according to specific MT numbers, denoted by

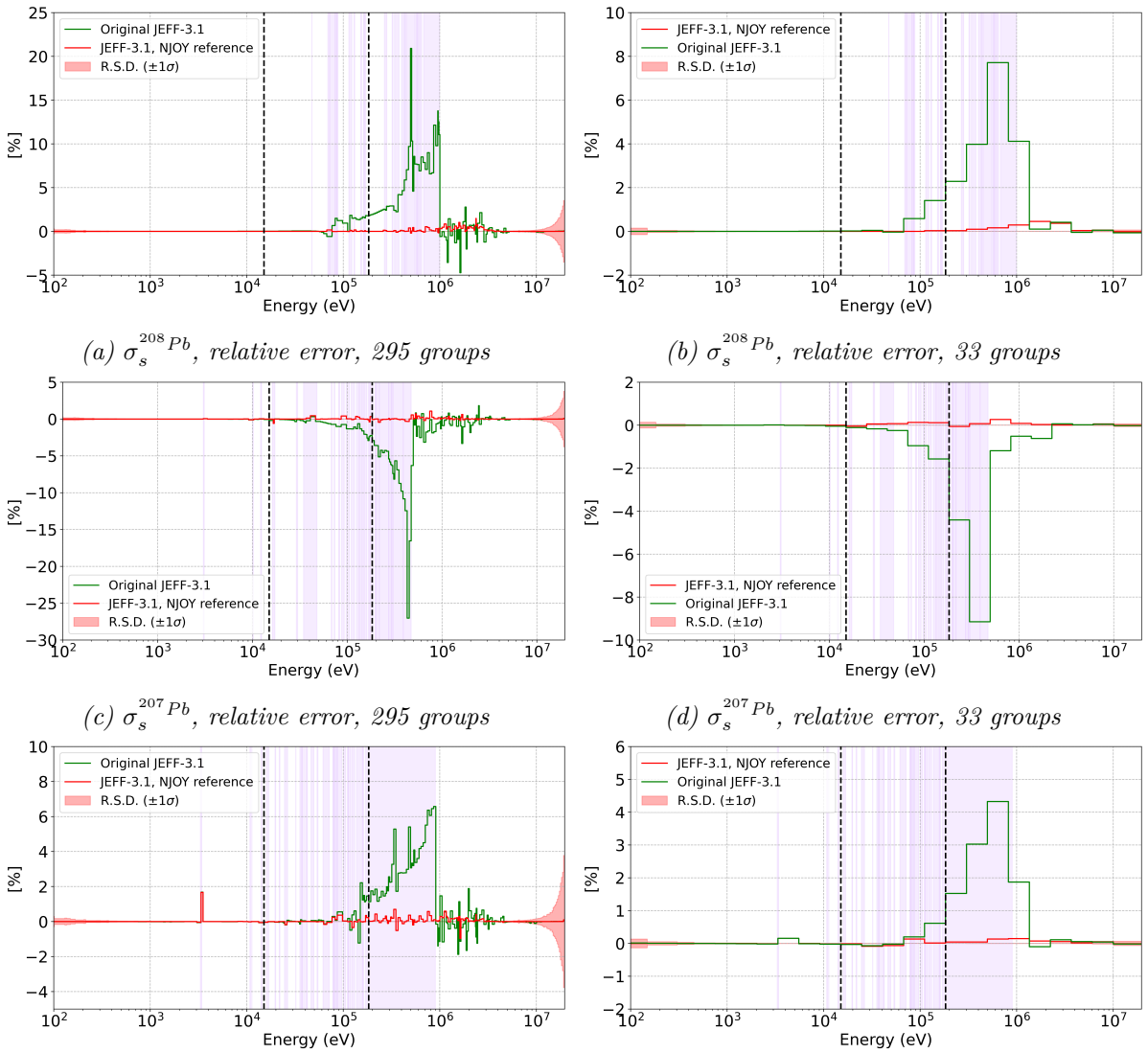


*(a)* $\sigma_s^{^{208}Pb}$*, relative error, 295 groups*

*(b)* $\sigma_s^{^{208}Pb}$*, relative error, 33 groups*

*(c)* $\sigma_s^{^{207}Pb}$*, relative error, 295 groups*

*(d)* $\sigma_s^{^{207}Pb}$*, relative error, 33 groups*

*(e)* $\sigma_s^{^{206}Pb}$*, relative error, 295 groups*

*(f)* $\sigma_s^{^{206}Pb}$*, relative error, 33 groups*

*Figure 7.4: LFR infinite and homogeneous fuel pin. The relative error of ECCO with respect to OpenMC is calculated using the original CEA JEFF-3.1 ECCOLIB (green line) and the modified JEFF-3.1 ECCOLIB (red line), where lead data are replaced with a new library obtained using the NJOY values as a reference in MERGE. The comparison is made for the elastic scattering cross sections of Pb-208, Pb-206, and Pb-207, using 33 and 295 group structures. The black dashed lines indicate the URR bounds of U-238. Purple coloured band highlight energy groups containing PTS in the CEA JEFF-3.1 ECCOLIB.*

the "KP" term in the output headers. For example, the third column contains quadrature points for elastic scattering (KP=2), the fourth for capture (KP=101), and so on. As described in Section 3.2.2, the MT=15 is used for the grouping of the (n,xn) reactions. The 833th group contains PTs for the (n,xn), which are instead absent in the 834th. This implies that all PTs at higher energies, including those for the unresolved range, will be excluded by MERGE. As the PTs are removed for all reactions, this includes the PTs for the U-238 capture reaction.

However, PTs are not expected for the (n,xn) reactions at energies below the MeV order. In fact, analysis of the ENDF-6 tape revealed that the threshold for the pointwise data of these reactions is considerably higher than the energies at which PTs are produced by CALENDF (e.g. the (n,2n) reaction has a threshold at 7 MeV for U-238). Indeed, when PTs are produced using the JEFF-3.1 ENDF-6 tapes for U-238, subgroup values for the (n,xn) reactions are only produced at energies higher than the threshold. This suggests that CALENDF is erroneously

producing PTs for the (n,xn) reactions, below their threshold, using the resonance parameters. Further investigation is needed to determine the cause of this misinterpretation of the raw data.

```
 IG  833 ENG=1.995887E+4 2.012589E+4 NOR=11 I=-10 NPAR=4 KP=   2 101  18  15   0
  8.577177-3  2.702000-1  2.553813-1  1.473369-2  8.503814-5  2.345894-9
  3.056989-2  3.356845-1  2.721168-1  6.348261-2  8.504764-5  2.333613-9
  5.346622-2  4.862693-1  4.212695-1  6.491268-2  8.710055-5  2.351507-9
  8.956268-2  9.477604-1  7.324945-1  2.151805-1  8.534999-5  2.319240-9
  1.642089-1  2.454326+0  2.107824+0  3.464147-1  8.757842-5  2.364274-9
  3.371137-1  7.634160+0  7.146410+0  4.876781-1  7.025548-5  1.253467-9
  2.286285-1  1.734318+1  1.617666+1  1.166443+0  7.169697-5  1.361733-9
  5.136123-2  4.533995+1  4.441522+1  9.246360-1  9.160289-5  2.574466-9
  2.388510-2  8.221654+1  8.118740+1  1.029055+0  8.481638-5  2.179661-9
  9.418547-3  1.162899+2  1.153413+2  9.485815-1  8.688142-5  2.474245-9
  3.208227-3  1.463174+2  1.447221+2  1.595256+0  8.517331-5  2.272760-9
 IG  834 ENG=1.979324E+4 1.995887E+4 NOR= 7 I= -6 NPAR=3 KP=   2 101  18   0   0
  2.450187-2  5.182770+0  4.871726+0  3.109943-1  4.962008-5
  1.578773-1  6.938149+0  6.722362+0  2.157374-1  4.968623-5
  4.647417-1  9.674722+0  9.275415+0  3.992562-1  4.963301-5
  2.179142-1  1.410824+1  1.351148+1  5.967084-1  4.974602-5
  6.585366-2  2.525063+1  2.490452+1  3.460587-1  4.977161-5
  5.205890-2  3.693145+1  3.606454+1  8.668687-1  4.972921-5
  1.705230-2  4.697313+1  4.639920+1  5.738785-1  4.984615-5
```

*Listing 7.3: Portion of the CALENDF output file containing PTs for U-238 at 294 K, produced using the ENDF/B-VIII.0 NDL. The first column contains the weight, while the second column contains the quadrature points for the total reaction. The following columns contain the quadrature points of the partial reactions associated with the MTs numbers indicated by the "KP" term in the headers.*

## 7.3 Conclusions about the production of an ECCOLIB based on the ENDF/B-VIII.0 NDL

The analysis of the production workflow of an ECCOLIB based on the ENDF/B-VIII.0 NDL revealed two main issues. The first issue concerned the lead isotopes and also occurred when the JEFF-3.1 NDL was used. Specifically, the NJOY and CALENDF codes differ in the cross sections reconstruction starting from the raw data in the ENDF-6 tapes. In order to quantify the impact of these discrepancies, the ECCOLIB production process had to be put in good use internally at *new*cleo. The NJOY, CALENDF, MERGE and GECCO codes were therefore used to generate a new ECCOLIB based on the JEFF-3.1 NDL for the lead isotopes. The quality of these new libraries was assessed by comparing them with the original CEA JEFF-3.1 ECCOLIB.

Once good adherence with the original library was ensured, the production workflow of the ECCOLIB could be revised for the lead isotopes by using the NJOY values as a reference in the MERGE code and adjusting the CALENDF PTs accordingly. The LFR homogeneous and infinite fuel pin, which was analysed in Chapter 5, was simulated again using the ECCO code and the internally produced JEFF-3.1 ECCOLIB. Considerably better agreement was found between the ECCO and OpenMC results when the new library was used. Notably, the relative errors in the elastic scattering cross sections of the lead isotopes (Pb-206, Pb-207, and Pb-208) decreased significantly compared to those observed in Chapter 5.

However, this result should be seen as a consequence of consistency being achieved between the NDLs of the two codes, and it does not imply that ECCO calculations are inaccurate when the CALENDF values are prioritised over those of NJOY. Although the numerical validation process involves making comparisons with Monte Carlo results, complete validation requires referencing the numerical results against experimental benchmarks. Only the latter process can determine which codes fail in the cross section reconstruction. Nevertheless, inconsistencies

in the nuclear data processing for ECCO and OpenMC complicate the numerical validation process. In fact, the discrepancies in the NDLs overshadow the errors arising from the self-shielding module, as detailed in Chapters 5 and 6.

The second issue concerned the absence of PTs for the URR of U-238 and U-235. These data are removed by the MERGE code, which clears the PTs for all energy groups in which subgroup data are present for the (n,xn) reactions. However, subgroup data for these reactions should not be included within the URR of these nuclides, as the energy threshold is considerably higher. Therefore, the latest version of CALENDF used to generate ECCOLIB (the 2010 version) could possibly be out of date with respect to the most recent NDLs. Although the ENDF-6 format has remained unchanged in recent years, significant progress has been made in experimental accuracy and detailed datasets that were previously inaccessible are now available. Indeed, when older NDLs such as JEFF-3.1 are used, the PTs for (n,xn) reactions are produced correctly above the threshold. Therefore, a revision of the CALENDF code is suggested in order to make it compatible with the most recent ENDF-6 tapes.

# Conclusions and future perspectives

The *new*cleo company adopted the ERANOS codes and data system for the neutronic analysis of its LFR units. ERANOS includes the ECCO cell and lattice code, which is a computational tool used to prepare homogenised, energy-averaged cross sections for subsequent full core calculations. For the licensing process, *new*cleo requires its scientific computing tools to be extensively validated for LFR applications. The aim of this thesis was to numerically validate the ECCO code by comparing simulations of LFR cells with those of the OpenMC Monte Carlo code. Specifically, the goal was to validate the ECCO self-shielding module. The analysis presented in this study revealed that this module alone, together with the ENDF/B-VIII.0 based ECCO Nuclear Data Library (NDL), explains most of the discrepancies encountered during previous validation work on ECCO for LFR cells [11].

The first part of this thesis provides an overview of the analytical models that are employed in the ECCO cell code, including the Multigroup formalism and the Collision Probability (CP) method. Particular focus was given to the analytical description of the Subgroup method used in ECCO to treat self-shielding effects. This method recasts the Riemann integrals required for the energy condensation of cross sections into Lebesgue integrals, and consequently applying Gauss quadrature formulas to numerically compute them. These quadrature formulas, also known as Probability Tables (PTs), are produced for ECCO by the nuclear data processing code CALENDF and integrated into the ECCO NDLs. The procedure for generating ECCO NDLs is outlined in Chapter 3.

The second part of this thesis was dedicated to the numerical validation of the self-shielding module. First, a Sensitivity Analysis (SA) was performed on a case representative of LFR applications, namely the Nuclear Energy Agency (NEA) lead-cooled fast reactor benchmark [12]. This analysis identified the nuclides and reactions with the greatest influence on the effective multiplication factor and Doppler reactivity change. The selected set of nuclides and reactions - for instance, U-238 capture, Pu-239 fission, and Pb-208 and Fe-56 elastic scattering - was focused during the validation of the ECCO self-shielding module. The numerical validation followed the approach adopted by P. Jacquet for the ECCO validation in SFR cells [9]. The analysis was performed on both LFR and SFR cells, using the ENDF/B-VIII.0 ECCOLIB. For specific purposes, the JEFF-3.1 NDL was also adopted.

Analysis of simple homogeneous media revealed that the significant discrepancies between ECCO and OpenMC could primarily be attributed to the PTs contained in the ENDF/B-VIII.0 ECCO library. Noteworthy differences were found for U-238 and lead isotopes in particular. For the former, the PTs are absent in the unresolved resonance range, resulting in ECCO overestimating the capture cross section. For the latter, significant errors in the elastic scattering cross sections were associated with energy groups containing PTs. Even when heterogeneous media were analysed, the same cross section errors induced by the NDLs were evident. However, in this case, numerical approximations induced by the CP method were also present.

Chapter 6 then presented the results of a Decomposition Analysis (DA), which broke down the differences between ECCO/ERANOS and OpenMC according to the individual errors in the nuclide cross sections that caused them. This determined the influence of the errors in the U-238

capture and Pb-208 elastic scattering cross sections on the errors in the multiplication factor and Doppler reactivity change. The DA was performed in two media: a simplified one, such as the LFR heterogeneous and infinite fuel pin, and a more complex one, such as the LFR reactor core, both defined according to the NEA numerical benchmark. In the former case, errors in the U-238 capture cross section accounted for two thirds of the discrepancy observed in the infinite multiplication factor of the fuel pin. In the latter case, the error in the effective multiplication factor of the core, determined by the errors in the U-238 capture cross section, was compensated for by that induced by the errors in the Pb-208 elastic scattering cross sections. This result highlights the need for counteractive measures for the ECCO libraries. Indeed, the absence of PTs for U-238 may complicate the ECCO validation.

Finally, Chapter 7 assessed the cause of the discrepancies in the ENDF/B-VIII.0 NDL. Discrepancies in the lead isotopes cross sections are caused by different reconstructions of the pointwise data operated by the NJOY and CALENDF codes. By revising the ECCOLIB production workflow and applying corrective factors to the CALENDF PTs to match the NJOY multigroup cross sections, differences in the lead cross sections within the homogeneous LFR fuel pin could be significantly reduced. For U-238 (and U-235), the reason for the missing PTs lies in the CALENDF misinterpretation of the threshold value for (n,xn) reactions. This value determines the energy groups that contain PTs in the final ECCO NDL version.

In light of these results, the main conclusion to be drawn from this study is that the CALENDF code needs to be updated. In fact, the (n,xn) threshold value is not misinterpreted with older NDLs, such as the JEFF-3.1. Therefore, the CALENDF code may be outdated with respect to the most modern NDLs, such as the ENDF/B-VIII.0. Although its format is still the ENDF-6 one, they could contain datasets that were not foreseen at the time the code was developed. The primary objective of future work is therefore to modernise and update the system of codes for the ECCOLIB generation, making it compatible with modern NDLs. Furthermore, it would be valuable to develop a platform to assist users in managing the suite of codes for the ECCOLIB generation. This would automate many informatics operations and reduce the number of user-dependent actions that could affect the NDL quality, enhancing also the reproducibility of the process.

Furthermore, detailed investigations are required to determine whether normalising the CALENDF values for the lead isotopes, with respect to the NJOY values, can produce reliable results. In fact, the reduction in the cross sections errors for these nuclides is simply the result of consistency being achieved between the ECCO and OpenMC NDLs. However, this result alone does not imply that the cross sections reconstruction performed by NJOY is more accurate than that performed by CALENDF. Comparisons with experimental benchmark data are needed to determine which code more accurately reproduces the physical world. Moreover, the investigation should be expanded to assess the impact of using the NJOY values as a reference for all other nuclides. In particular, it should be determined whether this could reduce the discrepancy observed for Pu-239 in the unresolved range, found when using the JEFF-3.1 NDL in OpenMC and TRIPOLI-4®.

Chapter 6 showed that the Doppler reactivity change calculated using ECCO or ERANOS is poorly affected by errors originating from the NDLs. Furthermore, a significant discrepancy in the effective multiplication factor of the LFR benchmark core was observed. Nevertheless, it was determined that this discrepancy is likely unrelated to NDLs. However, the analysis was limited to a small set of isotopes located in the fuel assemblies. It would be worthwhile to extend the analysis investigating the role of other nuclides located in different regions of the reactor, particularly focusing on the effect of the errors in the lead cross sections on neutron leakage. Moreover, achieving a precise DA may require performing SA using the exact perturbation theory in ERANOS, which could potentially reduce the discrepancies observed with Serpent2 Monte Carlo results. Nevertheless, the main constraint for both sensitivity and decomposition analyses is the limitation of deriving sensitivity coefficients for a two-dimensional R-Z geometry

in ERANOS.

In conclusion, this thesis demonstrated the crucial importance of achieving consistency between the NDLs for the deterministic and stochastic tools when carrying out a numerical validation. Generating the NDLs correctly for ECCO would lay the foundation for a comprehensive validation of the ECCO cell code. Otherwise, errors arising from NDLs would complicate the assessment of the code's accuracy by overshadowing those arising from the models implemented in ECCO. Resolving these issues would enable the validation activity to be extended in the future by assessing the accuracy of the other numerical modules, such as the Collision Probabilities, the Leakage model, and the homogenisation module.

# Appendices

## Appendix A

# Complete derivation of the scattering term

The scattering cross section is commonly expressed as the product between the pointwise cross section and a Probability Density Function (PDF) [15, 14], i.e.

$$\Sigma_s(\overline{r}, E' \to E, \overline{\Omega}' \to \overline{\Omega}) = \Sigma_s(\overline{r}, E') f(E' \to E, \overline{\Omega}' \to \overline{\Omega}), \tag{A.1}$$

where the scattering function $f$ must satisfy the normalisation condition

$$\int_0^\infty dE' \oint_{4\pi} d\Omega' f(E' \to E, \overline{\Omega}' \to \overline{\Omega}) = 1. \tag{A.2}$$

Under the assumption of isotropic medium, the elastic scattering function has an angular dependence only on the cosine of the scattering angle. Is therefore more convenient to express the PDF with another function $\eta$ that preserves the normalisation on this latter variable, i.e.

$$\oint_{4\pi} d\Omega' f(E' \to E, \overline{\Omega}' \to \overline{\Omega}) = \int_0^{2\pi} d\varphi \int_{-1}^{1} d\mu_0 \, \frac{1}{2\pi} \eta(E' \to E, \mu_0), \tag{A.3}$$

where the cosine of the scattering angle is expressed as $\mu_0 = \overline{\Omega}' \cdot \overline{\Omega}$. The PDF is then expanded on a infinite series of Legendre polynomials, leading to

$$\eta(E' \to E, \mu_0) = \sum_{l=0}^{\infty} \frac{2l+1}{2} \eta_l(E' \to E) P_l(\mu_0), \tag{A.4}$$

The expansion coefficients are the $l$-order moments of the scattering function, and are defined by the projection of the PDF on the Legendre polynomials, i.e.

$$\eta_l(E' \to E) = \int_{-1}^{1} \eta(E' \to E, \mu_0) P_l(\mu_0) d\mu_0. \tag{A.5}$$

The Legendre polynomials [25, 14, 26] are a complete orthogonal set of functions that allows the expansion of a generic function defined on the interval [-1,1]. These polynomials are defined through the relations

$$P_0(x) = 1, \tag{A.6}$$

$$P_l(x) = \frac{1}{2l!} \frac{d^l}{dx^l} (x^2 - 1)^l \quad \text{for} \quad l = 1, 2 \ldots \tag{A.7}$$

The first few Legendre polynomials are then

$$P_0(x) = 1, \tag{A.8}$$

$$P_1(x) = x, \tag{A.9}$$

$$P_2(x) = \frac{1}{2}(3x^2 - 1). \tag{A.10}$$

The orthogonality is ensured by the satisfaction of the relation

$$\int_{-1}^{1} P_m(x)P_l(x)dx = \frac{2\delta_{m,l}}{2l+1}, \tag{A.11}$$

where $\delta_{m,l}$ is the Kronecker delta. In practice, the summation in equation (A.4) is truncated at a specific order $L$. This is called the scattering anisotropy order, from the observation that for $L = 0$,

$$\eta(E' \to E, \mu_0) \approx \frac{1}{2}\eta_0(E' \to E), \tag{A.12}$$

and therefore any possible PDF is characterised by a completely isotropic distribution. For every increase of $L$, the representation of the angular dependence of the scattering function increases in accuracy.

These polynomials are introduced since they allow the factorization of the cosine of the scattering angle through the use of the Legendre addition theorem, i.e.

$$P_l(\mu_0) = \sum_{\beta=-l}^{l} \frac{(l-\beta)!}{(l+\beta)!} P_l^\beta(\mu)P_l^\beta(\mu')e^{i\beta(\varphi-\varphi')}, \tag{A.13}$$

where the Legendre associated function is defined for a positive $\beta$ as

$$P_l^\beta(x) = (1-x^2)^{\frac{\beta}{2}} \frac{d^\beta}{dx^\beta} P_l(x), \tag{A.14}$$

while for negative $\beta$ they are related to positive indexes by means of

$$P_l^{-\beta} = (-1)^\beta \frac{(l-\beta)!}{(l+\beta)!} P_l^\beta. \tag{A.15}$$

The scattering cross section can now be expressed in terms of the preceding relations to obtain

$$\Sigma_s(\overline{r}, E' \to E, \overline{\Omega}' \cdot \overline{\Omega}) = \sum_{l=0}^{\infty} \sum_{\beta=-l}^{l} \frac{2l+1}{4\pi} \frac{(l-\beta)!}{(l+\beta)!} \Sigma_{s,l}(\overline{r}, E' \to E) P_l^\beta(\mu)P_l^\beta(\mu')e^{i\beta(\varphi-\varphi')}, \tag{A.16}$$

where the $l$-order moment of the scattering cross section has been expressed as the product of the pointwise definition and the PDF expressed by $\eta$. In order to complete the derivation, it is necessary to introduce an additional set of functions, namely the spherical harmonics [15, 14]. These are a complete orthonormal base on the surface of a sphere, defined as

$$Y_l^\beta(\overline{\Omega}) = \left( \frac{2l+1}{4\pi} \frac{(l-\beta)!}{(l+\beta)!} \right)^{\frac{1}{2}} P_l^\beta(\mu)e^{i\beta\varphi}. \tag{A.17}$$

As for the Legendre polynomials, the orthogonality of the spherical harmonics is ensured by

$$\oint_{4\pi} Y_l^\beta(\overline{\Omega})Y_m^{\alpha*}(\overline{\Omega})\, d\Omega = \delta_{l,m}\delta_{\alpha,\beta}, \tag{A.18}$$

with $Y_m^{\alpha*}(\overline{\Omega})$ being the complex conjugate of the spherical harmonic. In conclusion, the scattering operator can be expressed by separating the different terms according to the variable of integration, i.e.

$$\oint_{4\pi} d\Omega' \int_0^\infty dE'\ \Sigma_s(\overline{r}, E' \to E, \overline{\Omega}' \cdot \overline{\Omega})\phi(\overline{r}, E', \overline{\Omega}') = \tag{A.19}$$

$$\int_0^\infty dE' \sum_{l=0}^{\infty} \Sigma_{s,l}(\overline{r}, E' \to E) \sum_{\beta=-l}^{l} Y_l^\beta(\overline{\Omega}) \oint_{4\pi} d\Omega' \phi(\overline{r}, E', \overline{\Omega}')Y_l^{\beta*}(\overline{\Omega}'), \tag{A.20}$$

where the last term, i.e.

$$\phi_l^\beta(\overline{r}, E') = \oint_{4\pi} d\Omega' \phi(\overline{r}, E', \overline{\Omega}')Y_l^{\beta*}(\overline{\Omega}'), \tag{A.21}$$

is defined as the moment of the angular flux.

## Appendix B

# Derivation of the integral transport equation

The integral form of the transport equation represents an equivalent form to the integro-differential Boltzmann equation. Within the framework of the multigroup method, Eq. (1.24) can be expressed by including the self-scattering term into the source term, which leads to

$$\overline{\Omega} \cdot \nabla \phi_g(\overline{r}, \overline{\Omega}) + \Sigma_{t,g}(\overline{r}) \phi_g(\overline{r}, \overline{\Omega}) = Q_g(\overline{r}, \overline{\Omega}) \quad \text{for } g = 1 \dots G. \tag{B.1}$$

In the framework of the method of characteristics, the total derivative of the neutron flux can be defined as [14, 25]

$$\frac{d\phi_g(\overline{r}, \overline{\Omega})}{ds} = \frac{\partial \phi_g(\overline{r}, \overline{\Omega})}{\partial x}\frac{dx}{ds} + \frac{\partial \phi_g(\overline{r}, \overline{\Omega})}{\partial y}\frac{dy}{ds} + \frac{\partial \phi_g(\overline{r}, \overline{\Omega})}{\partial z}\frac{dz}{ds}, \tag{B.2}$$

under the assumption of steady-state conditions. Considering the leakage term on the LHS of Eq. B.1, i.e.

$$\overline{\Omega} \cdot \nabla \phi_g(\overline{r}, \overline{\Omega}) = \left( \Omega_x \frac{\partial}{\partial x} + \Omega_y \frac{\partial}{\partial y} + \Omega_z \frac{\partial}{\partial z} \right) \phi_g(\overline{r}, \overline{\Omega}), \tag{B.3}$$

it can be noticed that this term coincides with the term in Eq.(B.2) where

$$\begin{aligned} \Omega_x &= \frac{dx}{ds}, \\ \Omega_y &= \frac{dy}{ds}, \\ \Omega_z &= \frac{dz}{ds}, \end{aligned} \tag{B.4}$$

which has solution

$$\begin{aligned} x &= x_0 + \Omega_x s, \\ y &= y_0 + \Omega_y s, \\ z &= z_0 + \Omega_z s, \end{aligned} \tag{B.5}$$

which are the coordinates of the so-called characteristic line $\overline{r} = \overline{r}_0 + s\overline{\Omega}$ [14, 24]. Along this line, which is specific to each point $\overline{r}_0$ and a fixed $\overline{\Omega}$, the leakage term corresponds to the total derivative of the neutron flux under steady-state conditions, and the Boltzmann equation can be expressed along this line leading to

$$\frac{d}{ds}\phi_g(\overline{r}_0 + s\overline{\Omega}, \overline{\Omega}) + \Sigma_{t,g}(\overline{r}_0 + s\overline{\Omega})\phi_g(\overline{r}_0 + s\overline{\Omega}, \overline{\Omega}) = Q_g(\overline{r}_0 + s\overline{\Omega}, \overline{\Omega}). \tag{B.6}$$

This equation is solved using the method of Lagrange [24], which first involves determining the solution to the homogeneous problem, i.e.

$$\phi_g^h(\overline{r}_0 + s\overline{\Omega}, \overline{\Omega}) = C \exp\left[ - \int^s ds' \Sigma_{t,g}(\overline{r}_0 + s'\overline{\Omega}) \right], \tag{B.7}$$

which is also the solution to Eq. (B.6), but this time with $C$ as a function of the variable $s$ [24]. Inserting the angular flux in Eq. (B.6) leads to an expression for $C(s)$ that reads

$$\frac{d}{ds}C(s) = Q_g(\overline{r}_0 + s\overline{\Omega}, \overline{\Omega}) \exp\left[\int^s ds' \Sigma_{t,g}(\overline{r}_0 + s'\overline{\Omega})\right], \tag{B.8}$$

which is then integrated for all the previous points to $\overline{r}_0$ along the characteristic line, i.e. for $s$ that ranges from $-\infty$ to 0, which leads to

$$C(s) = C(-\infty) + \int_{-\infty}^{s} ds' Q_g(\overline{r}_0 + s'\overline{\Omega}, \overline{\Omega}) \exp\left[\int^{s'} ds'' \Sigma_{t,g}(\overline{r}_0 + s''\overline{\Omega})\right]. \tag{B.9}$$

This term can then be substituted into Eq. (B.7) in place of $C$, yielding the final shape of the angular flux. It is then assumed that neutrons are not present at the extreme boundaries of the domain, which is equivalent to affirming that for $s \to -\infty$, $\phi_g(\overline{r}_0 + s\overline{\Omega}, \overline{\Omega}) \to 0$ [24]. This condition determines that $C(-\infty) = 0$, and the angular flux now reads

$$\phi_g(\overline{r}_0 + s\overline{\Omega}, \overline{\Omega}) = \int_{-\infty}^{s} ds' Q_g(\overline{r}_0 + s'\overline{\Omega}, \overline{\Omega}) \exp\left[-\int_{s'}^{s} ds'' \Sigma_{t,g}(\overline{r}_0 + s''\overline{\Omega})\right], \tag{B.10}$$

from which the integral transport equation for the angular flux can easily be derived for $s = 0$. Finally, changing the sign of the integration variables yields

$$\phi_g(\overline{r}, \overline{\Omega}) = \int_0^{\infty} ds' Q_g(\overline{r}_0 - s'\overline{\Omega}, \overline{\Omega}) \exp\left[-\int_0^{s'} ds'' \Sigma_{t,g}(\overline{r}_0 - s''\overline{\Omega})\right]. \tag{B.11}$$

The physical interpretation of this equation is that the angular flux at a given position is made by the contribution of all neutrons that appear along the characteristic line, due to scattering and fission reactions, and reach that specific position with the required angular direction. However, along this path, neutrons can undergo several reactions that remove them from the characteristic line. This attenuation of the flux is given by the exponential term in Eq. (B.11), i.e.

$$e^{-\tau_g(\overline{r} - s'\overline{\Omega} \to \overline{r})} = \exp\left[-\int_0^{s'} ds'' \Sigma_{t,g}(\overline{r}_0 - s''\overline{\Omega})\right], \tag{B.12}$$

which is indeed the probability of the neutron undergoing a reaction at any point along its path from the emission to the location $\overline{r}$. Usually, the exponent in this term, $\tau_g(\overline{r} - s'\overline{\Omega} \to \overline{r})$, is referred to as the optical path length [14, 24, 25, 13]. Furthermore, Eq. (B.11) does not require integration to an infinite distance along the characteristic line. In fact, it is sufficient for the integration to be performed up to the system boundaries, where the incoming flux is known [14, 24].

As the angular flux is generally of little interest in reactor physics applications, an integral equation for the scalar flux is generally employed. Its derivation requires the assumption of an isotropic source (isotropic fission and scattering) [14, 24], i.e.

$$Q_g(\overline{r}', \overline{\Omega}) = \frac{1}{4\pi} Q_g(\overline{r}'). \tag{B.13}$$

Then, Eq. (B.11) is integrated over all angular directions to obtain

$$\Phi_g(\overline{r}) = \oint d\Omega \int_0^{\infty} ds' \frac{1}{4\pi} Q_g(\overline{r}') e^{-\tau_g(\overline{r}' \to \overline{r})}, \tag{B.14}$$

where $\overline{r}' = \overline{r}_0 - s'\overline{\Omega}$. It can be noted that the integration in Eq. (B.14) with respect to $\overline{\Omega}$ and $s'$ can be further elaborated as a volume integral [13]. Using a spherical coordinate system, as shown in Figure B.1, the incremental volume can be determined as

$$dV' = d\Omega ds' (s')^2, \tag{B.15}$$

where $(s')^2 = |\overline{r} - \overline{r}'|^2$.

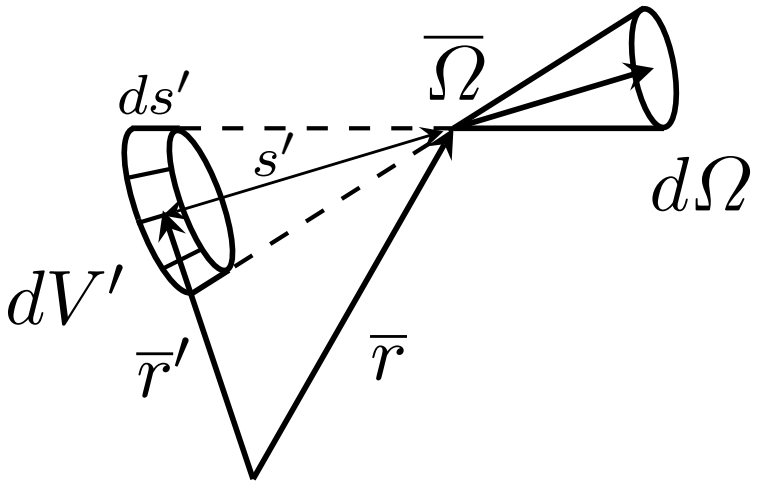


*Figure B.1: Schematization of the incremental volume $dV$, for a distance $s'$ from the location $\overline{r}$. Adapted from [13].*

In conclusion, the integral equation for the scalar flux reads

$$\Phi_g(\overline{r}) = \int dV' \frac{Q_g(\overline{r}')}{4\pi|\overline{r} - \overline{r}'|^2} e^{-\tau_g(\overline{r}' \to \overline{r})}, \tag{B.16}$$

where the term that multiplies the isotropic source is known as the Kernel of the integral transport equation. This represents the probability that neutrons, emitted isotropically in $\overline{r}'$ due to scattering and fission reactions, are transported without colliding in $\overline{r}$ [24]. Therefore, the physical interpretation of Eq. (B.16) is that the scalar flux at a given position is the sum of the contributions from all neutrons emitted at any point within the domain, attenuated by the probability of these neutrons reaching that specific location. Furthermore, although the volume integral is performed over the infinite space, it is restricted to a finite domain if this is surrounded by vacuum boundary conditions. In fact, in this case, the source term in Eq. (B.16) will vanish outside the boundaries.

## Appendix C

# The elastic scattering and the resonance models

The scattering of neutrons with the medium of a fission nuclear reactor plays a key role in the intended use of the nuclear fuel. The behaviour of neutrons strongly depends on the interactions with the atoms composing the medium, laying the foundation for the reactor core design. Whenever a neutron collides with an atom and a scattering reaction occurs, a fundamental distinction must be made between whether the scattering is elastic or inelastic [15]. In the latter case, as a result of the collision, the neutron is absorbed into the atom and an excited compound is generated. The excited state is derived by the atom's acquisition of the neutron kinetic energy, in addition to the binding energy resulting from the interactions between the neutron and the atom's nucleus.

The excited energy can only take discrete values, also called energy levels. In the case of heavy elements, the distribution of the energy levels is highly dense with low threshold values. In the case of U-238, for example, the threshold energy is about 40 KeV and the energy difference between the different levels is of the order of several KeV [15]. For light elements, on the other hand, the thresholds can be of the order of the MeV and the spacing between the few levels of the same order. Inelastic scattering is therefore a dominant effect only for heavy elements and in the high-energy range.

Elastic scattering, on the contrary, is the dominant reaction for both heavy and light elements in the whole energy range. Nevertheless, some distinctions can be made depending on the energy interval [14]. In the thermal region (in the eV range) the thermal motion of medium's atoms is not negligible and up-scattering reactions, with a consequent increase of the colliding neutron's energy, must be considered. In addition, in the thermal region, the particles that bound in molecules are not free to recoil as a consequence of the collision, resulting in a strong influence on the scattering cross section. In fast-spectrum reactors, however, only a very small fraction of neutrons reside in the thermal energy range, and these effects can be neglected in slowing down theory.

For the derivation of the scattering term for elastic collisions [88, 20, 15, 25], Figure C.1 shows the schematisation of a collision between an incident neutron and a stationary nuclide. As a result of the collision, the neutron is deflected with a lower energy $E$. Since the collision is elastic, the internal quantum states of the nucleus remain unchanged, and therefore the energy lost by the neutron is transferred to the kinetic energy of the recoiling nucleus. The conservation law is then applied in two reference systems: the LAB system and the Centre of Mass system (CM). In the LAB, the position of the CM is given by

$$(m + m_A)\overline{r}_{CM} = m\ \overline{r} + m_A\ \overline{r}_A, \tag{C.1}$$

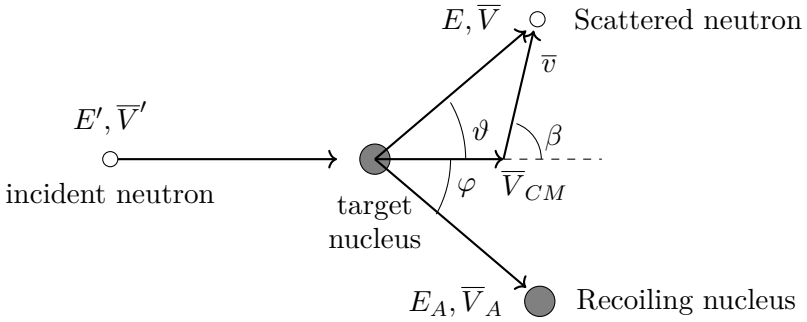


*Figure C.1: Schematization of the elastic collision between the incident neutron and the target nucleus at rest, in which momentum and kinetic energy are conserved. The neutron, initially moving at velocity $\overline{V'}$, is deflected with velocity $\overline{V}$ and angle $\theta$.*

where $m$ and $m_A$ are respectively the mass of the neutron and of the nucleus. The velocity of the CM in the LAB is expressed as

$$(1 + A)\overline{V}_{CM} = \overline{V}' = \overline{V} + A\ \overline{V}_A, \tag{C.2}$$

where $\overline{V}'$ and $\overline{V}$ are the velocities of the neutron before and after the collision, $\overline{V}_A$ the recoil velocity of the nucleus, $A$ is the mass ratio between the neutron and the nucleus, approximated by the mass number of the latter. The target nucleus is assumed at rest prior to the collision, i.e. $\overline{V}'_A = 0$. From Eq. (C.2) follows

$$\overline{V}_{CM} = \frac{1}{A+1}\overline{V}'. \tag{C.3}$$

The neutron and recoiling nucleus are then described with respect to the CM reference frame using Eq. (C.2), which leads to

$$\overline{v}' = \overline{V}' - \overline{V}_{CM} = \frac{A}{A+1}\overline{V}', \tag{C.4}$$

$$\overline{v} = \overline{V} - \overline{V}_{CM} = \frac{A}{A+1}(\overline{V} - \overline{V}_A), \tag{C.5}$$

$$\overline{v}'_A = \overline{V}'_A - \overline{V}_{CM} = -\frac{1}{A+1}\overline{V}', \tag{C.6}$$

$$\overline{v}_A = \overline{V}_A - \overline{V}_{CM} = -\frac{1}{A+1}(\overline{V} - \overline{V}_A). \tag{C.7}$$

It can be observed that in the CM reference frame, before and after the collision, the velocities of the neutron and the nucleus have opposite direction and the total momentum of the system is conserved [15], i.e.

$$\overline{v}' + A\ \overline{v}'_A = \overline{v} + A\ \overline{v}_A = 0. \tag{C.8}$$

In the CM reference frame, the energy conservation equation is expressed as

$$\frac{1}{2}(v')^2 + \frac{1}{2}A\ (v'_A)^2 = \frac{1}{2}v^2 + \frac{1}{2}A\ v_A^2, \tag{C.9}$$

and inserting $v'_A$ and $v_A$ from Eq.(C.8) in Eq. (C.9), it is obtained $(v')^2 = v^2$. This information is used to compute the kinetic energy of the neutron after the collision, in the LAB reference frame, by computing $V^2$ starting from Eq. (C.5) [15], which leads to

$$V^2 = (\overline{v} + \overline{V}_{CM})^2 = v^2 + V_{CM}^2 + 2\ \overline{v}\ \cdot\ \overline{V}_{CM}. \tag{C.10}$$

The first term is retrieved using the previous result and equation (C.4), i.e.

$$v^2 = (v')^2 = \left(\frac{A}{A+1}\right)^2 (V')^2, \tag{C.11}$$

while the last term is obtained by the cosine of the scattered neutron in the CM reference frame, as described in figure C.1, i.e.

$$2\ \overline{v}\cdot\overline{V}_{CM} = 2\ v\ V_{CM}\cos\beta = \frac{2A}{(A+1)^2}(V')^2\Psi, \tag{C.12}$$

where $\Psi = \cos\beta$ and $v = \frac{A}{A+1}V'$, since $v^2 = (v')^2$.

The kinematic energy of the neutron after the collision can finally be expressed as a function of the kinetic energy prior the collision as

$$E = \frac{1}{2}mV^2 = \frac{E'}{(A+1)^2}(A^2 + 2\Psi A + 1). \tag{C.13}$$

From this relation it can be observed that the neutron conserves its initial energy when $\Psi = 1$ (the neutron indeed maintains its initial direction), while the minimum energy that can remain after the collision is obtained when $\Psi = -1$, and the neutron is reflected back. In this case $E = \alpha E'$, where

$$\alpha = \left(\frac{A-1}{A+1}\right)^2. \tag{C.14}$$

Therefore, the lighter the target nucleus, the closer $\alpha$ will be to 0 and the greater the maximum fraction of energy that a neutron can lose in a collision. So far, valuable information has been retrieved about the energy values that a neutron can exhibit upon emerging from a collision, but the actual probability of the neutron assuming these values remains to be determined. This information can be recovered by introducing a probability density function $f(\Psi)$, such that $f(\Psi)d\Psi$ gives the probability that the neutron emerges from the collision with an angle in the neighbourhood $d\Psi$ in the CM reference frame. In reality, the neutron energy is the real variable of interest, but since these two quantities are related, as already observed in Eq. (C.13), the preservation of probability can be applied [15], which leads to

$$|\eta(E' \to E)dE| = |f(\Psi)d\Psi|, \tag{C.15}$$

which implies that the probability that the neutron emerges from the collision with an angle around $\Psi$ in the CM reference frame must be equal to the probability that the neutron emerges with an energy around $E$. The absolute value is introduced because an increase in $E$ corresponds to a decrease in $\Psi$ (the largest is the energy of the neutron after the collision, the smallest is its deflection). The PDF in terms of energy is then:

$$\eta(E' \to E) = f(\Psi)\left|\frac{d\Psi}{dE}\right| \tag{C.16}$$

And then, having obtained the Jacobian of the transformation from Eq. (C.13), it follows

$$\eta(E' \to E) = f(\Psi)\frac{(A+1)^2}{2AE'}, \tag{C.17}$$

which is further simplified by assuming isotropic scattering in the CM, i.e. $f(\Psi) = \frac{1}{2}$, leading to

$$\eta(E' \to E) = \frac{(A+1)^2}{4AE'} = \frac{1}{(1-\alpha)E'}. \tag{C.18}$$

Thus, the neutron has the same probability of assuming any energy value in the interval $[\alpha E', E']$ upon a collision, as shown in Figure C.2.

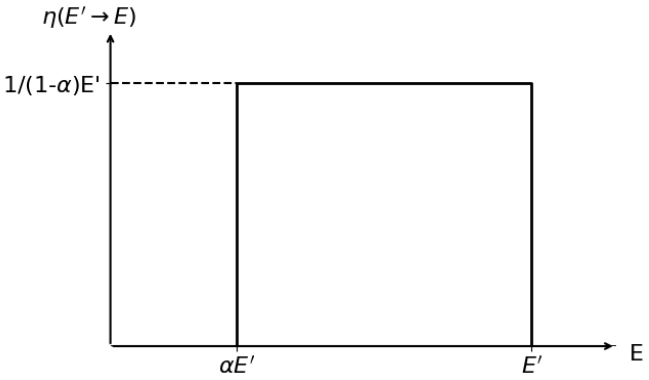


*Figure C.2: The PDF describing the neutron's energy after the scattering, in the case of isotropic scattering in the centre of mass reference frame. Under this hypothesis, the neutron has the same probability of emerging with any energy value in* $[\alpha E', E']$.

However, it must be emphasised that the assumption of isotropic scattering in the CM does not imply isotropy in the LAB. Indeed, the relation between the scattering angle in the CM and in the LAB is given by [15]

$$\mu_0 = \frac{1 + A\Psi}{(A^2 + 2\Psi A + 1)^{\frac{1}{2}}}, \tag{C.19}$$

where the assumption of isotropic scattering in the CM implies that $\overline{\Psi} = 0$, but

$$\overline{\mu_o} = \int_{-1}^{1} \mu_0(\Psi) f(\Psi)\ d\Psi = \frac{2}{3A}, \tag{C.20}$$

which corresponds to the condition of forward scattering [15], and it tends to isotropy only for the heavy elements. As a last remark, Appendix A showed that the scattering cross section is defined with the use of a joint PDF in energy and angular direction. The expansion of the scattering operator with the Legendre polynomial leads to

$$\hat{\theta}_s\phi = \int_0^\infty dE' \oint_{4\pi} d\Omega'\ \Sigma_s(\overline{r}, E') \sum_{l=0}^{L} \frac{2l+1}{4\pi} \eta_l(E' \to E) P_l(\mu_0) \phi(\overline{r}, E', \overline{\Omega}'), \tag{C.21}$$

which can be further simplified by assuming isotropic scattering (e.g. $L = 0$), leading to

$$\hat{\theta}_s\phi = \int_0^\infty dE' \oint_{4\pi} d\Omega'\ \Sigma_s(\overline{r}, E') \frac{1}{4\pi} \eta_0(E' \to E) \phi(\overline{r}, E', \overline{\Omega}'), \tag{C.22}$$

since $P_0(\mu_0) = 1$. The projection coefficient of the PDF is then

$$\eta_0(E' \to E) = \int_{-1}^{1} \eta(E' \to E, \mu_0) d\mu_0, \tag{C.23}$$

which requires knowledge of the joint PDF. However, all neutrons having an energy $E$ after the scattering will have the same scattering angle in the CM and in the LAB, and therefore the PDF can be expressed with a Dirac delta in the angle corresponding to the energy $E$ [25], which yields

$$\eta(E' \to E, \mu_0) = \eta(E' \to E)\ \delta[\mu_0 - f(E)]. \tag{C.24}$$

The computation of the zeroth order of the projection coefficient is straightforward thanks to the properties of the Dirac delta and it coincides with the energy PDF. Since the PDF is zero outside the interval $[\alpha E', E']$, the scattering operator is finally expressed as

$$\hat{\theta}_s\phi = \frac{1}{4\pi} \int_E^{E/\alpha} \frac{\Sigma_s(\overline{r}, E') \Phi(\overline{r}, E')}{(1-\alpha)E'} dE', \tag{C.25}$$

where the angular integration is carried out introducing the scalar flux.

Before proceeding further, additional information on the elastic scattering cross section must be provided. In general, this can be seen as the sum of three components [16, 26] : the resonance scattering, the interference scattering, and the potential scattering. The first term is related to the formation of a compound nucleus upon a collision, in analogy to the inelastic collision, but in this case with the re-emission of the neutron with unvaried kinetic energy. This term is highly dependent on the energy, showing classical resonant structures. The second therm describes the distortion of the resonances due to quantum interference with potential scattering [16]. The latter term is independent of energy for large intervals and describes the classical "billiard-ball" collision, which depends only on the atomic radius of the scattered nucleus. Figure C.3 reports the elastic scattering cross sections for some representative nuclides, showing how the resonance structures are imposed over an essentially constant cross section across almost the entire energy range.

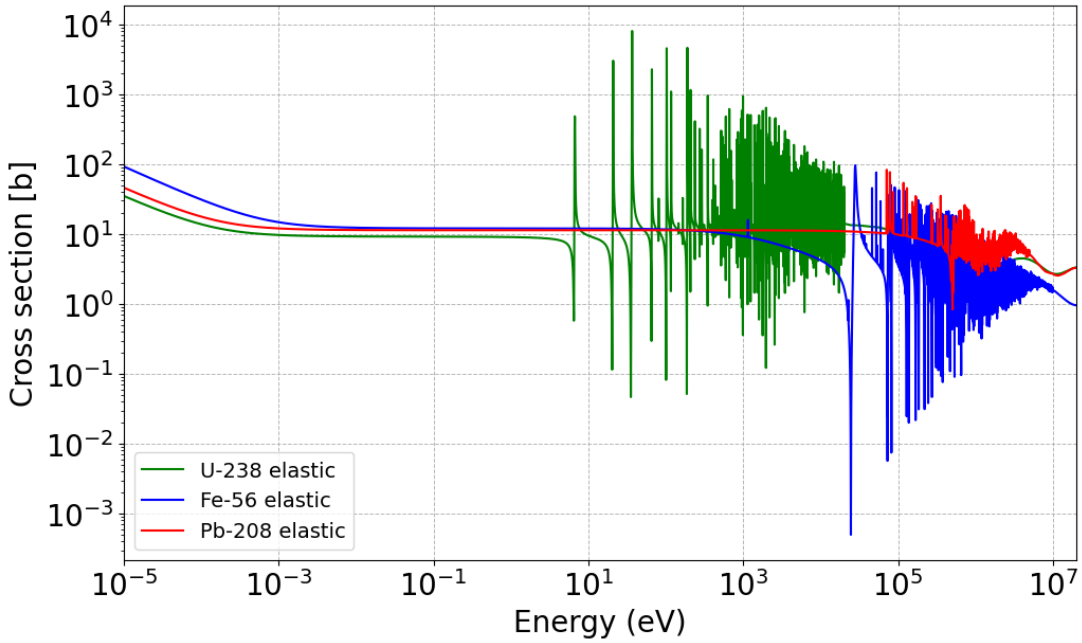


*Figure C.3: Plot of the elastic scattering cross section for three representative nuclides. It can be noted that, away from the resonance structures, the cross section is approximately constant.*

Therefore, when considering a specific energy group $g$, it is more convenient to separate the scattering term between the resonant elements $re$ and the non-resonant elements $nre$. The scattering term takes the form

$$\hat{\theta}_s\phi = \frac{1}{4\pi}\int_E^{E/\alpha^{re}} \frac{\Sigma_s^{re}(\bar{r},E')\Phi(\bar{r},E')}{(1-\alpha^{re})E'}dE' + \frac{1}{4\pi}\int_E^{E/\alpha^{nre}} \frac{\Sigma_p^{nre}(\bar{r})\Phi(\bar{r},E')}{(1-\alpha^{nre})E'}dE', \tag{C.26}$$

where, for the non-resonant elements, the scattering cross sections are reduced to only the potential scattering term [16],[20] . The previous expression can be further simplified by using three resonance models: the Narrow Resonance (NR), the Wide Resonance (WR), and the Intermediate Resonance (IR) models [16, 20, 25, 14, 23], . The following will briefly go through each of these assumptions and detail how they apply to the scattering term. These approximations can be applied to both the resonant and non-resonant terms of Eq. (C.26), depending on the specific situation.

In the NR model [23, 20], it is assumed that the width of the isolated resonance is much smaller than the average energy loss of a neutron in a collision, which is particularly true for light elements. It is assumed that the energy shape of the flux can be expressed as the product

of two terms, i.e.

$$\Phi(E) = f(E)\varphi(E), \tag{C.27}$$

where $f(E)$ describes the flux variations away from the resonances and $\varphi(E)$ describes the flux distribution close to the narrow resonance. Furthermore, it is assumed that, within the energy interval of the scattering term, which is much larger than the narrow resonance, the flux is essentially unperturbed by its presence. The flux shape is therefore described by $f$, and the scattering cross section is described only by the potential scattering, which is independent of the resonance structures, leading to

$$\hat{\theta}_s\phi = \frac{1}{4\pi}\int_E^{E/\alpha} \frac{\Sigma_s(\overline{r},E')\Phi(\overline{r},E')}{(1-\alpha)E'}dE' \approx \frac{1}{4\pi}\int_E^{E/\alpha} \frac{\Sigma_p(\overline{r})f(E')}{(1-\alpha)E'}\,dE' = \frac{1}{4\pi}\Sigma_p(\overline{r})C(E), \tag{C.28}$$

where

$$C(E) = \int_E^{E/\alpha} \frac{f(E')}{(1-\alpha)E'}\,dE'. \tag{C.29}$$

In a homogeneous and non-absorbing medium, it can be shown that the energy dependence of the flux is of the type $\Phi(E) \approx 1/E$, which is usually referred to as the asymptotic condition [16, 20] . Since the resonances are narrow, it is assumed that they are spaced far enough apart such that the flux assumes the asymptotic shape between them. This is commonly referred to as the flux recovery approximation [14]. Using the asymptotic shape of the flux in Eq. (C.29) gives

$$C(E) = \int_E^{E/\alpha} \frac{f(E')}{(1-\alpha)E'}\,dE' = \int_E^{E/\alpha} \frac{1}{(1-\alpha)(E')^2}\,dE' = \frac{1}{E}. \tag{C.30}$$

As mentioned above, the NR model is extremely valid for light elements, and it can be used to a good extent for the moderator. For the absorber, this model may not be valid and the WR model may provide better results. In this model [20, 23], on the contrary, the resonance interval is very large compared to the average energy loss of a neutron in a collision, which remains within the resonance interval. This condition can be taken to an extreme limit by assuming an infinite mass of the heavy nuclide, which implies taking $A \to \infty$, or $\alpha \to 1$. This is equivalent to the assumption that the neutron does not loose energy after a collision with the nucleus. Therefore, $E' \approx E$, and

$$\begin{aligned}\hat{\theta}_s\phi = \frac{1}{4\pi}\int_E^{E/\alpha} \frac{\Sigma_s(\overline{r},E')\Phi(\overline{r},E')}{(1-\alpha)E'}dE' = \lim_{\alpha\to 1}\frac{1}{4\pi}\int_E^{E/\alpha} \frac{\Sigma_s(\overline{r},E')\Phi(\overline{r},E')}{(1-\alpha)E'}dE' = \\ \frac{1}{4\pi}\Sigma_s(\overline{r},E)\Phi(\overline{r},E)\lim_{\alpha\to 1}\frac{1}{E}\int_E^{E/\alpha}\frac{1}{(1-\alpha)}dE' = \frac{1}{4\pi}\Sigma_s(\overline{r},E)\Phi(\overline{r},E)\lim_{\alpha\to 1}\frac{(\frac{1}{\alpha})-1}{1-\alpha} = \\ \frac{1}{4\pi}\Sigma_s(\overline{r},E)\Phi(\overline{r},E).\end{aligned} \tag{C.31}$$

However, both the NR and the WR models represent two extreme cases, which may not be appropriate for more complex cases, particularly when a mixture of nuclides is present. The Intermediate Resonance (IR) model represents a linear combination of the above models using the so called Goldstein-Cohen parameter $\lambda$ [25, 24], leading to

$$\hat{\theta}_s\phi = \frac{1}{4\pi}[\lambda\Sigma_p(\overline{r})C(E) + (1-\lambda)\Sigma_s(\overline{r},E)\Phi(\overline{r},E)], \tag{C.32}$$

where $\lambda$ ranges between 0 and 1, and must be specified for each energy group $g$ depending on the internal resonance structures (and therefore on the relative concentration of the heavy nuclides). It can be noted that when $\lambda$ is equal to one, the IR model reduces to the NR model, while on the contrary, when $\lambda$ is equal to 0, it reduces to the WR model.

## Appendix D

# Mathematical probability tables and generation of partial cross sections

The derivation of the Gauss quadrature for partial cross sections is straightforward once the quadrature $Q_{t,g} = \{\omega_k, \sigma_{t,k}\}_{g,k=1,K}$ for the total self-shielded cross section is known. In the framework of the method of moments [20, 37, 35, 8]. The evaluation of the l-th order moments of the total cross section is defined as

$$\mathcal{M}_{l,g} = \frac{1}{\Delta u_g} \int_{\Delta u_g} \sigma_t^l(u)\ du = \int_{D_g} \sigma_t^l\ \omega(\sigma_t)\ d\sigma_t, \tag{D.1}$$

and computed by the knowledge of the pointwise cross section. The moment can also be determined by using Gauss quadrature formula, which leads to

$$\tilde{M}_{l,g}(Q_{t,g}) = \sum_{k=1}^{K} \omega_{g,k}\ \sigma_{t,g,k}^l, \tag{D.2}$$

where $K$ is the number of subgroups into which the group $g$ has been divided. The method of moments retrieves the quadrature points as the ones that satisfy the system of $2K$ equations (in $2K$ unknowns $\{\omega_k, \sigma_{t,k}\}_{g,k=1,K}$) that reads

$$\mathcal{M}_{l,g} \approx \tilde{M}_l(Q_{t,g}) \quad \text{for } L \leq l \leq L + 2K - 1, \tag{D.3}$$

preserving $2K$ order moments. One degree of freedom is removed by imposing

$$\sum_{k=1}^{N} \omega_{g,k} = 1, \tag{D.4}$$

which is equivalent to preserving the 0-th order moment. The choice of the order moments to be preserved is completely arbitrary. A logical choice would be to preserve the order moments from 0 to $2K-1$, but it has been shown that the best choice is to preserve negative order moments [37], as for instance partial orders between -1 and 0 [54]. Solving the system of $2K$ nonlinear equations (D.3) involves the procedure shown below for $0 < l < 2K-1$, which can be extended to other cases. Introducing the function

$$F(z) = \int_{D_g} \frac{\omega(\sigma_t)}{1 - z\ \sigma_t}\ d\sigma_t = \int_{D_g} \omega(\sigma_t) \sum_{l=0}^{\infty} (z\sigma_t)^l\ d\sigma_t, \tag{D.5}$$

where a geometrical series expansion has been used [23, 8, 37, 20] , it can be noted that

$$F(z) = \sum_{l=0}^{\infty} z^l \int_{D_g} \sigma_t^l \omega(\sigma_t)\ d\sigma_t = \sum_{l=0}^{2K-1} z^l \mathcal{M}_{l,g} + \mathcal{O}(z^{2K}), \tag{D.6}$$

and then the PADE approximation [89] is used to expand $F(z)$, that now reads

$$F(z) = \frac{a_0 + a_1 z + a_2 z^2 + \cdots + a_{K-1} z^{K-1}}{1 + b_1 z + b_2 z^2 + \cdots + b_K z^K} + \mathcal{O}(Z^{2K}). \tag{D.7}$$

Equalizing Eqs. (D.6) and (D.7), and multiplying the final term of the former by the denominator of the latter, it is obtained

$$\sum_{j=0}^{K-1} a_j z^j = \left( \sum_{l=0}^{2K-1} z^l \mathcal{M}_{l,g} \right) \left( 1 + \sum_{m=1}^{K} b_m z^m \right), \tag{D.8}$$

with $b_0 = 1$. By collecting terms of the same power of $z$ [35], the set of $2K$ linear equations reads as

$$a_n = \sum_{m=0}^{n} \mathcal{M}_{(n-m),g}\ b_m \quad \text{for} \quad n = 0, 1, \ldots, K-1, \tag{D.9}$$

$$0 = \sum_{m=0}^{n} \mathcal{M}_{(N+n-m),g}\ b_m \quad \text{for} \quad n = 0, 1, \ldots, K-1. \tag{D.10}$$

The system of $K$ equations (D.10) can be solved for the coefficients $b_n$, which are then used in the system of $K$ equations (D.9) to solve for the coefficients $a_n$. The next step is to factorise the denominator of the PADE approximation, in Eq. (D.7), and then use a partial fraction expansion [35], i.e.

$$F(z) = \frac{\sum_{n=0}^{K-1} a_n z^n}{\prod_{k=1}^{K} (z - z_k)} + \mathcal{O}(z^{2K}) = \sum_{k=1}^{K} \frac{c_k}{z - z_k} + \mathcal{O}(z^{2K}) = \sum_{k=1}^{K} \frac{\tilde{c_k}}{\left(1 - \frac{z}{z_k}\right)} + \mathcal{O}(z^{2K}). \tag{D.11}$$

The conservation of moments is then applied in the expression of $F(z)$ in Eq. (D.6), which leads to

$$\begin{aligned} F(z) = \sum_{l=0}^{2K-1} z^l \mathcal{M}_l + \mathcal{O}(z^{2K}) \approx \sum_{l=0}^{2K-1} z^l \sum_{k=1}^{K} \omega_{g,k}\ \sigma_{t,g,k}^l + \mathcal{O}(z^{2K}) = \\ \sum_{k=1}^{K} \omega_{g,k} \sum_{l=0}^{2K-1} (z\ \sigma_{t,g,k})^l + \mathcal{O}(z^{2K}) = \sum_{k=1}^{K} \frac{\omega_{g,k}}{1 - z\ \sigma_{t,g,k}} + \mathcal{O}(z^{2K}). \end{aligned} \tag{D.12}$$

By similarity between Eqs. (D.11) and (D.12), it is possible to obtain

$$\sigma_{t,g,k} = \frac{1}{z_k}, \tag{D.13}$$

with the probability weight that are $\omega_{g,k} = \tilde{c_k}$. These can now be obtained without the partial fraction expansion: once the terms $z_k$ are known from the factorisation of the PADE approximation denominator, the $\sigma_{t,g,k}$ terms are computed and the solution to the linear system of K equations (D.2) (using the exact definition of the moments) will provide the missing terms. Once the quadrature for the total cross section has been derived, producing the quadrature of the partial cross section is straightforward. The moments for the partial cross section are defined and solved using the quadrature $Q_{x,g} = \{\omega_k, \sigma_{x,k}\}_{g,k=1,K}$ [23, 8], i.e.

$$\mathcal{M}_{l,x,g} = \frac{1}{\Delta u_g} \int_{\Delta u_g} \sigma_x(u)\ \sigma_t^l(u) du = \int_{D_{t,g}} d\sigma_t \int_{D_{x,g}} d\sigma_x\ \sigma_x\ \sigma_t^l\ \frac{\omega^*(\sigma_t, \sigma_x)}{\omega(\sigma_t)} \omega(\sigma_t), \tag{D.14}$$

and defining

$$h(\sigma_t) = \int_{D_{x,g}} d\sigma_x\ \sigma_x\ \frac{\omega^*(\sigma_t, \sigma_x)}{\omega(\sigma_t)}, \tag{D.15}$$

it is possible to obtain

$$\mathcal{M}_{l,x,g} = \int_{D_{t,g}} d\sigma_t \; \sigma_t^l \; h(\sigma_t) \; \omega(\sigma_t) = \sum_{k=1}^{K} \omega_{g,k} \; \sigma_{x,g,k} \; \sigma_{t,g,k}^l \quad \text{for } L \leq l \leq L + K - 1, \tag{D.16}$$

where it has been set [23]

$$\sigma_{x,g,k} = h(\sigma_{t,g,k}). \tag{D.17}$$

The solution of the $K$ linear equations (D.16) will then provide the partial quadrature set.

## Appendix E

# Sensitivity analysis results

## E.1 Sensitivity coefficients of the effective multiplication factor in the NEA LFR benchmark

| $S(k, \sigma_{n,x,r})$ MOX | | $x$ | | | | | |
|---|---|---|---|---|---|---|---|
| $n$ | $r$ | CAPTURE | FISSION | ELASTIC | INELASTIC | N,XN | SUM |
| U-235 | FINN | -4.47E-04 | 3.42E-03 | 3.90E-06 | -4.74E-05 | 6.50E-07 | 2.93E-03 |
| | FOUT | -2.34E-04 | 1.72E-03 | 7.46E-06 | -2.32E-05 | 3.93E-07 | 1.47E-03 |
| | REACTOR | -6.82E-04 | 5.15E-03 | 1.14E-05 | 7.06E-05 | 1.04E-06 | 4.41E-03 |
| Am-241 | FINN | -2.56E-03 | 1.09E-03 | 7.38E-06 | -5.95E-05 | 1.00E-07 | -1.52E-03 |
| | FOUT | -1.83E-03 | 8.25E-04 | 1.93E-05 | -3.96E-05 | 8.47E-08 | -1.02E-03 |
| | REACTOR | -4.39E-03 | 1.92E-03 | 2.67E-05 | -9.91E-05 | 1.85E-07 | -2.55E-03 |
| Pu-238 | FINN | -1.56E-03 | 7.40E-03 | 1.18E-05 | -7.24E-05 | 4.85E-08 | 5.79E-03 |
| | FOUT | -1.12E-03 | 5.26E-03 | 3.11E-05 | -4.63E-05 | 4.15E-08 | 4.13E-03 |
| | REACTOR | -2.68E-03 | 1.27E-02 | 4.30E-05 | -1.19E-04 | 9.00E-08 | 9.91E-03 |
| Pu-242 | FINN | -3.26E-03 | 5.78E-03 | 4.77E-05 | -3.55E-04 | 3.00E-06 | 2.22E-03 |
| | FOUT | -2.39E-03 | 4.33E-03 | 1.21E-04 | -2.31E-04 | 2.52E-06 | 1.83E-03 |
| | REACTOR | -5.65E-03 | 1.01E-02 | 1.69E-04 | -5.85E-04 | 5.52E-06 | 4.04E-03 |
| O-16 | FINN | -1.45E-03 | 0.00E+00 | -2.63E-02 | -1.16E-04 | 1.58E-10 | -2.78E-02 |
| | FOUT | -8.58E-04 | 0.00E+00 | -8.78E-03 | -5.91E-05 | 1.13E-10 | -9.70E-03 |
| | REACTOR | -2.49E-03 | 0.00E+00 | -3.64E-02 | -1.79E-04 | 3.17E-10 | -3.91E-02 |
| Pu-240 | FINN | -1.36E-02 | 2.87E-02 | 1.52E-04 | -1.25E-03 | 5.41E-06 | 1.40E-02 |
| | FOUT | -9.72E-03 | 2.11E-02 | 3.89E-04 | -8.17E-04 | 4.58E-06 | 1.10E-02 |
| | REACTOR | -2.33E-02 | 4.98E-02 | 5.42E-04 | -2.07E-03 | 9.98E-06 | 2.50E-02 |
| Pu-241 | FINN | -2.71E-03 | 4.43E-02 | 2.29E-05 | -3.39E-04 | 8.04E-06 | 4.13E-02 |
| | FOUT | -1.97E-03 | 3.09E-02 | 5.96E-05 | -2.18E-04 | 6.65E-06 | 2.88E-02 |
| | REACTOR | -4.68E-03 | 7.52E-02 | 8.27E-05 | -5.58E-04 | 1.47E-05 | 7.00E-02 |
| U-238 | FINN | -1.14E-01 | 3.38E-02 | 2.30E-03 | -2.55E-02 | 3.75E-04 | -1.03E-01 |
| | FOUT | -5.81E-02 | 1.90E-02 | 4.41E-03 | -1.24E-02 | 2.29E-04 | -4.68E-02 |
| | REACTOR | -1.72E-01 | 5.28E-02 | 6.73E-03 | -3.79E-02 | 6.04E-04 | -1.50E-01 |
| Pu-239 | FINN | -2.86E-02 | 2.92E-01 | 2.69E-04 | -2.05E-03 | 1.42E-05 | 2.62E-01 |
| | FOUT | -2.07E-02 | 2.04E-01 | 7.08E-04 | -1.33E-03 | 1.18E-05 | 1.83E-01 |
| | REACTOR | -4.94E-02 | 4.97E-01 | 9.79E-04 | -3.38E-03 | 2.60E-05 | 4.45E-01 |
| SUM (FINN + FOUT) | | -2.65E-01 | 7.04E-01 | -2.65E-02 | -4.49E-02 | 6.62E-04 | 3.69E-01 |
| SUM (REACTOR) | | -2.65E-01 | 7.04E-01 | -2.78E-02 | -4.49E-02 | 6.62E-04 | 3.67E-01 |

*Table E.1: NEA LFR benchmark core. Energy-integrated SCs for the effective multiplication factor for the most important nuclides of the MOX material in the fuel assemblies.*

| $S(k,\sigma_{n,x,r})$ AIM1 | | $x$ | | | | | |
|---|---|---|---|---|---|---|---|
| $n$ | $r$ | CAPTURE | FISSION | ELASTIC | INELASTIC | N,XN | SUM |
| | FINN | -3.87E-04 | 0.00E+00 | -6.81E-05 | -5.69E-04 | 9.16E-07 | -1.02E-03 |
| **Fe-57** | FOUT | -2.07E-04 | 0.00E+00 | 5.40E-05 | -2.73E-04 | 6.32E-07 | -4.25E-04 |
| | REACTOR | -9.03E-04 | 0.00E+00 | 1.27E-04 | -1.12E-03 | 1.93E-06 | -1.89E-03 |
| | FINN | -4.16E-04 | 0.00E+00 | 1.18E-04 | -2.57E-04 | 6.82E-07 | -5.55E-04 |
| **Cr-53** | FOUT | -2.30E-04 | 0.00E+00 | 2.12E-04 | -1.38E-04 | 4.72E-07 | -1.54E-04 |
| | REACTOR | -1.13E-03 | 0.00E+00 | 6.15E-04 | -4.55E-04 | 1.47E-06 | -9.67E-04 |
| | FINN | -7.56E-04 | 0.00E+00 | 6.48E-05 | -5.37E-04 | 5.49E-08 | -1.23E-03 |
| **Mn-55** | FOUT | -4.46E-04 | 0.00E+00 | 1.43E-04 | -2.72E-04 | 5.14E-08 | -5.74E-04 |
| | REACTOR | -2.57E-03 | 0.00E+00 | 4.55E-04 | -1.06E-03 | 1.56E-07 | -3.17E-03 |
| | FINN | -7.76E-04 | 0.00E+00 | -1.77E-04 | -4.56E-04 | 8.83E-08 | -1.41E-03 |
| **Ni-60** | FOUT | -4.18E-04 | 0.00E+00 | 2.16E-04 | -2.43E-04 | 6.51E-08 | -4.46E-04 |
| | REACTOR | -1.76E-03 | 0.00E+00 | 6.62E-04 | -7.88E-04 | 2.05E-07 | -1.88E-03 |
| | FINN | -1.11E-03 | 0.00E+00 | -1.35E-04 | -3.49E-04 | -8.66E-07 | -1.59E-03 |
| **Fe-54** | FOUT | -6.14E-04 | 0.00E+00 | 2.48E-04 | -1.85E-04 | -4.91E-07 | -5.52E-04 |
| | REACTOR | -2.36E-03 | 0.00E+00 | 7.01E-04 | -6.00E-04 | -1.55E-06 | -2.26E-03 |
| | FINN | -8.51E-04 | 0.00E+00 | -2.14E-04 | -1.33E-03 | 1.96E-07 | -2.39E-03 |
| **Cr-52** | FOUT | -4.63E-04 | 0.00E+00 | 5.51E-04 | -7.02E-04 | 1.45E-07 | -6.14E-04 |
| | REACTOR | -2.05E-03 | 0.00E+00 | 1.71E-03 | -2.27E-03 | 4.58E-07 | -2.60E-03 |
| | FINN | -3.53E-03 | 0.00E+00 | -8.95E-04 | -8.66E-04 | 1.45E-08 | -5.29E-03 |
| **Ni-58** | FOUT | -1.98E-03 | 0.00E+00 | 3.28E-04 | -4.63E-04 | 1.05E-08 | -2.12E-03 |
| | REACTOR | -7.39E-03 | 0.00E+00 | 8.21E-05 | -1.49E-03 | 3.30E-08 | -8.80E-03 |
| | FINN | -5.51E-03 | 0.00E+00 | -1.09E-03 | -7.80E-03 | -1.69E-06 | -1.44E-02 |
| **Fe-56** | FOUT | -3.07E-03 | 0.00E+00 | 2.07E-03 | -4.12E-03 | -7.11E-07 | -5.12E-03 |
| | REACTOR | -1.36E-02 | 0.00E+00 | 5.50E-03 | -1.35E-02 | -2.33E-06 | -2.16E-02 |
| **SUM (FINN + FOUT)** | | -2.08E-02 | 0.00E+00 | 1.43E-03 | -1.86E-02 | -4.32E-07 | -3.79E-02 |
| **SUM (REACTOR)** | | -3.17E-02 | 0.00E+00 | 9.86E-03 | -2.13E-02 | 3.69E-07 | -4.32E-02 |

*Table E.2: NEA LFR benchmark core. Energy-integrated SCs for the effective multiplication factor for the most important nuclides of the AIM1 material in the fuel assemblies.*

| $S(k,\sigma_{n,x,r})$ COOLANT | | $x$ | | | | | |
|---|---|---|---|---|---|---|---|
| $n$ | $r$ | CAPTURE | FISSION | ELASTIC | INELASTIC | N,XN | SUM |
| | FINN | -8.91E-04 | 0.00E+00 | 9.00E-05 | -3.41E-04 | 1.29E-06 | -1.14E-03 |
| **Pb-204** | FOUT | -4.80E-04 | 0.00E+00 | 1.98E-04 | -1.82E-04 | 9.29E-07 | -4.63E-04 |
| | REACTOR | -2.17E-03 | 0.00E+00 | 7.31E-04 | -5.94E-04 | 2.89E-06 | -2.03E-03 |
| | FINN | -1.39E-03 | 0.00E+00 | 1.21E-03 | -3.53E-03 | 8.72E-05 | -3.63E-03 |
| **Pb-207** | FOUT | -7.51E-04 | 0.00E+00 | 2.91E-03 | -1.81E-03 | 5.82E-05 | 4.15E-04 |
| | REACTOR | -3.17E-03 | 0.00E+00 | 1.05E-02 | -6.18E-03 | 1.83E-04 | 1.38E-03 |
| | FINN | -2.24E-03 | 0.00E+00 | 1.49E-03 | -5.21E-03 | 3.73E-05 | -5.93E-03 |
| **Pb-206** | FOUT | -1.19E-03 | 0.00E+00 | 3.04E-03 | -2.76E-03 | 2.58E-05 | -8.88E-04 |
| | REACTOR | -4.90E-03 | 0.00E+00 | 1.12E-02 | -9.03E-03 | 8.08E-05 | -2.69E-03 |
| | FINN | -4.17E-04 | 0.00E+00 | 4.00E-03 | -2.69E-03 | 1.29E-04 | 1.02E-03 |
| **Pb-208** | FOUT | -2.29E-04 | 0.00E+00 | 7.78E-03 | -1.37E-03 | 8.66E-05 | 6.27E-03 |
| | REACTOR | -8.73E-04 | 0.00E+00 | 2.86E-02 | -4.32E-03 | 2.72E-04 | 2.37E-02 |
| **SUM (FINN + FOUT)** | | -7.59E-03 | 0.00E+00 | 2.07E-02 | -1.79E-02 | 4.26E-04 | -4.34E-03 |
| **SUM (REACTOR)** | | -1.11E-02 | 0.00E+00 | 5.11E-02 | -2.01E-02 | 5.38E-04 | 2.04E-02 |

*Table E.3: NEA LFR benchmark core. Energy-integrated SCs for the effective multiplication factor for the most important nuclides of the coolant material in the fuel assemblies.*

| $S(k, \sigma_{n,x,g})$ MOX | $n, x$ | | | | | | |
|---|---|---|---|---|---|---|---|
| $g$ | **U-238** CAPTURE | **U-238** FISSION | **Pu-239** CAPTURE | **Pu-239** FISSION | **Pu-241** FISSION | **Pu-240** FISSION | **O-16** ELASTIC |
| 1 | -1.66E-07 | 2.53E-04 | -2.05E-08 | 1.11E-04 | 1.07E-05 | 5.10E-05 | -2.71E-05 |
| 2 | -1.23E-06 | 3.21E-03 | -2.03E-07 | 1.50E-03 | 1.38E-04 | 6.71E-04 | -9.10E-05 |
| 3 | -3.35E-05 | 7.84E-03 | -1.77E-06 | 5.13E-03 | 4.36E-04 | 2.14E-03 | 7.14E-04 |
| 4 | -5.41E-04 | 1.77E-02 | -2.39E-05 | 1.39E-02 | 1.23E-03 | 5.79E-03 | 3.38E-04 |
| 5 | -2.12E-03 | 2.14E-02 | -1.19E-04 | 2.16E-02 | 2.03E-03 | 8.47E-03 | -3.06E-03 |
| 6 | -4.77E-03 | 2.06E-03 | -2.82E-04 | 2.57E-02 | 2.47E-03 | 1.01E-02 | -1.49E-03 |
| 7 | -1.00E-02 | 2.39E-04 | -1.14E-03 | 5.05E-02 | 5.00E-03 | 1.16E-02 | -6.57E-03 |
| 8 | -7.35E-03 | 2.79E-05 | -1.41E-03 | 3.97E-02 | 4.40E-03 | 2.63E-03 | -5.84E-03 |
| 9 | -9.77E-03 | 1.43E-05 | -2.29E-03 | 4.82E-02 | 6.30E-03 | 1.59E-03 | -6.08E-03 |
| 10 | -1.13E-02 | 1.78E-05 | -2.77E-03 | 4.81E-02 | 6.96E-03 | 1.10E-03 | -7.23E-03 |
| 11 | -1.18E-02 | 5.41E-06 | -2.71E-03 | 4.17E-02 | 6.39E-03 | 1.03E-03 | -6.55E-03 |
| 12 | -1.55E-02 | 1.15E-05 | -2.97E-03 | 3.73E-02 | 6.12E-03 | 9.52E-04 | -3.60E-03 |
| 13 | -1.50E-02 | 3.60E-06 | -2.87E-03 | 2.87E-02 | 4.99E-03 | 9.47E-04 | -9.49E-04 |
| 14 | -1.60E-02 | 9.22E-06 | -3.54E-03 | 2.73E-02 | 5.17E-03 | 6.83E-04 | -1.52E-04 |
| 15 | -1.46E-02 | 6.25E-06 | -3.84E-03 | 2.17E-02 | 4.55E-03 | 5.19E-04 | 1.23E-03 |
| 16 | -1.11E-02 | 4.84E-06 | -3.67E-03 | 1.62E-02 | 3.49E-03 | 2.13E-04 | 7.85E-04 |
| 17 | -1.04E-02 | 5.83E-07 | -4.41E-03 | 1.55E-02 | 3.82E-03 | 2.63E-04 | 8.02E-04 |
| 18 | -9.76E-03 | 8.69E-07 | -4.25E-03 | 1.46E-02 | 3.29E-03 | 3.37E-04 | 6.20E-04 |
| 19 | -7.44E-03 | 5.26E-07 | -4.06E-03 | 1.26E-02 | 3.08E-03 | 4.67E-04 | 4.13E-04 |
| 20 | -5.89E-03 | 7.29E-06 | -2.49E-03 | 9.81E-03 | 1.87E-03 | 2.37E-04 | 9.39E-04 |
| 21 | -3.87E-03 | 1.18E-05 | -2.47E-03 | 6.66E-03 | 1.22E-03 | 1.50E-05 | 3.35E-05 |
| 22 | -1.19E-03 | 3.50E-09 | -8.17E-04 | 2.05E-03 | 6.18E-04 | 3.90E-06 | 1.39E-04 |
| 23 | -1.84E-03 | 2.86E-09 | -1.74E-03 | 4.01E-03 | 7.48E-04 | 5.24E-06 | -6.63E-05 |
| 24 | -4.70E-04 | 1.84E-10 | -4.85E-04 | 1.15E-03 | 1.74E-04 | 4.80E-07 | -2.71E-05 |
| 25 | -1.50E-04 | 3.19E-10 | -2.70E-04 | 6.73E-04 | 7.62E-05 | 3.05E-07 | -1.92E-04 |
| 26 | -2.93E-04 | 9.17E-10 | -2.75E-04 | 8.48E-04 | 8.08E-05 | 1.34E-07 | -1.31E-04 |
| 27 | -2.03E-04 | 2.47E-10 | -5.06E-05 | 1.48E-04 | 1.69E-04 | 1.08E-07 | -1.76E-05 |
| 28 | -2.46E-04 | 9.02E-10 | -1.26E-04 | 3.74E-04 | 5.91E-05 | 5.19E-07 | -4.93E-05 |
| 29 | -1.37E-05 | 1.99E-11 | -1.21E-04 | 1.96E-04 | 7.72E-05 | 1.65E-09 | -1.66E-04 |
| 30 | -1.67E-04 | 1.37E-10 | -6.85E-05 | 1.82E-04 | 1.38E-04 | 2.87E-09 | -8.99E-05 |
| 31 | -1.18E-05 | 1.50E-10 | -6.25E-06 | 2.00E-04 | 6.69E-05 | 9.44E-08 | -2.04E-05 |
| 32 | -4.42E-07 | 2.21E-12 | -3.57E-05 | 6.08E-05 | 3.82E-06 | 2.46E-09 | -1.30E-05 |
| 33 | -7.19E-08 | 3.32E-13 | -1.81E-06 | 4.17E-06 | 6.10E-07 | 1.48E-10 | 1.69E-07 |
| PART >0 | 0.00E+00 | 5.28E-02 | 0.00E+00 | 4.97E-01 | 7.52E-02 | 4.98E-02 | 6.01E-03 |
| PART <0 | -1.72E-01 | 0.00E+00 | -4.93E-02 | 0.00E+00 | 0.00E+00 | 0.00E+00 | -4.24E-02 |
| SUM | -1.72E-01 | 5.28E-02 | -4.93E-02 | 4.97E-01 | 7.52E-02 | 4.98E-02 | -3.64E-02 |

*Table E.4: NEA LFR benchmark core. Space-integrated SCs for the effective multiplication factor for the most important nuclides of the MOX material in the fuel assemblies.*

| $S(k, \sigma_{n,x,g})$ **AIM1 & COOLANT** | $n, x$ | | | | | |
|---|---|---|---|---|---|---|
| $g$ | **Fe-56** INELASTIC | **Fe-56** CAPTURE | **Ni-58** CAPTURE | **Pb-208** ELASTIC | **Pb-206** ELASTIC | **Pb-207** ELASTIC |
| 1 | -1.63E-06 | -2.63E-05 | -2.93E-05 | 1.49E-06 | 6.23E-07 | 5.79E-07 |
| 2 | 1.34E-05 | -1.32E-04 | -3.68E-04 | 4.90E-05 | 2.12E-05 | 1.97E-05 |
| 3 | 2.38E-04 | -3.59E-05 | -1.03E-03 | 3.59E-04 | 1.32E-04 | 1.49E-04 |
| 4 | 6.53E-04 | -6.91E-05 | -1.06E-03 | 1.75E-03 | 5.79E-04 | 6.38E-04 |
| 5 | 5.54E-04 | -1.26E-04 | -3.19E-04 | 2.64E-03 | 8.23E-04 | 8.23E-04 |
| 6 | 9.31E-04 | -2.82E-04 | -1.52E-04 | 2.67E-03 | 1.13E-03 | 9.82E-04 |
| 7 | 8.52E-04 | -8.73E-04 | -2.80E-04 | 5.92E-03 | 2.76E-03 | 2.44E-03 |
| 8 | 1.42E-03 | -6.75E-04 | -2.50E-04 | 2.88E-03 | 1.10E-03 | 1.03E-03 |
| 9 | -6.04E-04 | -8.32E-04 | -3.81E-04 | 3.33E-03 | 1.35E-03 | 1.33E-03 |
| 10 | -4.49E-05 | -7.67E-04 | -4.86E-04 | 2.91E-03 | 1.05E-03 | 1.19E-03 |
| 11 | 2.97E-04 | -1.44E-03 | -3.63E-04 | 1.81E-03 | 5.17E-04 | 5.90E-04 |
| 12 | -5.76E-04 | -8.87E-04 | -4.20E-04 | 1.33E-03 | 5.22E-04 | 2.98E-04 |
| 13 | 9.90E-04 | -1.39E-03 | -5.93E-04 | 8.76E-04 | 3.74E-04 | 2.34E-04 |
| 14 | 5.70E-05 | -5.23E-04 | -4.27E-04 | 1.08E-03 | 4.20E-04 | 4.15E-04 |
| 15 | 4.25E-04 | -1.88E-04 | -6.57E-04 | 7.85E-04 | 3.08E-04 | 3.05E-04 |
| 16 | 2.97E-04 | -1.46E-04 | -6.04E-05 | 3.91E-04 | 1.55E-04 | 1.53E-04 |
| 17 | 3.71E-04 | -1.83E-04 | -4.73E-05 | 3.63E-04 | 1.65E-04 | 1.44E-04 |
| 18 | 3.41E-04 | -1.87E-04 | -4.67E-05 | 2.50E-04 | 1.02E-04 | 9.95E-05 |
| 19 | 1.69E-04 | -2.07E-04 | -5.56E-05 | 1.21E-04 | 5.00E-05 | 4.80E-05 |
| 20 | 6.90E-04 | -3.45E-03 | -4.37E-05 | 1.75E-04 | 7.52E-05 | 7.00E-05 |
| 21 | -1.46E-04 | -1.50E-04 | -4.15E-05 | 9.16E-05 | 3.95E-05 | 3.65E-05 |
| 22 | 1.15E-04 | -7.29E-05 | -2.01E-05 | 4.81E-06 | 1.81E-06 | 1.84E-06 |
| 23 | -3.23E-04 | -1.78E-04 | -4.89E-05 | 2.15E-04 | 9.49E-05 | 8.55E-05 |
| 24 | -1.48E-04 | -9.71E-05 | -2.65E-05 | 1.17E-04 | 5.24E-05 | 4.67E-05 |
| 25 | -2.80E-04 | -5.90E-05 | -1.61E-05 | 1.34E-04 | 6.04E-05 | 5.35E-05 |
| 26 | -2.10E-04 | -9.45E-05 | -2.56E-05 | 1.37E-04 | 6.17E-05 | 5.45E-05 |
| 27 | -8.54E-05 | -8.45E-05 | -2.29E-05 | 6.24E-05 | 2.82E-05 | 2.49E-05 |
| 28 | -1.09E-04 | -7.52E-05 | -2.05E-05 | 7.12E-05 | 3.23E-05 | 2.84E-05 |
| 29 | -2.07E-04 | -6.81E-05 | -1.85E-05 | 1.04E-04 | 4.75E-05 | 4.17E-05 |
| 30 | -1.21E-04 | -7.22E-05 | -1.96E-05 | 6.91E-05 | 3.14E-05 | 2.76E-05 |
| 31 | -4.78E-05 | -1.30E-04 | -3.51E-05 | 3.94E-05 | 1.79E-05 | 1.57E-05 |
| 32 | -2.01E-05 | -4.45E-05 | -1.20E-05 | 1.50E-05 | 6.81E-06 | 5.97E-06 |
| 33 | -2.05E-07 | -5.33E-06 | -1.41E-06 | 5.22E-07 | 2.37E-07 | 2.08E-07 |
| PART >0 | 8.41E-03 | 0.00E+00 | 0.00E+00 | 2.97E-02 | 1.16E-02 | 1.10E-02 |
| PART <0 | -2.92E-03 | -1.36E-02 | -7.38E-03 | -1.06E-03 | -4.75E-04 | -4.23E-04 |
| SUM | 5.49E-03 | -1.36E-02 | -7.38E-03 | 2.86E-02 | 1.11E-02 | 1.05E-02 |

*Table E.5: NEA LFR benchmark core. Space-integrated SCs for the effective multiplication factor for the most important nuclides of the AIM1 & coolant materials in the fuel assemblies.*

## E.2 Sensitivity coefficients for Doppler coefficient

| $S(\Delta\rho_T, \sigma_{n,x,r})$ MOX | | $x$ | | | | | |
|---|---|---|---|---|---|---|---|
| $n$ | $r$ | **CAPTURE** | **FISSION** | **ELASTIC** | **INELASTIC** | **N,XN** | **SUM** |
| **U-235** | FINN | -2.84E-03 | -6.20E-03 | 6.42E-05 | 2.51E-04 | 4.45E-07 | -8.73E-03 |
| | FOUT | -1.25E-03 | -3.89E-03 | 1.30E-05 | 1.20E-04 | -9.93E-08 | -5.01E-03 |
| | REACTOR | -4.09E-03 | -1.01E-02 | 7.73E-05 | 3.72E-04 | 3.45E-07 | -1.37E–02 |
| **Am-241** | FINN | -1.48E-02 | -2.36E-03 | 1.18E-04 | 3.52E-04 | 5.84E-08 | -1.66E-02 |
| | FOUT | -8.50E-03 | -2.30E-03 | 3.51E-05 | 2.24E-04 | -2.91E-08 | -1.05E-02 |
| | REACTOR | -2.32E-02 | -4.66E-03 | 1.53E-04 | 5.76E-04 | 2.93E-08 | -2.72E-02 |
| **Pu-238** | FINN | -1.08E-02 | -1.45E-02 | 2.23E-04 | 4.12E-04 | 4.01E-08 | -2.47E-02 |
| | FOUT | -6.37E-03 | -1.34E-02 | 8.07E-05 | 2.62E-04 | -7.08E-09 | -1.95E-02 |
| | REACTOR | -1.72E-02 | -2.80E-02 | 3.04E-04 | 6.74E-04 | 3.30E-08 | -4.42E-02 |
| **Pu-242** | FIN | -2.03E-02 | -1.32E-02 | 8.16E-04 | 1.87E-03 | 2.32E-06 | -3.08E-02 |
| | FOUT | -1.05E-02 | -1.25E-02 | 2.84E-04 | 1.22E-03 | -4.84E-07 | -2.15E-02 |
| | REACTOR | -3.08E-02 | -2.57E-02 | 1.10E-03 | 3.10E-03 | 1.84E-06 | -5.24E-02 |
| **Pu-241** | FINN | -1.78E-02 | -4.91E-02 | 4.43E-04 | 2.11E-03 | 8.10E-06 | -6.44E-02 |
| | FOUT | -1.04E-02 | -4.90E-02 | 1.80E-04 | 1.31E-03 | 4.15E-08 | -5.79E-02 |
| | REACTOR | -2.82E-02 | -9.81E-02 | 6.23E-04 | 3.42E-03 | 8.14E-06 | -1.22E-01 |
| **Pu-240** | FINN | -7.17E-02 | -6.82E-02 | 2.84E-03 | 6.93E-03 | 4.31E-06 | -1.30E-01 |
| | FOUT | -3.06E-02 | -6.32E-02 | 1.14E-03 | 4.49E-03 | -8.31E-07 | -8.81E-02 |
| | REACTOR | -1.02E-01 | -1.31E-01 | 3.98E-03 | 1.14E-02 | 3.47E-06 | -2.18E-01 |
| **U-238** | FINN | 4.57E-02 | -8.09E-02 | 3.60E-02 | 1.22E-01 | 2.96E-04 | 1.24E-01 |
| | FOUT | 1.19E-01 | -5.74E-02 | 5.98E-03 | 6.05E-02 | -4.10E-05 | 1.28E-01 |
| | REACTOR | 1.65E-01 | -1.38E-01 | 4.19E-02 | 1.83E-01 | 2.55E-04 | 2.51E-01 |
| **O-16** | FINN | 1.38E-03 | 0.00E+00 | 4.45E-01 | 2.48E-04 | 1.78E-10 | 4.47E-01 |
| | FOUT | 1.32E-03 | 0.00E+00 | 1.87E-01 | 1.62E-04 | -4.76E-12 | 1.88E-01 |
| | REACTOR | 2.81E-03 | 0.00E+00 | 7.20E-01 | 4.26E-04 | 1.84E-10 | 7.23E-01 |
| **Pu-239** | FINN | -2.18E-01 | -5.35E-01 | 4.86E-03 | 1.48E-02 | 8.00E-06 | -7.34E-01 |
| | FOUT | -1.07E-01 | -5.02E-01 | 1.96E-03 | 9.14E-03 | -4.06E-06 | -5.98E-01 |
| | REACTOR | -3.24E-01 | -1.04E+00 | 6.82E-03 | 2.39E-02 | 3.95E-06 | -1.33E+00 |
| **SUM (FINN + FOUT)** | | -3.63E-01 | -1.47E+00 | 6.87E-01 | 2.27E-01 | 2.73E-04 | -9.23E-01 |
| **SUM (REACTOR)** | | -3.63E-01 | -1.47E+00 | 7.75E-01 | 2.27E-01 | 2.73E-04 | -8.35E-01 |

*Table E.6: NEA LFR benchmark core. Energy-integrated SCs for the Doppler reactivity change for the most important nuclides of the MOX material in the fuel assemblies.*

| $S(\Delta\rho_T, \sigma_{n,x,r})$ AIM1 | | $x$ | | | | | |
|---|---|---|---|---|---|---|---|
| $n$ | $r$ | CAPTURE | FISSION | ELASTIC | INELASTIC | N,XN | SUM |
| Ni-60 | FINN | -2.22E-03 | 0.00E+00 | 9.97E-03 | 1.47E-03 | 1.51E-07 | 9.21E-03 |
| | FOUT | -6.92E-04 | 0.00E+00 | 3.77E-03 | 8.95E-04 | 1.99E-08 | 3.97E-03 |
| | REACTOR | -5.47E-03 | 0.00E+00 | 2.02E-02 | 2.78E-03 | 2.07E-07 | 1.75E-02 |
| Fe-57 | FINN | -1.85E-03 | 0.00E+00 | 4.86E-03 | 8.87E-03 | 8.79E-07 | 1.19E-02 |
| | FOUT | -6.63E-04 | 0.00E+00 | 1.94E-03 | 3.82E-03 | -7.93E-08 | 5.10E-03 |
| | REACTOR | -4.35E-03 | 0.00E+00 | 9.58E-03 | 1.69E-02 | 1.01E-06 | 2.22E-02 |
| Fe-54 | FINN | -1.97E-03 | 0.00E+00 | 1.64E-02 | 1.11E-03 | 1.11E-06 | 1.56E-02 |
| | FOUT | -4.06E-04 | 0.00E+00 | 6.43E-03 | 6.76E-04 | 9.04E-07 | 6.70E-03 |
| | REACTOR | -4.95E-03 | 0.00E+00 | 3.22E-02 | 2.10E-03 | 2.18E-06 | 2.94E-02 |
| Cr-52 | FINN | -4.47E-03 | 0.00E+00 | 1.19E-02 | 4.24E-03 | 3.56E-07 | 1.17E-02 |
| | FOUT | -1.72E-03 | 0.00E+00 | 3.73E-03 | 2.58E-03 | 5.22E-08 | 4.59E-03 |
| | REACTOR | -1.06E-02 | 0.00E+00 | 2.17E-02 | 7.99E-03 | 5.05E-07 | 1.91E-02 |
| Cr-53 | FINN | -2.76E-03 | 0.00E+00 | 1.90E-02 | 8.81E-04 | 6.31E-07 | 1.71E-02 |
| | FOUT | -1.16E-03 | 0.00E+00 | 7.99E-03 | 5.27E-04 | -7.61E-08 | 7.36E-03 |
| | REACTOR | -7.07E-03 | 0.00E+00 | 3.69E-02 | 1.71E-03 | 7.06E-07 | 3.15E-02 |
| Mn-55 | FINN | -1.17E-02 | 0.00E+00 | 1.47E-02 | 3.52E-03 | 2.98E-07 | 6.45E-03 |
| | FOUT | -5.63E-03 | 0.00E+00 | 6.74E-03 | 1.70E-03 | 9.99E-08 | 2.81E-03 |
| | REACTOR | -3.03E-02 | 0.00E+00 | 2.89E-02 | 6.91E-03 | 4.64E-07 | 5.59E-03 |
| Ni-58 | FINN | -2.55E-03 | 0.00E+00 | 6.74E-02 | 2.81E-03 | 1.82E-08 | 6.77E-02 |
| | FOUT | 2.34E-04 | 0.00E+00 | 2.65E-02 | 1.71E-03 | 1.87E-10 | 2.84E-02 |
| | REACTOR | -7.87E-03 | 0.00E+00 | 1.24E-01 | 5.30E-03 | 2.30E-08 | 1.22E-01 |
| Fe-56 | FINN | -2.79E-02 | 0.00E+00 | 8.82E-02 | 2.74E-02 | 6.69E-06 | 8.78E-02 |
| | FOUT | -1.13E-02 | 0.00E+00 | 3.23E-02 | 1.62E-02 | 3.70E-06 | 3.72E-02 |
| | REACTOR | -6.96E-02 | 0.00E+00 | 1.56E-01 | 5.25E-02 | 1.17E-05 | 1.39E-01 |
| SUM (FINN + FOUT) | | -7.68E-02 | 0.00E+00 | 3.22E-01 | 7.85E-02 | 1.48E-05 | 3.24E-01 |
| SUM (REACTOR) | | -1.40E-01 | 0.00E+00 | 4.30E-01 | 9.63E-02 | 1.68E-05 | 3.86E-01 |

*Table E.7: NEA LFR benchmark core. Energy-integrated SCs for the Doppler reactivity change for the most important nuclides of the AIM1 material in the fuel assemblies.*

| $S(\Delta\rho_T, \sigma_{n,x,r})$ COOLANT | | $x$ | | | | | |
|---|---|---|---|---|---|---|---|
| $n$ | $r$ | CAPTURE | FISSION | ELASTIC | INELASTIC | N,XN | SUM |
| Pb-204 | FINN | -5.53E-03 | 0.00E+00 | 1.29E-03 | 1.08E-03 | 2.44E-06 | -3.17E-03 |
| | FOUT | -2.10E-03 | 0.00E+00 | 2.20E-04 | 6.62E-04 | 4.30E-07 | -1.22E-03 |
| | REACTOR | -1.30E-02 | 0.00E+00 | 2.52E-03 | 2.06E-03 | 3.61E-06 | -8.39E-03 |
| Pb-207 | FINN | -3.54E-03 | 0.00E+00 | 2.22E-02 | 1.29E-02 | 5.69E-05 | 3.16E-02 |
| | FOUT | -1.04E-03 | 0.00E+00 | 4.28E-03 | 7.32E-03 | -1.80E-05 | 1.05E-02 |
| | REACTOR | -9.11E-03 | 0.00E+00 | 4.26E-02 | 2.52E-02 | 5.86E-05 | 5.88E-02 |
| Pb-206 | FINN | -2.84E-03 | 0.00E+00 | 1.93E-02 | 1.65E-02 | 4.31E-05 | 3.31E-02 |
| | FOUT | -3.13E-04 | 0.00E+00 | 2.98E-03 | 1.01E-02 | 3.73E-07 | 1.27E-02 |
| | REACTOR | -7.72E-03 | 0.00E+00 | 3.62E-02 | 3.16E-02 | 5.64E-05 | 6.01E-02 |
| Pb-208 | FINN | 1.16E-04 | 0.00E+00 | 4.41E-02 | 7.96E-03 | 6.40E-05 | 5.22E-02 |
| | FOUT | 2.20E-04 | 0.00E+00 | 5.68E-03 | 4.84E-03 | -3.80E-05 | 1.07E-02 |
| | REACTOR | 1.03E-04 | 0.00E+00 | 8.29E-02 | 1.43E-02 | 4.73E-05 | 9.73E-02 |
| SUM (FINN + FOUT) | | -1.50E-02 | 0.00E+00 | 1.00E-01 | 6.13E-02 | 1.11E-04 | 1.46E-01 |
| SUM (REACTOR) | | -2.97E-02 | 0.00E+00 | 1.64E-01 | 7.31E-02 | 1.66E-04 | 2.08E-01 |

*Table E.8: NEA LFR benchmark core. Energy-integrated SCs for the Doppler reactivity change for the most important nuclides of the coolant material in the fuel assemblies.*

| $S(\Delta\rho_T, \sigma_{n,x,g})$ MOX | $n, x$ | | | | | | |
|---|---|---|---|---|---|---|---|
| $g$ | **U-238** CAPTURE | **U-238** FISSION | **Pu-239** CAPTURE | **Pu-239** FISSION | **Pu-241** FISSION | **Pu-240** FISSION | **O-16** ELASTIC |
| 1 | 2.05E-07 | -6.37E-04 | 2.63E-08 | -2.76E-04 | -2.65E-05 | -1.27E-04 | 2.94E-05 |
| 2 | 1.55E-06 | -7.84E-03 | 2.63E-07 | -3.62E-03 | -3.31E-04 | -1.62E-03 | 2.09E-04 |
| 3 | 3.90E-05 | -1.98E-02 | 2.14E-06 | -1.26E-02 | -1.07E-03 | -5.29E-03 | -1.37E-03 |
| 4 | 6.38E-04 | -4.65E-02 | 2.93E-05 | -3.49E-02 | -3.08E-03 | -1.46E-02 | -1.74E-04 |
| 5 | 2.34E-03 | -5.68E-02 | 1.37E-04 | -5.50E-02 | -5.15E-03 | -2.16E-02 | 1.02E-02 |
| 6 | 4.50E-03 | -5.54E-03 | 2.79E-04 | -6.63E-02 | -6.37E-03 | -2.61E-02 | 3.29E-03 |
| 7 | 8.93E-03 | -6.37E-04 | 1.07E-03 | -1.30E-01 | -1.28E-02 | -2.99E-02 | 4.68E-02 |
| 8 | 4.57E-03 | -7.68E-05 | 9.43E-04 | -1.04E-01 | -1.15E-02 | -6.93E-03 | 5.24E-02 |
| 9 | 4.03E-03 | -4.05E-05 | 1.06E-03 | -1.30E-01 | -1.69E-02 | -4.28E-03 | 5.56E-02 |
| 10 | 1.29E-03 | -5.18E-05 | 4.64E-04 | -1.32E-01 | -1.90E-02 | -3.00E-03 | 7.05E-02 |
| 11 | -3.08E-03 | -1.63E-05 | 5.46E-04 | -1.18E-01 | -1.79E-02 | -2.92E-03 | 6.56E-02 |
| 12 | -1.09E-02 | -3.58E-05 | 1.92E-03 | -1.09E-01 | -1.77E-02 | -2.77E-03 | 6.76E-02 |
| 13 | -1.96E-02 | -1.19E-05 | 3.45E-03 | -8.84E-02 | -3.83E-03 | -2.95E-03 | 6.06E-02 |
| 14 | -1.76E-02 | -4.60E-05 | 6.70E-03 | -8.84E-02 | -9.98E-03 | -2.23E-03 | 5.49E-02 |
| 15 | -4.86E-03 | -6.20E-05 | 1.16E-02 | -7.17E-02 | -1.17E-02 | -1.78E-03 | 6.50E-02 |
| 16 | 5.75E-03 | -6.27E-05 | 1.58E-02 | -5.33E-02 | -9.82E-03 | -7.54E-04 | 4.21E-02 |
| 17 | 2.22E-02 | -1.75E-06 | 2.57E-02 | -4.78E-02 | -9.62E-03 | -1.04E-03 | 4.72E-02 |
| 18 | 4.69E-02 | -1.58E-06 | 3.65E-02 | -2.70E-02 | -3.60E-03 | -2.22E-03 | 3.29E-02 |
| 19 | 5.66E-02 | -5.22E-08 | 5.02E-02 | 7.51E-03 | 3.99E-03 | -6.66E-04 | 2.85E-02 |
| 20 | 4.14E-02 | -9.79E-05 | 4.13E-02 | 4.25E-02 | 9.07E-03 | 1.63E-04 | 2.06E-02 |
| 21 | 2.09E-02 | -1.76E-05 | 5.42E-02 | 5.98E-02 | 1.31E-02 | -7.28E-04 | 2.72E-03 |
| 22 | -1.00E-03 | -8.33E-08 | 2.04E-02 | 2.44E-02 | 9.28E-03 | 2.29E-06 | 5.90E-03 |
| 23 | 5.77E-03 | -5.20E-08 | 4.34E-02 | 5.77E-02 | 1.56E-02 | -3.19E-05 | -2.90E-03 |
| 24 | -3.50E-03 | 1.19E-09 | 1.24E-02 | 2.13E-02 | 3.38E-03 | 7.52E-07 | -1.55E-04 |
| 25 | -9.74E-04 | -5.27E-09 | 3.15E-03 | 9.62E-03 | 1.72E-03 | -3.03E-06 | -3.17E-03 |
| 26 | 1.60E-03 | -2.20E-08 | 3.04E-03 | 1.25E-02 | 1.53E-03 | 2.34E-06 | -5.41E-03 |
| 27 | -2.30E-03 | 3.68E-09 | 7.09E-04 | -1.70E-03 | 1.83E-03 | -9.52E-07 | 1.18E-03 |
| 28 | 1.24E-03 | -4.63E-09 | 7.17E-04 | -2.35E-04 | 4.38E-04 | 2.55E-05 | 4.13E-04 |
| 29 | -1.60E-04 | 2.38E-10 | 5.43E-04 | 1.86E-04 | 4.86E-04 | 1.93E-08 | -2.24E-04 |
| 30 | 9.44E-05 | -6.54E-10 | 3.63E-04 | -1.33E-03 | 1.66E-03 | 2.46E-08 | -4.17E-04 |
| 31 | -1.28E-04 | 1.08E-09 | 7.72E-05 | 1.67E-03 | 2.13E-04 | 3.46E-07 | -4.26E-04 |
| 32 | -3.40E-06 | 1.39E-11 | 4.39E-05 | 6.51E-05 | 9.54E-06 | 1.49E-08 | 4.74E-05 |
| 33 | -2.46E-07 | 8.34E-13 | 3.55E-06 | 8.04E-06 | 1.25E-06 | 3.54E-10 | 2.39E-06 |
| PART >0 | 2.29E-01 | 6.20E-09 | 6.31E-03 | 2.37E-01 | 6.24E-02 | 1.95E-04 | 7.34E-01 |
| PART <0 | -6.42E-02 | -1.38E-01 | -3.31E-01 | -1.28E+00 | -1.60E-01 | -1.32E-01 | -1.42E-02 |
| SUM | 1.65E-01 | -1.38E-01 | -3.24E-01 | -1.04E+00 | -9.81E-02 | -1.31E-01 | 7.20E-01 |

*Table E.9: NEA LFR benchmark core. Space-integrated SCs for the Doppler reactivity change for the most important nuclides of the MOX material in the fuel assemblies.*

| $S(\Delta\rho_T, \sigma_{n,x,g})$ AIM1 & COOLANT | $n, x$ | | | | | |
|---|---|---|---|---|---|---|
| $g$ | **Fe-56** ELASTIC | **Fe-56** CAPTURE | **Ni-58** ELASTIC | **Pb-208** ELASTIC | **Pb-206** ELASTIC | **Pb-207** ELASTIC |
| 1 | 5.19E-07 | 3.05E-05 | 1.17E-07 | -4.35E-06 | -1.81E-06 | -1.67E-06 |
| 2 | -1.85E-05 | 1.55E-04 | -3.67E-06 | -8.47E-05 | -3.67E-05 | -3.41E-05 |
| 3 | -4.19E-04 | 3.91E-05 | -7.22E-05 | -6.21E-04 | -2.29E-04 | -2.57E-04 |
| 4 | -8.67E-04 | 7.50E-05 | -1.39E-04 | -2.79E-03 | -9.26E-04 | -1.02E-03 |
| 5 | 1.77E-04 | 1.22E-04 | 1.58E-04 | -3.58E-03 | -1.06E-03 | -1.04E-03 |
| 6 | -1.02E-03 | 2.13E-04 | -3.23E-04 | -3.28E-03 | -1.40E-03 | -1.22E-03 |
| 7 | 8.84E-03 | 5.56E-04 | 1.24E-03 | -5.74E-03 | -1.35E-03 | -1.08E-03 |
| 8 | 2.70E-03 | 1.77E-04 | 2.41E-03 | 3.04E-03 | 1.10E-03 | 1.13E-03 |
| 9 | 1.46E-02 | 5.38E-05 | 1.36E-03 | 4.39E-03 | 1.32E-03 | 1.65E-03 |
| 10 | 9.94E-03 | 2.68E-04 | 3.19E-03 | 7.73E-03 | 3.60E-03 | 3.64E-03 |
| 11 | 7.22E-03 | 1.09E-03 | 1.17E-02 | 9.16E-03 | 3.86E-03 | 4.01E-03 |
| 12 | 2.06E-02 | 1.14E-03 | 4.16E-03 | 1.03E-02 | 3.99E-03 | 1.22E-02 |
| 13 | 7.07E-03 | 2.68E-03 | 1.43E-02 | 1.63E-02 | 6.63E-03 | 5.81E-03 |
| 14 | 7.11E-03 | 1.39E-03 | 5.65E-02 | 8.90E-03 | 3.48E-03 | 3.42E-03 |
| 15 | 1.68E-02 | 7.40E-04 | 4.26E-03 | 1.20E-02 | 4.75E-03 | 4.70E-03 |
| 16 | 1.20E-02 | 7.60E-04 | 4.43E-03 | 7.21E-03 | 2.88E-03 | 2.85E-03 |
| 17 | 1.93E-02 | 1.24E-03 | 7.81E-03 | 9.07E-03 | 5.31E-03 | 3.60E-03 |
| 18 | 1.68E-02 | 1.72E-03 | 6.79E-03 | 7.50E-03 | 3.07E-03 | 2.99E-03 |
| 19 | 1.44E-02 | 2.44E-03 | 5.63E-03 | 6.35E-03 | 2.65E-03 | 2.53E-03 |
| 20 | 1.31E-02 | 4.63E-02 | 4.92E-03 | 4.30E-03 | 1.83E-03 | 1.72E-03 |
| 21 | 3.22E-04 | 2.50E-03 | 1.27E-04 | 3.32E-04 | 1.41E-04 | 1.32E-04 |
| 22 | 4.69E-03 | 1.27E-03 | 1.66E-03 | 1.08E-03 | 4.80E-04 | 4.34E-04 |
| 23 | -5.37E-03 | 2.95E-03 | -1.87E-03 | -2.74E-03 | -1.22E-03 | -1.09E-03 |
| 24 | -2.30E-03 | 1.27E-03 | -8.01E-04 | -1.59E-03 | -7.13E-04 | -6.35E-04 |
| 25 | -3.82E-03 | 6.16E-04 | -1.30E-03 | -1.65E-03 | -7.46E-04 | -6.60E-04 |
| 26 | -6.06E-03 | 8.27E-04 | -2.06E-03 | -2.74E-03 | -1.24E-03 | -1.10E-03 |
| 27 | 1.26E-03 | 2.21E-04 | 4.27E-04 | 5.50E-04 | 2.50E-04 | 2.20E-04 |
| 28 | 3.43E-04 | 2.92E-04 | 1.15E-04 | 8.39E-05 | 3.83E-05 | 3.36E-05 |
| 29 | -3.14E-04 | 3.01E-04 | -1.06E-04 | -1.82E-04 | -8.26E-05 | -7.25E-05 |
| 30 | -4.97E-04 | 3.58E-04 | -1.69E-04 | -2.83E-04 | -1.29E-04 | -1.13E-04 |
| 31 | -2.47E-04 | 5.81E-04 | -8.46E-05 | -1.75E-04 | -7.97E-05 | -6.99E-05 |
| 32 | 1.14E-06 | 8.09E-05 | 3.17E-07 | -2.48E-06 | -1.12E-06 | -9.84E-07 |
| 33 | 1.77E-06 | 6.94E-06 | 5.95E-07 | 5.33E-07 | 2.44E-07 | 2.13E-07 |
| PART >0 | 1.77E-01 | 1.42E-03 | 1.31E-01 | 1.08E-01 | 4.54E-02 | 5.10E-02 |
| PART <0 | -2.09E-02 | 7.10E-02 | -6.93E-03 | -2.55E-02 | -9.22E-03 | -8.39E-03 |
| SUM | 1.56E-01 | 6.96E-02 | 1.24E-01 | 8.29E-02 | 3.62E-02 | 4.26E-02 |

*Table E.10: NEA LFR benchmark core. Space-integrated SCs for the Doppler reactivity change for the most important nuclides of the AIM1 & coolant materials in the fuel assemblies.*

## E.3 Sensitivity coefficients comparison against MC results

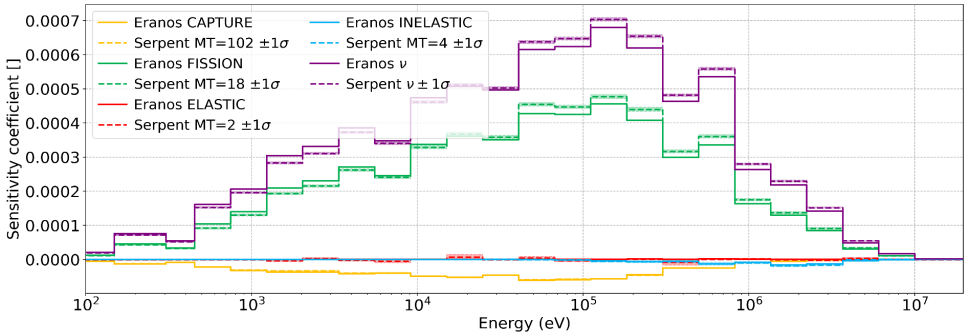


*(a) Sensitivity coefficients*

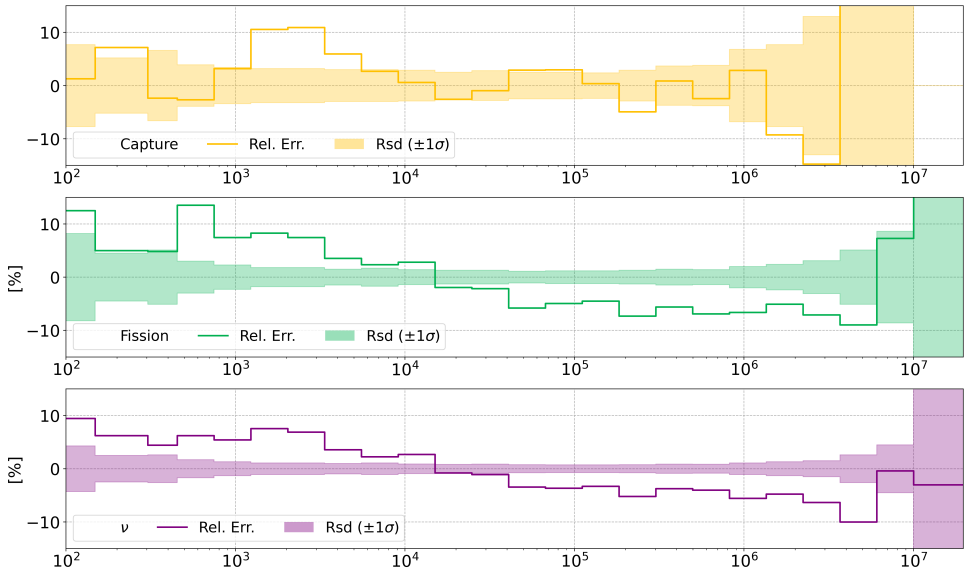


*(b) Relative errors*

*Figure E.1: NEA LFR benchmark reactor core. Comparison between the U-235 SCs produced by ERANOS and Serpent2 for the effective multiplication factor.*

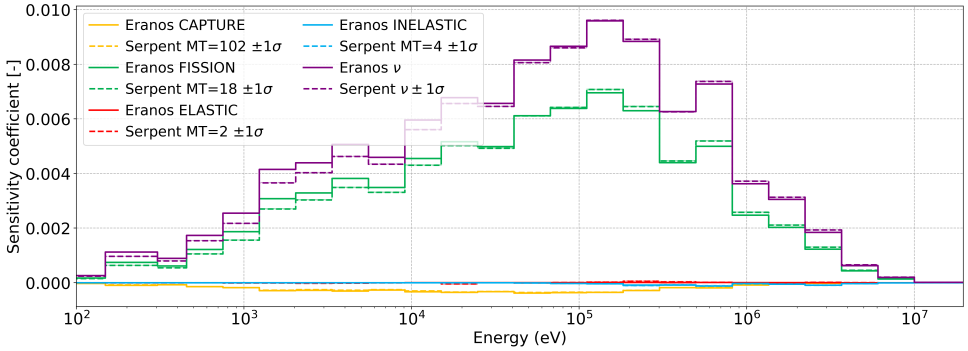


*(a) Sensitivity coefficients*

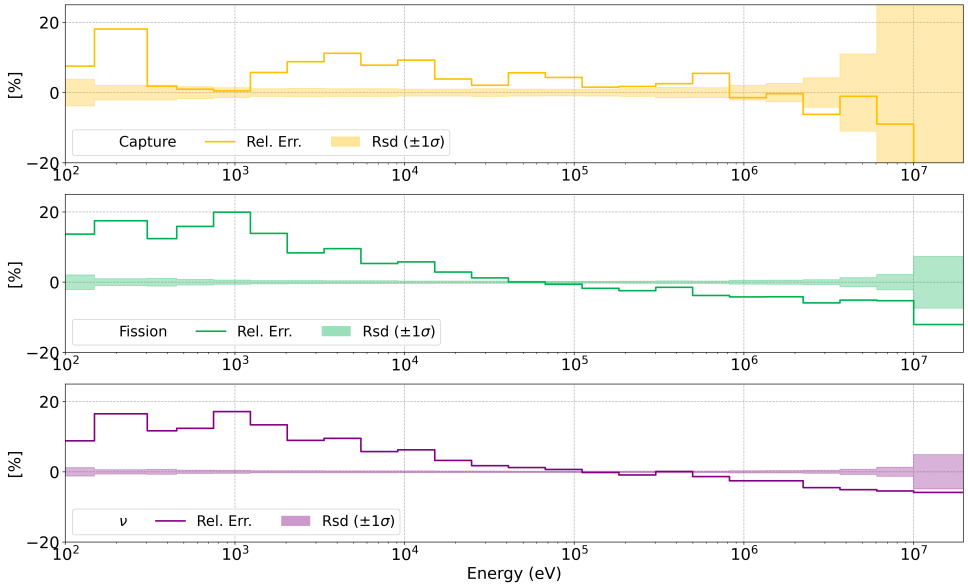


*(b) Relative errors*

*Figure E.2: NEA LFR benchmark core. Comparison between the Pu-241 SCs produced by ERANOS and Serpent2 for the effective multiplication factor.*

## Appendix F

# Energy bounds of 295 group structure

| Group | Upper bound [MeV] | Group | Upper bound [MeV] | Group | Upper bound [MeV] | Group | Upper bound [MeV] |
|---|---|---|---|---|---|---|---|
| 1 | 1.964033E+01 | 75 | 2.365332E+00 | 149 | 1.356856E-01 | 223 | 3.535750E-04 |
| 2 | 1.915541E+01 | 76 | 2.345703E+00 | 150 | 1.290681E-01 | 224 | 3.043248E-04 |
| 3 | 1.868246E+01 | 77 | 2.306932E+00 | 151 | 1.227734E-01 | 225 | 2.753645E-04 |
| 4 | 1.822119E+01 | 78 | 2.268802E+00 | 152 | 1.167857E-01 | 226 | 2.144541E-04 |
| 5 | 1.777131E+01 | 79 | 2.231302E+00 | 153 | 1.110900E-01 | 227 | 2.039950E-04 |
| 6 | 1.733253E+01 | 80 | 2.122480E+00 | 154 | 9.803655E-02 | 228 | 1.670170E-04 |
| 7 | 1.690459E+01 | 81 | 2.018965E+00 | 155 | 8.651695E-02 | 229 | 1.486254E-04 |
| 8 | 1.648721E+01 | 82 | 1.969117E+00 | 156 | 8.229747E-02 | 230 | 1.367420E-04 |
| 9 | 1.608014E+01 | 83 | 1.920499E+00 | 157 | 7.635094E-02 | 231 | 1.300730E-04 |
| 10 | 1.568312E+01 | 84 | 1.873082E+00 | 158 | 6.737947E-02 | 232 | 1.013009E-04 |
| 11 | 1.529590E+01 | 85 | 1.826835E+00 | 159 | 6.251086E-02 | 233 | 9.166088E-05 |
| 12 | 1.491825E+01 | 86 | 1.737739E+00 | 160 | 5.946217E-02 | 234 | 7.889325E-05 |
| 13 | 1.454991E+01 | 87 | 1.652989E+00 | 161 | 5.656217E-02 | 235 | 7.567357E-05 |
| 14 | 1.419068E+01 | 88 | 1.612176E+00 | 162 | 5.516564E-02 | 236 | 6.790405E-05 |
| 15 | 1.384031E+01 | 89 | 1.572372E+00 | 163 | 5.247518E-02 | 237 | 6.144212E-05 |
| 16 | 1.349859E+01 | 90 | 1.533550E+00 | 164 | 4.630919E-02 | 238 | 5.559513E-05 |
| 17 | 1.316531E+01 | 91 | 1.495686E+00 | 165 | 4.086771E-02 | 239 | 5.157802E-05 |
| 18 | 1.284025E+01 | 92 | 1.422741E+00 | 166 | 3.697864E-02 | 240 | 4.785117E-05 |
| 19 | 1.252323E+01 | 93 | 1.353353E+00 | 167 | 3.606563E-02 | 241 | 4.551744E-05 |
| 20 | 1.221403E+01 | 94 | 1.287349E+00 | 168 | 3.517517E-02 | 242 | 4.016900E-05 |
| 21 | 1.191246E+01 | 95 | 1.224564E+00 | 169 | 3.430669E-02 | 243 | 3.726653E-05 |
| 22 | 1.161834E+01 | 96 | 1.194330E+00 | 170 | 3.182781E-02 | 244 | 3.372015E-05 |
| 23 | 1.133148E+01 | 97 | 1.164842E+00 | 171 | 2.928300E-02 | 245 | 3.051126E-05 |
| 24 | 1.105171E+01 | 98 | 1.108032E+00 | 172 | 2.808794E-02 | 246 | 2.902320E-05 |
| 25 | 1.077884E+01 | 99 | 1.053992E+00 | 173 | 2.739445E-02 | 247 | 2.760773E-05 |
| 26 | 1.051271E+01 | 100 | 1.002588E+00 | 174 | 2.605841E-02 | 248 | 2.498050E-05 |
| 27 | 1.025315E+01 | 101 | 9.778344E-01 | 175 | 2.478752E-02 | 249 | 2.260329E-05 |
| 28 | 1.000000E+01 | 102 | 9.616723E-01 | 176 | 2.417552E-02 | 250 | 1.945484E-05 |
| 29 | 9.753099E+00 | 103 | 9.536916E-01 | 177 | 2.357862E-02 | 251 | 1.760346E-05 |
| 30 | 9.512294E+00 | 104 | 9.071795E-01 | 178 | 2.187491E-02 | 252 | 1.592827E-05 |
| 31 | 9.277435E+00 | 105 | 8.629359E-01 | 179 | 2.133482E-02 | 253 | 1.370959E-05 |
| 32 | 9.048374E+00 | 106 | 8.208500E-01 | 180 | 1.930454E-02 | 254 | 1.122446E-05 |
| 33 | 8.824969E+00 | 107 | 7.808167E-01 | 181 | 1.703620E-02 | 255 | 1.067704E-05 |
| 34 | 8.607080E+00 | 108 | 7.427358E-01 | 182 | 1.661557E-02 | 256 | 9.905554E-06 |
| 35 | 8.394570E+00 | 109 | 7.065121E-01 | 183 | 1.503439E-02 | 257 | 9.189814E-06 |
| 36 | 8.187308E+00 | 110 | 6.720551E-01 | 184 | 1.326780E-02 | 258 | 8.315287E-06 |
| 37 | 7.985162E+00 | 111 | 6.392786E-01 | 185 | 1.170880E-02 | 259 | 7.523983E-06 |

| **Group** | **Upper bound** [MeV] | **Group** | **Upper bound** [MeV] | **Group** | **Upper bound** [MeV] | **Group** | **Upper bound** [MeV] |
|---|---|---|---|---|---|---|---|
| 38 | 7.788008E+00 | 112 | 6.081006E-01 | 186 | 1.113775E-02 | 260 | 6.475952E-06 |
| 39 | 7.595721E+00 | 113 | 5.784432E-01 | 187 | 1.033298E-02 | 261 | 6.160116E-06 |
| 40 | 7.408182E+00 | 114 | 5.502322E-01 | 188 | 9.118820E-03 | 262 | 5.346430E-06 |
| 41 | 7.225274E+00 | 115 | 5.366469E-01 | 189 | 8.047330E-03 | 263 | 5.043477E-06 |
| 42 | 7.046881E+00 | 116 | 5.233971E-01 | 190 | 7.465858E-03 | 264 | 4.000000E-06 |
| 43 | 6.872893E+00 | 117 | 5.104743E-01 | 191 | 7.101744E-03 | 265 | 3.927860E-06 |
| 44 | 6.703200E+00 | 118 | 4.978707E-01 | 192 | 6.267267E-03 | 266 | 3.300000E-06 |
| 45 | 6.647573E+00 | 119 | 4.735892E-01 | 193 | 5.530844E-03 | 267 | 3.059020E-06 |
| 46 | 6.592406E+00 | 120 | 4.504920E-01 | 194 | 5.004514E-03 | 268 | 2.600000E-06 |
| 47 | 6.537698E+00 | 121 | 4.285213E-01 | 195 | 4.528272E-03 | 269 | 2.382370E-06 |
| 48 | 6.376282E+00 | 122 | 4.076220E-01 | 196 | 4.307425E-03 | 270 | 2.100000E-06 |
| 49 | 6.218851E+00 | 123 | 3.877421E-01 | 197 | 4.097350E-03 | 271 | 1.855390E-06 |
| 50 | 6.065307E+00 | 124 | 3.688317E-01 | 198 | 3.707435E-03 | 272 | 1.670000E-06 |
| 51 | 5.915554E+00 | 125 | 3.508435E-01 | 199 | 3.526622E-03 | 273 | 1.440000E-06 |
| 52 | 5.769498E+00 | 126 | 3.337327E-01 | 200 | 3.354626E-03 | 274 | 1.300000E-06 |
| 53 | 5.488116E+00 | 127 | 3.174564E-01 | 201 | 3.035391E-03 | 275 | 1.123000E-06 |
| 54 | 5.220458E+00 | 128 | 3.096183E-01 | 202 | 2.863392E-03 | 276 | 1.020000E-06 |
| 55 | 4.965853E+00 | 129 | 3.019738E-01 | 203 | 2.746536E-03 | 277 | 8.764250E-07 |
| 56 | 4.843246E+00 | 130 | 2.945181E-01 | 204 | 2.612586E-03 | 278 | 8.194500E-07 |
| 57 | 4.607038E+00 | 131 | 2.872464E-01 | 205 | 2.485168E-03 | 279 | 6.825600E-07 |
| 58 | 4.493290E+00 | 132 | 2.801543E-01 | 206 | 2.248673E-03 | 280 | 6.250000E-07 |
| 59 | 4.274149E+00 | 133 | 2.732372E-01 | 207 | 2.034684E-03 | 281 | 5.400000E-07 |
| 60 | 4.065697E+00 | 134 | 2.599113E-01 | 208 | 1.841058E-03 | 282 | 4.139900E-07 |
| 61 | 3.867410E+00 | 135 | 2.472353E-01 | 209 | 1.665858E-03 | 283 | 3.000000E-07 |
| 62 | 3.678794E+00 | 136 | 2.351775E-01 | 210 | 1.584613E-03 | 284 | 1.890000E-07 |
| 63 | 3.499377E+00 | 137 | 2.237077E-01 | 211 | 1.507331E-03 | 285 | 1.400000E-07 |
| 64 | 3.328711E+00 | 138 | 2.127974E-01 | 212 | 1.433817E-03 | 286 | 1.000000E-07 |
| 65 | 3.246525E+00 | 139 | 2.024191E-01 | 213 | 1.363889E-03 | 287 | 5.800000E-08 |
| 66 | 3.166368E+00 | 140 | 1.925470E-01 | 214 | 1.234098E-03 | 288 | 4.200000E-08 |
| 67 | 3.088190E+00 | 141 | 1.831564E-01 | 215 | 1.010394E-03 | 289 | 3.000000E-08 |
| 68 | 3.011942E+00 | 142 | 1.742237E-01 | 216 | 9.611165E-04 | 290 | 2.000000E-08 |
| 69 | 2.865048E+00 | 143 | 1.699221E-01 | 217 | 9.142423E-04 | 291 | 1.500000E-08 |
| 70 | 2.725318E+00 | 144 | 1.657268E-01 | 218 | 7.485183E-04 | 292 | 1.000000E-08 |
| 71 | 2.592403E+00 | 145 | 1.616349E-01 | 219 | 6.772874E-04 | 293 | 6.900000E-09 |
| 72 | 2.465970E+00 | 146 | 1.576442E-01 | 220 | 5.829466E-04 | 294 | 5.000000E-09 |
| 73 | 2.425211E+00 | 147 | 1.499558E-01 | 221 | 4.539993E-04 | 295 | 3.000000E-09 |
| 74 | 2.385126E+00 | 148 | 1.426423E-01 | 222 | 3.717032E-04 | | 1.000010E-11 |

*Table F.1: Energy bounds of the 295 group structure*

Appendix G

# Input files for the generation of an ECCOLIB for Pb-208

## G.1 NJOY input file for generating a 1968 GENDF for Pb-208

```
moder
20 -21
reconr
-21 -22
'pendf Pb208 JEFF-3.1'/
8237/
.001/
0/
broadr
-21 -22 -23
8237 5/
.001/
293.6 573.6 973.6 1473.6 2973.6/
0/
unresr
-21 -23 -24
8237 5 1 0/
293.6 573.6 973.6 1473.6 2973.6/
1.e+10/
0/
thermr
0 -24 -25
0 8237 8 5 1 0 0 1 221 0/
293.6 573.6 973.6 1473.6 2973.6/
0.001 4.0/
groupr
-21 -25 0 -26
8237 20 0 4 1 5 1 0/ ECCO-1968 P1 5 TEMP
'gendf Pb208 JEFF-3.1'/
293.6 573.6 973.6 1473.6 2973.6/
1.e+10/
0.1 0.0253 1.32E+06 1.29E+06/
3/
3 221/ free gas
6/
6 221/ free gas
0/
3/
3 221/ free gas
6 221/ free gas
0/
3/
3 221/ free gas
```

```
6 221/ free gas
0/
3/
3 221/ free gas
6 221/ free gas
0/
3/
3 221/ free gas
6 221/ free gas
0/
0/
moder
-26 27
stop
```

## G.2 NJOY input file for generating a 295 GENDF for Pb-208

```
moder
20 -21
reconr
-21 -22
'pendf Pb208 JEFF-3.1'/
8237/
.001/
0/
broadr
-21 -22 -23
8237 5/
.001/
293.6 573.6 973.6 1473.6 2973.6/
0/
unresr
-21 -23 -24
8237 5 1 0/
293.6 573.6 973.6 1473.6 2973.6/
1.e+10/
0/
thermr
0 -24 -25
0 8237 8 5 1 0 0 1 221 0/
293.6 573.6 973.6 1473.6 2973.6/
0.001 4.0/
groupr
-21 -25 0 -26
8237 1 0 4 1 5 1 0/ ECCO-1968 P1 5 TEMP
'gendf Pb208 JEFF-3.1'/
293.6 573.6 973.6 1473.6 2973.6/
1.e+10/
295 /
1.0000100E-05 3.0000000E-03 5.0000000E-03 6.9000000E-03
1.0000000E-02 1.5000000E-02 2.0000000E-02 3.0000000E-02
4.2000000E-02 5.8000000E-02 1.0000000E-01 1.4000000E-01
1.8900000E-01 3.0000000E-01 4.1399000E-01 5.4000000E-01
6.2500000E-01 6.8256000E-01 8.1945000E-01 8.7642500E-01
1.0200000E+00 1.1230000E+00 1.3000000E+00 1.4400000E+00
1.6700000E+00 1.8553900E+00 2.1000000E+00 2.3823700E+00
2.6000000E+00 3.0590200E+00 3.3000000E+00 3.9278600E+00
4.0000000E+00 5.0434770E+00 5.3464300E+00 6.1601160E+00
6.4759520E+00 7.5239830E+00 8.3152870E+00 9.1898140E+00
9.9055540E+00 1.0677040E+01 1.1224460E+01 1.3709590E+01
1.5928270E+01 1.7603460E+01 1.9454840E+01 2.2603290E+01
2.4980500E+01 2.7607730E+01 2.9023200E+01 3.0511260E+01
3.3720150E+01 3.7266530E+01 4.0169000E+01 4.5517440E+01
4.7851170E+01 5.1578020E+01 5.5595130E+01 6.1442120E+01
6.7904050E+01 7.5673570E+01 7.8893250E+01 9.1660880E+01
```

```
1.0130090E+02 1.3007300E+02 1.3674200E+02 1.4862540E+02
1.6701700E+02 2.0399500E+02 2.1445410E+02 2.7536450E+02
3.0432480E+02 3.5357500E+02 3.7170320E+02 4.5399930E+02
5.8294660E+02 6.7728740E+02 7.4851830E+02 9.1424230E+02
9.6111650E+02 1.0103940E+03 1.2340980E+03 1.3638890E+03
1.4338170E+03 1.5073310E+03 1.5846130E+03 1.6658580E+03
1.8410580E+03 2.0346840E+03 2.2486730E+03 2.4851680E+03
2.6125860E+03 2.7465360E+03 2.8633920E+03 3.0353910E+03
3.3546260E+03 3.5266220E+03 3.7074350E+03 4.0973500E+03
4.3074250E+03 4.5282720E+03 5.0045140E+03 5.5308440E+03
6.2672670E+03 7.1017440E+03 7.4658580E+03 8.0473300E+03
9.1188200E+03 1.0332980E+04 1.1137750E+04 1.1708800E+04
1.3267800E+04 1.5034390E+04 1.6615570E+04 1.7036200E+04
1.9304540E+04 2.1334820E+04 2.1874910E+04 2.3578620E+04
2.4175520E+04 2.4787520E+04 2.6058410E+04 2.7394450E+04
2.8087940E+04 2.9283000E+04 3.1827810E+04 3.4306690E+04
3.5175170E+04 3.6065630E+04 3.6978640E+04 4.0867710E+04
4.6309190E+04 5.2475180E+04 5.5165640E+04 5.6562170E+04
5.9462170E+04 6.2510860E+04 6.7379470E+04 7.6350940E+04
8.2297470E+04 8.6516950E+04 9.8036550E+04 1.1109000E+05
1.1678570E+05 1.2277340E+05 1.2906810E+05 1.3568560E+05
1.4264230E+05 1.4995580E+05 1.5764420E+05 1.6163490E+05
1.6572680E+05 1.6992210E+05 1.7422370E+05 1.8315640E+05
1.9254700E+05 2.0241910E+05 2.1279740E+05 2.2370770E+05
2.3517750E+05 2.4723530E+05 2.5991130E+05 2.7323720E+05
2.8015430E+05 2.8724640E+05 2.9451810E+05 3.0197380E+05
3.0961830E+05 3.1745640E+05 3.3373270E+05 3.5084350E+05
3.6883170E+05 3.8774210E+05 4.0762200E+05 4.2852130E+05
4.5049200E+05 4.7358920E+05 4.9787070E+05 5.1047430E+05
5.2339710E+05 5.3664690E+05 5.5023220E+05 5.7844320E+05
6.0810060E+05 6.3927860E+05 6.7205510E+05 7.0651210E+05
7.4273580E+05 7.8081670E+05 8.2085000E+05 8.6293590E+05
9.0717950E+05 9.5369160E+05 9.6167230E+05 9.7783440E+05
1.0025880E+06 1.0539920E+06 1.1080320E+06 1.1648420E+06
1.1943300E+06 1.2245640E+06 1.2873490E+06 1.3533530E+06
1.4227410E+06 1.4956860E+06 1.5335500E+06 1.5723720E+06
1.6121760E+06 1.6529890E+06 1.7377390E+06 1.8268350E+06
1.8730820E+06 1.9204990E+06 1.9691170E+06 2.0189650E+06
2.1224800E+06 2.2313020E+06 2.2688020E+06 2.3069320E+06
2.3457030E+06 2.3653320E+06 2.3851260E+06 2.4252110E+06
2.4659700E+06 2.5924030E+06 2.7253180E+06 2.8650480E+06
3.0119420E+06 3.0881900E+06 3.1663680E+06 3.2465250E+06
3.3287110E+06 3.4993770E+06 3.6787940E+06 3.8674100E+06
4.0656970E+06 4.2741490E+06 4.4932900E+06 4.6070380E+06
4.8432460E+06 4.9658530E+06 5.2204580E+06 5.4881160E+06
5.7694980E+06 5.9155540E+06 6.0653070E+06 6.2188510E+06
6.3762820E+06 6.5376980E+06 6.5924060E+06 6.6475730E+06
6.7032000E+06 6.8728930E+06 7.0468810E+06 7.2252740E+06
7.4081820E+06 7.5957210E+06 7.7880080E+06 7.9851620E+06
8.1873080E+06 8.3945700E+06 8.6070800E+06 8.8249690E+06
9.0483740E+06 9.2774350E+06 9.5122940E+06 9.7530990E+06
1.0000000E+07 1.0253150E+07 1.0512710E+07 1.0778840E+07
1.1051710E+07 1.1331480E+07 1.1618340E+07 1.1912460E+07
1.2214030E+07 1.2523230E+07 1.2840250E+07 1.3165310E+07
1.3498590E+07 1.3840310E+07 1.4190680E+07 1.4549910E+07
1.4918250E+07 1.5295900E+07 1.5683120E+07 1.6080140E+07
1.6487210E+07 1.6904590E+07 1.7332530E+07 1.7771310E+07
1.8221190E+07 1.8682460E+07 1.9155410E+07 1.9640330E+07
0.1 0.0253 1.32E+06 1.29E+06/
3/
3 221/ free gas
6/
6 221/ free gas
0/
3/
3 221/ free gas
```

```
    6 221/ free gas
    0/
    3/
    3 221/ free gas
    6 221/ free gas
    0/
    3/
    3 221/ free gas
    6 221/ free gas
    0/
    3/
    3 221/ free gas
    6 221/ free gas
    0/
    0/
    moder
    -26 27
    stop
```

## G.3 CALENDF input file for generating a 1968 groups Probability Table for Pb-208

```
CALENDF
    MODIFOPT LCORSCT .FALSE.
    MODIFOPT LFORMRF .FALSE.
    MODIFOPT LFORMUR .FALSE. 1
    MODIFOPT LPSTPOS .TRUE.
    ENERGIES 1.0E-5 20.0E+6
    MAILLAGE READ
    ECCO1968
    SPECTRE
    3 zones
    1.32E+6 1.29E+6
    0.1 -1
    0. 293.
    TEFF 293.6
    NDIL 1
    1.0E+10
    NFEV 9 8237 '../../NDL/Jeff_3_1_endf/JEFF31N8237_0.ASC'
    SORTies
        NFSFRL 0 './Pb208293.6.sfr'
        NFSF 12 './Pb208293.6.sf'
        NFSFTP 11 './Pb208293.6.sft'
        NFTP 10 './Pb208293.6.tp'
        NFCS 18 './Pb208293.6.cs'
    IPRECI 4
    NIMP 0 80
REGROUTP
        NFTP 10 './Pb208293.6.tp'
        NFTPR 17 './Pb208293.6.tpr'
    NIMP 0 80
REGROUSF
        NFSF 12 './Pb208293.6.sf'
        NFSFR 13 './Pb208293.6.sfdr'
    NIMP 0 80
REGROUSF
        NFSF 11 './Pb208293.6.sft'
        NFSFR 14 './Pb208293.6.sftr'
    NIMP 0 80
END
```

## G.4 CALENDF input file for generating a 295 groups Probability Table for Pb-208

```
CALENDF
    MODIFOPT LCORSCT .FALSE.
    MODIFOPT LFORMRF .FALSE.
    MODIFOPT LFORMUR .TRUE.
    MODIFOPT LPSTPOS .TRUE.
    ENERGIES 1.0E-5 20.0E+6
    MAILLAGE GENERE
    3 zones
    92  1.32E+6 1.9640330E+07
    1.9155410E+07 1.8682460E+07 1.8221190E+07 1.7771310E+07
    1.7332530E+07 1.6904590E+07 1.6487210E+07 1.6080140E+07
    1.5683120E+07 1.5295900E+07 1.4918250E+07 1.4549910E+07
    1.4190680E+07 1.3840310E+07 1.3498590E+07 1.3165310E+07
    1.2840250E+07 1.2523230E+07 1.2214030E+07 1.1912460E+07
    1.1618340E+07 1.1331480E+07 1.1051710E+07 1.0778840E+07
    1.0512710E+07 1.0253150E+07 1.0000000E+07 9.7530990E+06
    9.5122940E+06 9.2774350E+06 9.0483740E+06 8.8249690E+06
    8.6070800E+06 8.3945700E+06 8.1873080E+06 7.9851620E+06
    7.7880080E+06 7.5957210E+06 7.4081820E+06 7.2252740E+06
    7.0468810E+06 6.8728930E+06 6.7032000E+06 6.6475730E+06
    6.5924060E+06 6.5376980E+06 6.3762820E+06 6.2188510E+06
    6.0653070E+06 5.9155540E+06 5.7694980E+06 5.4881160E+06
    5.2204580E+06 4.9658530E+06 4.8432460E+06 4.6070380E+06
    4.4932900E+06 4.2741490E+06 4.0656970E+06 3.8674100E+06
    3.6787940E+06 3.4993770E+06 3.3287110E+06 3.2465250E+06
    3.1663680E+06 3.0881900E+06 3.0119420E+06 2.8650480E+06
    2.7253180E+06 2.5924030E+06 2.4659700E+06 2.4252110E+06
    2.3851260E+06 2.3653320E+06 2.3457030E+06 2.3069320E+06
    2.2688020E+06 2.2313020E+06 2.1224800E+06 2.0189650E+06
    1.9691170E+06 1.9204990E+06 1.8730820E+06 1.8268350E+06
    1.7377390E+06 1.6529890E+06 1.6121760E+06 1.5723720E+06
    1.5335500E+06 1.4956860E+06 1.4227410E+06 1.3533530E+06
    193 -1 1.3533530E+06
    1.2873490E+06 1.2245640E+06 1.1943300E+06 1.1648420E+06
    1.1080320E+06 1.0539920E+06 1.0025880E+06 9.7783440E+05
    9.6167230E+05 9.5369160E+05 9.0717950E+05 8.6293590E+05
    8.2085000E+05 7.8081670E+05 7.4273580E+05 7.0651210E+05
    6.7205510E+05 6.3927860E+05 6.0810060E+05 5.7844320E+05
    5.5023220E+05 5.3664690E+05 5.2339710E+05 5.1047430E+05
    4.9787070E+05 4.7358920E+05 4.5049200E+05 4.2852130E+05
    4.0762200E+05 3.8774210E+05 3.6883170E+05 3.5084350E+05
    3.3373270E+05 3.1745640E+05 3.0961830E+05 3.0197380E+05
    2.9451810E+05 2.8724640E+05 2.8015430E+05 2.7323720E+05
    2.5991130E+05 2.4723530E+05 2.3517750E+05 2.2370770E+05
    2.1279740E+05 2.0241910E+05 1.9254700E+05 1.8315640E+05
    1.7422370E+05 1.6992210E+05 1.6572680E+05 1.6163490E+05
    1.5764420E+05 1.4995580E+05 1.4264230E+05 1.3568560E+05
    1.2906810E+05 1.2277340E+05 1.1678570E+05 1.1109000E+05
    9.8036550E+04 8.6516950E+04 8.2297470E+04 7.6350940E+04
    6.7379470E+04 6.2510860E+04 5.9462170E+04 5.6562170E+04
    5.5165640E+04 5.2475180E+04 4.6309190E+04 4.0867710E+04
    3.6978640E+04 3.6065630E+04 3.5175170E+04 3.4306690E+04
    3.1827810E+04 2.9283000E+04 2.8087940E+04 2.7394450E+04
    2.6058410E+04 2.4787520E+04 2.4175520E+04 2.3578620E+04
    2.1874910E+04 2.1334820E+04 1.9304540E+04 1.7036200E+04
    1.6615570E+04 1.5034390E+04 1.3267800E+04 1.1708800E+04
    1.1137750E+04 1.0332980E+04 9.1188200E+03 8.0473300E+03
    7.4658580E+03 7.1017440E+03 6.2672670E+03 5.5308440E+03
    5.0045140E+03 4.5282720E+03 4.3074250E+03 4.0973500E+03
    3.7074350E+03 3.5266220E+03 3.3546260E+03 3.0353910E+03
    2.8633920E+03 2.7465360E+03 2.6125860E+03 2.4851680E+03
    2.2486730E+03 2.0346840E+03 1.8410580E+03 1.6658580E+03
```

```
    1.5846130E+03 1.5073310E+03 1.4338170E+03 1.3638890E+03
    1.2340980E+03 1.0103940E+03 9.6111650E+02 9.1424230E+02
    7.4851830E+02 6.7728740E+02 5.8294660E+02 4.5399930E+02
    3.7170320E+02 3.5357500E+02 3.0432480E+02 2.7536450E+02
    2.1445410E+02 2.0399500E+02 1.6701700E+02 1.4862540E+02
    1.3674200E+02 1.3007300E+02 1.0130090E+02 9.1660880E+01
    7.8893250E+01 7.5673570E+01 6.7904050E+01 6.1442120E+01
    5.5595130E+01 5.1578020E+01 4.7851170E+01 4.5517440E+01
    4.0169000E+01 3.7266530E+01 3.3720150E+01 3.0511260E+01
    2.9023200E+01 2.7607730E+01 2.4980500E+01 2.2603290E+01
    1.9454840E+01 1.7603460E+01 1.5928270E+01 1.3709590E+01
    1.1224460E+01 1.0677040E+01 9.9055540E+00 9.1898140E+00
    8.3152870E+00 7.5239830E+00 6.4759520E+00 6.1601160E+00
    5.3464300E+00 5.0434770E+00 4.0000000E+00 3.9278600E+00
    3.3000000E+00 3.0590200E+00 2.6000000E+00 2.3823700E+00
    2.1000000E+00 1.8553900E+00 1.6700000E+00 1.4400000E+00
    1.3000000E+00 1.1230000E+00 1.0200000E+00 8.7642500E-01
    8.1945000E-01 6.8256000E-01 6.2500000E-01 5.4000000E-01
    4.1399000E-01 3.0000000E-01 1.8900000E-01 1.4000000E-01
    1.0000000E-01
    10 293.6 1.0000000E-01
    5.8000000E-02 4.2000000E-02 3.0000000E-02 2.0000000E-02
    1.5000000E-02 1.0000000E-02 6.9000000E-03 5.0000000E-03
    3.0000000E-03 1.0000100E-05
    TEFF 293.6
    NDIL 1
    1.0E+10
    NFEV 9 8237 '../../NDL/Jeff_3_1_endf/JEFF31N8237_0.ASC'
    SORTies
        NFSFRL 0 './Pb208293.6.sfr'
        NFSF 12 './Pb208293.6.sf'
        NFSFTP 11 './Pb208293.6.sft'
        NFTP 10 './Pb208293.6.tp'
        NFCS 18 './Pb208293.6.cs'
    IPRECI 4
    NIMP 0 80
REGROUTP
        NFTP 10 './Pb208293.6.tp'
        NFTPR 17 './Pb208293.6.tpr'
    NIMP 0 80
REGROUSF
        NFSF 12 './Pb208293.6.sf'
        NFSFR 13 './Pb208293.6.sfdr'
    NIMP 0 80
REGROUSF
        NFSF 11 './Pb208293.6.sft'
        NFSFR 14 './Pb208293.6.sftr'
    NIMP 0 80
END
```

## G.5 MERGE input file for generating a 1968 GENDF* for Pb-208

```
5
20 21 22 23 24 25 26
1968*0  /
/
/
```

## G.6 GECCO input file for generating a 1968 ECCOLIB for Pb-208

```
20 0 0 40 41
```

```
8192 8 16 8
    73
    7 7 8 8 8 8 8 9 10 9 9
    9 9 9 9 9 11 16 17 17 18 18 18
    18 19 19 19 19 20 20 20 20 20 21 21
    21 21 22 22 22 23 23 23 24 24 25 25
    26 26 27 28 28 29 30 31 32 34 35 36
    38 40 43 43 48 55 63 74 90 150 69 15
    67 49
'ECCO-1968 JEFF-3.1 LIBRARY'
'JEFF-3.1'
8237
'NON-FISSILE'
1
221
8237 207.9766 'Pb208' 'Pb'
0.000 3.937 0.000 0.000 0.000E+00
0.602214 1.602176E-13 0.0
0
0
0
0
    1
    1968
    0 0
0
```

# References


[1] Igor L. Pioro and Gilles H. Rodriguez. "Chapter 2 - Generation IV International Forum (GIF)". In: *Handbook of Generation IV Nuclear Reactors (Second Edition)*. Ed. by Igor L. Pioro. Second Edition. Woodhead Publishing Series in Energy. Woodhead Publishing, 2023, pp. 111–132.

[2] Esam M.A. Hussein. "Emerging small modular nuclear power reactors: A critical review". In: *Physics Open* 5 (2020), p. 100038. ISSN: 2666-0326. DOI: https://doi.org/10.1016/j.physo.2020.100038. URL: https://www.sciencedirect.com/science/article/pii/S2666032620300259.

[3] Neil Todreas. "1 - Small modular reactors (SMRs) for producing nuclear energy: An introduction". In: *Handbook of Small Modular Nuclear Reactors (Second Edition)*. Ed. by Daniel T. Ingersoll and Mario D. Carelli. Second Edition. Woodhead Publishing Series in Energy. Woodhead Publishing, 2021, pp. 3–27.

[4] Gérald Rimpault, Danièle Plisson, J. Tommasi, R. Jacqmin, and Jean-Marie Rieunier. "THE ERANOS CODE AND DATA SYSTEM FOR FAST REACTOR NEUTRONIC ANALYSES". In: Nov. 2002.

[5] G Rimpault. "Algorithmic features of the ECCO Cell Code for treating heterogeneous fast reactor subassemblies". In: American Nuclear Society, Inc., La Grange Park, IL (United States), Dec. 1995.

[6] Autorité de sûreté nucléaire (ASN) and Institut de radioprotection et de sûreté nucléaire (IRSN). *Qualification of scientific computing tools used in the nuclear safety case – 1st barrier, Guide no. 28*. Tech. rep. Guide Nº 28. July 2017.

[7] G Rimpault, Y Peneliau, JF Vidal, S Mirotta, and A Gandini. *In depth uncertainty estimation of the neutron computational tools*. Tech. rep. 2015.

[8] Stephan Rahlfs. "Validation physique du nouveau code de cellule européen ECCO pour le calcul des coefficients de réactivité des réacteurs REP et RNR". PhD thesis. Aix-Marseille 1, 1995.

[9] Philippe Jacquet. "Nouvelles méthodes de modélisation neutronique des réacteurs rapides de quatrième Génération". Theses. Université de Grenoble, May 2011.

[10] *Neutronic analyses of the ALFRED LEADER core with deterministic (ECCO/ERANOS) and Monte Carlo (Serpent) codes*. Technical Report SICNUC–P000–037. Saluggia, Italy: ENEA, Centro Ricerche Saluggia, 2020.

[11] Salvatore Scarpati. "Benchmarking of ECCO calculations of LFR fuel assemblies by Monte Carlo calculations." July 2025.

[12] OECD Nuclear Energy Agency. *Lead-cooled Fast Reactor Benchmark (LFR)*. https://www.oecd-nea.org/jcms/pl_66836/lead-cooled-fast-reactor-benchmark-lfr. Access: May 2025.

[13] E E Lewis and W F Miller. *Computational methods of neutron transport*. John Wiley and Sons, Inc.,New York, NY, Jan. 1984.

[14] G. I. Bell and S. Glasstone. *Nuclear Reactor Theory*. 1970, Oct. 1970.

[15] R.V. Meghreblian and D.K. Holmes. *Reactor Analysis*. McGraw-Hill, 1960.

[16] James J. Duderstadt, Louis J. Hamilton, S. Moorthy, and C. C. Scott. *Nuclear Reactor Analysis by James J. Duderstadt and Louis J. Hamilton*. Vol. 24. 4. 1977, pp. 1983–1983.

[17] Antonio Galia. “A Dynamic Homogenization Method for Nuclear Reactor Core Calculations”. Theses. Université Paris-Saclay, 2020.
[18] Matteo Falabino. “Contribution to ray-effect mitigation in discrete-ordinates based transport solvers”. Theses. Université Grenoble Alpes [2020-....], Oct. 2022.
[19] Allan F Henry and Edward Melkonian. *Nuclear-Reactor Analysis*. American Institute of Physics, 1977.
[20] Nathan Gibson. “Novel Resonance Self-Shielding Methods for Nuclear Reactor Analysis”. PhD thesis. Jan. 2016.
[21] Mireille Coste-Delclaux, Cheikh M’Backé Diop, Fausto Malvagi, Anne Nicolas, et al. *Neutronics*. Commissariat à l’énergie atomique et aux énergies alternatives (CEA), 2015.
[22] Robert Macfarlane, Douglas W Muir, RM Boicourt, Albert Comstock Kahler III, and Jeremy Lloyd Conlin. *The NJOY nuclear data processing system, version 2016*. Tech. rep. Los Alamos National Laboratory (LANL), Los Alamos, NM (United States), 2017.
[23] Mireille Coste-Delclaux. “Modélisation du phénomène d’autoprotection dans le code de transport multigroupe APOLLO2”. PhD thesis. Paris, CNAM, 2006.
[24] R.J.J. Stammler and M.J. Abbate. *Methods of steady-state reactor physics in nuclear design*. Academic Press., Jan. 2025.
[25] Alain Hébert. *Applied Reactor Physics, 3rd ed*. Nov. 2024.
[26] W.M. Stacey. *Nuclear Reactor Physics*. Wiley, 2007.
[27] Jerome Spanier and Ely M Gelbard. *Monte Carlo principles and neutron transport problems*. Courier Corporation, 2008.
[28] Alireza Haghighat. *Monte Carlo methods for particle transport*. Crc Press, 2020.
[29] D. Honde, P. Palmiotti, J.M. Rieunier, and G. Rimpault. *ERANOS : Manuel des Méthodes — Les Calculs de Perturbations et les Analyses de Sensibilité*. Note Technique. 1996.
[30] J TOMMASI. “ERANOS USER’S MANUAL–APPLICATIONS OF PERTURBATION THEORY WITH FINITE DIFFERENCE DIFFUSION AND SN TRANSPORT FLUX SOLVERS”. In: *CEA Technical* (2003).
[31] Tanguy Courau. *Application de la théorie des perturbations généralisées aux calculs de cellules utilisant la méthode des probabilités de collision*. École Polytechnique de Montréal, 2001.
[32] Jean Michel Ruggieri et al. “ERANOS 2.1: International code system for GEN IV fast reactor analysis”. In: *Proceedings of ICAPP*. Vol. 6. 2006, pp. 2432–2439.
[33] G Rimpault et al. “Physics documentation of ERANOS: the ECCO cell code”. In: *CEA Technical Note RT-SPRC-LEPh-97-001* (1997).
[34] Pietro Mosca. “Conception et développement d’un mailleur énergétique adaptatif pour la génération des bibliothèques multigroupes des codes de transport”. PhD thesis. Université Paris Sud-Paris XI, 2009.
[35] Liangzhi Cao, Hongchun Wu, Qian Zhang, Qingming He, and Tiejun Zu. *Resonance Self-Shielding Calculation Methods in Nuclear Reactors*. Woodhead Publishing, 2022.
[36] Jean-Christophe Sublet and Pierre Ribon. “A Probability Table Based Cross Section Processing System: CALENDF - 2001”. In: *Journal of Nuclear Science and Technology* 39.sup2 (2002), pp. 856–859.
[37] Pierre Ribon and Jean-Marie Maillard. *Les tables de probabilité (application au traitement des sections efficaces pour la neutronique. premiere partie, dans l’hypothese statistique)*. Tech. rep. tech. rep., Note CEA-N-2185, 1986.
[38] Saverio Quaranta. “Benchmarking Acvities on the ALFRED Core with the Deterministic Neutronic Code ERANOS”. PhD thesis. Politecnico di Torino, 2025.
[39] Paul K Romano and Benoit Forget. “The OpenMC monte carlo particle transport code”. In: *Annals of Nuclear Energy* 51 (2013), pp. 274–281.
[40] Paul K Romano et al. “OpenMC: A state-of-the-art Monte Carlo code for research and development”. In: *Annals of Nuclear Energy* 82 (2015), pp. 90–97.

[41] David A Brown. *Endf-6 formats manual-data formats and procedures for the evaluated nuclear data files endf/b-vi, endf/b-vii and endf/b-viii*. Tech. rep. Brookhaven National Laboratory (BNL), Upton, NY (United States), 2023.
[42] Arjan JM Plompen et al. "The joint evaluated fission and fusion nuclear data library, JEFF-3.3". In: *The European Physical Journal A* 56 (2020), pp. 1–108.
[43] Arjan Koning and oters. "The JEFF-3.1 Nuclear Data Library - JEFF Report 21". In: (2006).
[44] J Ch Sublet, Ch Dean, and Daniele Plisson-Rieunier. *Eccolib-Jeff-3.1 libraries*. Tech. rep. CEA Cadarache, 2006.
[45] G. Rimpault et al. *Note Technique: The ECCO / JEF2 Library*. Tech. rep. CEA, 1992.
[46] Jean-Christophe Sublet. *Modifications to MERGE*. Tech. rep. CEA Cadarache, DEN/DER/SPRC.
[47] Jean-Christophe Sublet and Danielle Niddam. *GECCO: User Manual*. CEA, DEN/DER/SPRC and CS SI. 2003.
[48] D. Plisson-Rieunier. *Procédures de création et de modification des bibliothèques de données multi-corps pour ERANOS*. Note Technique. CEA, 2009.
[49] I. I. Bondarenko, M. N. Nikolaev, L. P. Abagyan, and N. O. Bazazyants. *Group Constants for Nuclear Reactor Calculations*. New York: Consultants Bureau, 1964.
[50] JP Both, H Derriennic, B Morillon, and JC Nimal. "A survey of TRIPOLI-4". In: (1994).
[51] Emeric Brun et al. "Tripoli-4®, CEA, EDF and AREVA reference Monte Carlo code". In: *SNA+ MC 2013-Joint International Conference on Supercomputing in Nuclear Applications+ Monte Carlo*. EDP Sciences. 2014, p. 06023.
[52] François-Xavier Hugot et al. "Overview of the TRIPOLI-4 Monte Carlo code, version 12". In: *EPJ Nuclear Sciences & Technologies* 10 (2024), p. 17.
[53] Jean-Christophe Sublet, Pierre Ribon, and Mireille Coste-Delclaux. *CALENDF-2010: User manual*. Tech. rep. Commissariat a l'energie Atomique-CEA (France), 2011.
[54] Go Chiba and Hironobu Unesaki. "Improvement of moment-based probability table for resonance self-shielding calculation". In: *Annals of Nuclear energy* 33.13 (2006), pp. 1141–1146.
[55] J Ch Sublet, Roger N Blomquist, Sedat Goluoglu, and Robert E Mac Farlane. *Unresolved resonance range cross section, probability tables and self shielding factor*. Tech. rep. CEA Saclay, 2009.
[56] Robert E MacFarlane, Roger M Blomquist, Dermott E Cullen, Edward Lent, and Jean Christophe Sublet. *A code comparison study for the bigten critical assembly*. Tech. rep. Technical Report LA-UR-08-4668, Los Alamos National Laboratory, 2008.
[57] C. J. Dean, C. R. Eaton, M. J. Grimstone, and B. Thom. *Production of an ECCO Library from JEF-1 Data*. Technical Report. CFSM, 1988.
[58] C. J. Dean and C. R. Eaton. *Generation of a Fine Group ECCO Library for U238 from JEF-1.1*. Technical Report. CFSM, 1989.
[59] Paul Romano and Sterling Harper. "Nuclear data processing capabilities in OpenMC". In: *EPJ Web of Conferences*. Vol. 146. 2017.
[60] Paul K. Romano and Adam G. Nelson. "Methods for processing and use of thermal neutron scattering data in OpenMC". In: *EPJ Web of Conferences*. Vol. 284. EPJ Web of Conferences. EDP Sciences, 2023, p. 17011.
[61] Albert Comstock Kahler. *Using NJOY to Create MCNP ACE Files and Visualize Nuclear Data*. Tech. rep. Los Alamos National Laboratory (LANL), Los Alamos, NM (United States), Oct. 2016.
[62] Leo B Levitt. "The probability table method for treating unresolved neutron resonances in Monte Carlo calculations". In: *Nuclear Science and Engineering* 49.4 (1972), pp. 450–457.
[63] OpenMC Development Team. *Neutron physics*. `https://docs.openmc.org/en/stable/methods/neutron_physics.html`. Accessed: 2025-07-22. 2024.
[64] M Frogheri, A Alemberti, and L Mansani. "The advanced lead fast reactor European demonstrator (ALFRED)". In: *Proceedings of the 15th International Topical Meeting on Nuclear Reactor Thermal—Hydraulics, Pisa, Italy*. 2013, pp. 12–17.

[65] Alessandro Alemberti. “Status of the ALFRED Project”. In: *ESNII Biennial conference*. 2021, pp. 17–19.

[66] G Grasso et al. “The core design of ALFRED, a demonstrator for the European lead-cooled reactors”. In: *Nuclear Engineering and Design* 278 (2014), pp. 287–301.

[67] CJ Gho and G Palmiotti. “BISTRO: Bidimensional Sn TRansport Optimise. Un programme bidimensionnel de transport Sn aux differences finies. Note n 1. Definition des algorithms pour la geometrie XY”. In: *CEA Technical Note NT-SPRC-LEPh-84-270* (1984).

[68] CGHOG PALMIOTTI. “BISTRO-NOTE N 2”. In: *CEA Technical Note NT-SPRC-LEPh-85-202* 88 (1984), p. 8.

[69] J Tommasi, JF Lebrat, P Archier, and JM Ruggieri. “Status of ERANOS-2 code system validation for sodium fast reactor applications”. In: *Physor Conference, Pittsburgh, USA*. 2010.

[70] M. Griseri, L. Fiorito, A. Stankovskiy, and G. Van den Eynde. “Nuclear data uncertainty propagation on a sodium fast reactor”. In: *Nuclear Engineering and Design* 324 (2017), pp. 122–130. ISSN: 0029-5493. DOI: https://doi.org/10.1016/j.nucengdes.2017.08.018. URL: https://www.sciencedirect.com/science/article/pii/S0029549317304016.

[71] Ouadie Kabach et al. “Processing of the ENDF/B-VIII. 0$\beta$6 neutron cross-section data library and testing with critical benchmarks, OKTAVIAN shielding benchmarks and the doppler reactivity defect benchmarks”. In: *Ann. Univ. Craiova, Phys* 28 (2018), pp. 78–98.

[72] L Thilagam et al. “Doppler coefficient of reactivity-benchmark calculations for different enrichments of UO2”. In: *Joint International Topical Meeting on Mathematics & Computation and Supercomputing in Nuclear Applications, Monterey, California*. Citeseer. 2007.

[73] Kyung-O Kim and Daeseong Jo. “Analysis of Doppler coefficients for typical PWR UO2 and MTR U3Si2-Al fuels using ENDF/B-VI and VII”. In: *Annals of Nuclear Energy* 85 (2015), pp. 1024–1028.

[74] P. Romojaro, R. Jacqmin, and E. González. *Report on ESFR, MYRRHA, and ALFRED Sensitivity and Impact Studies*. Tech. rep. SANDA Project, Solving Challenges in Nuclear Data for the Safety of European Nuclear Facilities, 2022.

[75] Luca Fiorito, Matteo Zanetti, Federico Grimaldi, and Gert van den Eynde. “Uncertainty Quantification for the Doppler Reactivity Feedback Coefficient of MYRRHA”. In: *Nuclear Science and Engineering* 199.sup1 (2025), S56–S72.

[76] S. Panizo et al. “Sensitivity and uncertainty analyses for advanced nuclear systems (ALFRED, ASTRID, ESFR and MYRRHA)”. In: *Progress in Nuclear Energy* 172 (2024), p. 105207. ISSN: 0149-1970. DOI: https://doi.org/10.1016/j.pnucene.2024.105207. URL: https://www.sciencedirect.com/science/article/pii/S0149197024001574.

[77] Jaakko Leppänen, Maria Pusa, Tuomas Viitanen, Ville Valtavirta, and Toni Kaltiaisenaho. “The Serpent Monte Carlo code: Status, development and applications in 2013”. In: *Annals of Nuclear Energy* 82 (2015), pp. 142–150.

[78] Forrest B Brown et al. “MCNP version 5”. In: *Trans. Am. Nucl. Soc* 87.273 (2002), pp. 02–3935.

[79] Saeed Zare Ganjaroodi and Ehsan Zarifi. “Neutronic investigation of ALFRED lead-Cooled fast reactor core using monte carlo modeling”. In: *Atomic Energy* 134.3 (2023), pp. 264–274.

[80] D.A. Brown et al. “ENDF/B-VIII.0: The 8th Major Release of the Nuclear Reaction Data Library with CIELO-project Cross Sections, New Standards and Thermal Scattering Data”. In: *Nuclear Data Sheets* 148 (2018), pp. 1–142.

[81] P Tamagno, WFG Van Rooijen, T Takeda, and M Konomura. “Sensitivity analysis of Monju using ERANOS with JENDL-4.0”. In: *PHYSOR 2012 Advances in Reactor Physics* (2012).

[82] WFG van Rooijen. “Analysis of the MZA/MZB benchmarks with modern nuclear data sets”. In: *Annals of Nuclear Energy* 62 (2013), pp. 504–525.

[83] Keiichi Shibata et al. “JENDL-4.0: a new library for nuclear science and engineering”. In: *Journal of Nuclear Science and Technology* 48.1 (2011), pp. 1–30.

[84] OECD Nuclear Energy Agency. *The JEFF-3.1.1 Nuclear Data Library: Validation Results from JEF-2.2 to JEFF-3.1.1*. Tech. rep. JEFF Report 22. Accessed: 2025-08-07. Paris, France: OECD/NEA, 2009. URL: https://www.oecd-nea.org/dbdata/jeff/jeffreport-22/.

[85] Mark B Chadwick et al. “ENDF/B-VII. 1 nuclear data for science and technology: cross sections, covariances, fission product yields and decay data”. In: *Nuclear data sheets* 112.12 (2011), pp. 2887–2996.

[86] John Rowlands, Atsushi Zukeran, Masayuki Nakagawa, Peter Smith, and Udo K Wehmann. *The ZEBRA MOZART programme. part 1. MZA and MZB Zebra assemblies 11 and 12*. 2008.

[87] J-Ch. Sublet and P. Ribon. “Current Status of CALENDF-2005”. In: *Proceedings of the WONDER 2006 Workshop*. CEA Cadarache, France, 2006.

[88] J.R. Lamarsh. *Introduction to Nuclear Reactor Theory*. Addison-Wesley Publishing Company, 1966.

[89] Luc Wuytack. “Padé approximation and its applications”. In: (1979).